Arts & Sciences Electronic Theses and Dissertations

Arts & Sciences

Winter 1-15-2021

Prodrug Activation in Staphylococci and the Implications for Antimicrobial Development

Justin J. Miller
Washington University in St. Louis

WASHINGTON UNIVERSITY IN ST. LOUIS

Division of Biology and Biomedical Sciences
Biochemistry, Biophysics, and Molecular Biology

Dissertation Examination Committee:
Audrey R. Odom John, Chair
Joseph Jez, Co-chair
Juliane Bubeck-Wardenburg
Daniel Goldberg
Jeffrey Henderson
Timothy Wencewicz

Prodrug Activation in Staphylococci and the Implications for Antimicrobial Development
by
Justin Miller

A dissertation presented to
The Graduate School
of Washington University in
partial fulfillment of the
requirements for the degree
of Doctor of Philosophy

January 2021
St. Louis, Missouri

Table of Contents

List of Figures

Chapter 4: Establishing the structural basis and feasibility for S. aureus targeted lipophilic prodrugs

Chapter 5: Conclusion

Appendix A: FrmB mutational studies

Appendix B: Carboxy ester prodrug activation by Plasmodium falciparum

Appendix C: Volatile Biomarkers of Malaria Infection

Appendix D: The malaria metabolite HMBPP does not trigger erythrocyte terpene release

List of Tables

Appendix A: FrmB mutational studies

Appendix C: Volatile Biomarkers of Malaria Infection

List of Abbreviations

μM	micromolar
μmol	micromole
Å	angstrom
A, Ala	alanine
Abs	absorbance
AU	arbitrary units
BOM	Benzoyloxymethyl
CDP-ME	4-diphosphocytidyl-2-C-methylerythritol
CHMI	controlled human malaria infection
D, Asp	aspartic acid
DHAP	dihydroxyacetone phosphate
DHAP	dihydroxyacetone phosphate
DMSO	dimethyl sulfoxide
DNA	deoxyribonucleic acid
DOXP	1-deoxy-D-xylulose 5-phosphate
DPBS	Dulbecco's phosphate-buffered saline
DTNB	5,5'-Dithiosbis(2-nitrobenzoic acid)
DTT	dithiothreitol
DXR	deoxyxylulose phosphate reductoisomerase
Ec	*Escherichia coli*
EDTA	Ethylenediaminetetraacetic acid
ENO	enolase
ERJ	isoprenoid biosynthesis inhibitor, analog of fosmidomycin
F, Phe	phenylalanine
FDA	Food and Drug Administration
FphF	Fluorophosphonate F (FrmB)
FrmB	S-formylglutathione hydrolase
FSM	fosmidomycin
G, Gly	glycine
GAP	glyceraldehyde-3-phosphate
GC-MS	gas chromatography-mass spectrometry
GloB	hydroxyacylglutathione hydrolase
GlpT	glycerol-3-phosphate/Pi antiporter
GNU	gene novelty unit
GPP	geranyl pyrophosphate
H, his	histidine
HCV	Hepatitis C Virus
HEX	inhibitor of enolase
HGXPRT	hypoxanthine-guanine-xanthine-phosphoribosyltransferase
HIV	Human immuno deficiency virus
HMBPP	(E)-4-Hydroxy-3-methyl-but-2-enyl pyrophosphate

HRP2	histidine rich protein 2
Hs	*Homo sapiens*
HSQC	heteronuclear single quantum correlation
I, Ile	Isoleucine
IC_{50}	half-maximal inhibtory concentration
ImmHP	Immucillin-H 5'phosphate
IPP	isopentenyl pyrophosphate
IPTG	isopropyl-β-D-thiogalactoside
IRB	institutional review board
K, Lys	lysine
k_{cat}	turnover number
kD	kilodaltons
K_m	Michaelis-Mententen constant
L	liter
L, Leu	leucine
LAMP	loop-attenuated isothermal amplification
LB	Luria broth
LC-MS/MS	liquid chromatography with tandem mass spectrometry
LMIC	low and middle income countries
MACS	magnetic cell fractionation system
MEcPP	2-C-methyl-D-erythritol 2,4-cyclopyrophosphate
MEP	methylerythritol phosphate pathway
mg	milligram
MIC	minimum inhibitory concentration
min	minute
mM	millimolar
MRSA	methicillin-resistant *S. aureus*
Mtb	*Mycobacterium tuberculosis*
MW	molecular weight
N.A.	numerical apperature
NMR	nuclear magnetic resonance
NMR	nanomolar
OD_{600}	optical density at 600 nm
P, Pro	proline
PAMP	pathogen-associated molecular pattern
PBS	phosphate buffered saline
PCR	polymerase chain reaction
PDB	Protein Data Bank
Pf	*Plasmodium falciparum*
PfPARE	*Plasmodium falciparum* Prodrug Activation and Resistance Esterase
pmol	picomole
PMSF	phenylmethylsulfonyl fluoride

POM	pivaloyloxymethyl
Q, Glu	glutamine
R	placeholder for remainder of chemical molecule
R, Arg	arginine
r.m.s.d.	root mean squared deviation
RBC	red blood cell, erythrocyte
RDTs	rapid diagnostic tests
RNA	ribonucleic acid
RpoB	DNA-directed RNA polymerase subunit beta
S, Ser	serine
Sa, Ss, Sp	*Staphylococcus aureus, schleiferi, pseudintermedius*
SD	standard deviation
SEM	standard error of measurement
SeMet	selenomethione
SIG	Staphylococcus intermedius group
SNP	single nucleotide polhymorphism
SPME	solid phase microextraction
T, Thr	threonine
TNB	2-nitro-5-thiobenzoate
V, Val	valine
V_{max}	maximal enzyme velocity
VOC	volatile organic compound
WGS	whole genome sequencing
WHO	World Health Organization
WT	wild-type
X	premature truncation
Y, Tyr	tyrosine

<u>Acknowledgments</u>

This work would not have been possible without the advice, support, lessons, mentoring, and aid from my teachers, mentors, colleagues, friends, and family. A sincerest thank you to everyone who has helped me along my journey.

First and foremost, I am thankful for my thesis mentors, Audrey. Audrey has continuously been a source of energy, curiosity, and wisdom throughout my thesis work. Her excitement for science and confidence in me has always appeared to me, endless, for which I am eternally grateful. She has instilled in me the urge to always try to think bigger and push further. I have been continually impressed by her commitment to trainees- she always seems to have time to talk about science and future career directions, even whilst juggling a busy conference schedule or case load. Thank you, Audrey.

Thank you to Joseph Jez, who eagerly accepted me into his lab for the terminus of my thesis. Beyond being simply offering a desk to do my work, Joe has been incredibly generous with his time, knowledge, and resources. I am grateful for all the lessons learned in your lab and all of the tasty scones we've consumed at lab meetings. This thesis would not be what it is without Joe's mentorship. Thank you, Joe.

Many thanks to my thesis committee for their time, guidance, support, and valuable feedback. I have been lucky to have such an engaged and expert committee guiding both my scientific and personal development.

I am grateful for the many collaborators who have made this work possible. A special thanks to Cindy Dowd, Florian Muller, and Damon Osbourn for their thoughts on this project as it developed. A special thanks to Lizzy Muller and Petra Levin for their expertise and help on microfluidics and single-cell analysis.

Thank you to the Biochemistry and Biophysics and Structural Biology (BBSB) graduate program, the BBSB program coordinators, Peter Burgers, Jeff Henderson, and Daved Fremount, and the BBSB graduate student coordinators: Andrea Krussel, Stacia Burd, and Danielle Gross. Thank you to all my fellow students and cohort members for your ideas and friendship.

A huge thank-you to Alexis Campbell and Basil Nikalou for your mentorship and support during my undergraduate career and beyond. Alexis- you have always been a source of inspiration, and a wonderful mentor. Thank you for all your help along this journey.

I deeply appreciate all the friends I have made during my time as a graduate student. Whether we were studying for an exam, trying to pass our qualifying exam, commiserating over failed experiments, or just exploring St. Louis- you have been an unending source of inspiration, help, and joy. A special thank you to the Friday morning think tank, the "Coffee Crew". Finally, a special thank you to my best friend in St. Louis and occasional roommate, Alex Polino. This journey would not have been nearly as fun without each and every one of you.

I am incredibly fortunate to have a supportive family. My parents, Dawn and Conrad, have always encouraged me to work hard, do right, and learn. Thank you for all of your support and

encouragement throughout this thesis. Thank you to my younger sister, Tasha, who embarked upon the graduate school journey with me and was always willing to commiserate and exchange ideas. Thank you to my partner's family- the Kennedys, for always cheering Elizabeth and I on. Finally, an enormous thank you to my partner, and co-chef Elizabeth Kennedy. You are an unending source of support- thank you for all your encouragement and love.

<div align="right">Justin Miller</div>

Washington University in St. Louis

January 2021

Abstract of the Dissertation

Prodrug Activation in Staphylococci and the Implications for Antimicrobial Development

Justin J Miller

Doctor of Philosophy in Biology and Biomedical Sciences

Biochemistry, Biophysics, and Molecular Biology

Washington University in St. Louis, 2020

Professor Audrey R. Odom John MD, PhD., Chair

Professor Joseph Jez PhD., Co-Chair

Antibiotic resistance is an increasing concern for global health care, with some estimates suggesting that 10 million people will die from antibiotic resistant infections in the year 2050. Fueling this prospect, few antimicrobials are being actively developed and recently commercial entities have fled from the development of new anti-infectives. New antimicrobials and drug development strategies are urgently needed to revitalize this critical pipeline. While many putative antibiotics demonstrate promising *in vitro* potency, they routinely fail *in vivo* due to poor drug-like properties (e.g. oral bioavailability, serum-half life, toxicity) resulting in overly expensive drug development pipelines. Fortunately, drug-like properties can be modified through the addition of chemical protecting groups to create "prodrugs". Lipophilic prodrugging strategies have been primarily deployed to remedy poor oral absorption but have also been utilized as a means of specifically delivering active drug to specific cells and tissue types. Here we demonstrate that lipophilic prodrugging of phosphonate antibiotics through a carboxy ester modification increases membrane permeability and enhances antimicrobial potency. Unfortunately, many lipophilic prodrugging strategies are rapidly cleaved *in vivo* by serum esterases rendering these potency and transport gains useless during clinical settings. Using three

species of staphylococci, we identify and biochemically characterize two esterases, GloB and FrmB responsible for the activation of carboxy ester prodrugs. Additionally, we solve the three-dimensional structures of both GloB and FrmB, facilitating additional structure-guided design of promoieties. Finally, we characterize the substrate specificity of human and mouse sera, enabling the development of promoieties which are selectively activated by microbial species. These findings not only allow the development of novel anti-staphylococcals but lay the framework for identification of microbial-specific prodrug design and design of long-lasting serum prodrugs. As lipophilic prodrugging expands the number of compounds that are membrane permeable, we expect that this approach will facilitate an expansion of the number of potential drugs.

Chapter 1: Introduction

1.1 Antibiotic resistance threatens modern medicine

1.1.1 The rise of antibiotics

The history of humans is strongly intertwined with microorganisms. Microbes are integral to the production of fermented foods and beverages such as bread, yogurt, and beer, they contribute to the production of several modern medical therapies such as insulin and the antibiotic, tetracycline, and remain with us through our life aiding in the digestion of complex carbohydrates as members of our "microbiome". While microbes have contributed many positives to humans, some contribute a significant disease burden. The microbial parasite, *Plasmodium falciparum*, has been estimated as having killed as much as 4-5% of all humans who have ever lived. In 2019, an estimated 1.4 million humans died due to infection with the bacteria, *Mycobacterium tuberculosis* (1). While most parasitic and bacterial infections are now relatively easy to treat, this has not always been the case.

In the late 19th and early 20th century, chemotherapeutics as we now know them began to develop. Paul Ehrlich developed the anti-syphilitic compound, arsphenamine, and cemented the idea that pure chemical compounds could be used to fight disease (2). In 1928 Alexander Fleming discovered the antibiotic penicillin, when the fungal contaminate, *Penicillium rubens*, prevented growth of his desired organism, *Staphylococcus aureus* (3). As was common at the time, Fleming was able to culture the fungal contaminant and isolate the growth inhibitory compound to demonstrate that the compound itself, rather than *P. rubens* was responsible for growth inhibition of *S. aureus*. The most striking observation, however, was that that the isolated compound was a potent inhibitor of many bacterial cultures and had no notable toxicity against mammals (3). While many chemicals can kill microbes, penicillin (penicillin G) was the first compound isolated that did so without also hurting humans.

Naturally, the identification of penicillin meant that individuals with otherwise life-threatening infections could be safely cured. Indeed, shortly after it's discovery, penicillin was utilized several times to cure bacterial infections (4–6). Unfortunately, as with many chemotherapeutics, transitioning from performance in laboratory models to humans was difficult. Penicillin G is rapidly excreted from humans, necessitating multiple doses of penicillin to effectively treat infections. Further, initial penicillin G production strategies yielded miniscule amounts of compound limiting the application of penicillin G in the clinic to only a few cases. Large scale production was eventually achieved in the early 1940s and penicillin became a common mechanism for curing bacterial infections.

1.1.2 Antibiotic resistance and new antimicrobials

The discovery of penicillin G was heralded as a promising success, yet even before mass administration was feasible, bacterial resistance to penicillin G existed (7). "Penicillinase", an enzyme found both intracellularly and extracellularly depending on the species of bacteria producing it, was first documented in 1940 and noted to rapidly degrade penicillin (Figure 1). Penicillin G resistance was, perhaps, to be expected. Penicillin G was isolated as a natural product of bacteria and its production was likely selected for as a mechanism of reducing competition for the *Penicillium* mold. If *Penicillium* had been producing penicillin G for a long time, bacteria were also dying from penicillin for a long time. Many experiments in laboratory settings have demonstrated the ease of resistance to chemical compounds within short time periods (8, 9). Long-term exposure of microbes to penicillin production, as would be expected through the co-evolution of microbes with *Penicillium*, thus would be more than sufficient time for resistance to arise in certain microbial species.

As penicillin treatment became common, so too did bacterial resistance to penicillin G. The first case of clinical resistance to penicillin was documented in 1942 when 4 strains of *Staphylococcus aureus* were isolated following penicillin treatment (10). By the late 1960s, over 80% of *S. aureus* strains were resistant to penicillin (11). Penicillin G resistance was also rapidly observed among *S. pneumoniae*, and *E. coli* (12).

Fortunately, following the discovery of penicillin G was an era of antimicrobial discovery where new antibiotics were rapidly discovered. Streptomycin was discovered in 1944 (13). Cephalosporins were discovered the following year and entered clinical use in the 1960s (14). While natural antibiotic scaffolds were expanding, developments in the field of medicinal chemistry enabled the scalable production of semi-synthetic antibiotics. Semi-synthetic antibiotics are produced through a combination of fermentation by an existing antimicrobial producing strain, and synthetic chemistry approaches to modify specific attributes of a developing compound. Semi-synthetic antibiotics have proven immensely valuable. In 1959, Beecham modified the benzyl group of penicillin G to an *ortho*-dimethoxyphenyl group, creating the β-lactamase resistant compound, methicillin (Figure 2) (15). While β-lactamases capable of hydrolyzing methicillin soon became commonplace, the principle that an antibiotic can be chemically modified to exhibit more favorable properties took hold. A total of four generations of penicillin modified compounds now exist. Penicillin G was among the first generation of β-lactamase sensitive compounds and methicillin and other β-lactamase resistant derivatives came with the second generation. Subsequent generations focused on extending the antibiotic spectrum, or number of bacteria that the antibiotic works upon, and altering the uptake, distribution, and stability of compounds within the human (also known as the pharmacokinetic and pharmacodynamic properties) (Figure 1). Similar semi-synthetic approaches have occurred

for the cephalosporin compounds with great success. In sum, semi-synthetic approaches are an efficient combination of synthetic chemistry and microbial fermentation that allow for the cheap production of a variety of antibiotics.

While humans have continued to race against expanding bacterial β-lactamase specificity, it is worth noting that penicillin resistance occurs via several additional mechanisms which highlight the flexibility of microbes. It was originally observed that different species of bacteria were naturally resistant to penicillin independent of any degrading enzymes (7). Later, it was realized that the action of penicillin G stems from binding to penicillin binding proteins (PBPs) to initiate bacterial lysis (16). Some of the naturally resistant bacterial species maintain PBPs which do not readily bind penicillin G, thus conferring natural immunity (Figure 1) (17). Further, some previously susceptible bacteria have accumulated mutations in PBPs which confer resistance to penicillin (18).

As penicillins require binding to PBPs to exert their antimicrobial action, altered transit of penicillins to PBPs is also a resistance mechanism (Figure 1). PBPs of gram-negative bacteria localize to the periplasm whereas gram-positive bacteria PBPs are localized to the cell surface (19, 20). In practice, this means that gram-positive PBPs are readily accessible by penicillins, whereas in gram-negative organisms, penicillin must first transit the outer membrane of the cell. Porin proteins are responsible for penicillin transit into the gram-negative periplasm, and mutation of these porin proteins is one mechanism of penicillin resistance (21–26).

Penicillin resistance highlights three mechanisms of antibiotic resistance; compound degradation (β-lactamases), target modification (PBP alteration), and reduced antibiotic penetration (porin disruption and deletion) (Figure 1). These resistance mechanisms are commonly observed for

5

other antibiotics, though several additional mechanisms are also possible (8, 27–31). Similar to porin mediated resistance to penicillin, microbes encode several efflux pumps which can reduce the intracellular concentrations of antibiotic (32–38). For some inhibitors, resistance may be achieved through altered metabolic regulation. For the competitive inhibitor of isoprenoid biosynthesis, fosmidomycin, resistance can be achieved by supplying more of the upstream competitive metabolite (39). Metabolic rerouting around the inhibited step is also possible in some instances (40). Finally, some antibiotics, known as prodrugs, require activation before their antimicrobial effects are realized. In these cases, if prodrug activation is performed via the microbe then deletion or modification of the prodrug activating enzyme(s) is an alternative resistance strategy (9, 41–43)

Three lessons should be taken from the story of penicillin. First, chemotherapeutics work, and many lives have been saved with the introduction of antibiotics. Second, microorganisms have an innate ability to evolve resistance to antibiotics. Finally, through careful and clever chemical strategies, new antibiotics can be developed which surpass the shortfalls of the previous. When antimicrobial development is in full force and there is a strong supply of novel antimicrobials and antimicrobial strategies and the production of novel antibiotics outpaces resistance. Alarmingly, in recent years there have been fewer antimicrobials entering the development pipeline and those that have tend to be modifications of existing antibiotics instead of new strategies (44–47). Simultaneously, there has been an exodus of companies investing in antibiotic development (44). As a result, several cases have already been documented where no effective antimicrobial therapy exists (48–51). We are already in a post-antibiotic world and as multi-drug resistant bacteria continue to spread there is an urgent need to revitalize antibiotic discovery.

1.1.3 Modern challenges in antibiotic development

The spread of antimicrobial resistance is a pending global health crisis. Recent estimates suggest that as many as 10 million people will die as a result of antimicrobial resistant infections in 2050 (52, 53). While existing antimicrobials are increasingly facing resistance, in parallel, there is a mass exodus from commercial antibiotic research and few new antimicrobials are entering the development pipeline (44). On the surface, this seems paradoxical. There is clearly a large demand for new antimicrobials, yet supply has not risen to meet this demand. While most public health inequities disparately impact poorer populations, antimicrobial resistance, like COVID-19, antimicrobial resistance will impact all individuals. Why then, are there not more antimicrobials in the development pipeline?

Financial challenges facing antimicrobial development

Perhaps the largest barrier to antimicrobial development is simply the cost. Most estimates place the cost of developing a new pharmaceutical (identification and optimization of the compound, development of production capacity, and clinical trials establishing safety and efficacy) at nearly $1B USD (54). Given that drug patents last approximately 20 years from initial disclosure and that initial testing typically takes ~10 years to complete, companies have approximately 10 years to recoup their investment. While this model is feasible for drugs that are frequently prescribed, antimicrobials are necessarily withheld to prevent unnecessary use and prevent the spread of antimicrobial resistance. Perhaps the final nail in the antimicrobial development coffin is simply the uncertainty in drug development. Compounds that appear highly successful in initial characterization in lab environments have approximately a 1-7% chance of securing approval from the Food and Drug Administration (FDA) (55). Even compounds, that are the most likely to

succeed- those that have passed clinical phases 1 and 2 of clinical development- only have approximately a 50% chance of entering the market. For these reasons, antibiotic development has stalled or has been converted to simple recombinations of existing antimicrobials as a risk-mitigation strategy.

While one could imagine a reinvention of the funding for drug development which encourages more antimicrobials to be developed, we may better served by asking the question, "why do novel drugs fail to secure approval so frequently?". Failure, especially in clinical trials, exorbitantly increases the cost of new therapeutics. Some drugs in development fail out of clinical trials as they are unable to recruit and retain sufficient patients. Others fail because the sponsoring company no longer has sufficient funds to complete the trials. Ultimately, these failures do not reflect issues with potential drugs. Rather, the two drug-specific reasons for trial failure are unexpected drug toxicity and/or failure of the drug to perform in humans. Of these two, drug safety is a less likely cause of drug failure (17% of failures) than poor efficacy (57% of failures) (55–57). Strategies that address these failures, hopefully in a universal manner, will be crucial in revitalizing the drug development pipeline.

Poor drug administration

Oftentimes, drugs are poorly efficacious because they do not reach the desired site in high enough concentrations. This may be because the drug is poorly absorbed via the route of administration. For example, orally administered drugs must pass through the stomach and be absorbed via the small or large intestine prior to systemic distribution of the drug. While this route of administration is facile and transportable, absorption constitutes a large barrier in drug efficacy. In contrast, drugs that are supplied intravenously (IV) are immediately systemic and do

not require absorption. While one may make the case that all drugs should be administered IV as this eliminates barriers to drug deliver; IV delivery is not without drawbacks. IV administration risks introduction of pathogenic microbes into the bloodstream (58). As a result, IV administration is non-portable and must be performed via trained healthcare professionals. Additionally, IV administration can result in tissue damage at the site of injection including nerve damage, tissue sloughing, and scarring (58).

Premature elimination

In addition to improper absorption, drugs can be ineffective if they are eliminated before they have had sufficient time to act at their target site. Penicillin G is rapidly removed from the blood via the kidneys, resulting in a half-life of ~1.4 hours in adults (59). Frequent dosing can be used to keep systemic drug concentrations high, but this is laborious, requires large amounts of drug, requires high rates of patient compliance, and missed doses make it more likely for resistance to arise. The two primary routes of elimination are filtration via the kidney (renal) before subsequent loss through the urine, and filtration via the liver (biliary) and subsequent secretion through the bile. Exact rates of elimination vary by individual patient, complicating exact determination of elimination parameters (60, 61).

Renal and biliary elimination selectively filter different compounds. Renal elimination often removes small, polar compounds that are not actively reabsorbed by renal tubules (62). Alternatively, larger molecular weight and lipophilic compounds tend to be excreted biliary (63). It is important to note, however, that compounds that have been excreted into the bile may be reabsorbed along the gastrointestinal tract (64–66). As a result, drug like molecules must thread a balance between size and lipophilicity to avoid secretion.

Poor drug penetrance

Drugs can fail even if they are optimally administered and have a long half-life if they do not reach the proper site. Humans naturally have several sites that are difficult to deliver drugs to. Perhaps most notoriously, the brain is surrounded by a blood-brain barrier which selectively excludes most compounds. Reflectively, drugs targeting the nervous system have the lowest likelihood of passing clinical trials (55). The other major tissue difficult to dose is the skeletal system, primarily due to regions that are avascular (67).

In parallel with specific tissues being difficult to deliver drugs to, the specific infection environment can make drug delivery problematic. *Mycobacterium tuberculosis* (*Mtb*) infections are characterized by granulomas- thick lesions designed to restrict replication of *Mtb*. Unfortunately, granulomas also restrict the delivery of antibiotics (68–70). Similarly, many bacteria can form biofilms- a series of layers of bacteria cells- during infection settings. Biofilms help bacteria adhere to a specific niche and prevents clearance via immune cells. Unfortunately, like granulomas, formation of a biofilm greatly reduces the efficacy of antibiotics, likely due to poor drug penetrance inside the biofilm.

Poor animal models

The final challenge facing drug development is a lack of good models for human disease. *In vitro* systems can be useful in the development of compounds and can rule potential compounds out as "too toxic", but they do not capture the complexity of a human. Notably, as highlighted before, pharmacokinetics are not included in *in vitro* experiments. Models of disease in mice, rats, guinea pigs and other small mammalian models are more complex, but still have several shortcomings. Notably, drug metabolism in rodents does not accurately reflect that of humans.

10

While simian models are likely more reflective of human disease, there are significant ethical and cost limitations on simian research. Animal models that poorly reflect human disease are not ultimately predictive of a compound's success.

With the immense cost associated with drug development and the likelihood of failure, it is unsurprising that relatively few drugs are developed annually. Risk mitigation strategies, such as the reformulation or slight modification of existing antibiotics are attractive as information about toxicity of the original compound are likely to translate. However, reformulations and minor compound modifications are unlikely to be severe deterrents to the evolution of antimicrobial resistance. In the next section we will discuss strategies to maximize drug efficacy without significant modification to the existing drug scaffold. This strategy, known as prodrugging, can aid in the cost of drug development, may serve to reduce drug toxicity, and can be used to expand the number of feasible microbial drug targets.

1.2. Prodrugs, novel tools for medicinal chemists

The most simplistic antibiotics are administered and immediately have inhibitory effects without any further action being needed. Penicillin G binds PBPs to prevent further growth of the target bacteria. The protein synthesis inhibitor, tetracycline, similarly requires no further processing before inhibiting protein synthesis. In contrast, prodrugs are compounds that are inactive and unable to exert any inhibitory action until they have been metabolized. This added complexity is useful during drug development as medicinal chemists can dissociate target inhibition from other pharmacokinetic and pharmacodynamic properties. Depending on the goal, different protecting groups, or promoieties, can be added to the active (parent) drug in effort to modify lipophilicity

or aqueous solubility. Prodrugging strategies that make use of tissue, cell, or organism specific activation mechanisms can also be employed to selectively deliver active compound.

Historically, prodrugging approaches have been most often employed to increase the oral bioavailability of compounds. As was discussed previously, lipophilic compounds are more likely to be absorbed in the intestinal tract than polar compounds which require specific transporters. Thus, when a compound is too polar for adequate absorption, polar moieties may be obfuscated by lipophilic ones. The third-generation cephalosporin, cefditoren, was developed with strong activity against gram-positive organisms *in vitro*. Unfortunately, poor oral bioavailability of cefditoren limited it's potential clinical use (71, 72). The compound was resynthesized as a pivaloyloxymethyl (POM) modification on the carboxylate motif and became orally bioavailable. Similar strategies have been employed for the antibiotics adefovir dipivoxil, pivampicillin, and pivmecillinam .

While prodrugs, especially POM-prodrugs, were originally applied as a last effort during drug development, increasingly prodrugs are implemented as a critical early strategy. Prodrugging approaches, namely lipophilic prodrugging, can be used to both increase cellular penetrance of otherwise cell impermeable drugs. Depending on the specificity of prodrug activation, prodrug formulation may also enable the targeted delivery of compounds with the potential to reduce compound toxicity. These two approaches will be explored in the following sections.

1.2.1 Prodrugs, opportunities to expand the druggable space

While many essential cellular processes utilize charged molecules, few charged molecules are found in drugs. Phosphates and phosphonates are utilized in the storage of genetic information (RNA and DNA), and metabolic processes regularly utilize activated di and tri-phosphate

moieties. While charged residues are critical for competitive inhibition these processes, charged residues are readily excluded from cellular membranes. As a result, any potential drugs utilizing phosphonate residues are unlikely to inhibit intracellular targets and thus will not make effective drugs. However, lipophilic prodrugging of these residues allows phosphonates to be used while still effectively transiting the compound inside the cell. In the following sections we will discuss the application of prodrugs allowing the development of nucleotide analogues, isoprenoid biosynthesis inhibitors, and glycolytic inhibitors.

Nucleotide prodrugs

Perhaps the most frequent application of lipophilic prodrugging is to nucleotide analogues. As nucleotide/side analogues are polar compounds, they tend to suffer from poor bioavailability, are readily excluded from cells, and have the potential to be toxic. Despite these limitations, several nucleotide analogues have been approved or given emergency use authorization to treat viral infections and cancer (73–75). The development of these compounds has been extensively reviewed elsewhere, thus we will focus on a few examples of how prodrugging strategies have improved nucleotide analogue bioavailability, cellular penetrance, and compound safety (75–80).

Oseltamivir carboxylate, the active form of oseltamivir (Figure 3, Tamiflu, anti-influenza) suffers from low bioavailability with <5% of compound entering circulation (81). As we have discussed, large polar compounds are unlikely to be absorbed orally. However, modification to more lipophilic compounds is likely to improve absorption. Since oseltamivir carboxylate had sufficient activity against whole cell assays, the primary barrier to clinical application was the lack of oral bioavailability. Prodrugging of the carboxylate moiety with an ethyl ester improved oral bioavailability to nearly 80% (Figure 3) (82). Once oseltamivir is absorbed, it is rapidly

hydrolyzed via the serum esterase carboxylesterase 1 to return the active compound (83). Similar approaches were applied during the development of adefovir dipivoxil (Figure 3, anti-HBV) and tenofovir disoproxil (anti-HIV/HBV), though both of these compounds employ a POM moeity (84, 85).

While some nucleotides/sides are sufficiently cell permeable to exert strong inhibitory action, most are unable to traverse the cell membrane to inhibit intracellular viral replication. Prodrugging approaches that increase nucleoside transporter mediated cell entrance have been pursued, but equally attractive is the development of compounds that passively diffuse into cells (86, 87). Lipophilic prodrugging can increase cell penetrance, to deliver the prodrug inside the cell where subsequent activation restores the parent compound. This strategy was pursued to generate the prodrug, Remdesivir (Figure 3), for the treatment of Ebola and SARS-CoV2 (88). Specifically, the phosphonate moiety of GS-441524 (Figure 3) was identified as likely responsible for poor cellular penetrance. Protection of the phosphonate with a McGuigan prodrug dramatically increased compound potency when used in whole cell assays (88, 89). Unfortunately, when Remdesivir is administered to humans and non-human primates, serum esterases rapidly remove the McGugian prodrug, resulting in the less permeable compound, GS-441524, as the relevant compound in the infection environment (90, 91). This example highlights how *in vitro* results can poorly model *in vivo* realities and exemplifies the need for compound development to consider both drug administration and activation (92).

HepDirect prodrugs elegantly achieve both tissue targeting while simultaneously improving the lipophilicity of phosphonates. Using the substrate specificity of a liver specific isoform of $P_{450,}$ CYP3A4, Erion and colleagues developed a promoiety that is selectively activated within the liver (93). The HepDirect strategy was applied to the parent compound of adefovir dipivoxil,

PMEA, and resulted in an almost 12-fold increase in PMEA levels in the liver (Figure 3) (94).

Simultaneously, this approach led to a 2-4 fold decrease of PMEA in the kidney, and virtually no

PMEA in the intestine (94). This prodrug specific prodrug of PMEA is currently in phase 2

clinical trials under the name Pradefovir mesylate. While it remains unclear the extent to which

prodrug activation is selectively in the liver and how much parent compound leaks into other

environments, it is clear that prodrug activation was successfully enriched for liver activation.

This approach is a shining example of the potential reductions in drug toxicity achieved through

targeted drug delivery as well as the possibility that promoieties may remain attached for

biologically relevant periods of time prior to reaching the desired site.

Isoprenoid biosynthesis prodrugs

Isoprenoid biosynthesis is an attractive candidate for several areas of drug development.

Isoprenoid biosynthesis is ubiquitously essential and begins with the synthesis of two five-carbon

building blocks, isopentenyl pyrophosphate (IPP) and dimethylallyl pyrophosphate (DMAPP).

Humans synthesize these building blocks via the mevalonate pathway, whereas some microbes

utilize a divergent, though equally essential, pathway, the 2-C-methyl-D-erythritol 4-phosphate

(MEP) pathway. The divergence in these two synthesis mechanisms makes the MEP pathway an

attractive target for antibiotics. Following IPP and DMAPP synthesis, isoprenoid biosynthesis

reconverges and yields subsequently larger carbon chains. In humans, the later stages of

isoprenoid biosynthesis are attractive targets for the treatment of osteoporosis, with

bisphosphonate inhibitors such as risedronate already in use. Unfortunately, intermediates along

the entire biosynthetic pathway maintain a phosphonate, and any competitive inhibitors

developed for these pathways likewise require a charged group like phosphonate to achieve strong enzyme inhibition. As we have discussed previously, these groups are largely cell impenetrable and tend to have poor oral bioavailability. Similarly, the charged phosphonate readily excludes these compounds from cell membranes requiring active transit for their entry. Lipophilic prodrugging has been applied to both bisphosphonate inhibitors and MEP pathway inhibitors.

Fosmidomycin is an antibiotic that competitively inhibits an early step in the MEP pathway. Fosmidomycin has efficacy against *Plasmodium falciparum*, the protozoan parasite responsible for most severe malaria cases, as well as *Escherichia coli*, several zoonotic staphylococci, and several additional bacteria (8, 95–97). While fosmidomycin is well tolerated at doses up to 8 g/day, it is poorly absorbed via oral administration and rapidly removed from circulation (98). As with nucleoside analogues, fosmidomycin is readily excluded from cell membranes and requires active transport to enter the cell (Figure 4) (8, 28, 99). Lipophilic prodrugging approaches, notably the POM moiety, bypass this requirement (Figure 4) (8, 28). Surprisingly, fosmidomycin is effective against *P. falciparum* despite the target enzyme being sequestered behind seven lipid bilayers (95). How fosmidomycin passes through these membranes remains unclear, but lipophilic prodrugging significantly increases the antimalarial efficacy of fosmidomycin and fosmidomycin analogues (100, 101). These potency gains have similarly been observed using fosmidomycin analogues against *Mycobacterium tuberculosis*, though have little increased efficacy against gran-negative bacteria (8, 102).

Similar prodrugging strategies have been deployed for bisphosphonates. Significant potency gains were achieved by converting the parental compound to a POM-prodrug (103). These *in vitro* potency gains are exciting, though *in vivo* trials have not yet been reported. As POM-

prodrugs are rapidly cleaved by serum esterases, it is unlikely that the same potency gains will be realized *in vivo* (100).

Glycolytic prodrugs

Glycolysis is significantly upregulated in cancerous cells and has emerged as a potential anti-cancer target. In humans, the penultimate step in glycolysis, the conversion of 2-phosphoglycerate to phosphoenolpyruvate, is catalyzed by three isoforms of enolase. In most cell types more than one isoform of enolase is present, however some cancerous cells disrupt a ENO1 while disrupting tumor suppression (104). Consequently, these cells are left with a single isoform of enolase, ENO2, and exhibit increased sensitivity to selective inhibitors of ENO2. Several potent and selective inhibitors of ENO2 have been developed, however they utilize phosphonate moieties to achieve their potency and are thus cell impermeable (104). POM-modification of the phosphonates affords increased cellular permeability, however serum esterases rapidly hydrolyze the POM moiety (105). Specific activation of these compounds by glial cells is predicted to both improve *in vivo* performance while simultaneously improving the safety profile of the compounds, however identification and formulation of these promoieties has yet to be achieved.

1.2.2 Prodrug activation and targeting

To present, we have covered how prodrugs can improve pharmacokinetic properties and increase cellular penetrance of polar compounds such as phosphonates. The latter benefit affords significant potency gains *in vitro*, however depending on the promoiety used, they are not realized in clinical settings due to premature promoiety removal by serum esterases (Figure 4). Enabling the development of phosphonate antibiotics through the development of serum stable and microbially labile promoieties opens a significant portion of antimicrobial space to be

17

developed. Further, targeting prodrug activation to specific cell types (human or microbial) is likely to increase the safety profile of any antibiotic as is observed with the HepDirect prodrugs (94). Here, we will discuss various strategies for prodrug activation and several esterases that have been noted for their involvement in carboxy ester prodrug activation. Ultimately, for any prodrug strategy, where the prodrug is activated to achieve the optimal effect is the most important consideration.

Host esterases- friends or foe?

For compounds that are sufficiently active in whole cell assays but do not achieve sufficient bioavailability, prodrugging to increase absorption, but not alter cell membrane permeability may be the best strategy. We have discussed numerous compounds where this strategy was employed including cefditoren pivoxil, oseltamivir, adefovir dipivoxil, and tenofovir disoproxil. In this case, rapid drug activation by host enzymes is considered a major benefit as the parent compound can rapidly take effect. However, in cases where prodrugs are intended to be delivered to discrete sites intact, host esterases represent a significant barrier. In humans, carboxy ester prodrug activation is performed by human carboxylesterase (hCES) and most frequently occurs in the liver or serum (106, 107).

Three isoforms of hCES are expressed in various tissues, though the predominant isoforms in the liver and to a lesser extent plasma are hCES1 and 2 (108–110). hCES1 and 2 have broad substrate specificities, however they do have substrate specificity. hCES1 prefers to hydrolyze substrates with a small alcohol group and a bulky acyl group. In contrast, hCES2 hydrolyzes compounds with a large alcohol group and a small acyl group (111, 112). While these esterases seemingly cover the entire substrate range, there is still hope that ester substrates can be designed

to avoid or reduce cleavage via these two esterases, as is demonstrated by the HepDirect prodrugging approach (93, 94). It is also worth noting that esterase substrate specificity and activity, especially for each tissue type and location within the host, is variable depending on the species (113–119). As a result, performance of ester prodrugs in pre-clinical models may not reflect their ultimate performance in the clinic.

Bacterial prodrug activation

We have highlighted the broad application of prodrugs and promoieties for drug development. The largest barrier to prodrug targeting is identifying promoieties that are specifically activated by microbial sources. Structure-guided approaches to microbially targeted prodrug activation have been hindered by a lack of information of microbial esterases and their specificities. In this thesis, we will present the discovery and characterization of two staphylococcal esterases, FrmB and GloB, which activate POM prodrugs in combination with at least one additional esterase. *In vitro* GloB and FrmB are both capable of partially deprotecting di-POM prodrugs. Neither enzyme either individually or in combination can fully activate a di-POM prodrug suggesting at least one among at least one additional enzyme is critical for the complete activation of carboxy ester prodrugs *in vivo* (chapter 3 and 4). In addition to identifying GloB and FrmB, we determined the three-dimensional structure of each enzyme and performed an extensive structure-activity relationship study using a library of ester substrates. While FrmB and GloB are both conserved amongst microbial populations, there is a significant amount of sequence variation in these two loci (chapter 4). Identification of FrmB and GloB is a major step towards structure guided design of prodrugs (chapter 4 115). How broadly these prodrugs will be applicable remains an intriguing and open question.

It is worth noting that both FrmB and GloB were identified because mutations in each prevented prodrug activation *in vivo*. While these mutations are well tolerated in rich axenic media, both GloB and FrmB are involved in cellular detoxification and may be more essential during infection settings. While future studies should focus on the essentiality and "native function" for GloB and FrmB, it may also be worthwhile to identify and characterize esterases that are known to be essential. Recently, 10 functional *S. aureus* serine hydrolases were identified using an activity based protein profiling approach (121). It is worth noting that one of the identified esterases, FphF, is the same enzyme as FrmB which has been previously discussed. Several of the identified serine hydrolases already have potent and selective inhibitors that have been developed against them, though these compounds do not have anti-staphylococcal activity suggesting that either the inhibitor is unable to enter the cell or these esterases are dispensable in culture media (121). However, disruption of one esterase, FphB, appears to disrupt *S. aureus* virulence in the liver and heart, but not the kidney (121). Esterases in other organisms similarly appear to play a role specifically in infection. For example, deletion of the *Francisella tularensis* outer membrane vesicle lipase, FtlA, results in avirulent bacteria (122). Identification of essential, or virulence essential, esterases and the characterization of them, is an important step towards the development of microbe specific prodrugs.

Prodrug activation in *P. falciparum*

Recently, mutations in the *P. falciparum* carboxylesterase, *Pf*PARE (*P. falciparum* prodrug activation and resistance esterase) were found to confer resistance to carboxy ester prodrugs of pepstatin (43). Further analysis revealed that *Pf*PARE mutant strains are unable to activate the

pepstatin prodrug and that *Pf*PARE can hydrolyze pepstatin butyl ester *in vitro*. *Pf*PARE mutations also confer resistance to prodrug esters of the lindenane sesquiterpenoid, Chlorajaponilide C, and prodrug esters of benzoxaboroles (42, 123). Based on enzyme assays on *Pf*PARE and patterns of cross resistance, *Pf*PARE appears to preferentially hydrolyze unbranched and minimally branched C6 substrates (42, 43, 123).

Identification of *Pf*PARE is a critical step towards the development of *P. falciparum* targeted prodrugs. However, as with GloB and FrmB in *S. aureus*, the rapid evolution of prodrug resistance through *Pf*PARE disruption and the apparent non-essentiality of *Pf*PARE raise concerns about the long-term efficacy of this as a targeting strategy. In addition to identifying essential esterases, one strategy for *P. falciparum* targeted prodrugs is the development of erythrocyte targeted prodrugs. *P. falciparum* is unique in that it continually resides within erythrocytes for most of its lifecycle. Nutrient channels have been identified which promote nutrient exchange between the erythrocyte cytosol and the parasite cytosol, and these may additional transit drug-like molecules between the two cytosols (124). Erythrocyte targeted prodrug activation has the benefit that esterase mutations are not a feasible resistance mechanism for the parasite. Indeed, some prodrugs appear to already be activated selectively by erythrocyte esterases as opposed to parasite esterases (125). Whether this strategy is ultimately feasible will depend on the substrate specificities of serum and liver esterases as opposed to erythrocyte esterases.

1.3 Challenges and opportunities for prodrugs

The utility of prodrugs is undeniable and has begun to be realized in drug development. Between 2008 and 2018, 30 new FDA approved prodrugs entered the market (126). This expansion of

prodrug production has continued. In quarter 3 of 2020 alone, four new prodrugs (31% of approved Q3 drugs) entered the market (127). As prodrugs continue to attract attention for their potential, new developments in prodrug targeting will enable an expanded druggable space for antimicrobials while simultaneously de-risking antibiotic development. However, several challenges and open questions should be addressed prior to widespread prodrug development.

Ideally, lipophilic prodrugging strategies can be developed such that any phosphonate compound becomes orally bioavailable, membrane permeable, and is specifically cleaved by the microorganism(s) of interest. This will enable any metabolic process inside the cell to be targeted when this was previously unachievable. Simultaneously, the specific targeting of prodrugs to microbial populations will reduce potential toxicity in human cells as the compound will be ineffective until activated. Unfortunately, promoieties that achieve this have not yet been identified. New research should focus on identifying prodrug activators in pathogenic microbes and subsequently determining the substrates cleavable by those activators. Additionally, we have highlighted that animal models do not accurately human esterase activity. New animal models need to be developed for effective pre-clinical prodrug assessment. Perhaps the best route forward is the development of large, high-throughput substrate libraries to enable massive screening of esterase activity. This has already started, and should continue (128).

One aspect of prodrug biology that needs to be considered during drug development is the toxicity of promoiety biproducts upon parental compound release. POM-prodrugs are expected to release pivalate and formaldehyde upon activation, and long-term treatment of POM prodrugs has lead to depletion of carnitine (129). It remains unclear how microbe-specific prodrug delivery will impact promoiety toxicity, especially if activation is incredibly specific for the microbe(s) that are targeted.

Confusingly, potency increases as a result of lipophilic prodrugging are not universal. In zoonotic staphylococci, POM-modification of fosmidomycin analogues improves potency by 500-1000 fold (8). Lipophilic prodrugging of bisphosphonates confers a 25-fold potency increase against human cells (103). Conversely, lipophilic prodrugs of fosmidomycin have no activity against many gram negatives, despite the parent compound being efficacious (8). Whether these differences are a result of poor activation *in vivo* by gram-negative organisms, activation in the incorrect cellular compartment, or a failure to transit the hydrophilic periplasmic space remains unknown. Understanding the limitations surrounding gram-negative prodrug activation will impact the scope of lipophilic prodrugging approaches.

Finally, we have thoroughly discussed the benefits of lipophilic prodrugging regarding oral bioavailability. Less is known about how lipophilic prodrugs will distribute systemically. It is well established that lipophilic compounds are more likely to bind serum proteins and are less likely to undergo renal elimination. Whether lipophilic prodrugs will have a release rate from serum proteins sufficient to deliver active compound to microbial targets remains an open question.

Lipophilic prodrugging strategies have been recognized and employed as modifiers of oral bioavailability for many years. Lipophilic prodrugging may also increase cell membrane penetration and reduce toxicity concerns around developing compounds. Targeted prodrug delivery is feasible for some compounds, however lipophilic promoieties that specifically target compounds to microbial cells have not been identified. Identification of microbial prodrug activators represent an attractive first step towards the development of microbe specific prodrugs.

1.4   Figures
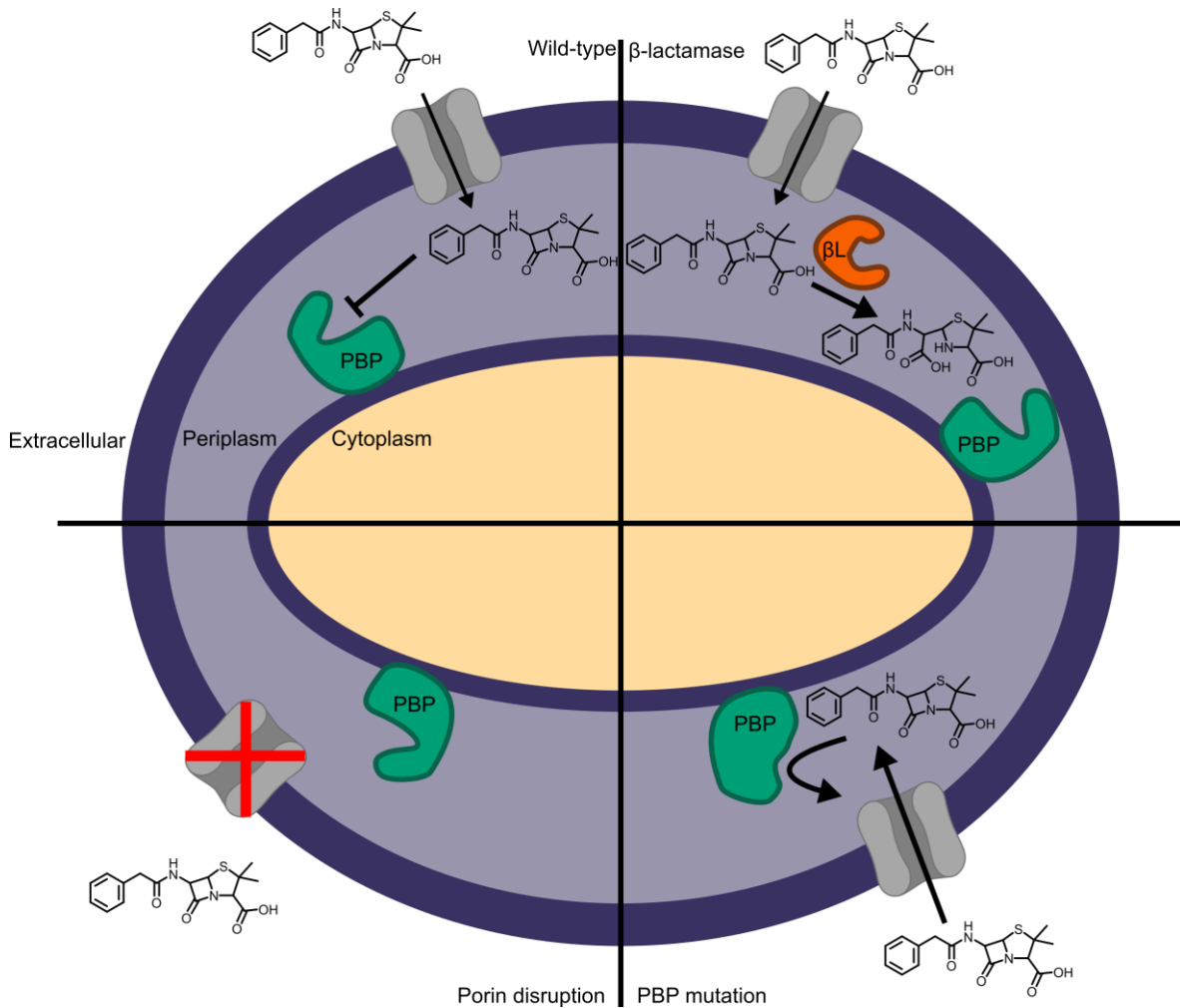
Figure 1 Penicillin resistance mechanisms. Top left- in wild-type gram negative bacteria sensitive to penicillin, extracellular penicillin is transited by porin proteins to reach periplasmic or cytoplasmic penicillin binding proteins (PBPs). Top right- expression of β-lactamase enzymes (βLs) confers protection via penicillin hydrolysis. Bottom left- Disruption of the transit mechanism confers penicillin resistance. Bottom right- mutation of penicillin binding protein confers resistance to penicillins.
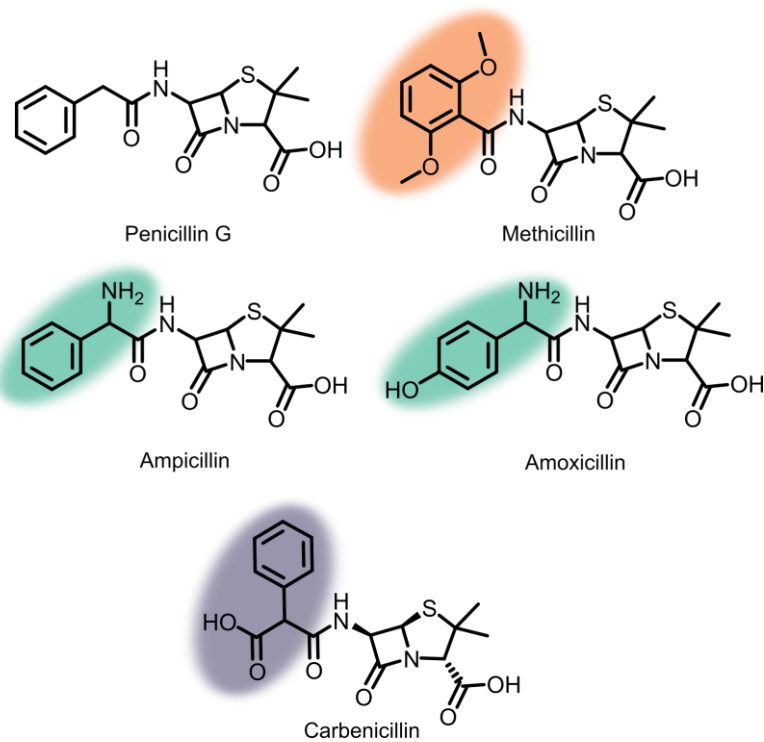
Figure 2 Structures of Penicillin and Penicillin derivatives. Highlighting identifies variation from Penicillin G. Orange highlighting indicates the molecule is resistant to β-lactamases (second generation penicillin), green compounds are more likely to be uptaken by cells (third generation penicillins), and the purple highlighting illustrates expanded antimicrobial susceptibility (third generation penicillin).
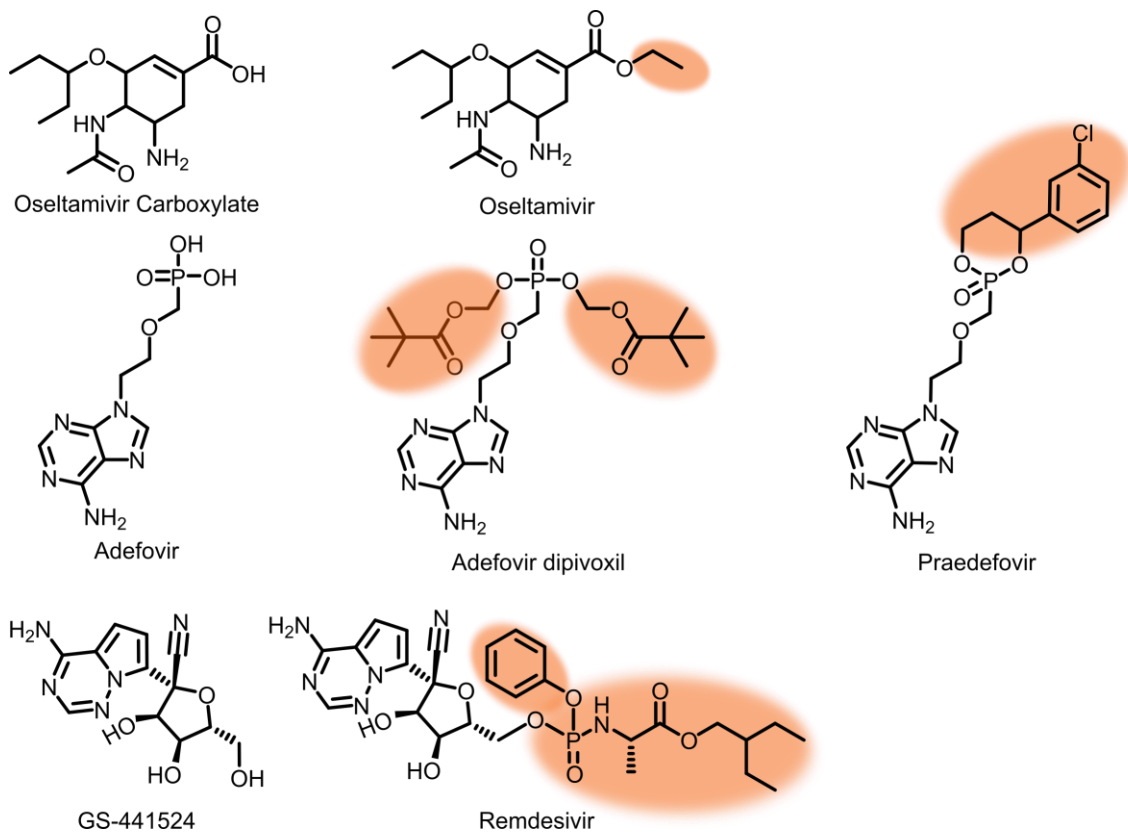
Figure 3 Nucleotide prodrug structures. Parent compounds are displayed on the left and prodrug variants to the right. Promoieties highlighted in orange.
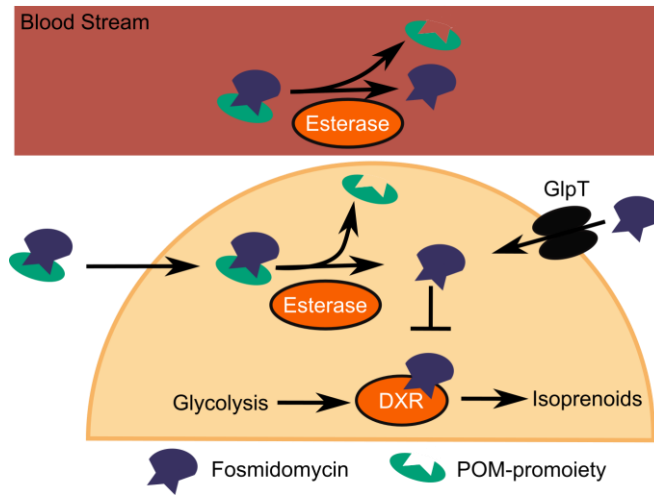
Figure 4 MEPicide and MEPicide prodrug action. Prodrugging bypasses GlpT mediated transit. Promoeities are removed via an intracellular esterase prior to DXR inhibition. Serum esterases rapidly hydrolyze POM-promoieties.

1.5 References

1. WHO (World Health Organisation) (2020) *Global Tuberculosis Report* (Geneva) Available at: https://apps.who.int/iris/bitstream/handle/10665/336069/9789240013131-eng.pdf?ua=1.

2. Strebhardt K, Ullrich A (2008) Paul Ehrlich's magic bullet concept: 100 years of progress. *Nat Rev Cancer* 8(6):473–480.

3. Fleming A (1929) On the antibacterial action of cultures of a penicillium, with special reference to their use in the isolation of *B. influenzæ*. *Br J Exp Pathol* 10(3):226–236.

4. Howie J (1986) Penicillin: 1929-40. *BMJ* 293(6540):158–159.

5. Wainwright M, Swan HT (1986) C.G. Paine and the earliest surviving clinical records of penicillin therapy. *Med Hist* 30(1):42–56.

6. Chain E, et al. (1940) Penicillin as a chemotherapeutic agent. *Lancet* 236(6104):226–228.

7. Abraham EP, Chain E An enzyme from bacteria able to destroy penicillin. 1940. *Rev Infect Dis* 10(4):677–8.

8. Edwards RL, et al. (2020) Potent, specific MEPicides for treatment of zoonotic staphylococci. *PLoS Pathog* 16(6):e1007806.

9. Mikati MO, et al. (2020) Antimicrobial prodrug activation by the staphylococcal glyoxalase GloB. *ACS Infect Dis*:acsinfecdis.0c00582.

10. Rammelkamp CH, Maxon T (1942) Resistance of *Staphylococcus aureus* to the Action of Penicillin. *Exp Biol Med* 51(3):386–389.

11. Lowy FD (2003) Antimicrobial resistance: the example of *Staphylococcus aureus*. *J Clin Invest* 111(9):1265–1273.

12. Lobanovska M, Pilla G (2017) Penicillin's discovery and antibiotic resistance: lessons for the future? *Yale J Biol Med* 90(1):135–145.

13. Schatz A, et al. (1944) Streptomycin, a substance exhibiting antibiotic activity against gram-positive and gram-negative bacteria. *Proc Soc Exp Biol Med* 55:66–69.

14. Brotzu G Research on a new antibiotic. *Labor Inst Hygine Cagliari*.

15. Knox R (1960) A new penicillin (BRL 1241) active against penicillin-resistant Staphylococci. *BMJ* 2(5200):690–693.

16. Tomasz A (1979) The mechanism of the irreversible antimicrobial effects of penicillins: how the beta-lactam antibiotics kill and lyse bacteria. *Annu Rev Microbiol* 33(1):113–137.

17. Eymard D, et al. (1990) Non-beta-lactamase-producing penicillin-resistant *Enterococcus faecium* in a clinical setting. *Can J Infect Dis* 1(3):73–6.

18. Hakenbeck R, et al. (1999) Penicillin-binding proteins in β-lactam–resistant *Streptococcus pneumoniae*. *Microb Drug Resist* 5(2):91–99.

19. Mueller EA, Levin PA (2020) Bacterial cell wall quality control during environmental stress. *MBio* 11(5). doi:10.1128/mBio.02456-20.

20. Egan AJF, Errington J, Vollmer W (2020) Regulation of peptidoglycan synthesis and remodelling. *Nat Rev Microbiol* 18(8):446–460.

21. Dever LA, Dermody TS (1991) Mechanisms of bacterial resistance to antibiotics. *Arch Intern Med* 151(5):886–895.

22. Nikaido H, Rosenberg EY, Foulds J (1983) Porin channels in *Escherichia coli*: studies with beta-lactams in

intact cells. *J Bacteriol* 153(1):232–40.

23. Yoshimura F, Zalman LS, Nikaido H (1983) Purification and properties of *Pseudomonas aeruginosa* porin. *J Biol Chem* 258(4):2308–14.

24. Nikaido H (1988) Bacterial resistance to antibiotics as a function of outer membrane permeability. *J Antimicrob Chemother* 22(Supplement_A):17–22.

25. Sanders CC (1983) Novel resistance selected by the new expanded-spectrum Cephalosporins: a concern. *J Infect Dis* 147(3):585–589.

26. Yoshimura F, Nikaido H (1985) Diffusion of beta-lactam antibiotics through the porin channels of *Escherichia coli* K-12. *Antimicrob Agents Chemother* 27(1):84–92.

27. C Reygaert W (2018) An overview of the antimicrobial resistance mechanisms of bacteria. *AIMS Microbiol* 4(3):482–501.

28. McKenney ES, et al. (2012) Lipophilic prodrugs of FR900098 are antimicrobial against *Francisella novicida in vivo* and *in vitro* and show GlpT independent efficacy. *PLoS One* 7(10):e38167.

29. Armstrong CM, Meyers DJ, Imlay LS, Freel Meyers C, Odom AR (2015) Resistance to the antimicrobial agent fosmidomycin and an FR900098 prodrug through mutations in the deoxyxylulose phosphate reductoisomerase gene (dxr). *Antimicrob Agents Chemother* 59(9):5511–5519.

30. Blair JMA, Webber MA, Baylay AJ, Ogbolu DO, Piddock LJ V. (2015) Molecular mechanisms of antibiotic resistance. *Nat Rev Microbiol* 13(1):42–51.

31. Wright GD (2011) Molecular mechanisms of antibiotic resistance. *Chem Commun* 47(14):4055.

32. Tanabe M, et al. (2009) The multidrug resistance efflux complex, EmrAB from *Escherichia coli* forms a dimer in vitro. *Biochem Biophys Res Commun* 380(2):338–342.

33. Jonas BM, Murray BE, Weinstock GM (2001) Characterization of emeA, anorA Homolog and Multidrug Resistance Efflux Pump, in *Enterococcus faecalis*. *Antimicrob Agents Chemother* 45(12):3574–3579.

34. Truong-Bolduc QC, Dunman PM, Strahilevitz J, Projan SJ, Hooper DC (2005) MgrA Is a Multiple Regulator of Two New Efflux Pumps in *Staphylococcus aureus*. *J Bacteriol* 187(7):2395–2405.

35. Kourtesi C, et al. (2013) Microbial efflux systems and inhibitors: approaches to drug discovery and the challenge of clinical implementation. *Open Microbiol J* 7(1):34–52.

36. Costa SS, Viveiros M, Amaral L, Couto I (2013) Multidrug efflux pumps in *Staphylococcus aureus*: an update. *Open Microbiol J* 7(1):59–71.

37. Lubelski J, Konings WN, Driessen AJM (2007) Distribution and physiology of ABC-type transporters contributing to multidrug resistance in bacteria. *Microbiol Mol Biol Rev* 71(3):463–476.

38. Putman M, van Veen HW, Konings WN (2000) Molecular properties of bacterial multidrug transporters. *Microbiol Mol Biol Rev* 64(4):672–693.

39. Guggisberg AM, et al. (2015) A sugar phosphatase regulates the methylerythritol phosphate (MEP) pathway in malaria parasites. *Nat Commun* 2(2):1–27.

40. Gil-Gil T, Corona F, Martínez JL, Bernardini A (2020) The inactivation of enzymes belonging to the central carbon metabolism is a novel mechanism of developing antibiotic resistance. *mSystems* 5(3). doi:10.1128/mSystems.00282-20.

41. Laborde J, Deraeve C, Bernardes-Génisson V (2017) Update of antitubercular prodrugs from a molecular perspective: mechanisms of action, bioactivation pathways, and associated resistance. *ChemMedChem* 12(20):1657–1676.

42.   Sindhe KM V., et al. (2020) *Plasmodium falciparum* Resistance to a lead benzoxaborole due to blocked compound aActivation and altered ubiquitination or sumoylation. *MBio* 11(1). doi:10.1128/mBio.02640-19.

43.   Istvan ES, et al. (2017) Esterase mutation is a mechanism of resistance to antimalarial compounds. *Nat Commun* 8(1):14240.

44.   Cooper MA, Shlaes D (2011) Fix the antibiotics pipeline. *Nature* 472(7341):32–32.

45.   Butler MS, Blaskovich MA, Cooper MA (2017) Antibiotics in the clinical pipeline at the end of 2015. *J Antibiot (Tokyo)* 70(1):3–24.

46.   CDC (2019) Antibiotic resistance threats in the United States 2019. Available at: https://www.cdc.gov/drugresistance/pdf/threats-report/2019-ar-threats-report-508.pdf.

47.   Antimicrobial resistance in the age of COVID-19 (2020) *Nat Microbiol* 5(6):779–779.

48.   Schooley RT, et al. (2017) Development and use of personalized bacteriophage-based therapeutic cocktails to treat a patient with a disseminated resistant *Acinetobacter baumannii* infection. *Antimicrob Agents Chemother* 61(10). doi:10.1128/AAC.00954-17.

49.   Aslam S, et al. (2020) Lessons learned from the first 10 consecutive cases of intravenous bacteriophage therapy to treat multidrug-resistant bacterial infections at a single center in the United States. *Open Forum Infect Dis* 7(9). doi:10.1093/ofid/ofaa389.

50.   Law N, et al. (2019) Successful adjunctive use of bacteriophage therapy for treatment of multidrug-resistant *Pseudomonas aeruginosa* infection in a cystic fibrosis patient. *Infection* 47(4):665–668.

51.   Aslam S, et al. (2019) Early clinical experience of bacteriophage therapy in 3 lung transplant recipients. *Am J Transplant* 19(9):2631–2639.

52.   Laxminarayan R, et al. (2013) Antibiotic resistance—the need for global solutions. *Lancet Infect Dis* 13(12):1057–1098.

53.   Chokshi A, Sifri Z, Cennimo D, Horng H (2019) Global contributors to antibiotic resistance. *J Glob Infect Dis* 11(1):36.

54.   Towse A, et al. (2017) Time for a change in how new antibiotics are reimbursed: development of an insurance framework for funding new antibiotics based on a policy of risk mitigation. *Health Policy (New York)* 121(10):1025–1030.

55.   Dowden H, Munro J (2019) Trends in clinical success rates and therapeutic focus. *Nat Rev Drug Discov* 18(7):495–496.

56.   Hwang TJ, et al. (2016) Failure of investigational drugs in late-stage clinical development and publication of trial results. *JAMA Intern Med* 176(12):1826.

57.   Fogel DB (2018) Factors associated with clinical trials that fail and opportunities for improving the likelihood of success: A review. *Contemp Clin Trials Commun* 11:156–164.

58.   Bernaerts K, Evers G, Sermeus W (2000) Frequency of intravenous medication administration to hospitalised patients: secondary data-analysis of the Belgian Nursing Minimum Data Set. *Int J Nurs Stud* 37(2):101–110.

59.   Corporation BH (2016) *Penicillin G Potassium*.

60.   Bilbao-Meseguer I, Rodríguez-Gascón A, Barrasa H, Isla A, Solinís MÁ (2018) Augmented renal clearance in critically ill patients: a systematic review. *Clin Pharmacokinet* 57(9):1107–1121.

61.   Johnson TN, Jamei M, Rowland-Yeo K (2016) How does *in vivo* biliary elimination of drugs change with age? Evidence from *in vitro* and clinical data using a systems pharmacology approach. *Drug Metab Dispos* 44(7):1090–1098.

62.   Ballard P, et al. (2013) Metabolism and pharmacokinetic optimization strategies in drug discovery. *Drug Discovery and Development* (Elsevier), pp 135–155.

63.   Ghibellini G, Leslie EM, Brouwer KLR (2006) Methods to evaluate biliary excretion of drugs in humans: an updated review. *Mol Pharm* 3(3):198–211.

64.   Roberts MS, Magnusson BM, Burczynski FJ, Weiss M (2002) Enterohepatic circulation: physiological, pharmacokinetic and clinical implications. *Clin Pharmacokinet* 41(10):751–790.

65.   Bullingham RES, Nicholls AJ, Kamm BR (1998) Clinical pharmacokinetics of mycophenolate mofetil. *Clin Pharmacokinet* 34(6):429–455.

66.   Jahnchen E, Meinertz T, Gilfrich H, Kersting F, Groth U (1978) Enhanced elimination of warfarin during treatment with cholestyramine. *Br J Clin Pharmacol* 5(5):437–440.

67.   Stapleton M, et al. (2017) Development of bone targeting drugs. *Int J Mol Sci* 18(7):1345.

68.   Cicchese JM, Dartois V, Kirschner DE, Linderman JJ (2020) Both pharmacokinetic variability and granuloma heterogeneity impact the ability of the first-line antibiotics to sterilize tuberculosis granulomas. *Front Pharmacol* 11. doi:10.3389/fphar.2020.00333.

69.   Strydom N, et al. (2019) Tuberculosis drugs' distribution and emergence of resistance in patient's lung lesions: A mechanistic model and tool for regimen and dose optimization. *PLOS Med* 16(4):e1002773.

70.   Prideaux B, et al. (2015) The association between sterilizing activity and drug distribution into tuberculosis lesions. *Nat Med* 21(10):1223–1227.

71.   Sakagami K, et al. (1990) Synthesis and oral activity of ME 1207, a new orally active cephalosporin. *J Antibiot (Tokyo)* 43(8):1047–1050.

72.   Center for drug evaluation and Research (2001) *Broad spectrum cephalosporin (Cephem)* Available at: https://www.accessdata.fda.gov/drugsatfda_docs/nda/2001/21-222_Spectracef_microbr.pdf.

73.   Eastman RT, et al. (2020) Remdesivir: a review of its discovery and development leading to emergency use authorization for treatment of COVID-19. *ACS Cent Sci* 6(5):672–683.

74.   De Clercq E, Li G (2016) Approved antiviral drugs over the past 50 years. *Clin Microbiol Rev* 29(3):695–747.

75.   Sinokrot H, Smerat T, Najjar A, Karaman R (2017) Advanced prodrug strategies in nucleoside and non-nucleoside antiviral agents: a review of the recent five years. *Molecules* 22(10):1736.

76.   Ray AS, Hostetler KY (2011) Application of kinase bypass strategies to nucleoside antivirals. *Antiviral Res* 92(2):277–291.

77.   Mackman RL, Cihlar T (2004) Prodrug strategies in the design of nucleoside and nucleotide antiviral therapeutics, pp 305–321.

78.   Zhang Y, Gao Y, Wen X, Ma H (2014) Current prodrug strategies for improving oral absorption of nucleoside analogues. *Asian J Pharm Sci* 9(2):65–74.

79.   Poijarvi-Virta P, Lonnberg H (2006) Prodrug approaches of nucleotides and oligonucleotides. *Curr Med Chem* 13(28):3441–3465.

80.   Peyrottes S (2004) SATE pronucleotide approaches: an overview. *Mini Rev Med Chem* 4(4). doi:10.2174/1389557043404007.

81.   Li W, et al. (1998) Identification of GS 4104 as an orally bioavailable prodrug of the influenza virus neuraminidase inhibitor GS 4071. *Antimicrob Agents Chemother* 42(3):647–53.

82.   Aoki FY, Doucette KE (2001) Oseltamivir: a clinical and pharmacological perspective. *Expert Opin*

Pharmacother 2(10):1671–1683.

83.   Shi D, et al. (2006) Anti-influenza prodrug Oseltamivir is activated by carboxylesterase human carboxylesterase 1, and the activation is inhibited by antiplatelet agent clopidogrel. *J Pharmacol Exp Ther* 319(3):1477–1484.

84.   Noble S, Goa KL (1999) Adefovir dipivoxil. *Drugs* 58(3):479–487.

85.   Dando TM, Plosker GL (2003) Adefovir dipivoxil: a review of its use in chronic hepatitis B. *Drugs* 63(20):2215–2234.

86.   Löffler M, Morote-Garcia JC, Eltzschig SA, Coe IR, Eltzschig HK (2007) Physiological roles of vascular nucleoside transporters. *Arterioscler Thromb Vasc Biol* 27(5):1004–1013.

87.   Molina-Arcas M, Casado F, Pastor-Anglada M (2009) Nucleoside transporter proteins. *Curr Vasc Pharmacol* 7(4):426–434.

88.   Siegel D, et al. (2017) Discovery and synthesis of a phosphoramidate prodrug of a pyrrolo[2,1-*f*][triazin-4-amino] adenine *C*-nucleoside (GS-5734) for the treatment of Ebola and emerging viruses. *J Med Chem* 60(5):1648–1661.

89.   Mehellou Y, Balzarini J, McGuigan C (2009) Aryloxy phosphoramidate triesters: a technology for delivering monophosphorylated nucleosides and sugars into cells. *ChemMedChem* 4(11):1779–1791.

90.   Williamson BN, et al. (2020) Clinical benefit of remdesivir in rhesus macaques infected with SARS-CoV-2. *Nature* 585(7824):273–276.

91.   Warren TK, et al. (2016) Therapeutic efficacy of the small molecule GS-5734 against Ebola virus in rhesus monkeys. *Nature* 531(7594):381–385.

92.   Yan VC, Muller FL (2020) Advantages of the parent nucleoside GS-441524 over remdesivir for Covid-19 treatment. *ACS Med Chem Lett* 11(7):1361–1366.

93.   Erion MD, et al. (2004) Design, synthesis, and characterization of a series of cytochrome P 450 3A-activated Prodrugs (HepDirect prodrugs) useful for targeting phosph(on)ate-based drugs to the liver §. *J Am Chem Soc* 126(16):5154–5163.

94.   Erion MD, et al. (2005) Liver-targeted drug delivery using HepDirect prodrugs. *J Pharmacol Exp Ther* 312(2):554–60.

95.   Jomaa H (1999) Inhibitors of the nonmevalonate pathway of isoprenoid biosynthesis as antimalarial drugs. *Science (80)* 285(5433):1573–1576.

96.   Mackie RS, McKenney ES, van Hoek ML (2012) Resistance of *Francisella Novicida* to fosmidomycin associated with mutations in the glycerol-3-phosphate transporter. *Front Microbiol* 3. doi:10.3389/fmicb.2012.00226.

97.   Uh E, et al. (2011) Antibacterial and antitubercular activity of fosmidomycin, FR900098, and their lipophilic analogs. *Bioorg Med Chem Lett* 21(23):6973–6.

98.   Kuemmerle H, Murakawa T, Soneoka K, Konishi T (1985) Fosmidomycin: a new phosphonic acid antibiotic. Part I: Phase I tolerance studies. *Int J Clin Pharmacol Ther Toxicol*:515–520.

99.   Sakamoto Y, Furukawa S, Ogihara H, Yamasaki M (2003) Fosmidomycin resistance in adenylate cyclase deficient (cya) mutants of *Escherichia coli*. *Biosci Biotechnol Biochem* 67(9):2030–2033.

100.   Edwards RL, et al. (2017) MEPicides: potent antimalarial prodrugs targeting isoprenoid biosynthesis. *Sci Rep* (June):1–11.

101.   Wang X, et al. (2018) MEPicides: α,β-unsaturated fosmidomycin analogues as DXR inhibitors against Malaria. *J Med Chem* 61:8847–8858.

102. San Jose G, et al. (2013) Design of potential bisubstrate inhibitors against *Mycobacterium tuberculosis* (Mtb) 1-Deoxy-D-Xylulose 5-Phosphate Reductoisomerase (Dxr)-evidence of a novel binding mode. *Medchemcomm* 4(7):1099–1104.

103. Zhang Y, et al. (2006) Activity of nitrogen-containing and non-nitrogen-containing bisphosphonates on tumor cell lines. *J Med Chem* 49(19):5804–14.

104. Muller FL, et al. (2012) Passenger deletions generate therapeutic vulnerabilities in cancer. *Nature* 488(7411):337–342.

105. Lin Y, et al. (2018) Eradication of ENO1-deleted glioblastoma through collateral lethality. *bioRxiv*. doi:10.1101/331538.

106. Wang D, et al. (2018) Human carboxylesterases: a comprehensive review. *Acta Pharm Sin B* 8(5):699–712.

107. Sanghani SP, Sanghani PC, Schiel MA, Bosron WF (2009) Human carboxylesterases: an update on CES1, CES2 and CES3. *Protein Pept Lett* 16(10):1207–1214.

108. Sato Y, Miyashita A, Iwatsubo T, Usui T (2012) Simultaneous absolute protein quantification of carboxylesterases 1 and 2 in human liver tissue fractions using liquid chromatography-tandem mass spectrometry. *Drug Metab Dispos* 40(7):1389–1396.

109. Taketani M, Shii M, Ohura K, Ninomiya S, Imai T (2007) Carboxylesterase in the liver and small intestine of experimental animals and human. *Life Sci* 81(11):924–932.

110. Diczfalusy MA, Björkhem I, Einarsson C, Hillebrant CG, Alexson SE (2001) Characterization of enzymes involved in formation of ethyl esters of long-chain fatty acids in humans. *J Lipid Res* 42(7):1025–32.

111. Hosokawa M (2008) Structure and catalytic properties of carboxylesterase isozymes involved in metabolic activation of prodrugs. *Molecules* 13(2):412–431.

112. Imai T (2006) Human carboxylesterase isozymes: catalytic properties and rational drug design. *Drug Metab Pharmacokinet* 21(3):173–185.

113. Rudakova E V., Boltneva NP, Makhaeva GF (2011) Comparative analysis of esterase activities of human, mouse, and rat blood. *Bull Exp Biol Med* 152(1):73–75.

114. Cohen O, et al. (2006) Comparison of polyethylene glycol-conjugated recombinant human acetylcholinesterase and serum human butyrylcholinesterase as bioscavengers of organophosphate compounds. *Mol Pharmacol* 70(3):1121–1131.

115. Yang ZP, Dettbarn W-D (1998) Prevention of tolerance to the organophosphorus anticholinesterase paraoxon with carboxylesterase inhibitors. *Biochem Pharmacol* 55(9):1419–1426.

116. Due AH, Trap HC, Van Der Wiel HJ, Benschop HP (1993) Effect of pretreatment with CBDP on the toxicokinetics of soman stereoisomers in rats and guinea pigs. *Arch Toxicol* 67(10):706–711.

117. Bahar FG, Ohura K, Ogihara T, Imai T (2012) Species difference of esterase expression and hydrolase activity in plasma. *J Pharm Sci* 101(10):3979–3988.

118. Du B (1971) Plasma esterase activity and the metabolism of drugs with ester groups. *Ann N Y Acad Sci* 179(1 Drug Metaboli):684–694.

119. Williams FM (1985) Clinical significance of esterases in man. *Clin Pharmacokinet* 10(5):392–403.

120. Fellner M, et al. (2020) Structural basis for the inhibitor and substrate specificity of the unique Fph serine hydrolases of *Staphylococcus aureus*. *ACS Infect Dis* 6(10):2771–2782.

121. Lentz CS, et al. (2018) Identification of a *S. aureus* virulence factor by activity-based protein profiling (ABPP). *Nat Chem Biol* 14(6):609–617.

122. Chen F, et al. (2017) Outer membrane vesicle-associated lipase FtlA enhances cellular invasion and virulence in *Francisella tularensis* LVS. *Emerg Microbes Infect* 6(1):1–12.

123. Butler JH, et al. (2020) Resistance to some but not other dimeric lindenane sesquiterpenoid esters Is mediated by mutations in a *Plasmodium falciparum* esterase. *ACS Infect Dis*:acsinfecdis.0c00487.

124. Desai SA, Rosenberg RL (1997) Pore size of the malaria parasite's nutrient channel. *Proc Natl Acad Sci* 94(5):2045–2049.

125. Hazleton KZ, et al. (2012) Acyclic immucillin phosphonates: second-generation inhibitors of *Plasmodium falciparum* hypoxanthine-guanine-xanthine phosphoribosyltransferase. *Chem Biol* 19(6):721–730.

126. Rautio J, Meanwell NA, Di L, Hageman MJ (2018) The expanding role of prodrugs and development. *Nat Rev Drug Discov* 17:559–587.

127. Urquhart L (2020) FDA new drug approvals in Q3 2020. *Nat Rev Drug Discov*. doi:10.1038/d41573-020-00182-1.

128. White A, et al. (2018) Fluorogenic structure activity library pinpoints molecular variations in substrate specificity of structurally homologous esterases. *JBC*:1–23.

129. Brass E (2003) Impact on carnitine homeostasis of short-term treatment with the pivalate prodrug cefditoren pivoxil. *Clin Pharmacol Ther* 73(4):338–347.

Chapter 2: Potent, specific MEPicides for treatment of zoonotic staphylococci

Preface

The following work was performed by Rachel L. Edwards, Isabel Heueck, Soon G. Lee, Ishaan T. Shah, Andrew J. Jezewski, myself, Marwa O. Mikati, Xu Wang, Robert C. Brothers, Kenneth M. Heidel, Carey-Ann D. Burnham, Sophie Alvarez, Staphanie A. Fritz, Cynthia S. Dowd, Joseph M. Jez, and Audrey R. Odom John. I designed and optimized protein constructs, oversaw and assay development. IH and RLE performed enzymatic and bactericidal assays, ITS, AJJ, and MOM aided in whole genome sequence analysis and development of resistant staphylococci. SA quantified MEP intermediate levels, RCB, KMH, and CSD provided chemical compounds, SAF provided strains, SGL and JMJ solved the structure of DXR. JMJ, AOJ, RLE, and myself designed experiments. RLE prepared manuscript figures.

This chapter has been published in its entirety (Edwards RL, Heueck I, Lee SG, Shah IT, Miller JJ, Jezewski AJ, Mikati MO, Wang X, Brothers RC, Heidel KM, Osbourn DM, Burnham CD, Alvarez S, Fritz SA, Dowd CS, Jez JM, Odom John AR. Potent, specific MEPicides for treatment of zoonotic staphylococci. PLoS Pathog. 2020 Jun). Reproduction is allowed by authors per the license agreement term set out by PLOS PATHOGENS.

The authors (AROJ, RLE, CSD) declare their status as co-inventors of U.S. provisional patent 62/686,416 filed June 18, 2018.

2.1 Abstract

Coagulase-positive staphylococci, which frequently colonize the mucosal surfaces of animals, also cause a spectrum of opportunistic infections including skin and soft tissue infections, urinary tract infections, pneumonia, and bacteremia. However, recent advances in bacterial identification have revealed that these common veterinary pathogens are in fact, zoonoses that cause serious infections in human patients. The global spread of multidrug-resistant zoonotic staphylococci, in particular the emergence of methicillin-resistant organisms, is now a serious threat to both animal and human welfare. Accordingly, new therapeutic targets that can be exploited to combat staphylococcal infections are urgently needed. Enzymes of the methylerythritol phosphate pathway (MEP) of isoprenoid biosynthesis represent potential targets for treating zoonotic staphylococci. Here we demonstrate that fosmidomycin (FSM) inhibits the first step of the isoprenoid biosynthetic pathway catalyzed by deoxyxylulose phosphate reductoisomerase (DXR) in staphylococci. In addition, we have both enzymatically and structurally determined the mechanism by which FSM elicits its effect. Using a forward genetic screen, the glycerol-3-phosphate transporter GlpT that facilitates FSM uptake was identified in two zoonotic staphylococci, Staphylococcus schleiferi and Staphylococcus pseudintermedius. A series of lipophilic ester prodrugs (termed MEPicides) structurally related to FSM were synthesized, and data indicate that the presence of the prodrug moiety not only substantially increased potency of the inhibitors against staphylococci, but also bypassed the need for GlpT-mediated cellular transport. Collectively, our data indicate that the prodrug MEPicides selectively and robustly inhibit DXR in zoonotic staphylococci, and further, DXR represents a promising, druggable target for future development

2.2 Introduction

Coagulase-positive staphylococci, such as S. pseudintermedius and S. schleiferi subsp. coagulans, are leading causes of skin, soft tissue, and invasive infections in companion animals such as dogs and cats. In addition, these organisms cause zoonotic infections in humans that are clinically indistinguishable from infections with S. aureus including pneumonia, skin and soft tissue infections, hardware infections, and bacteremia(1–5). Newer clinical microbiological techniques, such as mass spectrometry, now readily distinguish S. aureus from zoonotic coagulase-positive staphylococci, which were previously often misidentified(3,6,7). Thus, there is a growing recognition of the importance of zoonotic staphylococci in human disease. Because mecA-mediated methicillin resistance is on the rise in both veterinary and human clinical isolates, new antibacterial strategies to specifically target zoonotic staphylococci are highly desirable(8–10).

Two distinct and independent pathways for isoprenoid biosynthesis have evolved, the mevalonate pathway and a mevalonate-independent route that proceeds through methylerythritol phosphate, called the MEP pathway(11). Unusual among bacteria, the least common ancestor of all Staphylococcus spp. appears to have possessed both pathways. Primate-associated staphylococcal lineages, including S. aureus, possess the mevalonate pathway, and evidence suggests that mevalonate pathway activity is required for peptidoglycan synthesis, growth, and virulence(12–14). In contrast, nonprimate-associated staphylococcal species, including S. pseudintermedius and S. schleiferi, utilize the MEP pathway for isoprenoid biosynthesis(15). Importantly, humans and other mammals lack homologs of MEP pathway enzymes, and MEP

pathway activity is required for cellular growth in all organisms in which it has been experimentally determined(16–21). Thus, new chemical inhibitors of MEP pathway enzymes hold promise as effective antimicrobials that may provide a high margin of safety.

The first dedicated enzyme of the MEP pathway, deoxyxylulose phosphate reductoisomerase (DXR; E.C. 1.1.1.267), is rate-limiting for MEP pathway activity. DXR is known to be susceptible to small molecule inhibition. For example, the phosphonic acid antibiotic fosmidomycin (FSM) is a slow, tight-binding, competitive inhibitor of DXR(22). FSM is safe and well-tolerated in humans and animals(23–25). Unfortunately, FSM has poor oral bioavailability and a short serum half-life, which has hampered clinical efficacy. Moreover, the charged nature of FSM and its phosphonate analogs has challenged their clinical development as the compounds are excluded from cells unless actively transported. As a result, many microorganisms, such as Mycobacterium tuberculosis and Toxoplasma gondii, are inherently resistant to FSM (due to poor cellular uptake) even though FSM potently inhibits their DXR orthologs in vitro(16,18,26). In Gram-negative organisms, FSM import is dependent on a glycerol-3-phosphate/Pi antiporter (GlpT), and FSM resistance can be achieved by reduced expression or activity of GlpT(27,28).

In this work, we use the highly specific inhibitor FSM to chemically validate the MEP pathway enzyme DXR as an essential, druggable antibacterial target for zoonotic staphylococcal infections. Furthermore, we establish the structural and enzymatic mechanism of staphylococcal DXR inhibition by FSM. Using a chemical genomics approach, we define the genetic basis of

FSM resistance in zoonotic staphylococci and define the FSM transporter GlpT in these strains. Finally, we reveal that structurally related lipophilic ester prodrugs (called MEPicides) yield substantially increased potency and circumvent the need for GlpT-dependent import. Thus, lipophilic prodrugs provide a promising new approach to combat zoonotic staphylococcal infections.

2.3 Methods

2.3.1 DXR Inhibitors.

FSM (Millipore Sigma) and FR-900098 (Millipore Sigma) were resuspended in sterile water. Compounds 1-4 were synthesized and resuspended in DMSO as previously described(41,42,53).

2.3.2 Growth inhibition assays of *Staphylococcus* species.

Overnight cultures were diluted 1:200 in LB media and grown at 37°C until the mid-logarithmic phase (OD$_{600}$ = 0.5 – 0.8). Cultures were diluted in a 96-well plate to 1 x 10^5 in 150 µL LB media and treated with inhibitors at concentrations ranging from 2 nM to 100 µM. Bacteria were grown at 37°C for 20 h with cyclic shaking at 700 rpm in a FLUOstar Omega microplate reader (BMG Labtech). Growth was assessed over 20 h by measuring the OD$_{600}$ at 20 min increments. The half-maximal inhibitory concentration (IC$_{50}$) values were determined during logarithmic growth using GraphPad Prism software. All experiments were performed at least in triplicate and data reported represent the mean ± SEM.

2.3.3 Minimum bactericidal (MBC) assay.

Overnight cultures were diluted 1:200 in LB media and grown at 37°C until reaching mid-logarithmic phase of growth. Compounds were added to cultures at their respective IC$_{50}$ and at

10 x IC$_{50}$, and the bacteria were incubated at 37°C for 24 h while shaking. Cultures were serially diluted in Dulbecco's Phosphate Buffered Saline (PBS; Gibco) and plated on LB agar. Colonies were enumerated after overnight growth at 37°C. Values reflect the mean and standard deviations of at least three independent experiments.

2.3.4 Sample preparation for mass spectrometry analysis.

Overnight cultures of *Staphylococcus* spp. were diluted 1:200 in LB media and grown at 37°C until reaching mid-logarithmic phase. Cultures were then treated for 2 h with FSM at 10x their IC$_{50}$ while shaking at 37°C. For normalization, the OD$_{600}$ was determined after 2 h of treatment with the DXR inhibitors. Cells were pelleted by centrifugation for 5 min at 3000 x g at 4°C. The supernatants were removed and cells were washed twice with PBS (Gibco). The supernatants were removed and the pellets stored at -80°C until analysis. MEP intermediates were extracted from the samples using glass beads (212-300 u) and 600 μL chilled H$_2$O: chloroform: methanol (3:5:12 v/v) spiked with PIPES (piperazine-N,N′-bis(2-ethanesulfonic acid) as internal standard. The cells were disrupted with the TissueLyser II instrument (Qiagen) using a microcentrifuge tube adaptor set pre-chilled for 2 min at 20 Hz. The samples were then centrifuged at 16,000 x g at 4ºC for 10 min, the supernatants collected, and pellet extraction repeated once more. The supernatants were pooled and 300 μL chloroform and 450 μL of chilled water were added to the supernatants. The tubes were vortexed and centrifuged. The upper layer was transferred to a 2 mL tube PVDF filter (ThermoFisher, F2520-5) and centrifuged for 5 min at 4,000 x g at 4ºC. The samples were transferred to new tubes and dried using a speed-vac. The pellets were re-dissolved in 100 μL of 50% acetonitrile.

2.3.5 LC-MS/MS analysis.

For LC separation, Luna-NH2 column (3 μm, 150 x 2 mm, Phenomenex) was used flowing at 0.4 mL/min. The gradient of the mobile phases A (20 mM ammonium acetate, pH 9.8, 5% acetonitrile) and B (100% acetonitrile) was as follows: 60% B for 1 min, to 6% B in 3 min, hold at 6% B for 5 min, then back to 60% B for 0.5 min. The LC system was interfaced with a Sciex QTRAP 6500+ mass spectrometer equipped with a TurboIonSpray (TIS) electrospray ion source. Analyst software (version 1.6.3) was used to control sample acquisition and data analysis. The QTRAP 6500+ mass spectrometer was tuned and calibrated according to the manufacturer's recommendations. The metabolites were detected using MRM transitions that were previously optimized using standards. The instrument was set-up to acquire in negative mode. For quantification, an external standard curve was prepared using a series of standard samples containing different concentrations of metabolites and a fixed concentration of the internal standard. The limit of detection for 1-deoxy-D-xylulose 5-phosphate (DOXP), 4-diphosphocytidyl-2-C-methylerythritol (CDP-ME), and 2-C-methyl-D-erythritol 2,4-cyclopyrophosphate (MEcPP) was 0.0064 μM for a 10 μL injection volume. Data reflect the mean and SD of at least three independent experiments. T-tests were used to test for significance between untreated (UNT) and drug-treated bacteria (Prism).

2.3.6 Recombinant expression and purification of DXR.

Wild-type *dxr* from *S. schleiferi* was amplified from genomic DNA using the forward primer 5'-CTCACCACCACCACCACCAT ATGAAAAATATAGCAATTTTAGGCGC-3' and the reverse primer 3'-ATCCTATCTTACT CACCTACACCTCATATGATTTTGTTTTATAAT-5' The PCR product was cloned into vector BG1861 by ligation-independent cloning to introduce a N-terminal 6xHis tag, and transformed into Stellar™ chemically competent cells (Clontech

Laboratories)(68). The sequence was confirmed by Sanger sequencing and the plasmid was transformed into *E. coli* BL21(DE3) pLysS (Life Technologies). Gene expression was induced for 2 h with 1 mM isopropyl-β-D-thiogalactoside (IPTG) and cells were harvested by centrifugation at 4274 x g for 10 min at 4°C. The cell pellet was lysed by sonication in lysis buffer containing 25 mM Tris HCl (pH 7.5), 100 mM NaCl, 20 mM imidazole, 10% glycerol, 1 mM $MgCl_2$, 1 mM dithiothreitol (DTT), 1 mg/mL lysozyme, 75 U benzonase and 1 Complete Mini EDTA-free protease inhibitor tablet (Roche Applied Science). The hexahistidine-tagged DXR protein was affinity purified from soluble lysate via nickel agarose beads (Gold Biotechnology). Bound protein was eluted in 300 mM imidazole, 25 mM Tris HCl (pH 7.5), 1 mM $MgCl_2$ and 100 mM NaCl. Purified protein was dialyzed in buffer containing 10% glycerol without imidazole prior to analysis. The enzyme was frozen in liquid nitrogen and stored permanently at -80°C.

2.3.7 DXR enzyme activity and inhibitory constant determination.

Oxidation of NADPH to $NADP^+$ as a result of substrate turnover was monitored at 340 nm in a POLARstar Omega microplate reader (BMG Labtech)(69). The standard reaction had a final concentration of 62.5 nM purified DXR protein, 0.5 mM NADPH, 100 mM NaCl, 25 mM Tris pH 7.5, 10% glycerol, 1 mM $MgCl_2$ and 0.09 mg/mL BSA in 50 µL volume per assay. Reactions were initiated by the addition of DOXP after 15 min incubation of the reaction mixture without DOXP at 37°C. Absorption at 340 nm was measured continuously for up to 45 min. For K_m [DOXP] determination, DOXP concentrations between 0 and 2 mM were tested at 0.5 mM NADPH. The linear range of enzyme activity was determined by varying the DXR concentration at 1 mM DOXP and 1 mM NADPH. IC_{50} assays were performed using the standard reaction conditions with the respective amount of DXR inhibitor added to obtain the given final

concentrations. Data points from at least three independent replicates were analyzed by nonlinear regression using GraphPad Prism software. Slopes of changing absorbance values were converted to $(\mu M\ DOXP)(mg\ enzyme)^{-1}\ s^{-1}$ using a NADPH standard curve (data not shown). For the determination of the inhibitory constant Ki [FSM] of DXR, enzyme activity over a range of DOXP substrate concentrations between 0 and 2 mM was measured for FSM between 0 mM to 4 mM. Data points from at least three independent replicates were analyzed as described above.

2.3.8 Protein crystallography.

Crystals of *S. schleiferi* DXR were grown at 4°C using the vapor diffusion method in hanging drops of a 1:1 mixture of protein (10 mg mL^{-1}) and crystallization buffer (2 M ammonium sulfate, 100 mM sodium citrate/citric acid, pH 5.5). Crystals of the *S. schleiferi* DXR•FSM complex were obtained in 100 mM HEPES/MOPS (pH 7.5), 20 mM D-glucose, 20 mM D-mannose, 20 mM D-galactose, 20 mM L-fucose, 20 mM D-xylose, 20 mM N-acetyl-D-glucosamine, 20% glycerol, 10% PEG 4000, and 2 mM FSM. Prior to data collection, crystals were stabilized in cryoprotectant (mother liquor supplemented with 30% glycerol) before flash freezing in liquid nitrogen for data collection at 100 K. All diffraction images were collected at beamline 19-ID of the Argonne National Laboratory Advanced Photon Source at Argonne National Laboratory. HKL3000 was used to index, integrate, and scale the data sets(70). For phasing of the apoenzyme structure, molecular replacement was performed in PHASER using the x-ray crystal structure of *E. coli* DXR (PDB: 1T1S) as a search model(31,71). Two monomers were found in the asymmetric unit, with each forming a physiological dimer by crystallographic symmetry. For iterative rounds of model building and refinement, COOTand PHENIX were used, respectively(72,73). The resulting model was used to solve the structure of

the FSM complex by molecular replacement with PHASER. Two molecules were found in the asymmetric unit with crystallographic symmetry completing each dimer. Data collection and refinement statistics are summarized in Table S2. Atomic coordinates and structure factors of *S. schleiferi* DXR (PDB:6MH4) and the *S. schleiferi* DXR•FSM complex (PDB:6MH5) were deposited in the RCSB Protein Data Bank.

2.3.9 Generation of FSM-resistant mutants in *S. schleiferi* and *S. pseudintermedius*.

Clinical isolates of *S. schleiferi* (S53022327s) and *S. pseudintermedius* (H20421242p) were cloned and adapted to laboratory media via four rounds of sequential colony isolation and growth on LB agar plates. The isolated FSM-sensitive parental clones were incubated overnight on LB agar containing FSM (32 µM). Surviving single colonies were re-struck onto LB agar for clonal isolation. FSM resistance of isolated clones was confirmed by overnight growth on LB agar containing FSM (32 µM). The FSM-sensitive parental clones were used as a control to confirm growth and antibiotic-resistance.

2.3.10 Quantification of MEPicide resistance.

Minimum Inhibitory Concentration (MIC) assays were conducted by microtiter broth dilution in clear 96-well plates(74). MEPicides were serially diluted in duplicate at concentrations ranging from 1.5 mM – 19.5 nM in 75 µL of LB broth. Bacteria cultured without drug were used as a positive control for growth. The plates were inoculated with 75 µL bacteria diluted to 1×10^5 CFU/mL in LB. Plates were incubated for 18-20 h while shaking at 200 RPM at 37°C. The plates were then visually inspected, and the MIC value was defined as the lowest concentration of MEPicide that prevented visual growth.

2.3.11 Whole genome sequencing and variant discovery.

Genomic DNA was isolated from overnight cultures of *S. pseudintermedius* and *S. schleiferi*

using a standard phenol-chloroform extraction and ethanol precipitation protocol. Sequencing

libraries were prepared and sequenced by the Washington University Genome Technology

Access Center (GTAC). 1 µg of DNA was sonicated to an average size of 175 bp. Fragments

were blunt ended and had an A base added to the 3′ end. Sequence adapters were ligated to the

ends and the sequence tags were added via amplification. Resulting libraries were sequenced on

an Illumina HiSeq 2500 to generate 101 bp paired end reads. DNA quantity and quality were

assessed by GTAC using Agilent Tapestation.

For WGS, sequences from GenBank were retrieved from the following organisms: *S.*

pseudintermedius ED99 (accession number CP002478) and *S. schleiferi* 1360-13 (CP009470)

assemblies were downloaded from NCBI (ftp://ftp.ncbi.nlm.nih.gov*)*. Paired-end reads were

aligned to each of the available genomes using Novoalign v3.03. (Novocraft Technologies) and

deposited in NCBI (accession number PRJNA488092). Duplicates were removed and variants

were called using SAMtools(75). SNPs were filtered against parent variants and by mean depth

value and quality score (minDP =5, minQ = 37)(76). Genetic variants were annotated using

SnpEff v4.3 (Table S4)(77). For all samples, at least 90% of the genome was sequenced at 20x

coverage. All whole genome sequencing data is available in the NCBI BioProject database and

Sequence Read Archive. Point mutations found in the GlpT domain were mapped onto the

predicted transmembrane topology of GlpT using Protter(78).

2.3.12 Sanger Sequencing of *S. schleiferi* and *S. pseudintermedius glpT*.

Reference sequences for *glpT* in *S. schleiferi* (WP_016426432.1) and *S. pseudintermedius* (WP_014613322.1) were found with the Basic Local Alignment Search Tool (BLAST, v. 2/2/22). The regions of interest were amplified from *S. pseudintermedius* and *S. schleiferi* using gene-specific primers (Table S1). Amplicons were sequenced by the Washington University Protein and Nucleic Acid Laboratory using BigDye Terminator v3.1 Cycle Sequencing reagents (Life Technologies). Representative traces for all strains are available through the NCBI Trace Archive.

2.4   Results

2.4.1 Anti-staphylococcal activity of canonical MEP pathway inhibitors.

Because previous evidence had suggested that zoonotic staphylococci might be sensitive to MEP pathway inhibition, we quantified the dose-dependent antibacterial effects of FSM and FR-900098, a structurally similar DXR inhibitor (Table 1)(15). FSM was 5-10-fold more potent against both *S. schleiferi* ($IC_{50} = 0.78 \pm 0.13$ μM) and *S. pseudintermedius* ($IC_{50} = 0.31 \pm 0.04$ μM), respectively (Table 1), despite modest chemical differences between the two inhibitors. Data indicate that both compounds elicit their effect via a bacteriostatic mechanism-of-action, as neither caused a substantial drop in viable cells (Fig S1). Because *S. aureus* does not utilize the MEP pathway for isoprenoid biosynthesis, neither FSM nor FR-900098 inhibit *S. aureus* growth (Table 1). Together, these data indicate that both *S. schleiferi* and *S. pseudintermedius* have a functional MEP pathway that is required for bacterial growth.

2.4.2 Fosmidomycin inhibits isoprenoid metabolism in zoonotic staphylococci.

To establish the presence of MEP pathway intermediates and to determine the cellular mechanism-of-action of FSM, we performed targeted metabolic profiling of MEP pathway intermediates in *S. schleiferi* and *S. pseudintermedius*, with and without drug treatment. We confirmed that both species contain MEP pathway intermediates, including the DXR substrate, deoxyxylulose 5-phosphate (DOXP), and the downstream metabolite, methylerythritol cyclodiphosphate (MEcPP) (Fig 1). Upon FSM treatment, intracellular levels of DOXP increase dramatically (23.8-fold; $p < 0.05$ and 34.8-fold; $p < 0.05$ for *S. schleiferi* and *S. pseudintermedius*, respectively), consistent with DXR inhibition. Similarly, intracellular levels of MEcPP are substantially reduced following FSM treatment (4.5-fold; $p < 0.01$ and 2.4-fold; $p < 0.05$ for *S. schleiferi* and *S. pseudintermedius*, respectively), consistent with FSM-mediated reduction in MEP pathway metabolism. Together, these data confirm the presence of active MEP pathway metabolism in zoonotic staphylococci and establish that FSM inhibits growth through MEP pathway inhibition.

2.4.3 Fosmidomycin is a competitive inhibitor of *S. schleiferi* DXR.

To establish the enzymatic mechanism-of-action of DXR inhibitors against staphylococci, we cloned and purified *S. schleiferi* DXR (Fig S2; Table S1). Enzymatic characterization of DXR confirmed a Michaelis constant (K_m) [DOXP] (0.52 ± 0.08 mM), similar to that of other DXR orthologs (Fig 2A)(29,30). Both FSM and FR-900098 inhibit *S. schleiferi* DXR in a dose-dependent manner (Table 1). Further, we confirm that DXR inhibition by FSM is competitive with respect to the DOXP substrate, with a K_i [DOXP] of 0.29 ± 0.022 μM (Fig 2B).

2.4.4 Structural basis of fosmidomycin inhibition.

To establish the structural basis of FSM action, we solved the three-dimensional structures of *S. schleiferi* DXR as an apoenzyme and a FSM complex to 2.15 Å and 2.89 Å resolution, respectively (Table S2; Fig 3). *S. schleiferi* DXR is a physiologic dimer with each monomer related by crystallographic symmetry (Fig 3A). A DALI search identified multiple DXR from *Escherichia coli*, *Plasmodium falciparum*, *M. tuberculosis*, and other microbes (Z-scores: 49-51; r.m.s.d. ~1.6 Å^2 for 370-400 C$_\alpha$-atoms; 39-40% amino acid sequence identity)(31–36). The monomer consists of three regions (Fig 3A): an N-terminal α/β-domain with a central 7-stranded β-sheet (β1-β7) and 7 α-helices that serves as the nucleotide binding site; a middle region of the protein that includes a second β-sheet (β8- β11) and 4 α-helices (α8 and α12- α14); and a C-terminal α-helical domain (α9- α11 and α15- α18) that locks FSM into the active site(37).

Clear electron density for FSM was observed in the active site (Fig 3B) and revealed multiple protein-ligand interactions (Fig 3C). Interactions with Ser170, Ser206, Asn211, and Lys212 positions the FSM phosphonate toward the catalytic histidine (His241) and the NADP(H) binding site. The hydroxamic acid of the ligand contacts Asp144, Glu146, and Glu215. Additional van der Waals contacts are provided by Trp196, which resides in the α10- α11 loop. Comparison of the *S. schleiferi* DXR apoenzyme and FSM complex structures reveals how the C-terminal capping region (α9- α11 and α16-18) shift position to allow for the α10- α11 loop to position Trp196 adjacent to the inhibitor (Fig 3D). Movement of this flexible loop is a key feature for FSM inhibition of DXR from a variety of microorganisms(38). The residues that interact with FSM in the *S. schleiferi* DXR are conserved in the crystal structures of DXR from *E. coli*, *P. falciparum*, and *M. tuberculosis* with some variation in the sequence of the α10- α11 loop, although the tryptophan that contacts FSM is conserved in all these enzymes(34,36,37).

2.4.5 Resistance selection reveals a candidate FSM transporter, GlpT.

To establish the molecular basis of compound uptake, we performed independent, parallel, forward genetic screens for FSM resistance in both *S. schleiferi* and *S. pseudintermedius* (Fig 4A). Candidate FSM resistant (FSM^R) strains were colony purified and resistance was quantified by MIC determination (Fig 4B and Table S3). For both *S. schleiferi* and *S. pseudintermedius*, FSM^R strains possessed FSM MICs >100-fold higher than the wild-type parental lines. We employed whole genome sequencing to characterize the single-nucleotide polymorphisms (SNPs) that were present in the resistant strains (Table S4). In both species, FSM selective pressure enriched for new nonsynonymous changes in a single homologous locus, RN70_03745 (10/11 *S. schleiferi* strains) and SPSE_0697 (10/12 *S. pseudintermedius* strains) (Figs. S3A and S3B). These loci are close homologs (>90% sequence identity and 95.4% sequence similarity), which belong to the glycerol-3-phosphate transporter (GlpT) subfamily (Interpro: IPR005267) of the major facilitator superfamily (MFS) family of proteins (Interpro: IPR011701). These data suggest a model in which GlpT mediates FSM import, such that loss of GlpT function confers FSM resistance.

2.4.6 Fosmidomycin-resistance alleles of the candidate transporter, GlpT.

We predicted that the FSM-resistance alleles likely reduce GlpT function. In *S. schleiferi*, nine distinct alleles were found with GlpT changes: two with nonsense mutations and seven others with amino acid variants that are predicted to be highly deleterious (Polyphen-2 score >0.9; Table S3)(39). Similarly, in *S. pseudintermedius*, a total of seven distinct alleles were identified with GlpT sequence changes. Of these, one contained a nonsense mutation and six other GlpT variants contained amino acid substitutions that are strongly predicted to reduce function (Polyphen-2 score >0.9; Table S3). FSM-resistant variants map along the length of the nearly 50

Kd GlpT transporter, in both *S. schleiferi* and *S. pseudintermedius* (Figs S3A and S3B).

Altogether, the finding of multiple independent loss-of-function alleles, including nonsense

mutations, in two different selections in distinct organisms, strongly suggests that reduced GlpT

function is responsible for FSM resistance in these strains.

2.4.7 Lipophilic ester prodrugs with improved anti-staphylococcal potency.

Due to their charged nature, phosphonic acid antibiotics have poor cellular penetration and

bioavailability, and serum half-lives are relatively brief(23,25,40). In the ongoing effort to

develop new treatments for malaria and tuberculosis by improving upon the drug-like properties

of phosphonates, numerous lipophilic ester prodrugs that target DXR have been generated(41–

53) Our phosphonate parent compounds (1 and 3) are similar in anti-staphylococcal potency to

FSM and FR-900098 (Table 1); however, lipophilic modification of either compound

dramatically improves potency (in most cases by 100-fold) against both *S. schleiferi* and *S.*

pseudintermedius (compare compound 1 to its prodrug, compound 2, and compound 3 to its

prodrug, compound 4) (Table 1). As expected, prodrugs 2 and 4 poorly inhibit purified

recombinant *S. schleiferi* DXR *in vitro*, since cleavage of the prodrug moiety is required for

activity (Table 1). Our data suggest that lipophilic ester modifications improves uptake of the

DXR inhibitors, and that active phosphonates are released intracellularly for target inhibition

(model, Fig 6).

2.4.8 Lipophilic prodrugs bypass need for GlpT-mediated transport.

We anticipated that our lipophilic ester prodrugs do not require active cellular transport. To

evaluate whether GlpT is required for prodrug uptake, we characterized the MEPicide sensitivity

of four different FSM[R] *glpT* mutant *S. schleiferi* strains. As expected, we find that FSM[R] *glpT*

strains are cross-resistant to the phosphonate parent drug (compound 3), suggesting a common mechanism of transport (Fig 5). In contrast, FSM^R *glpT* strains remain sensitive to the MEPicide prodrugs compounds 2 and 4, supporting a model in which GlpT mediates phosphonate transport, with the ester modifications substantially improving cellular uptake (Fig 6)(21).

2.5 Discussion

S. schleiferi and the Staphylococcus intermedius group (SIG) (including S. pseudintermedius, S. intermedius, and S. delphini) cause pyodermic infections in companion animals, such as dogs and cats(8). Treatment of these infections is complicated by rising rates of antimicrobial resistance, particularly methicillin-resistance(54). A growing recognition that SIG species also cause zoonotic human infections, indistinguishable from infections with S. aureus, has led to new urgency in the search for additional therapeutics against these organisms. The non-mevalonate pathway of isoprenoid biosynthesis through MEP has been previously explored for development of targeted therapeutics for malaria and tuberculosis. In this current work, we establish the MEP pathway enzyme DXR as an attractive new therapeutic target for treatment of infections due to zoonotic staphylococci.

The MEP pathway has a number of major advantages as an antimicrobial target for veterinarian applications. Since mammals utilize the mevalonate pathway for isoprenoid biosynthesis, they lack homologs of the MEP pathway enzymes. As a result, MEP pathway inhibition is expected to have a high therapeutic index, and indeed, such inhibitors have been well-tolerated in preclinical and Phase I and II human studies(23–25,55,56). In addition, use of antibiotics in animal health and agriculture has been implicated as a major driver of antimicrobial resistance in human pathogens(57–60). Of particular relevance to treatment of canine and feline infections, the close physical contact between owners and household pets facilitates not only the cross-colonization of organisms, but also direct transfer of drug-resistance traits(61–63). Because human-associated staphylococci, including S. aureus, S. warnerii, and S. epidermidis, use the mevalonate pathway for isoprenoid biosynthesis, they are not susceptible to MEP pathway inhibitors (Table 1).

Importantly, while Gram-negative organisms such as E. coli and Klebsiella pneumoniae are modestly susceptible to MEP pathway inhibition, our lipophilic prodrug compound 2 does not inhibit growth of these organisms (Table S5). Our MEPicide compounds therefore have a highly specific and valuable antimicrobial spectrum, which may help break the cycle of resistance transfer from antibiotic-treated animals to the microbiota of humans.

In the current study, we establish the cellular, enzymatic, and structural mechanisms-of-action of FSM against zoonotic staphylococci. We confirm that FSM is a competitive inhibitor of staphylococcal DXR, interrupts cellular isoprenoid biosynthesis, and inhibits growth of zoonotic staphylococci. Of note, the staphylococcal DXR enzyme appears somewhat distinct from previously characterized orthologs, particularly in the $\alpha 10$- $\alpha 11$ loop sequence, which could be explored with additional SAR studies. Together, our work provides insights into differences in staphylococcal DXR that may be key to driving future structure-based inhibitor design efforts.

A well-appreciated liability of antibacterial phosphonates, including fosfomycin and FSM, has been the ready acquisition of resistance through loss of transport (27,64–66). Our work establishes GlpT as the likely phosphonate transporter in zoonotic staphylococci (Fig. 6). Identification of multiple, independent loss-of-function alleles from independent screens in two separate species is compelling evidence for a role of this locus in FSM-resistance in staphylococci. In addition, the homology between staphylococcal GlpT orthologs and Gram-negative phosphonate transporters suggests that the staphylococcal proteins are functionally similar. The finding that lipophilic prodrug MEPicides, which do not require active transport, are still active against the glpT mutant strains indicates that the molecular basis of phosphonate resistance is through loss of GlpT-mediated transport (Fig 6). The prodrug MEPicides circumvent GlpT, which our study has shown is easily mutated in staphylococci. Whether

staphylococci also readily develop resistance to the prodrug MEPicides is currently unclear, and is an important question for future studies.

It is important to note that while data indicate that the glpT mutants are resistant to phosphonate parent compound 3, the magnitude of resistance is substantially less than that of FSM. These data suggest that compound 3 may preferentially use an alternative transporter, thereby bypassing the dependence on GlpT. Surprisingly, staphylococcal glpT mutants are hypersensitive to MEPicide prodrugs, suggesting that after penetration and cleavage by cellular esterases, the compounds may accumulate intracellularly in the absence of GlpT (Fig 5). Future studies should examine the cellular transport of the MEPicide compounds, and further, explore whether synergy exists between the parent and prodrug varieties of this class of inhibitors.

The MEPicide prodrugs, including compounds 2 and 4, represent promising leads for ongoing preclinical testing and development of new therapeutics for zoonotic staphylococcal infections. The prodrugs harness the microbial specificity and thus safety of MEP pathway inhibition, while avoiding the dependency on active GlpT-mediated transport. In addition, we find that ester modification has a dramatic effect on anti-staphylococcal potency in vitro, suggesting that phosphonate transport limits the anti-bacterial efficacy of FSM and related compounds. Lipophilic ester modifications have previously been employed to improve pharmacokinetic properties and bioavailability of anti-staphylococcal agents (e.g., cefditoren pivoxil)(67). Since MEPicide ester modification at the site of infection is necessary to facilitate bacterial cell entry of inhibitors, future studies will aim to understand what chemical features drive intestinal and serum cleavage of the MEPicide prodrugs.

2.6 Figures
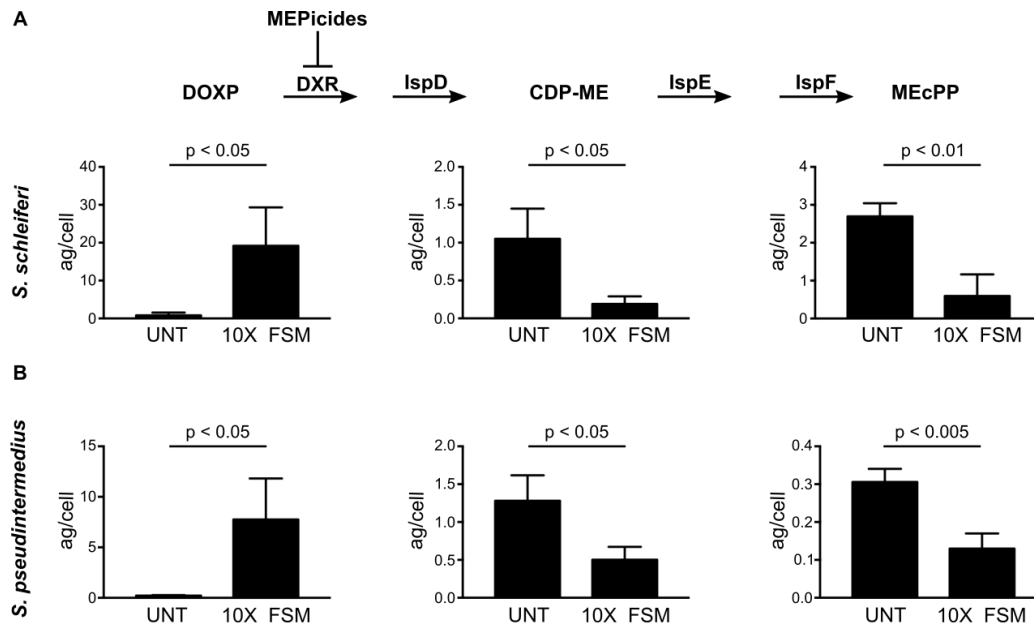
Figure 1 FSM inhibits the MEP pathway in *Staphylococcus* spp. MEP pathway metabolites were compared between untreated (UNT) *S. schleiferi* (A) and *S. pseudintermedius* (B) and bacteria treated with FSM at 10x the respective IC_{50} values. After 2 h treatment, bacterial cells were harvested and the cell pellets analyzed by LC-MS/MS. Displayed are the means ± SD of the metabolite levels from three independent experiments. P-values were determined using a Student's *t*-test.
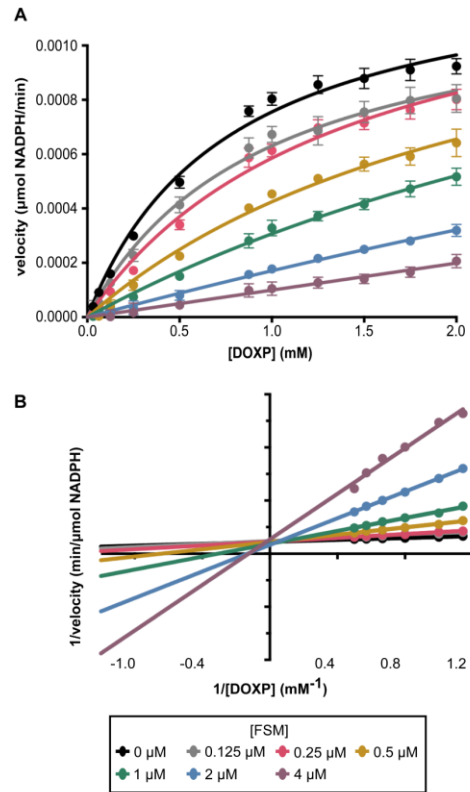
Figure 2 Inhibition of staphylococcal DXR by FSM is competitive with DOXP. (A) *S. schleiferi* DXR velocity in µmol NADPH/min with respect to the DOXP concentration in mM. Displayed are the means ± SD from three independent experiments. (B) Lineweaver−Burk double reciprocal plots of *S. schleiferi* DXR activity over a range of DOXP substrate concentrations, for illustrative purposes only.
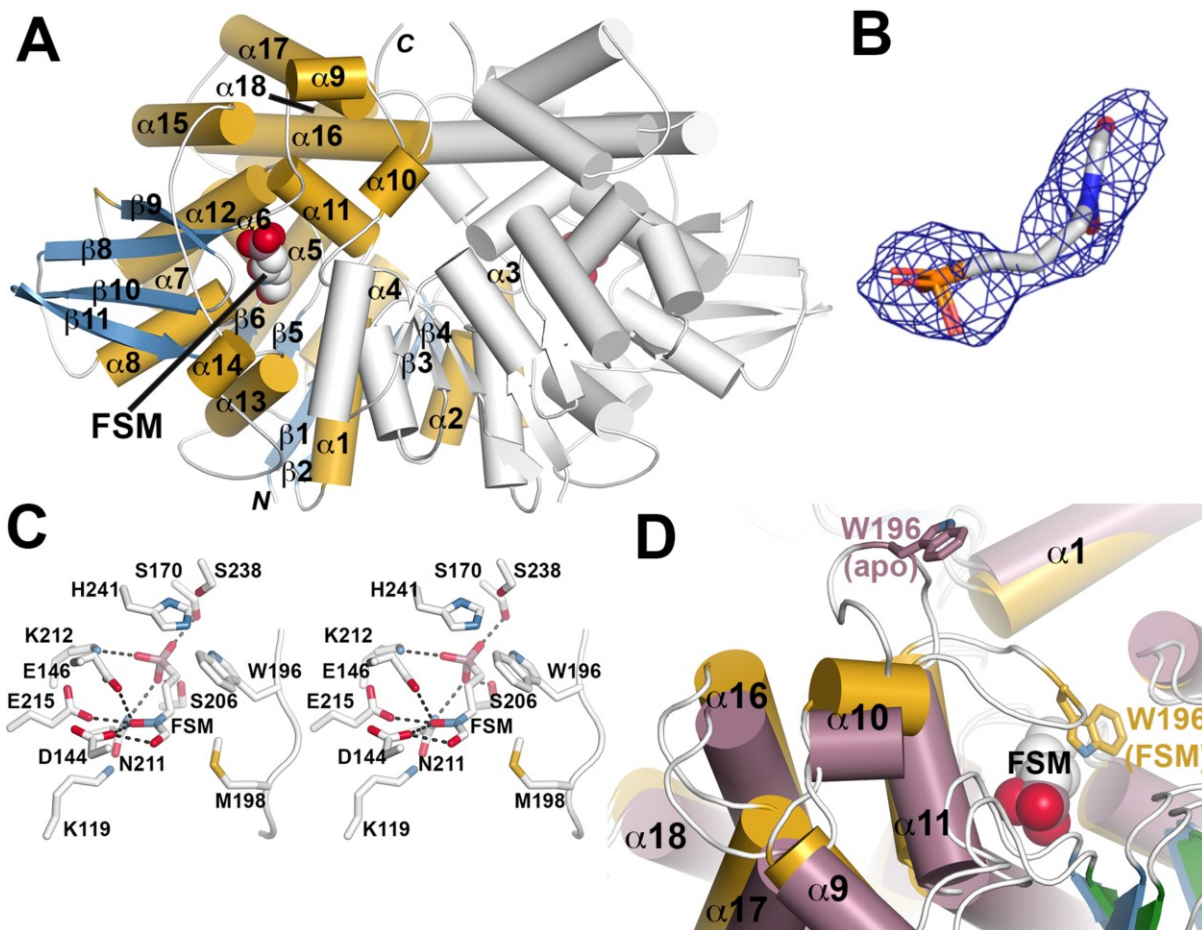
Figure 3 Crystal structure of S. schleiferi DXR. (A) Overall structure of the S. schleiferi DXR•FSM complex. The dimer is shown as a ribbon diagram with αhelices and β-strands of one monomer colored gold and blue, respectively. The position of FSM (space-filling model) in one monomer is indicated. (B) Electron density for FSM is shown as a 2Fo-Fc omit map (1 σ). (C) Stereoview of FSM binding in the active site. Dotted lines indicate protein-ligand interactions. (D) Comparison of S. schleiferi DXR apoenzyme and FSM complex structures. Structural changes in the active site region between the apoenzyme (rose) and FSM complex (gold) are shown. The major change in the position of the α10-α11 loop is emphasized by the position of Trp196 in each structure.

59
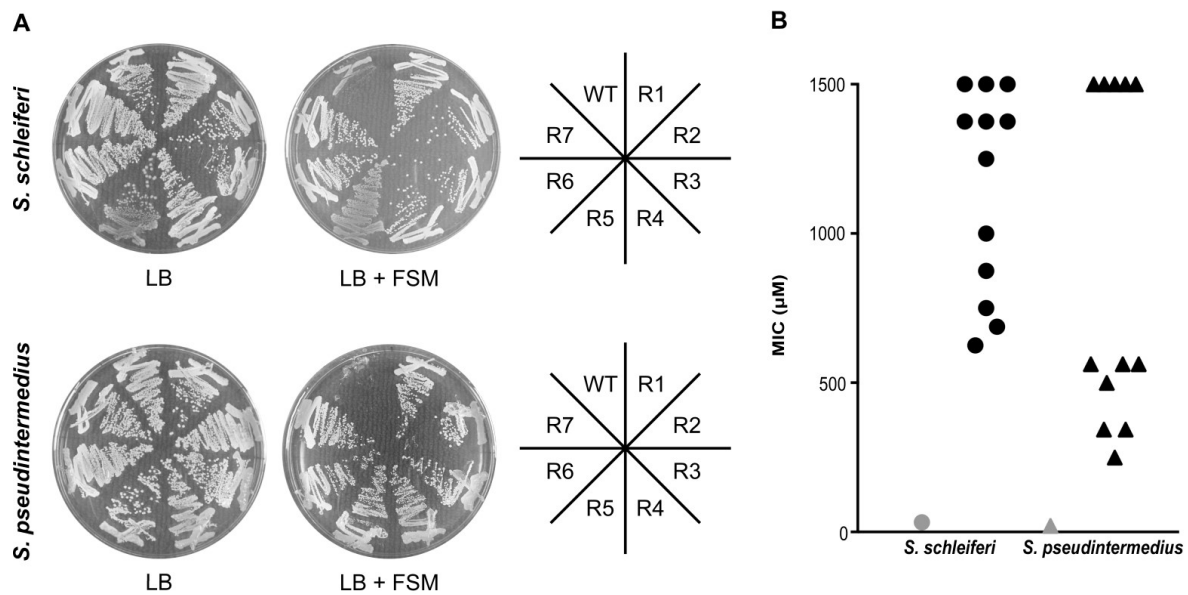
Figure 4 Successful evolution of FSM resistance. (A) Wild-type and FSM-resistant isolates from *S. schleiferi* (top) or *S. pseudintermedius* (bottom) were struck on LB agar plates with (right) and without (left) 32 µM FSM. (B) Distribution of the MIC values for WT (gray) and FSM-resistant mutants (black) from *S. schleiferi* (circles) and *S. pseudintermedius* (triangles). Displayed are the mean values for each strain from three independent experiments.
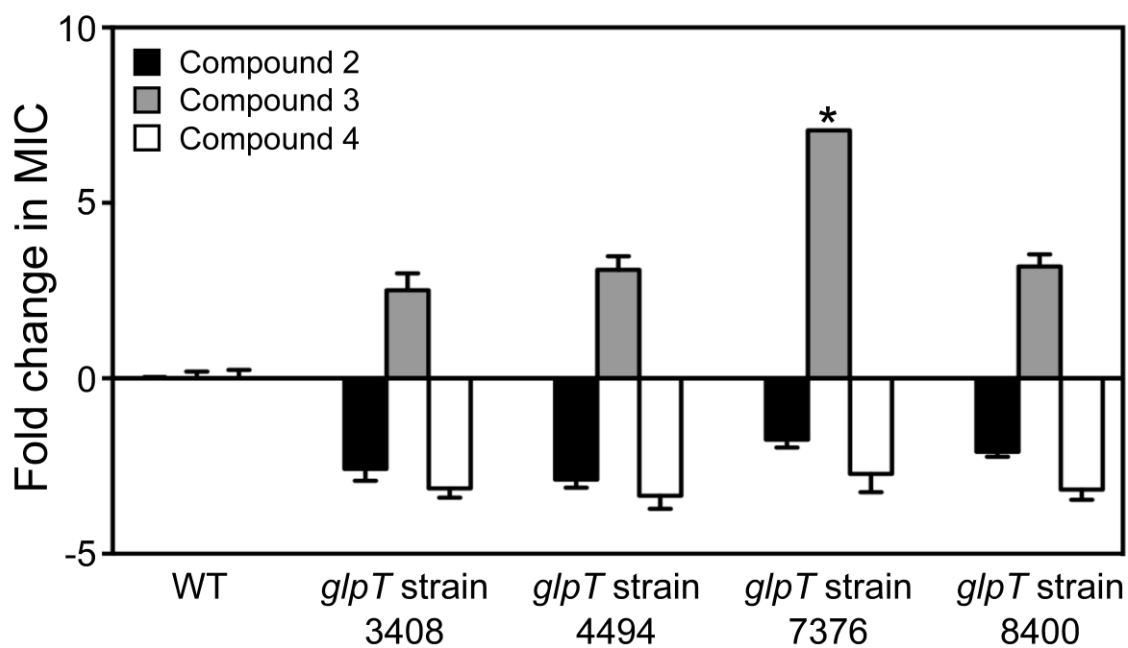
Figure 5 *glpT* mutant staphylococci are sensitive to MEPicide prodrugs. Wild-type (WT) and FSM-resistant, *glpT* mutant *S. schleiferi* isolates (strains 3408, 4494, 7376, and 8400) were treated with MEPicides and the MIC values determined during overnight growth. Displayed are the mean values of the fold change (resistant isolate/WT) ± SEM from at least three independent experiments. *MIC values observed for *glpT* strain 7376 were identical in three independent experiments performed in technical duplicate.
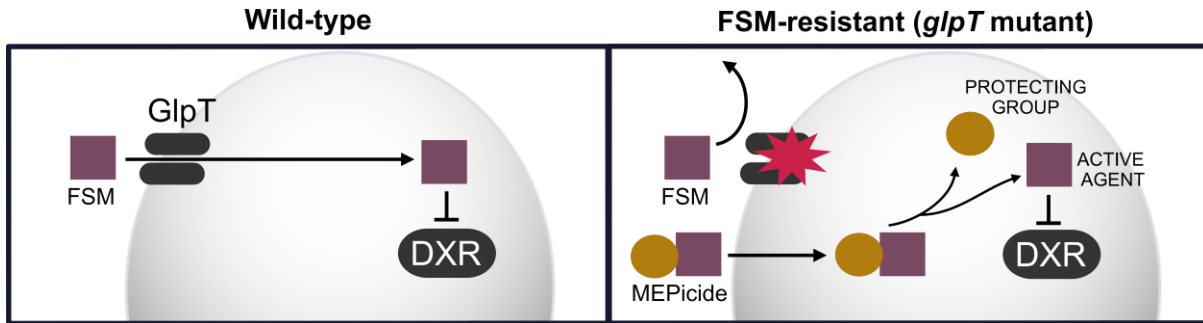
Figure 6 Model. In wild-type zoonotic staphylococci, GlpT transports the MEP pathway inhibitor FSM intracellularly where it inhibits its target, DXR. In staphylococci with *glpT* mutations, FSM is excluded from cells, resulting in FSM resistance. In contrast, lipophilic prodrug MEPicides do not require active transport and remain effective.
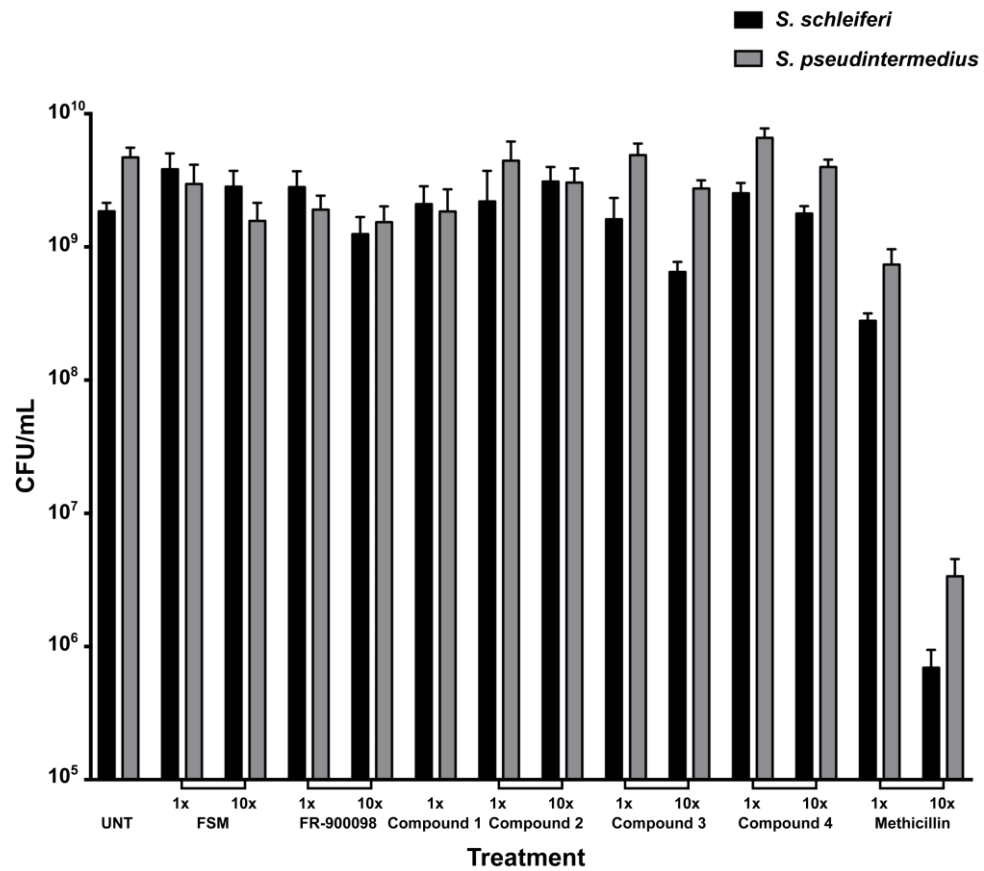
Figure S1 DXR inhibitors are bacteriostatic. Growth in CFU/mL of *S. schleiferi* and *S. pseudintermedius* after 24 h treatment is plotted against the respective treatment. Cultures were treated at 1 x IC$_{50}$ concentration and/or 10x IC$_{50}$ concentration of the inhibitors. Shown are the mean values + SD from at least three independent experiments.
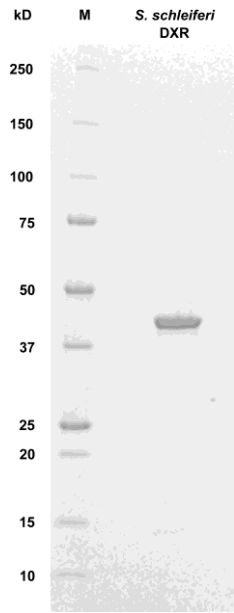
Figure S2 SDS-PAGE of purified *S. schleiferi* DXR. Molecular mass standard (M) and approximately 1 µg of purified recombinant *S. schleiferi* DXR.
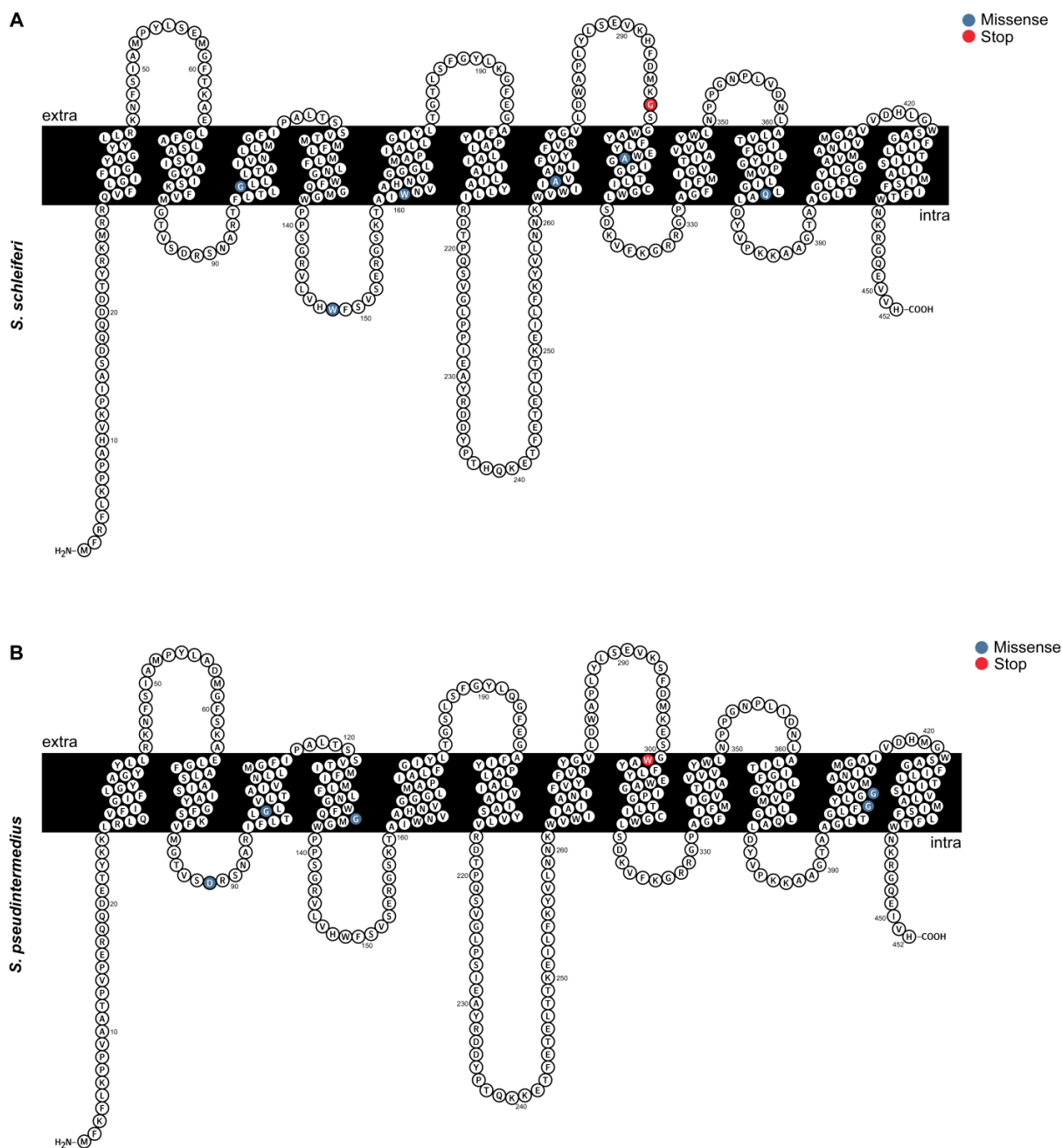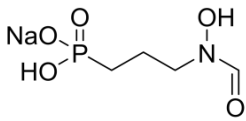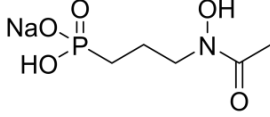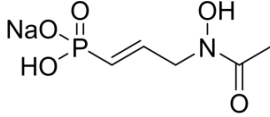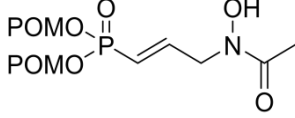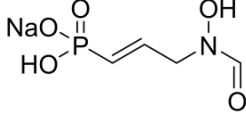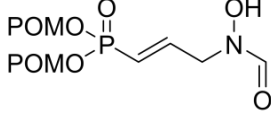
Figure S3 Membrane topology of GlpT. (A) Wild-type amino acid sequences and predicted transmembrane topology of *S. schleiferi* GlpT. Residues Gly-99, Trp-148, Trp-161, Ala-267, Gly-298, Ala-309, and Gln-379 are indicated in the sequence. Red indicates a stop mutation at the site, while blue indicates a missense mutation. (B) Wild-type amino acid sequences and predicted transmembrane topology of *S. pseudintermedius* GlpT. Residues Asp-88, Gly-99, Gly-135, Trp-301, Gly-400, and Gly-404 are indicated in the sequence. Red indicates a stop mutation at the site, while blue indicates a missense mutation. Schematic diagrams were prepared with the program Protter(5).

2.7 Tables

Table 1: Inhibitory effect of MEPicides against the *S. schleiferi* DXR enzyme and *in vitro* activity against Staphylococcus spp.

Compound	Structure	*S. schleiferi* DXR enzyme IC_{50} [μM]	*S. schleiferi* IC_{50} [μM]	*S. pseudintermedius* IC_{50} [μM]	*S. aureus* IC_{50} [μM]
FSM		0.67 ± 0.06	0.78 ± 0.13	0.31 ± 0.04	> 100
FR-900098		1.00 ± 0.18	41.06 ± 6.65	34.14 ± 6.54	> 100
1		3.31 ± 1.02	55.50 ± 2.41	54.45 ± 1.14	> 100
2		> 100	0.10 ± 0.01	0.26 ± 0.03	> 100
3		0.41 ± 0.11	4.17 ± 0.47	4.31 ± 0.51	> 100
4		12.56 ± 1.98	0.03 ± 0.00	0.21 ± 0.04	> 90

Data represent the mean ± SEM from at least three independent experiments. POM =

$(CH_3)_3CCOOCH_2$

Table S2: Primers used in this study.

Number	Primer Name	Species	Gene	Sequence (5'-3')
IH3	SS_DXR_LIC_FWD	*S. schleiferi*	*dxr*	CTCACCACCACCACCACCATATGAAAAATATAGCAATTTTAGGCGC
IH4	SS_DXR_LIC_REV	*S. schleiferi*	*dxr*	ATCCTATCTTACT CACCTACACCTCATATGATTTTGTTTTATAAT
ITS4	Sp_GlpT_dwn125_rev	*S. pseudintermedius*	*glpT*	GATACCCCTCCACTTTCCAC
ITS5	Sp_GlpT_in576_fwd	*S. pseudintermedius*	*glpT*	AGGCTTTGAAGGGGCATTTA
ITS6	Sp_GlpT_up86_fwd	*S. pseudintermedius*	*glpT*	TGTAGAAATGCGATTGACAAACT
ITS15	Ss_GlpT_up258_fwd	*S. schleiferi*	*glpT*	TTGGCTGCTGATAGTGGTTA
ITS16	Ss_GlpT_in171_fwd	*S. schleiferi*	*glpT*	AATGGGGTTTACAAAAGCAG
ITS17	Ss_GlpT_in1211_rev	*S. schleiferi*	*glpT*	CCGCCTAAATAGCCAAATAA
ITS18	Ss_GlpT_dwn387_rev	*S. schleiferi*	*glpT*	CAGCTTGATTCAACAGATCG

Table S3: Summary of crystallographic data collection and refinement statistics.

Crystal	apoenzyme	FSM complex
Space group	P3$_1$12	C2
Cell dimensions	a = b = 71.37 Å, c = 318.8 Å; g = 107.7°	a = 132.7 Å, b = 53.98 Å, c = 116.8 Å; b = 91.6°
Data collection		
Wavelength	0.98 Å	0.98 Å
Resolution range	40.3 - 2.15 Å	46.1 - 2.89 Å
(highest shell)	(2.23 - 2.15 Å)	(2.99 - 2.89 Å)
Reflections (total / unique)	96, 253 / 50,961	33,914 / 18,289
Completeness (highest shell)	99.2% (96.2%)	97.4% (91.1%)
I/s (highest shell)	33.9 (2.3)	14.7 (1.8)
R$_{sym}$ (highest shell)	10.1% (66.7%)	11.6% (53.2%)
Model and refinement		
R$_{cryst}$ / R$_{free}$	0.197 / 0.230	0.208 / 0.265
No. protein atoms	5,830	5,898
No. water molecules	81	-
No. ligand atoms	35	22
R.M.S.D. bond lengths	0.016 Å	0.010 Å
R.M.S.D. bond angles	1.07 °	1.26 °
Avg. B-factor - protein, ligand, water	64.6, 86.2, 55.5 Å^2	65.1, 70.3, - Å^2
Ramachandran plot - favored, allowed, outlier	97.5, 2.3, 0.3 %	95.7, 2.3, 2.0 %

2.8   References

1.   Jindal A, Shivpuri D, Sood S. *Staphylococcus schleiferi* meningitis in a child. Pediatr Infect J. 2015;34(3):329.

2.   Somayaji R, Rubin JE, Priyantha MA, Church D. Exploring *Staphylococcus pseudintermedius:* an emerging zoonotic pathogen? Future Microbiol. 2016;11(11):1371–4.

3.   Börjesson S, Gómez-Sanz E, Ekström K, Torres C, Grönlund U. *Staphylococcus pseudintermedius* can be misdiagnosed as *Staphylococcus aureus* in humans with dog bite wounds. Eur J Clin Microbiol Infect Dis. 2015;34(4):839–44.

4.   Lainhart W, Yarbrough ML, Burnham CA. The brief case: *Staphylococcus intermedius* group-look what the dog dragged in. J Clin Microbiol. 2018;56(2).

5.   Rojas-Marte G, Victor J, Shenoy A, Yakubov S, Chapnick E, Lin YS. Pacemaker-associated infective endocarditis caused by *Staphylococcus schleiferi*. Infect Dis Clin Pract. 2014;22(5):302–4.

6.   Pottumarthy S, Schapiro JM, Prentice JL, Houze YB, Swanzy SR, Fang FC, et al. Clinical isolates of *Staphylococcus intermedius* masquerading as methicillin-resistant *Staphylococcus aureus*. J Clin Microbiol. 2004;42(12):5881–4.

7.   Yarbrough ML, Lainhart W, Burnham CA. Epidemiology, clinical characteristics, and antimicrobial susceptibility profiles of human clinical isolates of *Staphylococcus intermedius* group. J Clin Microbiol. 2018;56(3):e01788-17.

8.   Ross Fitzgerald J. The *Staphylococcus intermedius* group of bacterial pathogens: species re-classification, pathogenesis and the emergence of meticillin resistance. Vet Dermatol. 2009;20(5–6):490–5.

9.   Humphries RM, Wu MT, Westblade LF, Robertson AE, Burnham C-AD, Wallace MA, et al. *In vitro* antimicrobial susceptibility of *Staphylococcus pseudintermedius* isolates of human and animal origin. J Clin Microbiol. 2016;54(5):1391–4.

10.   Beever L, Bond R, Graham PA, Jackson B, Lloyd DH, Loeffler A. Increasing antimicrobial resistance in clinical isolates of *Staphylococcus intermedius* group bacteria and emergence of MRSP in the UK. Vet Rec. 2015;176(7):172.

11.   Lange BM, Rujan T, Martin W, Croteau R. Isoprenoid biosynthesis: The evolution of two ancient and distinct pathways across genomes. Proc Natl Acad Sci. 2000;97(24):13172–7.

12.   Wilding EI, Kim DY, Bryant AP, Gwynn MN, Lunsford RD, McDevitt D, et al. Essentiality, expression, and characterization of the class II 3-hydroxy-3-methylglutaryl coenzyme A reductase of *Staphylococcus aureus*. J Bacteriol. 2000;182(18):5147–52.

13.   Matsumoto Y, Yasukawa J, Ishii M, Hayashi Y, Miyazaki S, Sekimizu K. A critical role of mevalonate for peptidoglycan synthesis in *Staphylococcus aureus*. Sci Rep. 2016;6:22894.

14.   Liu C-I, Liu GY, Song Y, Yin F, Hensler ME, Jeng W-Y, et al. A cholesterol biosynthesis inhibitor blocks *Staphylococcus aureus* virulence. Science. 2008;319(5868):1391–4.

15.   Misic AM, Cain CL, Morris DO, Rankin SC, Beiting DP. Divergent isoprenoid biosynthesis pathways in *Staphylococcus* species constitute a drug target for treating infections in companion animals. mSphere. 2014;1(5):1–11.

16.   Nair SC, Brooks CF, Goodman CD, Sturm A, Strurm A, McFadden GI, et al. Apicoplast isoprenoid precursor synthesis and the molecular basis of fosmidomycin resistance in *Toxoplasma gondii*. J Exp Med. 2011;208(7):1547–59.

17.   Odom AR, Van Voorhis WC. Functional genetic analysis of the *Plasmodium falciparum* deoxyxylulose 5-phosphate reductoisomerase gene. Mol Biochem Parasitol. 2010;170(2):108–11.

18.   Brown AC, Parish T. Dxr is essential in *Mycobacterium tuberculosis* and fosmidomycin resistance is due to a lack of uptake. BMC Microbiol. 2008;8:78.

19.   McAteer S, Coulson A, McLennan N, Masters M. The *lytB* gene of *Escherichia coli* is essential and specifies a product needed for isoprenoid biosynthesis. J Bacteriol. 2001;183(24):7403–7.

20.   Wagner WP, Helmig D, Fall R. Isoprene biosynthesis in *Bacillus subtilis* via the methylerythritol phosphate pathway. 1999; doi:10.1021/NP990286P.

21.   McKenney ES, Sargent M, Khan H, Uh E, Jackson ER, San Jose G, et al. Lipophilic prodrugs of FR900098 are antimicrobial against *Francisella novicida in vivo* and *in vitro* and show GlpT independent efficacy. PLoS One. 2012;7(10):e38167.

22.   Koppisch AT, Fox DT, Blagg BSJ, Poulter CD. *E. coli* MEP synthase: Steady-state kinetic analysis and substrate binding. Biochemistry. 2002;41(1):236–43.

23.   Kuemmerle HP, Murakawa T, Sakamoto H, Sato N, Konishi T, De Santis F. Fosmidomycin, a new phosphonic acid antibiotic. Part II: 1. Human pharmacokinetics. 2. Preliminary early phase IIa clinical studies. Int J Clin Pharmacol Ther Toxicol. 1985;23(10):521–8.

24.   Borrmann S, Lundgren I, Oyakhirome S, Impouma B, Matsiegui P-B, Adegnika AA, et al. Fosmidomycin plus clindamycin for treatment of pediatric patients aged 1 to 14 years with *Plasmodium falciparum* malaria. Antimicrob Agents Chemother. 2006;50(8):2713–8.

25.   Tsuchiya T, Ishibashi K, Terakawa M, Nishiyama M, Itoh N, Noguchi H. Pharmacokinetics and metabolism of fosmidomycin, a new phosphonic acid, in rats and dogs. Eur J Drug Metab Pharmacokinet. 7(1):59–64.

26.   Dhiman RK, Schaeffer ML, Bailey AM, Testa CA, Scherman H, Crick DC. 1-deoxy-D-xylulose 5-phosphate reductoisomerase (IspC) from *Mycobacterium tuberculosis*: towards understanding mycobacterial resistance to fosmidomycin. J Bacteriol. 2005;187(24):8395–402.

27.   Mackie RS, McKenney ES, van Hoek ML. Resistance of *Francisella novicida* to fosmidomycin associated with mutations in the glycerol-3-phosphate transporter. Front Microbiol. 2012;3:226.

28.   Sakamoto Y, Furukawa S, Ogihara H, Yamasaki M. Fosmidomycin resistance in adenylate cyclase deficient (*cya*) mutants of *Escherichia coli*. Biosci Biotechnol Biochem. 2003;67(9):2030–3.

29.   Argyrou A, Blanchard JS. Kinetic and chemical mechanism of *Mycobacterium tuberculosis* 1-deoxy-D-xylulose-5-phosphate isomeroreductase. Biochemistry. 2004;43(14):4375–84.

30.   Kuzuyama T, Takahashi S, Takagi M, Seto H. Characterization of 1-deoxy-D-xylulose 5-phosphate reductoisomerase, an enzyme involved in isopentenyl diphosphate biosynthesis, and identification of its catalytic amino acid residues. J Biol Chem. 2000;275(26):19928–32.

31.   Shunsuke Yajima, Kodai Hara, John M. Sanders, Fenglin Yin, Kanju Ohsawa, Jochen Wiesner, et al. Crystallographic structures of two bisphosphonate:1-deoxyxylulose-5-phosphate reductoisomerase complexes. 2004; doi:10.1021/JA040126M.

32.   Yajima S, Nonaka T, Kuzuyama T, Seto H, Ohsawa K. Crystal structure of 1-deoxy-D-xylulose 5-phosphate reductoisomerase complexed with cofactors: implications of a flexible loop movement upon substrate binding. J Biochem. 2002;131(3):313–7.

33.   Yajima S, Hara K, Iino D, Sasaki Y, Kuzuyama T, Ohsawa K, et al. Structure of 1-deoxy-D-xylulose 5-phosphate reductoisomerase in a quaternary complex with a magnesium ion, NADPH and the antimalarial drug fosmidomycin. Acta Crystallogr Sect F Struct Biol Cryst Commun. 2007;63(Pt 6):466–70.

34.   Behrendt CT, Kunfermann A, Illarionova V, Matheeussen A, Pein MK, Gräwert T, et al. Reverse fosmidomycin derivatives against the antimalarial drug target IspC (Dxr). J Med Chem. 2011;54(19):6796–802.

35.   Deng L, Endo K, Kato M, Cheng G, Yajima S, Song Y. Structures of 1-deoxy-D-xylulose-5-phosphate reductoisomerase/lipophilic phosphonate complexes. ACS Med Chem Lett. 2011;2(2):165–70.

36.   Sooriyaarachchi S, Chofor R, Risseeuw MDP, Bergfors T, Pouyez J, Dowd CS, et al. Targeting an aromatic hotspot in *Plasmodium falciparum* 1-deoxy-D-xylulose-5-phosphate reductoisomerase with β-arylpropyl analogues of fosmidomycin. ChemMedChem. 2016;11(18):2024–36.

37.   Mac Sweeney A, Lange R, Fernandes RPM, Schulz H, Dale GE, Douangamath A, et al. The crystal structure of *E. coli* 1-deoxy-D-xylulose-5-phosphate reductoisomerase in a ternary complex with the antimalarial compound fosmidomycin and NADPH reveals a tight-binding closed enzyme conformation. J Mol Biol. 2005;345(1):115–27.

38.   Kholodar SA, Tombline G, Liu J, Tan Z, Allen CL, Gulick AM, et al. Alteration of the flexible loop in 1-deoxy-D-xylulose-5-phosphate reductoisomerase boosts enthalpy-driven inhibition by fosmidomycin. Biochemistry. 2014;53(21):3423–31.

39.   Adzhubei IA, Schmidt S, Peshkin L, Ramensky VE, Gerasimova A, Bork P, et al. A method and server for predicting damaging missense mutations. Nat Methods. 2010;7(4):248–9.

40.   Murakawa T, Sakamoto H, Fukada S, Konishi T, Nishida M. Pharmacokinetics of fosmidomycin, a new phosphonic acid antibiotic. Antimicrob Agents Chemother. 1982;21(2):224–30.

41.   Jackson ER, San Jose G, Brothers RC, Edelstein EK, Sheldon Z, Haymond A, et al. The effect of chain length and unsaturation on Mtb Dxr inhibition and antitubercular killing activity of FR900098 analogs. Bioorg Med Chem Lett. 2014;24(2):649–53.

42.   Edwards RL, Brothers RC, Wang X, Maron MI, Ziniel PD, Tsang PS, et al. MEPicides: potent antimalarial prodrugs targeting isoprenoid biosynthesis. Sci Rep. 2017;7(1):8400.

43.   Uh E, Jackson ER, San Jose G, Maddox M, Lee RE, Lee RE, et al. Antibacterial and antitubercular activity of fosmidomycin, FR900098, and their lipophilic analogs. Bioorg Med Chem Lett. 2011;21(23):6973–6.

44.   San Jose G, Jackson ER, Haymond A, Johny C, Edwards RL, Wang X, et al. Structure–Activity Relationships of the MEPicides: *N* -Acyl and *O* -Linked Analogs of FR900098 as Inhibitors of Dxr from *Mycobacterium tuberculosis* and *Yersinia pestis*. ACS Infect Dis. 2016;2(12):923–35.

45.   Brücher K, Gräwert T, Konzuch S, Held J, Lienau C, Behrendt C, et al. Prodrugs of reverse fosmidomycin analogues. J Med Chem. 2015;58(4):2025–35.

46.   Faísca Phillips AM, Nogueira F, Murtinheira F, Barros MT. Synthesis and antimalarial evaluation of prodrugs of novel fosmidomycin analogues. Bioorg Med Chem Lett. 2015;25(10):2112–6.

47.   Brücher K, Illarionov B, Held J, Tschan S, Kunfermann A, Pein MK, et al. α-Substituted β-oxa isosteres of fosmidomycin: synthesis and biological evaluation. J Med Chem. 2012;55(14):6566–75.

48.	Haemers T, Wiesner J, Giessmann D, Verbrugghen T, Hillaert U, Ortmann R, et al. Synthesis of beta- and gamma-oxa isosteres of fosmidomycin and FR900098 as antimalarial candidates. Bioorg Med Chem. 2008;16(6):3361–71.

49.	Wiesner J, Ortmann R, Jomaa H, Schlitzer M. Double ester prodrugs of FR900098 display enhanced *in-vitro* antimalarial activity. Arch Pharm (Weinheim). 2007;340(12):667–9.

50.	Kurz T, Schlüter K, Pein M, Behrendt C, Bergmann B, Walter RD. Conformationally restrained aromatic analogues of fosmidomycin and FR900098. Arch Pharm (Weinheim). 2007;340(7):339–44.

51.	Kurz T, Schlüter K, Kaula U, Bergmann B, Walter RD, Geffken D. Synthesis and antimalarial activity of chain substituted pivaloyloxymethyl ester analogues of fosmidomycin and FR900098. Bioorg Med Chem. 2006;14(15):5121–35.

52.	Schlüter K, Walter RD, Bergmann B, Kurz T. Arylmethyl substituted derivatives of fosmidomycin: synthesis and antimalarial activity. Eur J Med Chem. 2006;41(12):1385–97.

53.	Wang X, Edwards R, Ball H, Johnson C, Haymond A, Girma M, et al. MEPicides: α,β-unsaturated fosmidomycin analogs as DXR inhibitors against malaria. J Med Chem. 2018;61(19):8847–58.

54.	Weese JS, van Duijkeren E. Methicillin-resistant *Staphylococcus aureus* and *Staphylococcus pseudintermedius* in veterinary medicine. Vet Microbiol. 2010;140(3–4):418–29.

55.	Kuemmerle HP, Murakawa T, Soneoka K, Konishi T. Fosmidomycin: a new phosphonic acid antibiotic. Part I: Phase I tolerance studies. Int J Clin Pharmacol Ther Toxicol. 1985;23(10):515–20.

56.	Borrmann S, Adegnika AA, Moussavou F, Oyakhirome S, Esser G, Matsiegui P-B, et al. Short-course regimens of artesunate-fosmidomycin in treatment of uncomplicated *Plasmodium falciparum* malaria. Antimicrob Agents Chemother. 2005;49(9):3749–54.

57.	Silbergeld EK, Graham J, Price LB. Industrial food animal production, antimicrobial resistance, and human health. Annu Rev Public Health. 2008;29(1):151–69.

58.	Holmes A, Moore L, Sundsfjord A, Steinbakk M, Regmi S, Karkey A, et al. Understanding the mechanisms and drivers of antimicrobial resistance. Lancet. 2016;387(10014):176–87.

59.	Robinson TP, Bu DP, Carrique-Mas J, Fèvre EM, Gilbert M, Grace D, et al. Antibiotic resistance is the quintessential One Health issue. Trans R Soc Trop Med Hyg. 2016;110(7):377–80.

60.	Robinson TP, Wertheim HFL, Kakkar M, Kariuki S, Bu D, Price LB. Animal production and antimicrobial resistance in the clinic. Lancet. 2016;387(10014):e1–3.

61.	Guardabassi L, Schwarz S, Lloyd DH. Pet animals as reservoirs of antimicrobial-resistant bacteria. Vol. 54, Journal of Antimicrobial Chemotherapy. 2004. p. 321–32.

62.	Martins LRL, Pina SMR, Simões RLR, de Matos AJF, Rodrigues P, da Costa PMR. Common phenotypic and genotypic antimicrobial resistance patterns found in a case study of multiresistant *E. coli* from cohabitant pets, humans, and household surfaces. J Environ Health. 75(6):74–81.

63.	Lloyd DH. Reservoirs of antimicrobial resistance in pet animals. Clin Infect Dis. 2007 Sep 1;45(Supplement_2):S148–52.

64.	Takahata S, Ida T, Hiraishi T, Sakakibara S, Maebashi K, Terada S, et al. Molecular mechanisms of fosfomycin resistance in clinical isolates of *Escherichia coli*. Int J Antimicrob Agents. 2010;35(4):333–7.

65.	Chekan JR, Cogan DP, Nair SK. Molecular basis for resistance against phosphonate antibiotics and herbicides. Medchemcomm. 2016;7(1):28–36.

66.   Castañeda-García A, Blázquez J, Rodríguez-Rojas A. Molecular mechanisms and clinical impact of acquired and intrinsic fosfomycin resistance. Antibiot (Basel, Switzerland). 2013;2(2):217–36.

67.   Guay DRP. Review of cefditoren, an advanced-generation, broad-spectrum oral cephalosporin. Clin Ther. 2001;23(12):1924–37.

68.   Alexandrov A, Vignali M, LaCount DJ, Quartley E, de Vries C, De Rosa D, et al. A facile method for high-throughput co-expression of protein pairs. Mol Cell Proteomics. 2004;3(9):934–8.

69.   Armstrong CM, Meyers DJ, Imlay LS, Freel Meyers C, Odom AR. Resistance to the antimicrobial agent fosmidomycin and an FR900098 prodrug through mutations in the deoxyxylulose phosphate reductoisomerase gene (dxr). Antimicrob Agents Chemother. 2015;59(9):5511–9.

70.   Minor W, Cymborowski M, Otwinowski Z, Chruszcz M, IUCr. *HKL* -3000: the integration of data reduction and structure solution – from diffraction images to an initial model in minutes. Acta Crystallogr Sect D Biol Crystallogr. 2006;62(8):859–66.

71.   McCoy AJ, Grosse-Kunstleve RW, Adams PD, Winn MD, Storoni LC, Read RJ. *Phaser* crystallographic software. J Appl Crystallogr. 2007;40(Pt 4):658–74.

72.   Emsley P, Cowtan K, IUCr. *Coot* : model-building tools for molecular graphics. Acta Crystallogr Sect D Biol Crystallogr. 2004;60(12):2126–32.

73.   Adams PD, Afonine P V., Bunkóczi G, Chen VB, Davis IW, Echols N, et al. *PHENIX* : a comprehensive Python-based system for macromolecular structure solution. Acta Crystallogr Sect D Biol Crystallogr. 2010;66(2):213–21.

74.   Determination of minimum inhibitory concentrations (MICs) of antibacterial agents by broth dilution. Clin Microbiol Infect. 2003;9(8):ix–xv.

75.   Li H, Handsaker B, Wysoker A, Fennell T, Ruan J, Homer N, et al. The sequence alignment/map format and SAMtools. Bioinformatics. 2009;25(16):2078–9.

76.   Danecek P, Auton A, Abecasis G, Albers CA, Banks E, DePristo MA, et al. The variant call format and VCFtools. Bioinformatics. 2011;27(15):2156–8.

77.   Cingolani P, Platts A, Wang LL, Coon M, Nguyen T, Wang L, et al. A program for annotating and predicting the effects of single nucleotide polymorphisms, SnpEff: SNPs in the genome of *Drosophila melanogaster* strain *w1118*; *iso-2*; *iso-3*. Fly (Austin). 2012;6(2):80–92.

78.   Omasits U, Ahrens CH, Müller S, Wollscheid B. Protter: interactive protein feature visualization and integration with experimental proteomic data. Bioinformatics. 2014;30(6):884–6.

Chapter 3: Antimicrobial prodrug activation by the staphylococcal glyoxalase GloB

Preface

The following work was performed with equal contribution between myself and Marwa O. Mikati. Additional authors include: Damon M. Osbourn, Naomi Ghebremichael, Ishaan T. Shah, Carey-Ann D. Burnham, Kenneth M. Heidel, Victoria C. Yan, Florian L. Muller, Cynthia S. Dowd, Rachel L. Edwards, Audrey R. Odom John. MOM generated POM-ERJ resistant staphylococci, quantified resistance, and performed sequencing of the resistant isolates. I characterized the resistant isolates, GloB, and performed the bioinformatic analysis. RLE performed and quantified the electron microscopy studies. KMH, VCY, FLM, and CSD provided compounds for study. CAB quantified resistance to frontline therapeutics. DMO performed LC-MS/MS analysis on these strains. YB, and FLM performed NMR experiments. MOM, I, RLE, and AROJ designed experiments. I prepared and wrote the manuscript and manuscript figures with help from AROJ and MOM. All authors approved the manuscript prior to submission.

This chapter has been published in its entirety (Mikati MO, Miller JJ, Osbourn DM, Barekatain Y, Ghebremichael N, Shah IT, Burnham CD, Heidel KM, Yan VC, Muller FL, Dowd CS, Edwards RL, Odom John AR. Antimicrobial prodrug activation by the staphylococcal glyoxalase GloB. ACS Infectious Diseases 2020 Oct). Reproduction is allowed by authors per the license agreement term set out by ACS Infectious Diseases.

(AROJ, RLE, CSD) declare themselves as co-inventors of U.S. provisional patent 62/686,416 filed June 18, 2018.

3.1 Abstract

With the rising prevalence of multidrug-resistance, there is an urgent need to develop novel antibiotics. Many putative antibiotics demonstrate promising *in vitro* potency but fail *in vivo* due to poor drug-like qualities (e.g. serum half-life, oral absorption, solubility, toxicity). These drug-like properties can be modified through the addition of chemical protecting groups, creating "prodrugs" that are activated prior to target inhibition. Lipophilic prodrugging techniques, including the attachment of a pivaloyloxymethyl group, have garnered attention for their ability to increase cellular permeability by masking charged residues and the relative ease of the chemical prodrugging process. Unfortunately, pivaloyloxymethyl prodrugs are rapidly activated by human sera, rendering any membrane permeability qualities absent during clinical treatment. Identification of the bacterial prodrug activation pathway(s) will allow for the development of host-stable and microbe-targeted prodrug therapies. Here, we use two zoonotic staphylococcal species, *S. schleiferi* and *S. pseudintermedius*, to establish the mechanism of carboxy ester prodrug activation. Using a forward genetic screen, we identify a conserved locus in both species encoding the enzyme hydroxyacylglutathione hydrolase (GloB), whose loss-of-function confers resistance to carboxy ester prodrugs. We enzymatically characterize GloB and demonstrate that it is a functional glyoxalase II enzyme, which has the capacity to activate carboxy ester prodrugs. As GloB homologs are both widespread and diverse in sequence, our findings suggest that GloB may be a useful mechanism for developing species- or genus-level prodrug targeting strategies.

3.2 Introduction

In 2019, the United States recorded 2.8 million antibiotic-resistant infections, resulting in over 35,000 deaths (1). The recent surge in antibiotic use in the setting of the COVID-19 pandemic

portends an acceleration of the antibiotic resistance threat (2, 3). *Staphylococcus aureus* is a formidable human pathogen that causes a wide variety of invasive and life-threatening infections. Closely related staphylococcal species, *S. pseudintermedius* and *S. schleiferi*, cause similar skin, soft tissue, and invasive infections in companion animals and are increasingly appreciated as serious pathogens of humans (4–7). Rising rates of methicillin resistance are reported in all three species, with methicillin-resistant *S. aureus* (MRSA) labeled a "serious threat" by the Centers for Disease Control and Prevention (CDC) (1, 8–10). Novel antimicrobial strategies that circumvent existing drug resistance mechanisms are urgently needed.

Bacterial metabolism is a promising area for antimicrobial development (11, 12). Many metabolic processes are essential for bacterial growth and pathogenesis. However, targeting metabolic processes can be inherently challenging, as a substantial portion of metabolism involves the catalytic transformation of highly charged substrates (e.g. phosphate transfer reactions). Substrate-competitive inhibitors of metabolic enzymes frequently deploy phosphonate functional groups as isosteric phosphate mimics (13). These negatively charged phosphonate antimetabolite inhibitors are prone to unacceptable drug-like characteristics and often diffuse poorly across membranes (14–19).

Prodrugging, or the modification of an inhibitor through addition of labile chemical adducts, is a common medicinal chemistry strategy to improve drug-like properties of an inhibitor under development (19–21). As promoieties are released prior to inhibitor-target engagement, prodrugging can temporarily cloak problematic pharmacokinetic properties such as poor

78

absorption or solubility. For example, the third-generation cephalosporin, cefditoren, is poorly absorbed in the small intestine unless its carboxylate is masked with a lipophilic pivaloyloxymethyl (POM) promoiety, in the form of cefditoren pivoxil (22). Similarly, nucleoside analogues are generally cell-impermeable, but their cognate prodrugs have much improved cellular penetration and antiviral efficacy, as seen in remdesivir (SARS-CoV2), tenofovir disoproxil (HIV), and sofosbuvir (hepatitis C virus, HCV) (23–26). We have recently employed lipophilic prodrugging strategies to increase the efficacy of broad-spectrum antimicrobial phosphonate antibiotics. Notably, POM ester modification of a phosphonate isoprenoid biosynthesis inhibitor (ERJ) increases antistaphyloccal activity by 200- and 500-fold for *S. schleiferi* and *S. pseudintermedius,* respectively (Figure 1A,B) (27). Similar dramatic potency gains are observed for the same class of compounds against *Mycobacterium tuberculosis*, *Yersinia pestis, Franciscella novicida*, and the malaria parasite, *Plasmodium falciparum* (16, 28–31).

While POM-prodrugs demonstrate remarkable potency *in vitro*, POM-promoieties are known to be rapidly hydrolyzed by serum carboxylesterases (32, 33). If cell-impermeable phosphonate antibiotics are to be effective at the site of infection, the promoiety must be resistant to premature bioactivation during absorption and distribution in the circulation. This specificity in prodrug activation has been successfully achieved for liver-targeted prodrugs, using the "HepDirect" prodrug approach, but has not yet been deployed for antibiotic delivery. HepDirect prodrugs are cleaved via a hepatocyte-specific cytochrome P450 enzyme, CYP3A4, and are resistant to cleavage by other human esterases (34). Selective bioactivation of prodrugs within microbes would not only increase the circulating half-life, but may also improve the therapeutic selectivity

of therapeutics that target microbial enzymes with human homologs. Understanding the molecular basis of host and microbe prodrug activation will facilitate design of microbially targeted prodrugs.

In this study, we use two zoonotic staphylococcal species, *S. schleiferi* and *S. pseudintermedius*, to uncover the enzymatic mechanism of prodrug activation in staphylococci. We identify and characterize the first bacterial carboxy ester prodrug activating enzyme, GloB, a type II glyoxalase. Using detailed biochemical analyses, we demonstrate that GloB recognizes the carboxy ester portion of the prodrug and is responsible for prodrug activation. Since GloB homologues are broadly maintained, yet have substantial sequence variation, we propose that this group of enzymes may be a strategy towards microbe-specific prodrug targeting.

3.3 Methods

3.3.1 Inhibitors.

Fosmidomycin (Millipore Sigma) and FR-900098 (Millipore Sigma) were resuspended in sterile water. POM-ERJ and POM-HEX were synthesized and stored in DMSO as described (29, 32). Cefditoren pivoxil (Millipore Sigma), cefditoren sodium (Clearsynth), and mupirocin (Millipore Sigma) were resuspended in DMSO. The synthesis of [({[(E)-benzoyloxy]methoxy}[(1E)-3-(N-hydroxyacetamido)prop-1-en-1-yl]phosphoryl)oxy]methyl benzoate (BOM-ERJ) followed that of POM-ERJ, except chloromethyl benzoate was substituted for chloromethyl pivalate (35). ^{1}H NMR (400 MHz,

Chloroform-d) δ 9.35 (s, 1H), 7.96 (dd, J = 8.1, 1.4 Hz, 4H), 7.61-7.45 (m, 2H), 7.37 (t, J = 7.8

Hz, 4H), 6.86-6.69 (m, 1H), 6.04-5.91 (m, 1H), 5.91-5.80 (m, 4H), 4.29 (s, 2H), 2.09 (s, 3H). ^{13}C

NMR (101 MHz, Chloroform-d) δ 165.04, 149.18, 134.20, 130.31-130.14, 128.87-128.54,

118.38, 116.46, 82.34, 50.64. High resolution mass-spectrometry (fast atom bombardment)

calculated for C21H23NO9P [M+H]$^{+}$, 464.1105; found, 464.1097. LC-MS (electrospray

ionization) m/z [M+H]$^{+}$ 464.1, [M+Na]$^{+}$ 486.1. Purity was greater than 95% as determined by

LC-MS.

3.3.2 Generation of POM-ERJ-resistant mutants in *S. schleiferi* and *S. pseudintermedius.*

Clinical isolates of *S. schleiferi* (S53022327s) and *S. pseudintermedius* (H20421242p) were

cloned and adapted to laboratory media through three rounds of sequential colony isolation and

growth on Luria Broth (LB) agar plates. The isolated POM-ERJ-sensitive parental clones were

incubated overnight on LB agar containing POM-ERJ at 3.56 µM and 7.12 µM for *S. schleiferi*

and 11.2 µM and 22.4 µM for *S. pseudintermedius*. Surviving single colonies were re-struck onto

LB agar for clonal isolation. POM-ERJ resistance of isolated clones was confirmed by overnight

growth on LB agar containing POM-ERJ (3.56-22.4 µM). The POM-ERJ-sensitive parental

clones were used as a control to confirm growth and antibiotic resistance.

3.3.3 Quantification of resistance.

Minimum Inhibitory Concentration (MIC) assays were performed using microtiter broth dilution in clear 96-well plates (83). Compounds were serially diluted in duplicate for a total of 10 serial dilutions. Top well concentrations were: POM-ERJ 280 µM , BOM-ERJ 53.95 µM, KMH-102 53.95 µM, cefditoren pivoxil 201.38 µM, cefditoren sodium 56.65 µM, POM-HEX 100 µM, mupirocin 2.50 µM, FR-900098 1 mM, fosmidomycin 100 µM. Bacteria cultured without drug were used as a positive control for growth, and LB without bacteria was used as a negative control for contamination. Plates were inoculated with 75 µL bacteria diluted to 1 x 10^5 CFU/mL in LB. After inoculation, plates were incubated for 16-24 h while shaking at 200 RPM at 37°C. Plates were visually inspected, and the lowest concentration of antibiotic suppressing visual growth was recorded as the MIC. All experiments were performed at least in triplicate and data reported represent the mean ± SD.

3.3.4 Transmission Electron Microscopy.

For ultrastructural analysis, bacteria were cultured in 5 mL LB while shaking at 37°C until OD_{600} = 0.25-1.0. A 1 mL sample of exponential phase bacteria was pelleted at 6,000 rcf and resuspended in 1 mL fix (2% paraformaldehyde/2.5% glutaraldehyde (Polysciences Inc., Warrington, PA) in 100 mM sodium cacodylate buffer, pH 7.2) for 1 h while rocking at RT. The fixed suspension of bacteria was washed in sodium cacodylate buffer and postfixed in 1% osmium tetroxide (Polysciences Inc.) for 1 h. Samples were then rinsed extensively in dH_2O prior to en bloc staining with 1% aqueous uranyl acetate (Ted Pella Inc., Redding, CA) for 1 h. Following several rinses in dH_2O, samples were dehydrated in a graded series of ethanol and

embedded in Eponate 12 resin (Ted Pella Inc.). Sections of 95 nm were cut with a Leica Ultracut UC7 ultramicrotome (Leica Microsystems Inc., Bannockburn, IL), and stained with uranyl acetate and lead citrate. Samples were viewed at 30,000X on a JEOL 1200EX transmission electron microscope (JEOL USA, Peabody, MA) equipped with an AMT 8 megapixel digital camera (Advanced Microscopy Techniques, Woburn, MA). Cell wall thickness was measured (ImageJ 1.38g customized for AMT images) for 100 bacteria in three independent samples (total n = 300).

3.3.5 Whole genome sequencing and variant discovery.

Using a standard phenol-chloroform extraction and ethanol precipitation protocol, genomic DNA was isolated from overnight cultures of *S. pseudintermedius* and *S. schleiferi.* Sequencing libraries were prepared and sequenced by the Washington University Genome Technology Access Center (GTAC). 1 µg of DNA was sonicated to an average size of 175 bp. Fragments were blunt ended and had an A base added to the 3′ end. Sequence adapters were ligated to the ends and the sequence tags were added via amplification. Resulting libraries were sequenced on an Illumina HiSeq 2500 to generate 101 bp paired end reads. DNA quantity and quality were assessed by GTAC using Agilent Tapestation.

For the analysis, sequences from GenBank were retrieved from the following organisms: *S. pseudintermedius* ED99 (accession number CP002478) and *S. schleiferi* 1360-13 (CP009470) assemblies were downloaded from NCBI (ftp://ftp.ncbi.nlm.nih.gov). Paired-end reads were aligned to each of the available genomes using Novoalign v3.03. (Novocraft Technologies). Duplicates were removed and variants were called using SAMtools (37). SNPs were filtered

against parent variants and by both mean depth value and quality score (minDP =5, minQ = 30) (38). Genetic variants were annotated using SnpEff v4.3 (39). For all samples, at least 90% of the genome was sequenced at 20x coverage. Whole genome sequencing data is available in the NCBI BioProject database and Sequence Read Archive under the BioProject ID 648133.

3.3.6 Sanger sequencing of *S. schleiferi* and *S. pseudintermedius* variants.

The SNPs, the reference sequences, and gene specific primers can be found in Table S4 for both *S. schleiferi* and *S. pseudintermedius*. Amplicons were sequenced by GENEWIZ.

3.3.7 Staphylococcal GloB homology modeling.

SWISS-MODEL (https://swissmodel.expasy.org/) was used to generate homology models. Modeling parameters were left at default. Both *Ss*GloB and *Sp*GloB models were built using the solved Metallo-β-lactamase superfamily protein, 2ZWR.1.A, which is 39.2% identical in sequence.

3.3.8 Recombinant expression and purification of GloB.

WT GloB from *S. schleiferi* was amplified using the forward and reverse primers in Table S4. The PCR product was then cloned into the BG1861 vector by ligation-independent cloning to introduce a N-terminal 6xHis tag and transformed into Stellar™ chemically competent cells (Clontech Laboratories) for plasmid propagation (40). Proper insertion was verified using restriction digest and Sanger sequencing. For *S. schleiferi* protein expression, the plasmid was

transformed into *E. coli* Arctic Express (Agilent). Cells were grown to OD_{600} = 0.4-0.7, chilled to

8°C, and GloB expression was induced with 0.5 mM isopropyl-β-D-thiogalactoside (IPTG)

overnight. For *S. aureus* protein expression, the plasmid was transformed into *E. coli* BL21

(DE3) pLysS cells (Promega). Cells were grown to OD_{600} = 0.4-0.7 and GloB expression was

induced with 0.5 mM IPTG for 2 h. Cells were harvested by centrifugation at 4274 x g for 5 min

at 4°C. The cell pellet was lysed by sonication in 50 mL lysis buffer containing 25 mM Tris HCl

(pH 7.5), 20 mM imidazole, 1 mM $MgCl_2$, 1 mM dithiothreitol (DTT), 1 mg/mL lysozyme, 75 U

benzonase and 1 Complete Mini EDTA-free protease inhibitor tablet (Roche Applied Science).

Insoluble proteins were removed by centrifugation twice at 20,000 x g for 20 min each. The

hexahistidine-tagged *Ss*GloB protein was affinity purified from soluble lysate via nickel agarose

beads (Gold Biotechnology). Bound protein was washed with 50 mL of lysis buffer and eluted in

300 mM imidazole, 25 mM Tris HCl (pH 7.5), 1 mM $MgCl_2$, 10% glycerol, and 250 mM NaCl.

Affinity purified protein was further purified over a HiLoad 16/60 Superdex 200 gel filtration

column (GE Healthsciences) using an AKTAExplorer 100 FPLC (GE Healthsciences). FPLC

buffer contained 25 mM Tris HCl (pH 7.5), 250 mM NaCl, 1 mM $MgCl_2$ and 10% glycerol.

Fractions containing >90% pure enzyme (evaluated by SDS-PAGE) were concentrated by

centrifugation using Amicon Ultra-15 centrifugal filter units (EMD Millipore) and flash frozen in

liquid nitrogen before permanent storage at -80°C. Protein identity was verified using mass

spectrometry at the University of Nebraska.

3.3.9 GloB mutant generation.

WT GloB for *S. schleiferi* was synthesized by GeneWiz, Inc (Beijing, China) with a CAT->AAT mutation in the 54th codon (H54N) and cloned into the BG1861 vector to introduce an N-terminal 6xHis tag. Proper insertion was verified by Sanger sequencing.

3.3.10 β-lactamase activity assay.

 S. schleiferi GloB was tested for β-lactamase activity using the chromogenic cephalosporin substrate Nitrocefin (Sigma Aldrich 484400) as in (41) but with minor changes. 50 μL reactions containing 25 mM Tris HCl (pH 7.5), 250 mM NaCl, 1 mM $MgCl_2$, 10% glycerol, and 200 μM Nitrocefin were preincubated for 15 min at 37°C, and reactions were initiated upon addition of GloB. Cleavage of Nitrocefin was allowed to proceed at 37°C and tracked kinetically at 486 nm. Assays were carried out over a range of GloB concentrations starting at 2 g of protein (1.6 M).

3.3.11 Glyoxalase II activity assay.

S. schleiferi GloB was tested for type II Glyoxalase activity as previously with minor changes (42). 50 μL reactions containing 25 mM Tris pH 7.5, 250 mM NaCl, 1 mM divalent salt, 10% glycerol, 200 μM 5,5′-Dithiobis(2-nitrobenzoic acid) (DTNB, Sigma D8130), and 1 mM D-lactoylglutathione (Sigma L7140) were monitored in a 96-well plate for an increase in absorbance at 412 nm. Reactions were pre-incubated at 37°C and initiated with the addition of GloB. The conversion of DTNB to the yellow colored substrate, TNB, by glutathione produced

by GloB, was measured through time at 37°C and 412 nm. Assays were carried out over a range of GloB concentrations to ensure that the reaction rates are linear over the period of the assay. To determine metal dependence of GloB, assays were performed using assay buffer with a final concentration of 1 mM divalent salts. Divalent salts were provided as follows: zinc chloride, manganese chloride, magnesium chloride, cobalt chloride, and calcium chloride.

3.3.12 Sample preparation for GloB vs. POM-ERJ mass spectrometry analysis.

Reactions containing 25 mM Tris HCl (pH 7.5), 250 mM NaCl, 10% glycerol, 1 mM $MnCl_2$, and 1 mM POM-ERJ were pre-warmed to 37°C before addition of WT GloB, catalytically inactive GloB (H54N), boiled GloB, or an equal amount of protein storage buffer to a final concentration of 1 μM. Reactions were placed at 37°C and sampled at 0, 15, 30, 60, 90, and 120 min. A 50 μL sample was withdrawn from each reaction at the times indicated, and the sample reaction was quenched by the addition of 200 μL acetonitrile containing 100 ng/μL enalapril as an internal standard. The samples were immediately frozen on dry ice and stored at -80°C until analysis.

The quenched reaction mixtures were centrifuged at 3200 rpm for 5 min, and 2 μL of the supernatant was diluted to 500 μL with water containing 100 ng/mL enalapril as an internal standard. Samples were analyzed by LC-MS/MS using an Applied Biosystems-Sciex API 4000. Analyte/internal standard peak area ratios were used to determine concentration and evaluate stability. Standards were evaluated over the range of 1 ng/mL to 1000 ng/mL. The MRM

transitions for enalapril and POM-ERJ were m/z: 376.9 > 91.2 and 424.0 > 364.0, respectively. A Phenomenex Luna Omega polar C18 column (2.1 × 50 mm, 5 μm) was used for chromatographic separation. Mobile phases were 0.1% formic acid in water and acetonitrile with a flow rate of 0.5 mL/min. The starting phase was 1% acetonitrile increased to 100% acetonitrile over 0.9 min. Peak areas were integrated using Analyst Software (AB Sciex, Foster City, CA).

3.3.13 In vivo cleavage of POM-ERJ.

S. schleiferi cultures of WT and POM-ERJ[R] strains were grown to an $OD_{600} = 0.5$-0.8 and then treated with 1 μM of POM-ERJ. The cultures were grown shaking at 37°C and 200 rpm and 50 μL were sampled at 0, 1, 2, and 3 h. The reactions were quenched by pelleting the cells at 4274 x g at 4°C and resuspending in 200 μL of acetonitrile with 100 ng/μL enalapril as an internal standard. The reactions were repeated in triplicate for each timepoint and strain. The LC-MS analysis was performed as described above.

3.3.14 NMR characterization of GloB POM-prodrug products.

Five hundred micromolar POM-ERJ and POM-HEX were incubated with 50 μl buffer (50 mM tris pH 7.5, 50 mM NaCl, 1mM $MgCl_2$) and 20 μl SaGloB or 40 μl SsGloB with stock concentrations of 200 μM and 100 μM respectively at 37 °C for 90 minutes. Samples were prepared for NMR studies by resuspending them in water and 10% (50 μl) D2O (Deuterium Oxide 99.9 atom % D, contains 0.75 wt %3-(trimethylsilyl)propionic -2,2,3,3-d4 acid, sodium salt, Sigma–Aldrich). NMR spectra are acquired on a Bruker Avance III HD 500 MHz

spectrometer equipped with a cryoprobe. Two-dimensional (2D) ^{1}H-^{31}P heteronuclear single quantum correlation (HSQC) measurements were obtained using hsqcetgp pulse program (with duration of 15 minutes and scan parameters of 4 scans, td=1024 and 128, gpz2 %=32.40, ^{31}P SW= 40 ppm, O2p=20 ppm, cnst2=22.95) and analyzed using 3.1 TopSpin. The 1D projection of columns excluding the water signal was obtained from the 2D ^{1}H-^{31}P HSQC spectrum by obtaining spectra of positive projection of columns 1 to 600 and 650 to 1024 and adding them.

3.3.15 Phylogenetic tree construction.

The sequences of *S. schleiferi* GloB and RpoB homologs were retrieved from NCBI using BlastP against each specified organism. Organisms were selected to represent a wide array of commensal and pathogenic bacteria (43). Additional sequences were added from *Mus musculus*, *Homo sapiens*, and other previously characterized GloB orthologs for additional comparison. Sequence alignment was performed using MUSCLE, and visualized using iTOL (44, 45).

3.4 Results

3.4.1 Selection of prodrug-resistant staphylococci.

In our previous study, we identified phosphonate antibiotics with activity against zoonotic staphylococci (*S. schleiferi* and *S. pseudintermedius*) (27). Lipophilic carboxy ester prodrug modification of these phosphonates dramatically increases antistaphylococcal potency, presumably through increased cellular penetration (Figure 1A, B). However, prodrug modifications block direct engagement of inhibitors with their enzyme target (27). For this

reason, we hypothesized that one or more staphylococcal esterases were required for intracellular prodrug activation (Figure 1A). To identify candidate prodrug activating enzymes, we designed a genetic screen/counter-screen strategy to enrich for staphylococcal strains that fail to activate lipophilic ester prodrugs.

In our strategy, we took advantage of inhibitor pairs with the same target engagement, with and without prodrug modification. We employed the phosphonate antibiotic ERJ, which selectively inhibits the intracellular enzyme deoxyxylulose phosphate reductoisomerase (DXR), and POM-ERJ, the bis-pivaloyloxymethyl prodrug form of ERJ, which inhibits intracellular DXR even though it has been shown to lack direct activity against purified recombinant DXR *in vitro* (27). We sought to enrich for staphylococcal strains that were resistant to prodrugged inhibitors (e.g. POM-ERJ) but remained sensitive to the parent phosphonate ERJ itself (27). For this reason, we first isolated staphylococcal colonies that arose from solid media containing POM-ERJ. Next, we screened these POM-ERJ-resistant isolates for cross-resistance to our parent compound, ERJ. POM-ERJ-resistant strains that remained sensitive to ERJ were subjected to whole genome sequencing to identify candidate genetic mutations giving rise to the resistance phenotype (Figure 1C). To identify conserved resistance mechanisms, we performed this screen/counter-screen independently in two staphylococcal species, *S. schleiferi* and *S. pseudintermedius*. We isolated and characterized a total of 18 POM-ERJ-resistant staphylococcal strains, with MIC_{90} values ~10-50 fold higher than that of the respective wild-type (WT) parental lines (Figure 1D). In axenic growth in rich media, no changes in growth rate are observed between WT and three POM-ERJ-resistant isolates (Figure S1).

3.4.2 POM-ERJ resistance does not alter cell wall size in staphylococci.

In previous work, we and others have found that cellular entry of the phosphonate antibiotic ERJ and ERJ analogs requires the phosphonate transporter GlpT (16, 27, 35, 36). In contrast, entry of POM-ERJ is transporter-independent (16, 27). POM-ERJ resistance could therefore arise through cell wall modifications that directly disrupt cell penetration of prodrugs. Such cell wall alterations might therefore lead to cross-resistance to other antimicrobials, such as daptomycin or vancomycin. To establish the selectivity of POM-ERJ-resistance, we determined the antimicrobial sensitivity of a subset of our prodrug-resistant strains against a panel of 18 clinical antibiotics with diverse mechanisms-of-action. We find that POM-ERJ-resistant strains are not cross-resistant to other inhibitors, including daptomycin and vancomycin (Table S1), suggesting a prodrug-specific mechanism of resistance. Additionally, we quantified the cell wall size in POM-ERJ-resistant staphylococci by transmission electron microscopy, because an established daptomycin and vancomycin resistance strategy for *S. aureus* is the generation of thickened cell walls that reduce inhibitor entry (48, 49). We find no changes in cell wall thickness in prodrug-resistant isolates compared to their prodrug-sensitive WT parental lines (Fig 2).

3.4.3 POM-ERJ-resistant staphylococci are cross-resistant to other carboxy ester prodrug antibiotics.

If POM-ERJ resistance is due to loss of a prodrug activating enzyme(s), we hypothesized that POM-ERJ-resistant staphylococci would likewise be cross-resistant to other carboxy ester prodrug antibiotics. To evaluate this possibility, we selected several additional pairs of inhibitors (carboxy ester prodrugs and their cognate parent (non-prodrugged) compounds), with distinct cellular targets (e.g. penicillin binding protein, deoxyxylulose reductoisomerase (DXR), and

enolase) (Figure 3) (22, 32). For three of our POM-ERJ-resistant *S. schleiferi* isolates, we determined the minimum inhibitory concentration (MIC) for each compound, compared to the WT parental strain (Figure 4).

We find that POM-ERJ-resistant staphylococci remain equally sensitive to non-prodrugged compounds (such as ERJ analogues) and the third-generation cephalosporin cefditoren. In contrast, POM-ERJ-resistant staphylococci exhibit significantly increased MICs to multiple classes of lipophilic ester prodrugs, exhibiting cross-resistance to both cefditoren pivoxil (cell wall inhibitor) and POM-HEX (inhibitor of enolase) (Figure 4, Table S2). Thus, POM-ERJ-resistant staphylococci are cross-resistant to other POM-prodrug inhibitors, regardless of the intracellular target. Our data suggest that POM-prodrugs follow a common and conserved activation mechanism that has been disrupted in our POM-ERJ-resistant isolates.

To explore how changes in the chemical structure of the prodrug group impacts prodrug resistance, we also evaluated whether our POM-ERJ-resistant isolates were cross-resistant to antimicrobial prodrugs that possess another common carboxy ester prodrug moiety, benzoyloxymethyl (BOM) (Figure 3). Indeed, we find our POM-ERJ-resistant isolates are also cross-resistant to BOM-ERJ (Figure 4).

Carboxy ester prodrugs are more lipophilic than their parental molecules. To evaluate whether prodrug resistance in our strains is driven by the lipophobicity of the molecule rather than its

92

ester bond, we selected an additional highly lipophilic antibiotic, mupirocin, which inhibits protein biosynthesis (Figure 3). POM-ERJ-resistant staphylococci were not cross-resistant to mupirocin, further supporting that prodrug resistance in these strains is specific to the carboxy ester bond of the prodrug (Figure 4).

3.4.4 POM-ERJ resistant staphylococci are enriched in mutations in the GloB gene.

To characterize the genetic changes associated with carboxy ester prodrug resistance, we performed whole genome sequencing of prodrug resistant isolates of both *S. schleiferi* and *S. pseudintermedius*. The whole genomes of each isolate were compared to the respective parental genome and candidate genetic changes were verified by Sanger sequencing. We prioritized nonsynonymous genetic changes that were represented in more than one strain. A complete list of identified mutations is found in Table S3.

In both independent genetic screens, we found that prodrug resistant staphylococci were enriched in mutations in an evolutionarily conserved locus. We identified multiple isolates (3/16 *S. schleiferi*, 14/18 *S. pseudintermedius*) with sequence modifications in the locus annotated as hydroxyacylglutathione hydrolase, *gloB* (LH95_06060 in *S. schleiferi*, SPSE_1252 in *S. pseudintermedius,* Table S3). Most genetic changes in *gloB* were nonsynonymous single nucleotide polymorphisms, though two nonsense alleles that would truncate approximately 50%

of the protein were also identified (Figure 5, Table S3). In several strains, the only genetic variation that distinguished WT and resistant genomes was within the *gloB* locus.

Of the 17 identified GloB mutations, 12 unique alleles were identified in prodrug-resistant staphylococci. Using PROVEAN, an algorithm which quantifies the predicted impact of amino acid substitutions on protein function, each of these 12 alleles is predicted to have deleterious effects on protein function (below the threshold score of -2.5) (Figure 5) (50). *S. schleiferi* and *S. pseudintermedius* are non-model organisms that possess endogenous CRISPR-Cas9 systems and transformation of these organisms has not yet been described (51). Attempts to ectopically complement *gloB* mutant strains with WT GloB (>90 independent transformation attempts using established methods for *S. aureus*, *S. epidermidis*, and *B. subtilis*) were unsuccessful in recovering transformed colonies, despite preparing plasmid from the *S. aureus* restriction deficient cloning intermediate, RN4220, and the cytosine methyltransferase negative *E. coli* mutant, DC10B (52–58). However, the independent selection of 12 unique loss-of-function alleles in two different species strongly suggests that loss of GloB function is responsible for prodrug resistance in *S. schleiferi* and *S. pseudintermedius*.

3.4.5 Structural basis of GloB loss-of-function.

As prodrug-resistance mutations in GloB map along its entire linear sequence, we next examined the structural basis for GloB loss-of-function. We generated homology models of both *Ss*GloB and *Sp*GloB using SWISS-MODEL (59). The resulting staphylococcal model is based on the sequence-similar metallo-β-lactamase superfamily member from *Thermus thermophilus* (PDB

94

2ZWR) (60). This hit had a global model quality estimate (GNQE) of 0.71 and 0.70 for *S. schleiferi* and *S. pseudintermedius* GloB homologs, respectively, suggesting the built models are reliable and accurate. In both protein models, we find that POM-ERJ-resistance mutations are primarily located towards the interior of the protein, occupying the same cavity as the well conserved glyoxalase II metal binding motif (THxHxDH) (61). This modeling thus indicates that these prodrug-resistance alleles impair the GloB active site (Figure 5).

3.4.6 GloB is a functioning type II glyoxalase, not a β-lactamase.

GloB is predicted to be a type II glyoxalase and a member of the large metallo-β-lactamase protein superfamily (INTERPRO IPR001279). Members of this superfamily hydrolyze thioester, sulfuric ester, and phosphodiester bonds, such as the ester linkage present in POM-ERJ (42, 61–63). Type II glyoxalases catalyze the second step in the glyoxalase pathway that is responsible for the conversion of methylglyoxal (a toxic byproduct endogenously produced during metabolism) to lactic acid. Specifically, GloB catalyzes the conversion of D-lactoylglutathione to D-lactate.

To determine whether *Ss*GloB encodes a functional type II glyoxalase, we evaluated whether *Ss*GloB hydrolyzes S-lactoylglutathione using an assay in which hydrolysis of S-lactoylglutathione is linked to a change in absorbance (Figure 6A). We purified recombinant WT *Ss*GloB protein and its catalytically inactive variant, *Ss*GloB[H54N], in which the histidine of the canonical metal binding motif (THxHxDH) has been altered to an asparagine (Figure S2) (61–63). We find that *Ss*GloB, but not *Ss*GloB[H54N], hydrolyzes S-lactoylglutathione with a specific activity of 0.493 μmol*min^{-1}mg^{-1} (Figure S3, Figure 6B,C). This activity is similar to other

characterized microbial type II glyoxalases (*Saccharomyces cerevisiae,* 1.34 μmol*min^{-1}mg^{-1}; *Trypanosoma brucei*, ~8 μmol*min^{-1}mg^{-1}), but is much lower than that of previously characterized type II glyoxalases from plants and mammals (20-2000 μmol*min^{-1}mg^{-1}) (64–72). We determined the metal dependence of *Ss*GloB and find that *Ss*GloB is a functional type II glyoxalase in manganese, cobalt, calcium, and zinc, with a modest preference noted towards magnesium (Figure S4).

As some members of the metallo-β-lactamase protein superfamily mediate hydrolysis of β-lactam antibiotics, we considered whether GloB also had β-lactamase activity. Because *gloB* mutant strains are not cross-resistant to the β-lactam-containing antibiotics (except for the prodrugged cephalosporin, cefditoren pivoxil) (Figure 4, Table S2), we predicted that GloB was not a functional metallo-β-lactamase. As expected, we find that *Ss*GloB does not hydrolyze the β-lactamase ring of nitrocefin (a canonical β-lactamase substrate), in contrast to the active *B. cereus* β-lactamase (Figure S3).

3.4.7 Staphylococcal GloB hydrolyzes POM-ERJ *in vitro* and *in vivo*.

Loss-of-function mutation in GloB is associated with resistance not only to POM-ERJ, but also to other ester prodrugs. Because GloB does not mediate resistance to ERJ or other phosphonates, our data suggested that GloB might directly catalyze the conversion of POM-ERJ to ERJ. To determine whether GloB de-esterifies POM-ERJ, we developed a liquid chromatography-mass spectrometry (LC-MS)-based assay to quantify POM-ERJ concentrations. Incubation of purified recombinant *Ss*GloB protein, but not its inactive variant (*Ss*GloB^{H54N}), with POM-ERJ results in

rapid loss of POM-ERJ, consistent with *Ss*GloB-mediated cleavage (Figure 7A). To determine whether prodrug activation activity is conserved among staphylococcal GloB homologs, we also purified recombinant GloB from the human pathogen *S. aureus* (Figure S2). We find that *Sa*GloB also directly hydrolyzes POM-ERJ (Figure 7A).

To determine whether GloB mediates intracellular prodrug activation, we evaluated the intracellular concentrations of POM-ERJ in drug-treated WT and *gloB* mutant staphylococci. We prepared staphylococcal cultures treated with POM-ERJ and quenched the reaction at several timepoints to monitor the course of intracellular prodrug depletion. As expected, we find that POM-ERJ is rapidly depleted in WT *S. schleiferi*, consistent with enzymatic activation. In contrast, POM-ERJ concentrations do not decrease over time in *gloB* mutant strains, in which the sole genetic change in each strain compared to WT is in the *gloB* locus (Figure 7B). This suggests that the initial step in carboxy ester prodrug activation in staphylococci lacks functional redundancy and is exclusively dependent on GloB.

3.4.8 POM-ERJ is a GloB substrate

We next characterized the reaction products resulting from POM-ERJ incubation with GloB. Using a highly sensitive ^{31}P-^{1}H HSQC NMR protocol, we find that WT *S. schleiferi* and WT *S. aureus* GloB remove at least one carboxy ester from POM-ERJ but are unable to fully deprotect the compound in appreciable quantities (Figure S5A). We hypothesize that the intermediate product may be the singly de-POMylated version of POM-ERJ (Hemi-POM-ERJ). To evaluate whether other POM-containing inhibitors were also direct substrates, we repeated this

experiment using POM-HEX (Figure S5B). We find that GloB is likewise capable of partially activating POM-HEX, but is unable to act upon Hemi-POM-HEX, suggesting at least one additional enzyme may be required for prodrug activation *in vivo*.

3.4.9 Staphylococcal GloB enzymes represent a distinct clade of bacterial glyoxalases.

Because staphylococcal GloB mediates de-esterification of ester prodrugs, we sought to evaluate the feasibility of using these enzymes to design prodrugs specifically targeted for activation in staphylococci. We constructed a phylogenetic tree of GloB homologs across diverse microbial genomes, as well as in humans and mice (Figure S6A), specifically including sequences of previously characterized GloB homologs. We find that considerable sequence variation exists within GloB homologs, with no clear clustering by phylogeny except for those GloB homologs originating in plants and mammals. This contrasts with a phylogenetic tree generated using the DNA-directed RNA polymerase subunit beta (rpoB), which generally follows the traditional tree of life (Figure S6B).

While sequence differences between staphylococcal GloB and human GloB suggest that there may be substrate utilization differences between humans and staphylococci, ultimately differences within the active site are likely to drive substrate specificity. Using pymol, we aligned our homology model of *Ss*GloB with the glutathione-bound GloB from humans (PDB ID: 1qh5) (73, 74). The two structures align well with a root-mean-square deviation (RMSD) of

1.528Å, and are well conserved in the overall structure as well as the characteristic Zn binding

motif, THxHxDH (Figure S7A,B). Notably, however, *Hs*GloB has a significant C-terminal

extension which is not present in *Ss*GloB. This C-terminal extension forms an α-helix which

borders the active site and contains two residues, K252 and R249, which appear to be involved in

coordinating the co-crystallized glutathione substrate (Figure S7C). The absence of this C-

terminal extension in our *Ss*GloB homology model suggests that *Hs*GloB and *Ss*GloB have

distinct active site chemistry that may be exploited to drive prodrug activation selectively by

*Ss*GloB vs *Hs*GloB.

3.5 Discussion

Antimicrobial resistance is a substantial challenge for treatment of both human and animal staphylococcal infections. Widespread methicillin resistance contributes both to poor clinical outcomes and increased treatment costs, and resistance is emerging to agents of last resort such as vancomycin and linezolid (1). Current antimicrobial therapies target a fraction of essential cellular processes, and metabolism remains a promising area for therapeutic development (11, 12). Many metabolic genes are essential for growth, especially in the nutrient limited setting of infection (75–78). Additionally, chemical ligands are readily designed with high potency by mimicking natural substrates used by metabolic enzymes. Finally, because active site mutations that disrupt binding of competitive inhibitors are likely to deleteriously affect enzyme function, the barrier to resistance can be high (79, 80). Although many metabolic processes are conserved between humans and microbes, selective targeting of microbes is achievable as is demonstrated by the success of folate antagonists (trimethoprim/sulfamethoxazole) and bedaquiline (a F_0F_1 ATP synthase inhibitor of *Mycobacterium tuberculosis*) (81–83).

Unfortunately, many metabolic inhibitors require cell-impermeable phosphonic acids for efficient target inhibition. Prodrugging strategies to increase cellular penetration have been developed for a variety of therapeutics, most notably the anti-cancer and anti-viral nucleosides (19). These prodrug strategies must be sufficient labile that the compound is activated within the target cell, yet stable enough to resist premature prodrug activation by the sera. Prodrugs which are selectively activated within target cells have the added benefit of reducing off-target toxicity effects. To achieve cell-targeted prodrug activation, knowledge of the activation mechanisms in

sera, as well the target cell, are essential. While prodrug targeting has been achieved for liver therapies, this strategy has yet to be employed for bacterial antibiotics that employ ester prodrug moieties (34).

In this work, we have identified a new mechanism for the de-esterification and activation of lipophilic ester prodrugs though a conserved staphylococcal esterase in the metallo-β-lactamase superfamily. Loss-of-function of GloB confers resistance to lipophilic carboxy ester prodrugs in two zoonotic pathogens, *S. schleiferi* and *S. pseudintermedius* (Figure 1D, Table S3). Purified recombinant GloB from *S. schleiferi* and the related human pathogen *S. aureus* directly catalyzes pro-drug de-esterification *in vitro* (Figure 7A). Because *gloB* mutant staphylococci are cross-resistant to other POM-containing prodrugs that differ in "warhead" and intracellular targets (Figure 4), we propose that substrate-specificity of GloB appears driven by recognition of the lipophilic promoiety, rather than the target inhibitory portion of each compound.

Bacterial prodrug ester activation through GloB hijacks a conserved bacterial protective mechanism in bacteria, as hydroxyacylglutathione hydrolase represents the second enzyme of the two-step glyoxalase pathway. During normal metabolism, the glycolytic intermediates glyceraldehyde-3-phosphate (GAP) and dihydroxyacetone phosphate (DHAP) undergo nonenzymatic decomposition to methylglyoxal, a toxic metabolite. GloB is required for glutathione mediated methylglyoxal detoxification, as methylglyoxal is highly reactive and irreversibly glycates proteins and nucleic acids (84–86). A secondary pathway for methylgloxal detoxification utilizing the glutathione independent enzyme, glyoxalase III, was recently

described in *S. aureus* and orthologs are found in *S. schleiferi* and *S. pseudintermedius* (77). The redundancy of the glutathione-dependent and -independent glyoxalase pathways remains unclear. In *S. aureus*, methylglyoxal accumulation potentiates antibiotic susceptibility (87). In addition, methylglyoxal is itself directly antibacterial and postulated to be the primary antistaphylococcal ingredient in Manduka honey (used on chronic wounds) (87–90). Our studies suggest that strains of *S. schleiferi* and *S. pseudintermedius* lacking GloB have preserved axenic growth in rich media, which raises concern for the ease of resistance development when GloB-targeted prodrugs are used as anti-infectives. However, the known toxicity of methylglyoxal in a host infection setting suggests that reduced methylglyoxal detoxification as the result of GloB loss-of-function would not be well tolerated *in vivo*.

Identification of GloB as a prodrug activating enzyme in staphylococci is a major step forward for highly selective microbial targeting of compounds. Though GloB homologs are widespread in microbes and are present in humans, significant sequence variation exists in GloB sequences, which results in a variety of GloB substrate preferences (Figure S6). For example, human GloB has an additional α-helix along the active site that introduces two additional residues, K252 and R249 to the substrate binding pocket (Figure S7) (74). These residues, and this α-helix, are notably absent in microbial GloBs, suggesting that there are underlying substrate differences between human and microbial GloB enzymes. Furthermore, there is substantial sequence variation in GloB orthologs across all microbes, suggesting that GloB substrate specificities may discern between individual clades of bacteria. We expect that development of prodrugs specific to GloB would result in a narrow-spectrum antibiotic, which would reduce off-target effects on the microbiome and decrease the broad pressure to evolve resistance.

3.6 Figures
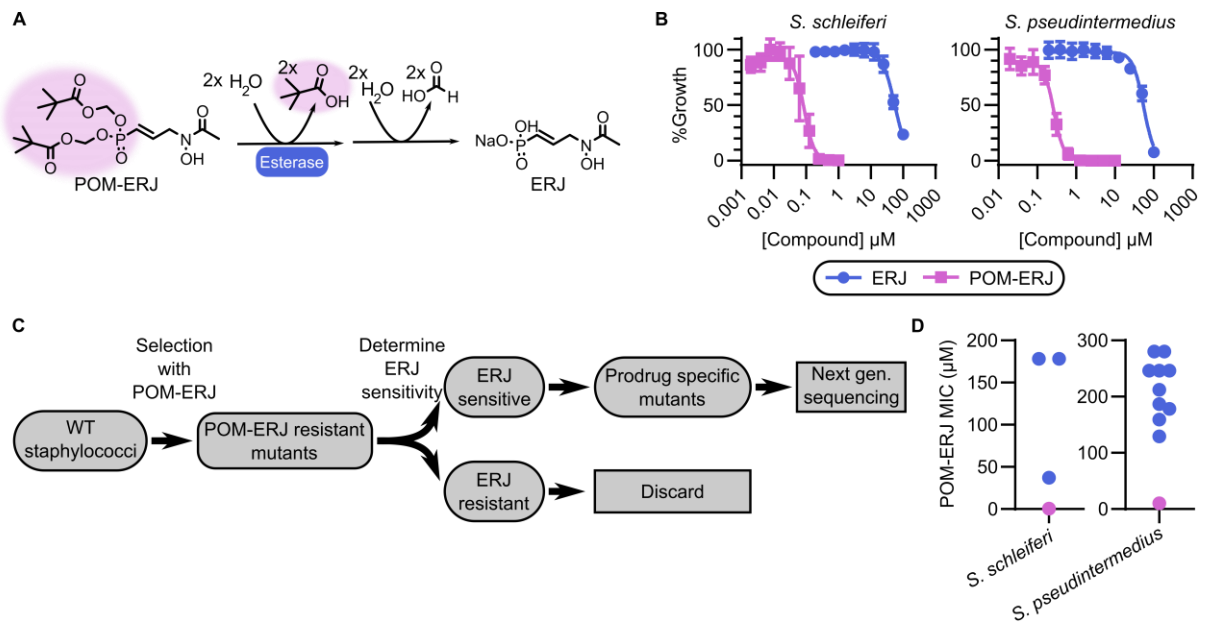
Figure 1 POM-prodrug activation and resistance generation. (A) Predicted POM-ERJ activation pathway. POM-promoiety highlighted in pink. (B) Dose-dependent growth inhibition of zoonotic staphylococci, *S. schleiferi* (left) and *S. pseudintermedius* (right), by ERJ (blue) and POM-ERJ (pink). Displayed values are the means ± SD of three independent experiments performed in technical duplicate. (C) Screening strategy to identify prodrug activating enzymes. (D) Distribution of MIC values for WT (pink) and POM-ERJ resistant mutants from *S. schleiferi* (left) and *S. pseudintermedius* (right). Displayed values are the means values for each strain from three independent experiments performed in technical duplicate.
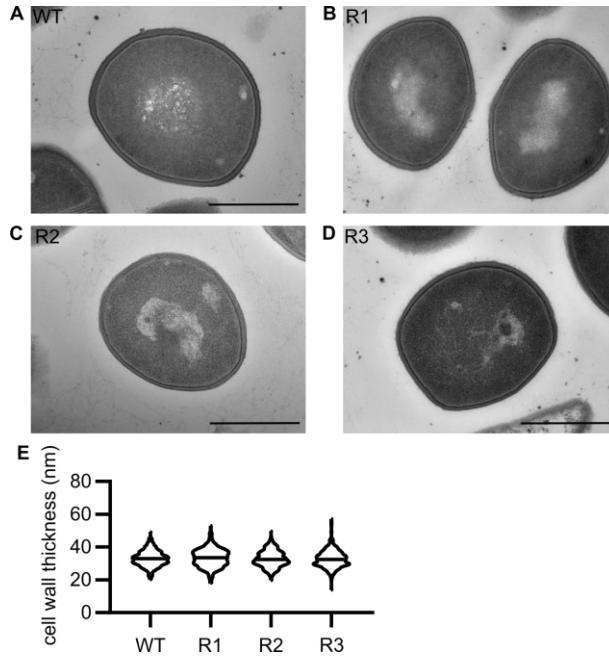
Figure 2 POM-ERJ resistant *Staphylococci* exhibit normal cell wall sizes. (A-D) Representative transmission electron micrographs of WT (A) or three independent POM-ERJ resistant *S. schleiferi* strains (B-D). Scale bars = 500 nm. (E) Distribution of cell wall thickness in WT and POM-ERJ resistant *S. schleiferi* as measured in a total of 300 cells from three independent experiments of 100 cells each. Midline indicates mean of all measurements.
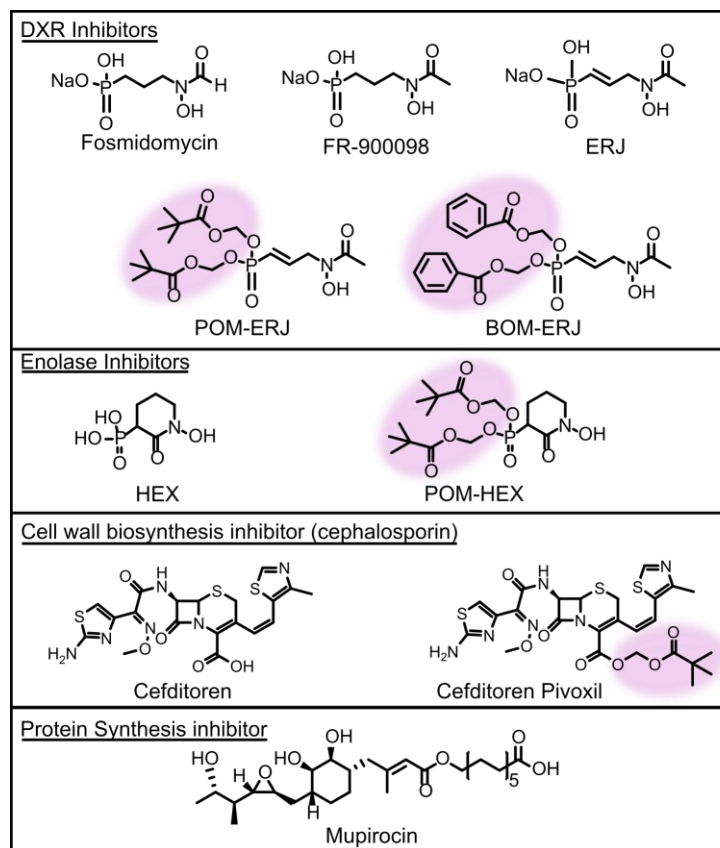
Figure 3 Structures of antistaphylococcal inhibitors used in this study. Structures are grouped by mechanism of action. For prodrugged compounds, promoieties are highlighted in pink.
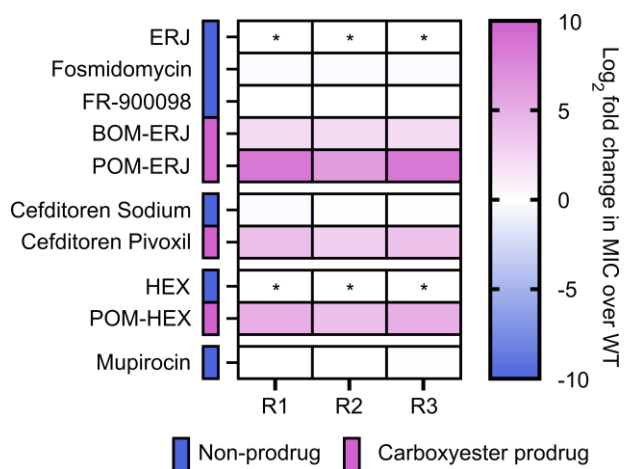
Figure 4 Cross-resistance to lipophilic ester prodrugs in POM-ERJ-resistant *S. schleiferi*. WT and POM-ERJ resistant *S. schleiferi* were treated with the compounds displayed in Figure 3. Compounds are grouped by mechanism of action and color coded to indicate whether a given compound is a carboxy ester prodrug. Displayed are the mean values of the fold change (resistant isolate/WT) of three independent experiments performed in technical duplicate. * indicates compounds whose MIC values were too high to measure. Numerical data additionally provided in Table S2.
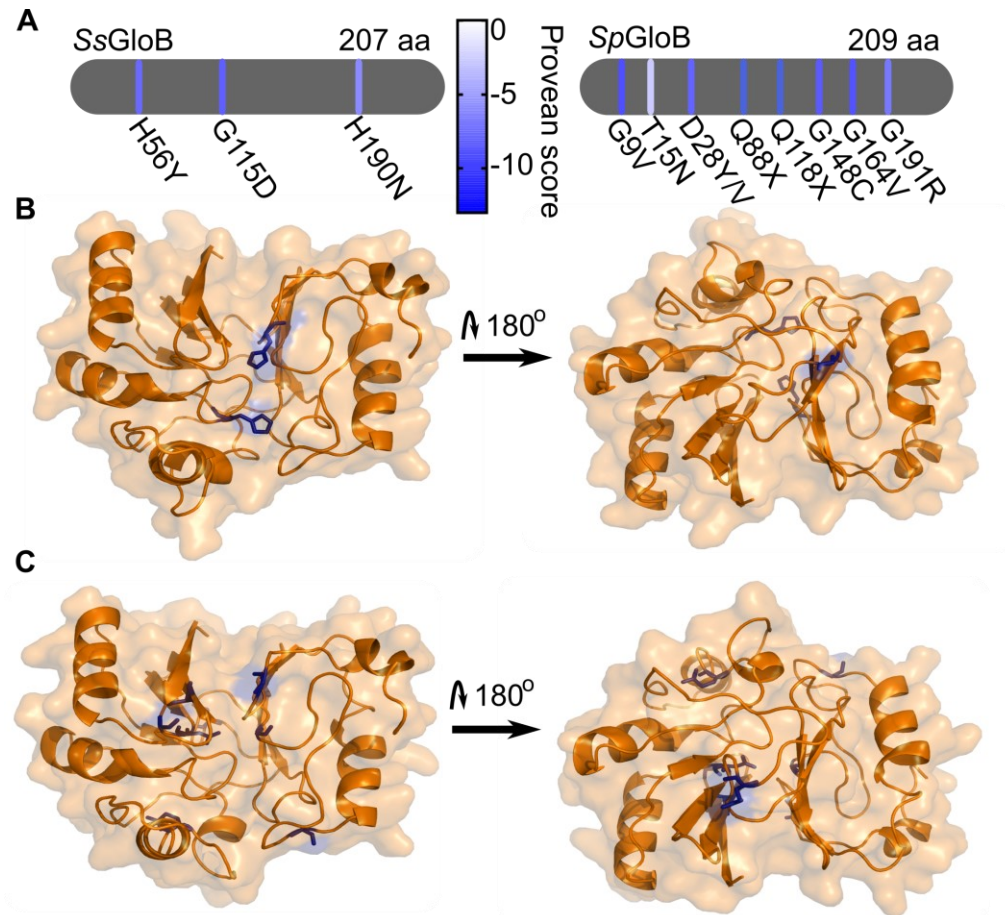
Figure 5 POM-ERJ resistant staphylococci are enriched for mutations in the locus encoding hydroxyacylglutathione hydrolase (GloB). (A) Locations and identities of GloB mutations discovered by whole-genome sequencing and independently verified by Sanger sequencing. Line coloring represents predicted impact of a given mutation on GloB function, scores below -2.5 are predicted to be deleterious. (B, C) Homology models of *S. schleiferi* (B) and *S. pseudintermedius* (C) GloB generated using SWISS-MODEL. Residues found to be mutated in POM-ERJ resistant staphylococci explicitly shown in blue.

107
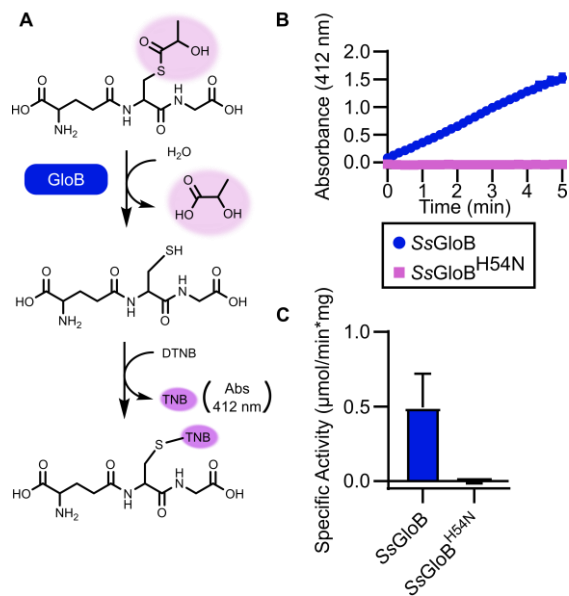
Figure 6 Enzymatic function of GloB. (A) Enzymatic catalysis of S-lactoylglutathione by GloB. DTNB conversion to TNB results in increased absorbance at 412 nm. (B) Reaction progress curve for *Ss*GloB (blue) and catalytically inactive *Ss*GloB H54N (pink), using S-lactoylglutathione as a substrate. (C) *Ss*GloB and *Ss*GloB H54N specific activity for S-lactoylglutathione. Displayed are the means ± SD from three independent experiments performed in technical duplicate.
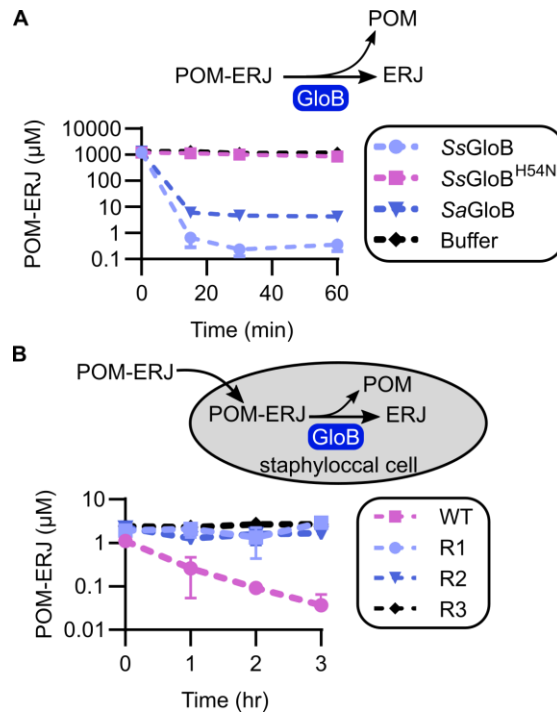
Figure 7 GloB functions activates POM-prodrugs *in vitro* and *in vivo*. (A) Recombinant *Ss*GloB, catalytically inactive *Ss*GloB H54N, GloB from *S. aureus* (*Sa*GloB), or buffer were incubated with POM-ERJ and prodrug concentrations were measured by LC-MS. (B) Wild-type and POM-ERJ-resistant *gloB* mutant *S. schleiferi* isolates were treated with POM-ERJ and intracellular drug concentrations were measured by LC-MS. Displayed are the mean values ± SD from three independent experiments. Error bars may not be visible due to precision in measurement.
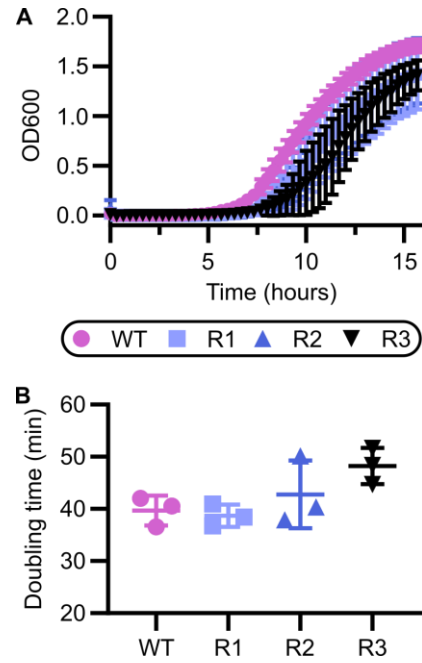
Figure S1 Growth rates of WT and POM-ERJ resistant *S. schleiferi*. (A) Average optical density (600 nm) of WT and POM-ERJ resistant *S. schleiferi* in LB media. Average is of three biological replicates in technical duplicate. (B) Doubling times for WT and POM-ERJ resistant *S. schleiferi* in LB media. Experiment performed in technical duplicate and biological triplicate. Error bars denote SEM. Means are not statistically different [Kruskal-Wallis test (p = 0.179)].
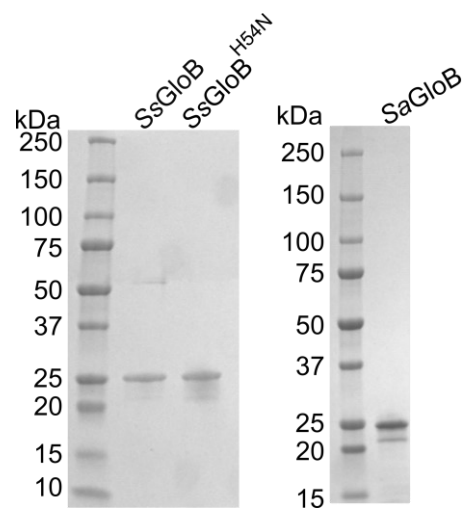
Figure S2 SDS-PAGE/Coomassie of purified recombinant *Ss*GloB, *Ss*GloB[H54N], and *Sa*GloB.
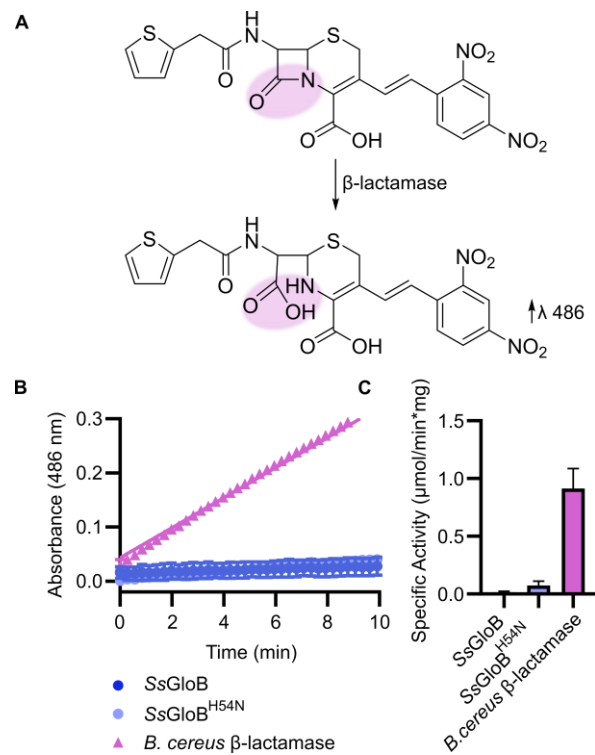
Figure S3 GloB does not have β-lactamase activity. (A) Nitrocefin activation mechanism. Cleavage of the β-lactam ring results in increased absorbance at 486 nm. (B) Progress curve for nitrocefin cleavage by *Ss*GloB, *Ss*GloB^{H54N}, and commercially available β-lactamase from *B. cereus*. (C). Specific activity for *Ss*GloB, *Ss*GloB^{H54N}, and *B. cereus* β-lactamase against nitrocefin.
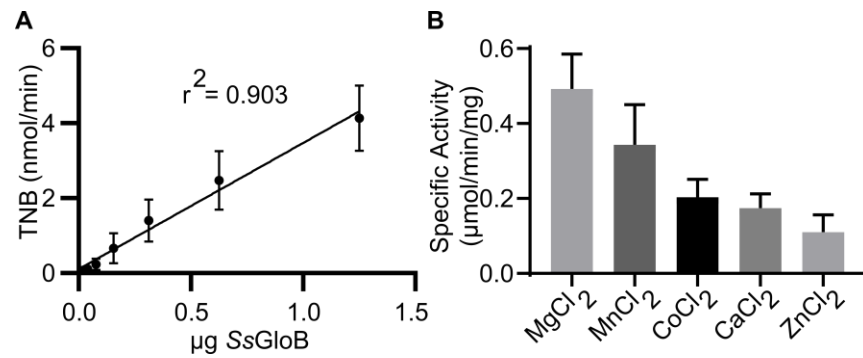
Figure S4 Assay validation for *Ss*GloB S-lactoylglutathione cleavage and detection via DTNB. (A) S-lactoylglutathione cleavage rate as a function of increasing *Ss*GloB. (B) *Ss*GloB metal dependence for cleavage of S-lactoylglutathione. *Ss*GloB was incubated with 1 mM of each divalent salt prior to S-lactoylglutathione reaction initiation.
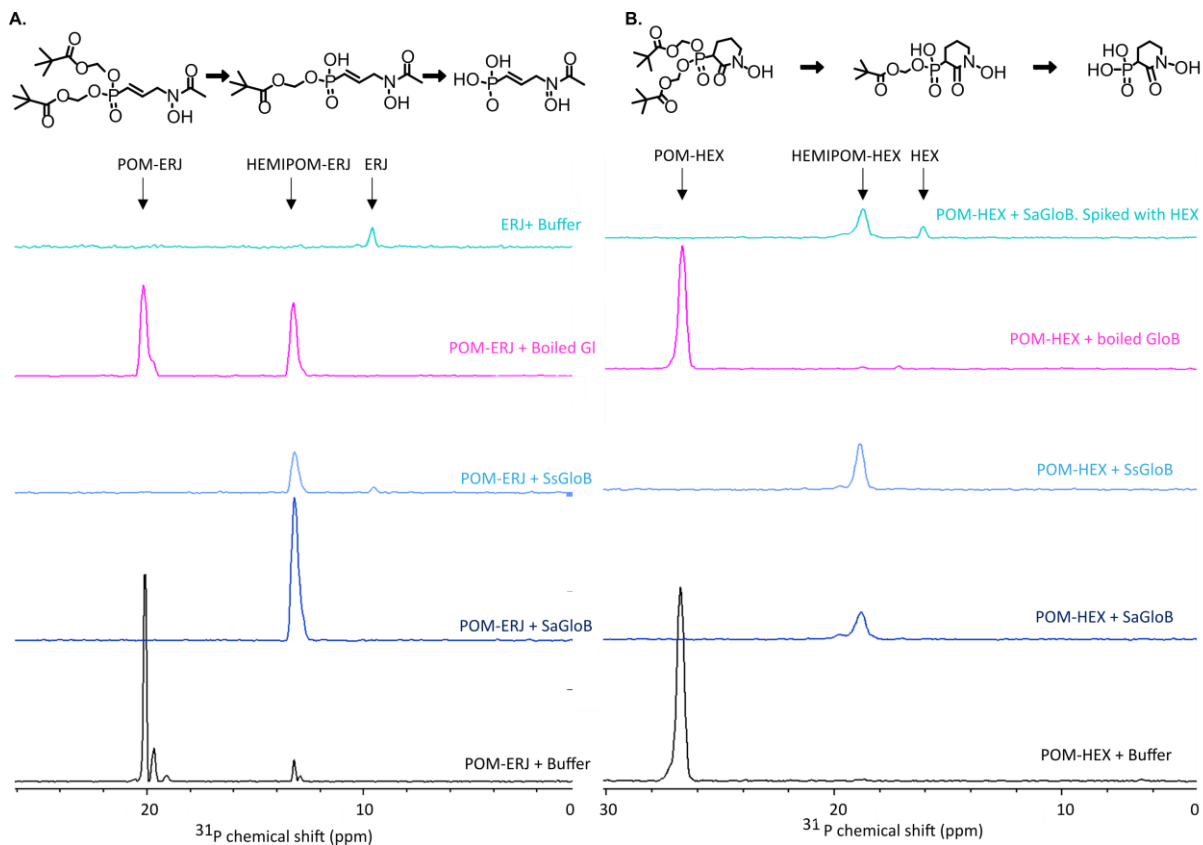
Figure S5 NMR characterization of POM-ERJ and POM-HEX prodrug activation by *Ss*GloB and *Sa*GloB. Two-dimensional (2D) ^{1}H-^{31}P HSQC NMR spectra of products following incubation of *Sa*GloB, *Ss*GloB, catalytically inactive (boiled) GloB, or buffer alone with POM-ERJ (A) or POM-HEX (B). Also included are the ^{1}H-^{31}P HSQC NMR spectra of ERJ and HEX. Displayed are representative traces of three independent experiments.
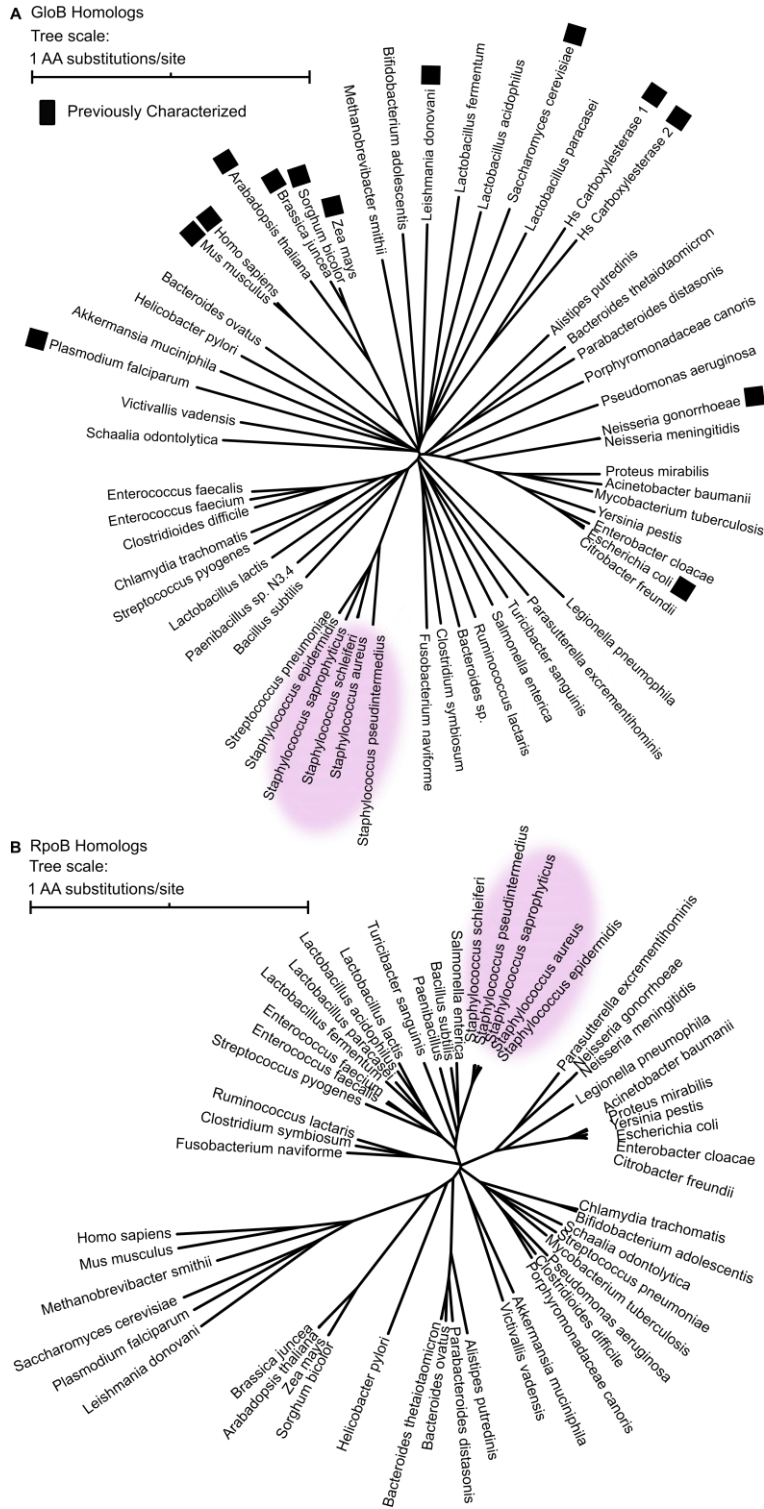
Figure S6 Phylogenetic trees of GloB (A) and RpoB (B) sequences. Pink highlighting overlain on staphylococcal species.
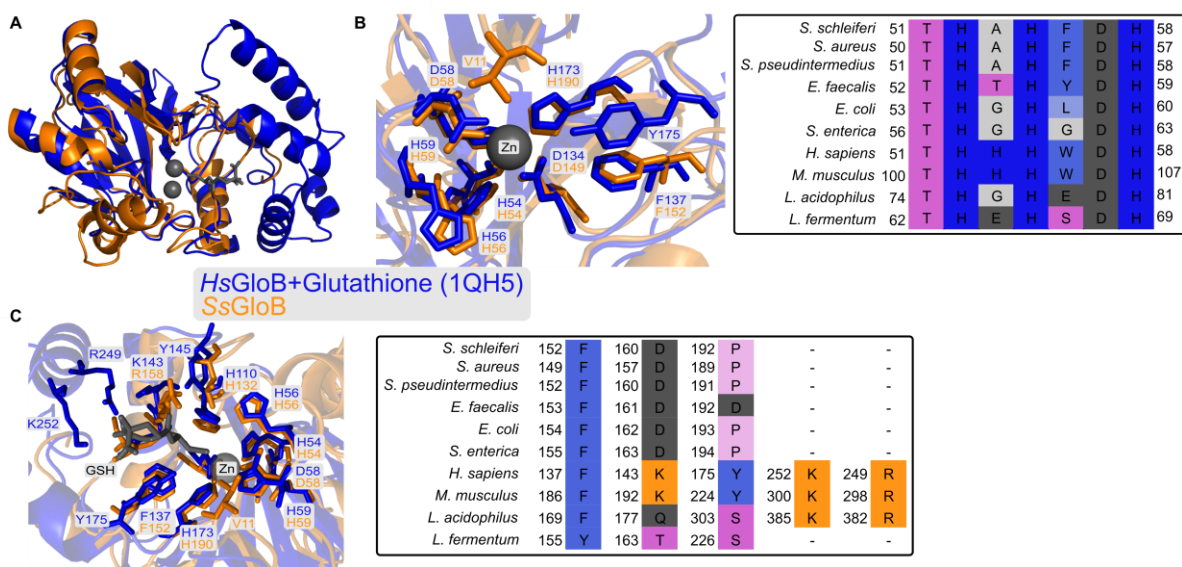
Figure S7 Structural conservation of GloB. Alignment between *Hs*GloB (orange, PDB ID: 1qh5) and *Ss*GloB (blue) homology model. (A) Overall protein alignment, RMSD = 1.528Å. (B) Metal binding pocket (left), sequence alignment of residues contacting the bound Zn (*Hs*GloB) and their analogous residues colored according to amino acid chemical properties (right). (C) Substrate binding pocket (left), sequence alignment of residues contacting the bound glutathione colored according to amino acid chemical properties (GSH, right).

3.7 Tables

Table S1: Zones of inhibition for POM-ERJ resistant zoonotic staphylococci against common frontline therapeutics. Presented are the zones of inhibition and whether the isolate is sensitive to the therapeutic (S), resistant (R), or intermediate (*) according to Clinical and Laboratory Standards Institute (CLSI) standard breakpoints.

Antimicrobial	Mechanism of Action	WT *S. pseudintermedius* Zone (in mm)	S/R?	Sp80xa Zone (in mm)	S/R?	Sp80xb Zone (in mm)	S/R?	Sp80xc Zone (in mm)	S/R?	Sp80xd Zone (in mm)	S/R?
Cefoxitin	Cell wall synthesis inhibitor	40	*	40	*	40	*	40	*	41	*
Penicillin	Cell wall synthesis inhibitor	21	R	24	R	24	R	26	R	22	R
Ceftaroline	Cell wall synthesis inhibitor	36	*	37	S	37	S	38	S	36	S
Linezolid	Protein Synthesis Inhibitor	38	S	38	S	37	S	39	S	38	S
Doxycycline	Protein Synthesis Inhibitor	32	S	34	S	34	S	36	S	34	S
Rifampin	RNA synthesis inhibitor	37	S	37	S	38	S	41	S	37	S
TMP-SMX	DHFR inhibitor (thymidine/DNA synthesis)	33	S	34	S	35	S	35	S	34	S
Clindamycin	Protein Synthesis Inhibitor	29	S	30	S	30	S	30	S	30	S
Erythromycin	Protein Synthesis Inhibitor	32	S	33	S	36	S	35	S	32	S
Vancomycin	Cell wall synthesis inhibitor	20	*	20	*	20	*	22	*	20	*
Delafloxacin	DNA gyrase inhibitor	51	*	53	*	52	*	54	*	52	*
Chloromphenicol	Protein Synthesis Inhibitor	25	S	25	S	25	S	26	S	25	S
Synercid	Protein Synthesis Inhibitor	30	S	32	S	32	S	31	S	32	S
Ciprofloxacin	DNA gyrase inhibitor	37	S	40	S	39	S	39	S	39	S
Gentamicin	PRotein Synthesis Inhibitor	33	S	35	S	34	S	35	S	34	S
Nitrofurantoin	RNA and DNA disruption	25	S	28	S	28	S	31	S	26	S
Oxacillin	Cell wall synthesis inhibitor	22	S	22	S	21	S	23	S	22	S
Daptomycin (e-test)	Cell membrane disruptor, cell depolarizer	0.032	S	0.032	S	0.032	S	0.064	S	0.047	S

117

Antimicrobial	Sp80xe Zone (in mm)	S/R?	Sp80xf Zone (in mm)	S/R?	Sp80xg Zone (in mm)	S/R?	Sp80xh Zone (in mm)	S/R?	SpMJ40.1 Zone (in mm)	S/R?	SpMJ40.2 Zone (in mm)	S/R?	Sp40xa Zone (in mm)	S/R?
Cefoxitin	41	*	40	*	41	*	40	*	40	*	40	*	37	*
Penicillin	24	R	24	R	24	R	23	R	23	R	21	R	17	R
Ceftaroline	37	S	38	S	36	S	36	S	37	S	36	S	33	S
Linezolid	37	S	37	S	38	S	38	S	38	S	36	S	34	S
Doxycycline	34	S	35	S	34	S	33	S	38	S	33	S	31	S
Rifampin	37	S	37	S	37	S	38	S	38	S	38	S	34	S
TMP-SMX	35	S	34	S	35	S	34	S	34	S	34	S	32	S
Clindamycin	30	S	30	S	30	S	29	S	29	S	29	S	26	S
Erythromycin	33	S	33	S	32	S	32	S	33	S	33	S	29	S
Vancomycin	20	*	21	*	20	*	20	*	20	*	20	*	18	*
Delafloxacin	52	*	53	*	52	*	53	*	52	*	52	*	42	*
Chloromphenicol	25	S	25	S	25	S	25	S	26	S	25	S	24	S
Synercid	32	S	32	S	32	S	32	S	33	S	31	S	30	S
Ciprofloxacin	40	S	39	S	39	S	39	S	39	S	38	S	36	S
Gentamicin	35	S	34	S	35	S	33	S	34	S	32	S	30	S
Nitrofurantoin	27	S	27	S	27	S	27	S	26	S	26	S	24	S
Oxacillin	22	S	21	S	22	S	22	S	22	S	22	S	22	S
Daptomycin (e-test)	0.047	S	0.032	S	0.032	S	0.032	S	0.032	S	0.047	S	0.047	S

118

Antimicrobial	Sp40xb Zone (in mm)	S/R?	Sp40xc Zone (in mm)	S/R?	Sp40xd Zone (in mm)	S/R?	Sp40xf Zone (in mm)	S/R?	Sp40xh Zone (in mm)	S/R?	Sp40xe Zone (in mm)	S/R?	Sp40xf Zone (in mm)	S/R?
Cefoxitin	39	*	36	*	38	*	38	*	38	*	40	*	38	*
Penicillin	22	R	18	R	21	R	22	R	21	R	21	R	20	R
Ceftaroline	36	S	34	S	34	S	34	S	34	S	35	S	35	S
Linezolid	36	S	35	S	33	S	35	S	34	S	36	S	35	S
Doxycycline	34	S	31	S	31	S	34	S	32	S	36	S	38	S
Rifampin	35	S	34	S	34	S	35	S	36	S	36	S	35	S
TMP-SMX	35	S	32	S	33	S	34	S	33	S	34	S	34	S
Clindamycin	29	S	26	S	27	S	28	S	28	S	28	S	28	S
Erythromycin	31	S	29	S	30	S	29	S	30	S	31	S	31	S
Vancomycin	20	*	18	*	19	*	19	*	20	*	20	*	20	*
Delafloxacin	50	*	48	*	49	*	49	*	49	*	50	*	50	*
Chloromphenicol	25	S	25	S	24	S	25	S	25	S	26	S	26	S
Synercid	31	S	30	S	30	S	30	S	30	S	31	S	30	S
Ciprofloxacin	38	S	37	S	36	S	36	S	36	S	36	S	37	S
Gentamicin	30	S	29	S	29	S	31	S	30	S	31	S	29	S
Nitrofurantoin	27	S	25	S	26	S	27	S	25	S	28	S	27	S
Oxacillin	23	S	21	S	22	S	27	S	22	S	22	S	22	S
Daptomycin (e-test)	0.023	S	0.047	S	0.032	S	0.047	S	0.016	S	0.023	S	0.023	S

Antimicrobial	WT *S. schleiferi* Zone (in mm)	S/R?	Ss40xa Zone (in mm)	S/R?	Ss40xd Zone (in mm)	S/R?	Ss40xg Zone (in mm)	S/R?	Ss40xe Zone (in mm)	S/R?
Cefoxitin	36	*	39	*	35	*	36	*	36	*
Penicillin	50	S	48	S	58	S	46	S	48	S
Ceftaroline	42	*	42	*	42	*	40	*	40	*
Linezolid	33	S	32	S	32	S	36	S	32	S
Doxycycline	33	S	32	S	31	S	38	S	31	S
Rifampin	37	S	36	S	36	S	38	S	35	S
TMP-SMX	29	S	27	S	27	S	28	S	28	S
Clindamycin	29	S	29	S	27	S	29	S	26	S
Erythromycin	30	S	28	S	29	S	30	S	27	S
Vancomycin	19	*	19	*	19	*	20	*	18	*
Delafloxacin	42	*	40	*	41	*	41	*	40	*
Chloromphenicol	25	S	26	S	25	S	24	S	23	S
Synercid	30	S	30	S	31	S	29	S	28	S
Ciprofloxacin	32	S	31	S	31	S	30	S	30	S
Gentamicin	33	S	30	S	29	S	30	S	28	S
Nitrofurantoin	25	S	25	S	24	S	24	S	23	S
Oxacillin	25	S	26	S	25	S	26	S	25	S
Daptomycin (e-test)	0.047	S	0.047	S	0.032	S	0.032	S	0.047	S

Antimicrobial	Ss80xa Zone (in mm)	S/R?	Ss80xe Zone (in mm)	S/R?	Ss80xf Zone (in mm)	S/R?	Ss80xg Zone (in mm)	S/R?
Cefoxitin	36	*	34	*	34	*	35	*
Penicillin	50	S	48	S	48	S	48	S
Ceftaroline	42	*	42	*	42	*	42	*
Linezolid	35	S	34	S	35	S	40	S
Doxycycline	33	S	31	S	33	S	35	S
Rifampin	37	S	35	S	38	S	37	S
TMP-SMX	27	S	29	S	29	S	30	S
Clindamycin	29	S	28	S	31	S	31	S
Erythromycin	32	S	30	S	35	S	35	S
Vancomycin	19	*	18	*	21	*	20	*
Delafloxacin	42	*	41	*	43	*	43	*
Chloromphenicol	25	S	24	S	28	S	27	S
Synercid	30	S	30	S	32	S	33	S
Ciprofloxacin	32	S	31	S	32	S	34	S
Gentamicin	30	S	29	S	31	S	33	S
Nitrofurantoin	24	S	24	S	26	S	27	S
Oxacillin	25	S	26	S	26	S	27	S
Daptomycin (e-test)	0.047	S	0.032	S	0.047	S	0.047	S

121

Table S2 Minimum inhibitory concentrations (MIC) for values for selected antistaphylococcals against POM-ERJ resistant staphylococci, R1-R3. Displayed are the mean ± SD of three independent biological experiments performed in technical duplicate. In some cases, SD is listed as N/A as MIC values are discrete measurements and each replicate provided the same measurement, hence there is no variability.

Compound	Wild-Type		R1		R2		R3	
	MIC (µM)	SD	MIC (µM)	SD	MIC (µM)	SD	MIC (µM)	SD
FSM	6.3	N/A	5.2	1.6	5.2	1.6	5.2	1.6
FR-900098	500	N/A	500	N/A	500	N/A	500	N/A
BOM-ERJ	7.9	4.6	27	N/A	27	N/A	27	N/A
POM-ERJ	0.50	N/A	180	N/A	37	13	180	N/A
Cefditoren Sodium	0.74	0.54	0.55	0.27	0.59	0.23	0.59	0.23
Cefditoren Pivoxil	0.76	N/A	12	N/A	6.0	N/A	10	3.1
HEX								
POM-HEX	3.1	N/A	100	N/A	50	N/A	100	N/A
Mupirocin	0.010	0.0041	0.010	0.0041	0.010	0.0041	0.0092	0.0032

Table S3. Single Nucleotide Polymorphisms identified via whole-genome sequencing.

Strain	Species	Base	WT Allele	SNP	Read Depth	Gene	Annotation
sp40xa	*S. pseudintermedius*	45418	G	A	5	SPSE_0038	P-type Copper Transporter
sp40xa	*S. pseudintermedius*	1282386	A	T	219	SPSE_1252	Hydroxyacylglutathione hydrolase
sp40xa	*S. pseudintermedius*	2227530	C	A	562	SPSE_2164	Putative glutamyl-endopeptidase
sp40xa	*S. pseudintermedius*	2228995	C	A	519	SPSE_2165	Putative glutamyl-endopeptidase
sp40xb	*S. pseudintermedius*	45418	G	A	5	SPSE_0038	P-type Copper Transporter
sp40xb	*S. pseudintermedius*	1282347	C	A	230	SPSE_1252	Hydroxyacylglutathione hydrolase
sp40xc	*S. pseudintermedius*	45418	G	A	5	SPSE_0038	P-type Copper Transporter
sp40xc	*S. pseudintermedius*	1110010	A	T	75	SPSE_1082	Transposase
sp40xc	*S. pseudintermedius*	2227530	C	A	722	SPSE_2164	Putative glutamyl-endopeptidase
sp40xd	*S. pseudintermedius*	1282655	C	T	358	SPSE_1252	Hydroxyacylglutathione hydrolase
sp40xe	*S. pseudintermedius*	1282745	G	T	406	SPSE_1252	Hydroxyacylglutathione hydrolase
sp40xe	*S. pseudintermedius*	1651160	C	A	493	SPSE_1610	Putative oxidoreductase
sp40xf	*S. pseudintermedius*	1282565	C	T	283	SPSE_1252	Hydroxyacylglutathione hydrolase
sp40xf	*S. pseudintermedius*	2228995	C	A	618	SPSE_2165	Putative glutamyl-endopeptidase
sp40xg	*S. pseudintermedius*	2228995	C	A	526	SPSE_2165	Putative glutamyl-endopeptidase
sp40xh	*S. pseudintermedius*	1282347	C	A	279	SPSE_1252	Hydroxyacylglutathione hydrolase
sp40xh	*S. pseudintermedius*	1651160	C	A	492	SPSE_1610	Putative oxidoreductase
sp40xh	*S. pseudintermedius*	2227530	C	A	611	SPSE_2164	Putative glutamyl-endopeptidase
sp80xa	*S. pseudintermedius*	1282655	C	T	328	SPSE_1252	Hydroxyacylglutathione hydrolase
sp80xb	*S. pseudintermedius*	2227530	C	A	679	SPSE_2164	Putative glutamyl-endopeptidase
sp80xc	*S. pseudintermedius*	1282655	C	T	372	SPSE_1252	Hydroxyacylglutathione hydrolase

Strain	Species	Base	WT Allele	SNP	Read Depth	Gene	Annotation
sp80xd	*S. pseudintermedius*	2228995	C	A	586	SPSE_2165	Putative glutamyl-endopeptidase
sp80xe	*S. pseudintermedius*	668455	T	G	5	SPSE_0610	RNA-directed DNA polymerase
sp80xe	*S. pseudintermedius*	1282874	G	A	292	SPSE_1252	Hydroxyacylglutathione hydrolase
sp80xe	*S. pseudintermedius*	1651160	C	A	415	SPSE_1610	Putative oxidoreductase
sp80xf	*S. pseudintermedius*	668455	T	G	6	SPSE_0610	RNA-directed DNA polymerase
sp80xf	*S. pseudintermedius*	1282386	A	T	327	SPSE_1252	Hydroxyacylglutathione hydrolase
sp80xf	*S. pseudintermedius*	2227530	C	A	545	SPSE_2164	Putative glutamyl-endopeptidase
sp80xg	*S. pseudintermedius*	1282347	C	A	280	SPSE_1252	Hydroxyacylglutathione hydrolase
sp80xg	*S. pseudintermedius*	2227530	C	A	613	SPSE_2164	Putative glutamyl-endopeptidase
sp80xh	*S. pseudintermedius*	1282385	G	T	35	SPSE_1252	Hydroxyacylglutathione hydrolase
sp80xh	*S. pseudintermedius*	2228043	A	C	174	SPSE_2164	Putative glutamyl-endopeptidase
sp80xh	*S. pseudintermedius*	2227746	C	A	226	SPSE_2164	Putative glutamyl-endopeptidase
sp80xh	*S. pseudintermedius*	2227738	G	A	242	SPSE_2164	Putative glutamyl-endopeptidase
sp80xh	*S. pseudintermedius*	2227731	C	A	251	SPSE_2164	Putative glutamyl-endopeptidase
sp80xh	*S. pseudintermedius*	2227735	G	C	255	SPSE_2164	Putative glutamyl-endopeptidase
sp80xh	*S. pseudintermedius*	2227530	C	A	579	SPSE_2164	Putative glutamyl-endopeptidase
sp80xh	*S. pseudintermedius*	2228995	C	A	589	SPSE_2165	Putative glutamyl-endopeptidase
spmj401	*S. pseudintermedius*	1282794	G	T	225	SPSE_1252	Hydroxyacylglutathione hydrolase
spmj401	*S. pseudintermedius*	2228995	C	A	520	SPSE_2165	Putative glutamyl-endopeptidase
spmj402	*S. pseudintermedius*	1282329	G	T	240	SPSE_1252	Hydroxyacylglutathione hydrolase
spmj402	*S. pseudintermedius*	2227530	C	A	597	SPSE_2164	Putative glutamyl-endopeptidase
ss40xa	*S. schleiferi*	925052	G	A	526	gatA	Galactitol PTS system EIIA component

Strain	Species	Base	WT Allele	SNP	Read Depth	Gene	Annotation
ss40xd	*S. schleiferi*	925052	G	A	465	gatA	Galactitol PTS system EIIA component
ss40xe	*S. schleiferi*	178904	G	T	543	LH95_00765	Putative Tributyrin Esterase
ss40xf	*S. schleiferi*	124153	G	T	564	murQ	N-acetylmuramic acid 6-phosphate etherase
ss40xg	*S. schleiferi*	971929	G	A	18	LH95_04455	tRNA Val
ss40xg	*S. schleiferi*	971915	A	T	43	LH95_04455	tRNA Val
ss40xg	*S. schleiferi*	971919	G	T	43	LH95_04455	tRNA Val
ss40xg	*S. schleiferi*	971911	C	A	45	LH95_04455	tRNA Val
ss40xg	*S. schleiferi*	971900	G	T	155	LH95_04455	tRNA Val
ss40xg	*S. schleiferi*	2095855	T	C	541	LH95_09910	Potassium-transporting ATPase potassium-binding subunit
ss80xa	*S. schleiferi*	1282737	C	A	347	LH95_06060	Hydroxyacylglutathione hydrolase
ss80xe	*S. schleiferi*	1282513	G	A	424	LH95_06060	Hydroxyacylglutathione hydrolase
ss80xe	*S. schleiferi*	1291886	G	A	386	LH95_06115	Lipoyl(octanoyl) transferase
ss80xf	*S. schleiferi*	1282335	C	T	289	LH95_06060	Hydroxyacylglutathione hydrolase
ss80xg	*S. schleiferi*	1291886	G	A	294	LH95_06115	Lipoyl(octanoyl) transferase
ss80xh	*S. schleiferi*	1319671	G	T	406	LH95_06255	Ribonuclease Z
ss80xh	*S. schleiferi*	1478053	C	G	458	LH95_07010	Unknown function

Table S4. Primers used during this study.

Primer Sequence	Gene	Species	Purpose
ATATCGCTGCATTAGATGATG	SPSE_1252(gloB)	S. pseudintermedius	Sequencing
AGGCACATCATATCGTGTTAG	SPSE_1252(gloB)	S. pseudintermedius	Sequencing
TGCTGCATTCCTTCATCAAGTG	SPSE_1252(gloB)	S. pseudintermedius	Sequencing
CCGTTCAATAAAGGGCTCGATC	SPSE_1252(gloB)	S. pseudintermedius	Sequencing
TGATGAATTTGCAGTAGTGGGC	SPSE_1252(gloB)	S. pseudintermedius	Sequencing
TTAACCTTGACCGTCTAAAAACG	SPSE_1252(gloB)	S. pseudintermedius	Sequencing
CTGGGCAAAAGCAGTATTGACAGGC	SPSE_2164	S. pseudintermedius	Sequencing
GTTAGCGGTTTCACAGATGCC	SPSE_2164	S. pseudintermedius	Sequencing
AGTTCGGGTTATTCATCCTAACACC	SPSE_2164	S. pseudintermedius	Sequencing
CGTCAACTGTCGCATTAACTGC	SPSE_2164	S. pseudintermedius	Sequencing
TAATTTGCGTTTTTGTTAACCC	SPSE_2164	S. pseudintermedius	Sequencing
GTTAGCGGTTTCACAGATGCC	SPSE_2164	S. pseudintermedius	Sequencing
ATGAAAATTTCCTACCTGACTTTAG	LH95_06060(gloB)	S. schleiferi	Sequencing
ATTTTTTTTGATTCTGAAGATGGG	LH95_06060(gloB)	S. schleiferi	Sequencing
ATGCACAGCCTACTGCGATCGAAG	LH95_06060(gloB)	S. schleiferi	Sequencing
TTACTCATGCACATTTTGATC	LH95_06060(gloB)	S. schleiferi	Sequencing
AATGCCCAGGTGTATGCAATGC	LH95_06060(gloB)	S. schleiferi	Sequencing
TTAGCCATGAAGATAAGGATTC	LH95_06060(gloB)	S. schleiferi	Sequencing
GGAGTGAGTATTTTGGCACG	LH95_00765	S. schleiferi	Sequencing
AGGATCAAAAGGTGTCCCCACAAC	LH95_00765	S. schleiferi	Sequencing
GCGGTGATTATGCCCAATGCAGACC	LH95_00765	S. schleiferi	Sequencing
TTATACCATCTCACGCGTATGATGG	LH95_00765	S. schleiferi	Sequencing
CTCACCACCACCACCACCATATGAAAATTTCCTACCTGACTTTAG	LH95_06060(gloB)	S. schleiferi	LIC Cloning
ATCCTATCTTACTCACTTAGCCATGAAGATAAGGATTC	LH95_06060(gloB)	S. schleiferi	LIC Cloning
CTCACCACCACCACCACCATATGAATATTTCTAATCTTACTTTAG	SPSE_1252(gloB)	S. pseudintermedius	LIC Cloning
ATCCTATCTTACTCACTTAACCTTGACCGTCTAAAAACG	SPSE_1252(gloB)	S. pseudintermedius	LIC Cloning

3.8   References

1.   CDC (2019) Antibiotic resistance threats in the United States 2019. Available at: https://www.cdc.gov/drugresistance/pdf/threats-report/2019-ar-threats-report-508.pdf.

2.   Hsu J (2020) How COVID-19 is accelerating the threat of antimicrobial resistance. *BMJ* 1983(May):m1983.

3.   Antimicrobial resistance in the age of COVID-19 (2020) *Nat Microbiol* 5(6):779–779.

4.   Jindal A, Shivpuri D, Sood S (2015) *Staphylococcus schleiferi* meningitis in a child. *Pediatr Infect Dis J* 34(3):329.

5.   Somayaji R, Rubin JE, Priyantha MA, Church D (2016) Exploring *Staphylococcus pseudintermedius*: an emerging zoonotic pathogen? *Future Microbiol* 11(11):1371–1374.

6.   Börjesson S, Gómez-Sanz E, Ekström K, Torres C, Grönlund U (2015) *Staphylococcus pseudintermedius* can be misdiagnosed as *Staphylococcus aureus* in humans with dog bite wounds. *Eur J Clin Microbiol Infect Dis* 34(4):839–44.

7.   Lainhart W, Yarbrough ML, Burnham CA (2018) The brief case: *Staphylococcus intermedius* group-look what the dog dragged In. *J Clin Microbiol* 56(2). doi:10.1128/JCM.00839-17.

8.   Fitzgerald JR (2009) The *Staphylococcus intermedius* group of bacterial pathogens: species re-classification, pathogenesis and the emergence of methicillin resistance. *Vet Dermatol* 20(5–6):490–5.

9.   Humphries RM, et al. (2016) In vitro antimicrobial susceptibility of *Staphylococcus pseudintermedius* isolates of human and animal origin. *J Clini* 54(5):1391–1394.

10.   Beever L, et al. (2015) Increasing antimicrobial resistance in clinical isolates of *Staphylococcus intermedius* group bacteria and emergence of MRSP in the UK. *Vet Rec* 176(7):172.

11.   Haag NL, Velk KK, Wu C (2012) Potential antibacterial targets in bacterial central metabolism. *Int J Adv life Sci* 4(1–2):21–32.

12.   Murima P, McKinney JD, Pethe K (2014) Targeting bacterial central metabolism for drug development. *Chem Biol* 21(11):1423–32.

13.   Azema L, Baron R, Ladame S (2006) Targeting enzymes with phosphonate-based inhibitors: mimics of tetrahedral transition states and stable isosteric analogues of phosphates. *Curr Enzym Inhib* 2(1):61–72.

14.   Kornberg RD, McNamee MG, McConnell HM (1972) Measurement of transmembrane potentials in phospholipid vesicles. *Proc Natl Acad Sci U S A* 69(6):1508–13.

15.   Ju L, Cheng Z, Fast W, Bonomo RA, Crowder MW (2018) The continuing challenge of metallo-β-lactamase inhibition: mechanism matters. *Trends Pharmacol Sci*:1–13.

16.   McKenney ES, et al. (2012) Lipophilic prodrugs of FR900098 are antimicrobial against Francisella novicida *in vivo* and *in vitro* and show GlpT independent efficacy. *PLoS One* 7(10):e38167.

17.   Zhang Y, et al. (2006) Activity of nitrogen-containing and non-nitrogen-containing bisphosphonates on tumor cell lines. *J Med Chem* 49(19):5804–14.

18.   Hsiao C-HC, et al. (2014) Synthesis of a phosphoantigen prodrug that potently activates Vγ9Vδ2 T-lymphocytes. *Chem Biol* 21(8):945–954.

19.   Wiemer AJ, Wiemer DF (2015) Prodrugs of phosphonates and phosphates: crossing the membrane barrier. 200(1):115–160.

20.   Hecker SJ, Erion MD (2008) Prodrugs of phosphates and phosphonates. *J Med Chem* 51(8):2328–2345.

21.   Heidel KM, Dowd CS (2019) Phosphonate prodrugs: an overview and recent advances. *Future Med Chem* 11(13):1625–1643.

22.   Sakagami K, et al. (1990) Synthesis and oral activity of ME 1207, a new orally active cephalosporin. *J Antibiot (Tokyo)* 43(8):1047–1050.

23.   Siegel D, et al. (2017) Discovery and synthesis of a phosphoramidate prodrug of a pyrrolo[2,1-*f*][triazin-4-amino] adenine *C*-nucleoside (GS-5734) for the treatment of Ebola and emerging viruses. *J Med Chem* 60(5):1648–1661.

24.   Shaw JP, et al. (1997) Metabolism and pharmacokinetics of novel oral prodrugs of 9-[(R)-2-(phosphonomethoxy)propyl]adenine (PMPA) in dogs. *Pharm Res* 14(12):1824–9.

25.   Robbins BL, Srinivas R V, Kim C, Bischofberger N, Fridland A (1998) Anti-human immunodeficiency virus activity and cellular metabolism of a potential prodrug of the acyclic nucleoside phosphonate 9-R-(2-phosphonomethoxypropyl)adenine (PMPA), Bis(isopropyloxymethylcarbonyl)PMPA. *Antimicrob Agents Chemother* 42(3):612–7.

26.   Sofia MJ, et al. (2010) Discovery of a β- d -2′-deoxy-2′-α-fluoro-2′-β- C-methyluridine nucleotide prodrug (PSI-7977) for the treatment of Hepatitis C virus. *J Med Chem* 53(19):7202–7218.

27.   Edwards RL, et al. (2020) Potent, specific MEPicides for treatment of zoonotic staphylococci. *PLoS Pathog* 16(6):e1007806.

28.   Uh E, et al. (2011) Antibacterial and antitubercular activity of fosmidomycin, FR900098, and their lipophilic analogs. *Bioorg Med Chem Lett* 21(23):6973–6976.

29.   Edwards RL, et al. (2017) MEPicides: potent antimalarial prodrugs targeting isoprenoid biosynthesis. *Sci Rep* (June):1–11.

30.   San Jose G, et al. (2013) Design of potential bisubstrate inhibitors against *Mycobacterium tuberculosis* (Mtb) 1-deoxy-D-xylulose 5-phosphate reductoisomerase (Dxr)—evidence of a novel binding mode. *Medchemcomm*:1099–1104.

31.   San Jose G, et al. (2016) Structure-activity relationships of the MEPicides: N-acyl and O-linked analogs of FR900098 as inhibitors of DXR from *Mycobacterium tuberculosis* and *Yersinia pestis*. *ACS Infect Dis* 2(12):923–935.

32.   Lin Y, et al. (2018) Eradication of ENO1-deleted glioblastoma through collateral lethality. *bioRxiv*. doi:10.1101/331538.

33.   Wang X, et al. (2018) MEPicides: α,β-Unsaturated Fosmidomycin Analogues as DXR Inhibitors against Malaria. *J Med Chem* 61:8847–8858.

34.   Erion MD, et al. (2005) Liver-targeted drug delivery using HepDirect prodrugs. *J Pharmacol Exp Ther* 312(2):554–60.

35.   Jackson ER, et al. (2014) The effect of chain length and unsaturation on Mtb Dxr inhibition and antitubercular killing activity of FR900098 analogs. *Bioorg Med Chem Lett* 24(2):649–653.

36.   Determination of minimum inhibitory concentrations (MICs) of antibacterial agents by broth dilution (2003) *Eur Soc Clin Microbiol Infect Dis* (March):1–7.

37.   Li H, et al. (2009) The sequence alignment/map format and SAMtools. *Bioinformatics* 25(16):2078–9.

38.   Danecek P, et al. (2011) The variant call format and VCFtools. *Bioinformatics* 27(15):2156–8.

39.   Cingolani P, et al. (2012) A program for annotating and predicting the effects of single nucleotide polymorphisms, SnpEff: SNPs in the genome of *Drosophila melanogaster* strain w1118; iso-2; iso-3. *Fly (Austin)* 6(2):80–92.

40.   Alexandrov A, et al. (2004) A facile method for high-throughput co-expression of protein pairs. *Mol Cell Proteomics* 3(9):934–8.

41.   O'Callaghan CH, Morris A, Kirby SM, Shingler AH (1972) Novel method for detection of β-lactamases by using a chromogenic cephalosporin substrate. *Antimicrob Agents Chemother* 1(4):283–8.

42.   Stamp AL, et al. (2010) Structural and functional characterization of *Salmonella enterica serovar typhimurium* YcbL: An unusual type II glyoxalase. *Protein Sci* 19(10):1897–1905.

43.   Yatsunenko T, et al. (2012) Human gut microbiome viewed across age and geography. *Nature* 486(7402):222–227.

44.   Madeira F, et al. (2019) The EMBL-EBI search and sequence analysis tools APIs in 2019. *Nucleic Acids Res* 47(W1):W636–W641.

45.   Letunic I, Bork P (2019) Interactive Tree Of Life (iTOL) v4: recent updates and new developments. *Nucleic Acids Res* 47(W1):W256–W259.

46.   Sakamoto Y, Furukawa S, Ogihara H, Yamasaki M (2003) Fosmidomycin resistance in adenylate cyclase deficient (cya) mutants of *Escherichia coli*. *Biosci Biotechnol Biochem* 67(9):2030–2033.

47.   Mackie RS, McKenney ES, van Hoek ML (2012) Resistance of *Francisella Novicida* to fosmidomycin associated with mutations in the glycerol-3-phosphate transporter. *Front Microbiol* 3. doi:10.3389/fmicb.2012.00226.

48.   Cui L, et al. (2003) Cell wall thickening is a common feature of vancomycin resistance in *Staphylococcus aureus*. *J Clin Microbiol* 41(1):5–14.

49.   Jones T, et al. (2016) Failures in clinical treatment of *Staphylococcus aureus* infection with daptomycin are associated with alterations in surface charge, membrane phospholipid asymmetry, and drug binding. 52(1):269–278.

50.   Choi Y, Sims GE, Murphy S, Miller JR, Chan AP (2012) Predicting the functional effect of amino acid substitutions and indels. *PLoS One* 7(10):e46688.

51.   Misic AM, Cain CL, Morris DO, Rankin SC, Beiting DP (2014) Divergent isoprenoid biosynthesis pathways in *Staphylococcus* species constitute a drug target for treating infections in companion animals. *mSphere* 1(5):1–11.

52.   Grosser MR, Richardson AR (2016) Method for preparation and electroporation of *S. aureus* and *S. epidermidis*. *Methods Mol Biol* 1373:51–7.

53.   Nair D, et al. (2011) Whole-genome sequencing of *Staphylococcus aureus* strain RN4220, a key laboratory strain used in virulence research, identifies mutations that affect not only virulence factors but also the fitness of the strain. *J Bacteriol* 193(9):2332–5.

54.   Schneewind O, Model P, Fischetti VA (1992) Sorting of protein A to the staphylococcal cell wall. *Cell* 70:267–281.

55.   Doron S, et al. (2018) Systematic discovery of antiphage defense systems in the microbial pangenome. *Science (80-)* 359(6379):eaar4120.

56.   Puyet A, et al. (1987) A simple medium for rapid regeneration of *Bacillus subtilis* protoplasts transformed with plasmid DNA. *FEMS Microbiol Lett* 40(1):1–5.

57.   Costa SK, Donegan NP, Corvaglia A-R, François P, Cheung AL (2017) Bypassing the restriction system To improve transformation of *Staphylococcus epidermidis*. *J Bacteriol* 199(16). doi:10.1128/JB.00271-17.

58.   Monk IR, Tree JJ, Howden BP, Stinear TP, Foster TJ (2015) Complete bypass of restriction systems for major *Staphylococcus aureus* lineages. *MBio* 6(3). doi:10.1128/mBio.00308-15.

59.   Waterhouse A, et al. (2018) SWISS-MODEL: homology modelling of protein structures and complexes. *Nucleic Acids Res* 46(W1):W296–W303.

60.   Yamamura A, et al. (2009) Structure of TTHA1623, a novel metallo-beta-lactamase superfamily protein from *Thermus thermophilus* HB8. *Acta Crystallogr Sect F Struct Biol Cryst Commun* 65(Pt 5):455–9.

61.   Melino S, Capo C, Dragani B, Aceto A, Petruzzelli R (1998) A zinc-binding motif conserved in glyoxalase II, beta-lactamase and arylsulfatases. *Trends Biochem Sci* 23(10):381–2.

62.   Zang TM, Hollman DA, Crawford PA, Crowder MW, Makaroff CA (2001) *Arabidopsis* glyoxalase II Contains a Zinc/iron binuclear metal center that is essential for substrate binding and catalysis. *J Biol Chem* 276(7):4788–4795.

63.   Park H-S, et al. (2006) Design and evolution of new catalytic activity with an existing protein scaffold. *Science* 311(5760):535–8.

64.   Murata K, et al. (1986) Metabolism of alpha-ketoaldehydes in yeasts: Purification and characterization of glyoxalase II from *Saccharomyces cerevisiae*. *Agric Biol Chem* 50(1):135–142.

65.   Irsch T, Krauth-Siegel RL (2004) Glyoxalase II of African trypanosomes is trypanothione-dependent. *J Biol Chem* 279(21):22209–22217.

66.   Norton SJ, Talesa V, Yuan WJ, Principato GB (1990) Glyoxalase I and glyoxalase II from *Aloe vera*: purification, characterization and comparison with animal glyoxalases. *Biochem Int* 22(3):411–418.

67.   Norton SJ (a), Principato GBB, Talesa V (b), Lupattelli M (c), Rosi G (b) (1989) Glyoxalase II from *Zea mays*: properties and inhibition study of the enzyme purified by use of a new affinity ligand. *Enzyme* 42(4):189–196.

68.   Talesa V, et al. (1990) Presence of glyoxalase II in mitochondria from spinach leaves: comparison with the enzyme from cytosol. *Biochem Int* 22(6):1115–20.

69.   Talesa V, et al. (1990) Isolation of glyoxalase II from bovine liver mitochondria. *Biochem Int* 20(1):53–8.

70.   vander Jagt D. (1989) The glyoxalase system. *Chem Biochem Med Asp*:597–641.

71.   Cho MY, Bae CD, Park JB, Lee TH (1998) Purification and cloning of glyoxalase II from rat liver. *Exp Mol Med* 30(1):53–7.

72.   Uotila L (1973) Purification and characterization of S-2-hydroxyacylglutathione hydrolase (glyoxalase II) from human liver. *Biochemistry* 12:3944–3951.

73.   Schrödinger The PyMOL molecular graphics system. Available at: https://pymol.org/2/.

74.   Cameron AD, Ridderström M, Olin B, Mannervik B (1999) Crystal structure of human glyoxalase II and its complex with a glutathione thiolester substrate analogue. *Structure* 7(9):1067–1078.

75.   Brown SA, Palmer KL, Whiteley M (2008) Revisiting the host as a growth medium. *Nat Rev Microbiol* 6(9):657–666.

76.   Fey PD, et al. (2013) A genetic resource for rapid and comprehensive phenotype screening of nonessential *Staphylococcus aureus* genes. *MBio* 4(1). doi:10.1128/mBio.00537-12.

77.   Baba T, et al. (2006) Construction of *Escherichia coli* K-12 in-frame, single-gene knockout mutants: the Keio collection. *Mol Syst Biol* 2(1). doi:10.1038/msb4100050.

78.   Joyce AR, et al. (2006) Experimental and computational assessment of conditionally essential genes in *Escherichia coli*. *J Bacteriol* 188(23):8259–8271.

79.   Armstrong CM, Meyers DJ, Imlay LS, Freel Meyers C, Odom AR (2015) Resistance to the antimicrobial agent fosmidomycin and an FR900098 prodrug through mutations in the deoxyxylulose phosphate reductoisomerase gene (dxr). *Antimicrob Agents Chemother* 59(9):5511–5519.

80.   Pines G, et al. (2018) Genomic deoxyxylulose phosphate reductoisomerase (DXR) mutations conferring resistance to the antimalarial drug fosmidomycin in *E. coli*. *ACS Synth Biol* 7(12):2824–2832.

81.   Koul A, et al. (2007) Diarylquinolines target subunit c of mycobacterial ATP synthase. *Nat Chem Biol* 3(6):323–324.

82.   Haagsma AC, et al. (2009) Selectivity of TMC207 towards Mycobacterial ATP synthase compared with that towards the Eukaryotic homologue. *Antimicrob Agents Chemother* 53(3):1290–1292.

83.   Andries K (2005) A diarylquinoline drug active on the ATP synthase of *Mycobacterium tuberculosis*. *Science (80-)* 307(5707):223–227.

84.   Gomes RA, et al. (2006) Yeast protein glycation in vivo by methylglyoxal. Molecular modification of glycolytic enzymes and heat shock proteins. *FEBS J* 273(23):5273–87.

85.   Rahman A, Shahabuddin, Hadi SM (1990) Formation of strand breaks and interstrand cross-links in DNA by methylglyoxal. *J Biochem Toxicol* 5(3):161–166.

86.   Migliore L, et al. (1990) Genotoxicity of methylglyoxal: cytogenetic damage in human lymphocytes in vitro and in intesting cells of mice. *Carcinogenesis* 11(9):1503–1507.

87.   Hayes G, et al. (2018) Manuka honey and methylglyoxal increase the sensitivity of *Staphylococcus aureus* to linezolid. *Lett Appl Microbiol* 66(6):491–495.

88.   Müller P, et al. (2013) Synergism between Medihoney and rifampicin against methicillin-resistant *Staphylococcus aureus* (MRSA). *PLoS One* 8(2):e57679.

89.   Bulman SEL, Tronci G, Goswami P, Carr C, Russell SJ (2017) Antibacterial properties of nonwoven wound dressings coated with manuka honey or methylglyoxal. *Mater (Basel, Switzerland)* 10(8). doi:10.3390/ma10080954.

90.   Paramasivan S, et al. (2014) Methylglyoxal-augmented manuka honey as a topical anti-Staphylococcus aureus biofilm agent: safety and efficacy in an *in vivo* model. *Int Forum Allergy Rhinol* 4(3):187–95.

Chapter 4: Establishing the structural basis and feasibility for *S. aureus* targeted lipophilic prodrugs

Preface

4.1 Abstract

Carboxy ester prodrugs have been widely employed as a means of increasing oral absorption and potency of phosphonate antibiotics. These prodrugs can be used to mask problematic drug residues that prevent cellular uptake as well as target delivery of compounds to specific tissue types. Unfortunately, many carboxy ester promoieties are rapidly hydrolyzed by serum esterases limiting their potential benefits in clinical applications. While carboxy ester-based prodrug targeting is feasible, it has been limited in microbes due to a paucity of information about the selectivity of microbial esterases. Here we identify the bacterial esterases, GloB and FrmB, which are required for carboxy ester prodrug activation in *Staphylococcus aureus.* Additionally, we determine the substrate specificities for FrmB and GloB, and demonstrate the structural basis of these preferences. Finally, we establish the carboxy ester substrate specificities of human and mouse sera, identifying several promoieties likely to be serum esterase resistant while still being microbially labile.

4.2   Introduction

Antimicrobial resistance presents a major challenge to modern healthcare (1, 2). In 2019, 2.8 million antibiotic resistant infections occurred in the United States and resulted in 35,000 deaths (3). Some estimates have suggested that antimicrobial resistant infections will cause as many as 10 million deaths annually in 2050 (4). *Staphylococcus aureus* is an efficient human pathogen capable of displaying methicillin-resistance and has been labeled a "serious threat" by the Centers for Disease Control and Prevention (3, 5, 6). New antimicrobials, especially those with novel mechanisms of action, are urgently needed, however most developing antiinfectives are reformulations of existing antibiotic scaffolds (7, 8).

While many metabolic processes are essential for microbial growth and pathogenesis, few existing antimicrobials exploit this target making bacterial metabolism a promising avenue for new antibiotic discovery (9–11). Metabolic drug design can be facile, using natural substrates as a template for competitive inhibitors. As metabolism often involves the transformation of highly charged metabolites, most metabolic inhibitors deploy phosphonate functional groups to achieve target binding (12). Unfortunately, these negatively charged phosphonate groups are readily excluded from cell membranes and often exhibit poor drug-like properties (13–21). New strategies enabling effective deployment of antimetabolites will serve to expand the druggable space for antimicrobials.

One means of improving phosphonate cellular permeability is to chemically mask the negative charge with lipophilic groups. This action, termed prodrugging, can be designed as a reversible process such that the original phosphonate antibiotic is returned following removal of the masking group, termed promoiety (Figure 1A) (19–21). We have previously demonstrated that addition of the lipophilic prodrugging motif, pivaloyloxymethyl (POM), to the isoprenoid

135

biosynthesis inhibitor, fosmidomycin, bypasses active cellular entry mechanisms while simultaneously increasing compound potency against the zoonotic staphylococci, *S. schleiferi* and *S. pseudintermedius* (14). Similar potency increases have been observed for this class of compounds against several additional microorganisms (16, 22–25). Regrettably, POM-promoieties are rapidly hydrolyzed by serum carboxylesterases limiting the efficacy of POM-prodrugs as a means of improving phosphonate cellular entry (15, 26).

To enable effective cellular delivery of phosphonate antibiotics, new lipophilic prodrugging strategies that are resistant to serum carboxylesterases yet cleavable by microbial esterases are needed. This feat has been achieved for prodrugs targeting delivery to human liver cells, but no strategies have been described yet enabling drug delivery specifically to microbes (27, 28). Notably, liver-targeted prodrug delivery was achieved by understanding the substrate specificity of the liver specific isoform of P450, CYP3A4 (27, 28). Accordingly, understanding how microbes activate prodrugs, and the specificities of their activating enzymes, will facilitate the development of microbe-specific prodrugs.

We recently described the staphylococcal enzyme, GloB, which is responsible for partially activating carboxy ester prodrugs in the zoonotic staphylococci *S. schleiferi* and *S. pseudintermedius* (29). Notably, GloB is unable fully activate prodrugs *in vitro*, suggesting that at least one additional enzyme is necessary for complete prodrug activation. Here, we describe how two staphylococcal esterases, GloB and FrmB, each act on carboxy ester prodrugs and contribute to carboxy ester prodrug activation in *S. aureus*. We demonstrate that both esterases

have defined substrate specificities which diverge from the substrate specificities of human and mouse sera. Additionally, we demonstrate that ester modifications have critical roles during the *in vivo* activation of prodrugs, and finally we present the three-dimensional structures of GloB and FrmB to enable structure-guided design of FrmB and GloB targeted prodrug activation.

4.3 Methods

4.3.1 Materials. POM-HEX, Hemi-HEX, and HEX were synthesized and resuspended in DMSO as described previously. Fluorescent ester compounds were generously provided by the laboratory of Geoffrey Hoops (30). Pooled, delipidated, defibronated, and lyophilized human and mouse serum was obtained from Rockland Inc.

4.3.2 Quantification of resistance. Half maximal inhibitory concentration (IC_{50}) determination was performed using microtiter broth dilution in clear 96-well plates (31). Briefly, POM-HEX was added to 75 µL LB media at a final concentration of $20 - 50$ µM POM-HEX and 0.5% DMSO, with POM-HEX concentrations varying according to resistant strain. Subsequently, POM-HEX was serially diluted in LB media containing 0.5% DMSO for a total of 10 dilutions. Two wells were left without drug, one used to define 100% growth, and the other used to control for media contamination and to define 0% growth. 75 µL of mid-log phase *S. aureus* diluted to 1×10^5 colony forming units/mL were subsequently added to the plate. Following inoculation, plates were incubated at 37 ºC with shaking, and OD_{600} measurements were taken every 20 minutes for a total of 16 hours. Half maximal inhibitory concentrations were determined by fitting the OD_{600} of each condition following 10 hours of growth to a nonlinear regression using GraphPad Prism software. Experiments were performed in triplicate with technical duplicates.

4.3.3 Generation of POM-HEX resistant strains was performed by plating log-phase *S. aureus* Newman on LB agar containing 3.33 µM POM-HEX and incubating at 37 °C overnight. Surviving single colonies were grown overnight in LB media and frozen in 10% glycerol for

long term storage. All assays were performed from fresh overnight inoculations from glycerol stocks.

4.3.4   Whole Genome Sequencing. Genomic DNA integrity was determined using Agilent 4200 Tapestation. Library preparation was performed with 0.25-0.5ug of DNA. DNA was fragmented using a Covaris E220 sonicator using peak incident power 175, duty factor 10%, cycles per burst 200 for 240 seconds at 4 degrees Celsius. DNA was blunt ended, had an A base added to the 3' ends, and then had Illumina sequencing adapters ligated to the ends. Ligated fragments were then amplified for 9 cycles using primers incorporating unique dual index tags. Fragments were sequenced on an Illumina MiSeq using paired-end reads extending 150 bases.

4.3.5   WhatsGNU Analysis. The *S. aureus* database was used to produce WhatsGNU proteomic reports for all the strains using WhatsGNU_main.py script in the ortholog mode. Eighteen *S. aureus* (9 atopic dermatitis (AD) and 9 soft and skin tissue infection (SSTI)) isolates from an ongoing project representing different clonal complexes (CC1/5/8/22/30) were used for the comparison. The CC details for the 18 isolates are provided in the attached excel sheet. The reports were then used to produce a heat map of the GNU scores of GloB and FrmB using the heat map function in the WhatsGNU_plotter.py script. The heatmap was annotated with the ortholog variant rarity index where 'r' represents a rare GNU score (in the context of other alleles in the same protein ortholog group).

4.3.6 Phylogenetic tree construction. Sequences of GloB, FrmB, and RpoB orthologs were retrieved from NCBI using the BlastP function with each organism on the tree as an individual search set. Of the returned sequences, the first complete sequence with the lowest E-value was selected for further analysis. Organisms were selected to include a wide variety of pathogenic and commensal microbes (32). In one instance, several of the top *E. coli* sequences were found to be highly similar to *S. aureus*, and on further analysis we discovered that the original sequencing samples had high levels of *S. aureus* reads. These contaminated sequences were disregarded in our analysis. Sequence alignment was performed using MUSCLE, and the unrooted phylogenetic trees were visualized using iTOL (33, 34).

4.3.7 Recombinant expression and purification of FrmB and GloB. WT FrmB and GloB sequences from *S. aureus* were cloned into the BG1861 vector by GeneWiz Inc (Beijing, China) to introduce a hexahistidine tag (35). The resultant plasmids were transformed into Stellar chemically competent cells (Clontech Laboratories), selected with carbenicillin, and the sequence was confirmed by Sanger sequencing. Subsequently, plasmids were transformed into chemically competent BL21 (DE3) cells and selected with ampicillin. Overnight liquid cultures were diluted 1:500 into LB media supplemented with ampicillin, grown shaking at 220 rpm to an OD_{600} of 0.5-0.8 at 37 °C, chilled to 16 °C and induced with 0.5 mM Isopropyl β-D-1-thiogalactopyranoside (IPTG) for 16-20 h. Cells were harvested by centrifugation at 6,000 x g for 10 min at 4°C. The cell pellet was lysed by sonication in 50 mL lysis buffer containing 25 mM tris HCl (pH 7.5), 250 mM NaCl, 20 mM imidazole, 1 mM $MgCl_2$, 10% glycerol, and 200 µM phenylmethylsulfonyl fluoride (PMSF). Insoluble proteins were removed by centrifugation twice at 20,000 x g for 20 min. The hexahistidine-tagged proteins were affinity purified from

soluble lysate using nickel agarose beads (Gold Biotechnology). Bound protein was washed with 50 mL lysis buffer before elution using 5 mL of elution buffer containing 25 mM tris HCl (pH 7.5), 250 mM NaCl, 300 mM imidazole, 1 mM $MgCl_2$, 10% glycerol. Affinity purified protein was further purified over a HiLoad 16/60 Superdex 200 gel filtration column (GE Healthsciences) using an AKTA Explorer. FPLC buffer contained 25 mM tris HCl (pH 7.5), 250 mM NaCl, 1 mM $MgCl_2$, and 10% glycerol. Fractions containing >90% pure protein (evaluated by SDS-PAGE) were concentrated using an Amicon Ultra-15 centrifugal unit (EMD Millipore) and flash frozen in liquid nitrogen before storage at -80°C.

Protein used during crystallography experiments was generated via the same FrmB and GloB sequences, but expression was performed from vector pET28a. FrmB was cloned into the pET28a vector by GeneWiz Inc (Beijing, China) and GloB was cloned from the BG1861 vector using the forward primer 5'- TGCTCGAGTGCGGCCGCTTAACCGTGTAAAAATGGATTT3' and the reverse primer 5'- CGCGCGGCAGCCATATGATGAGGATTTCAAGCTTAACTTT -3'. The PCR product was cloned into vector pET28a digested with restriction enzymes NotI and NdeI using InFusion HD Cloning (Takara Bio). Both cloning strategies introduce a hexahistidine tag followed by a thrombin cleavage sequence. FrmB and GloB encoding pET28a was transformed into chemically competent BL21 (DE3) cells. Protein expression of FrmB proceeded as previously, except FrmB containing cells were grown in Terrific broth.

Selenomethionine labeled GloB was prepared according to Van Duyne with minor modifications (36). Briefly, overnight cultures were grown in LB media, washed, and resuspended in M9

minimal media (per liter: 64 g Na_2HPO_4, 15g KH_2PO_4, 2.5 g NaCl, and 5 g NH_4Cl)

supplemented with 50 mg EDTA, 8 mg $FeCl_3$, 0.5 mg $ZnCl_2$, 0.1 mg $CuCl_2$, 0.1 mg $CoCl_2$, 0.1

mg H_3BO_3, 16 mg $MnCl_2$, 0.1 mg Ni_2SO_4, 0.1 mg molybdic acid, 0.5 mg riboflavin, 0.5 mg

niacinamide, 0.5 mg pyridoxine monohydrate, and 0.5 mg thiamine per liter. Resuspended

cultures were grown overnight. The following day, cultures were back diluted 1:50 and grown to

an OD_{600} of 0.5-0.8 at 37 °C. Once at the appropriate OD, the following amino acids were added

to the culture media at: 100 mg/L: lysine, phenylalanine, and threonine, 50 mg/L: isoleucine,

leucine, and valine, 60 mg/L: selenomethionine. Cultures were grown for an additional 15

minutes at 37 °C before cells were chilled to 16 °C and induced with 0.5 mM IPTG for 16-20

hours.

Protein purification of FrmB and selenomethionine labeled GloB for crystallography proceeded

as previously except following affinity purification the elution was dialyzed for 16-20 h at 4°C

with 20U thrombin protease to remove the hexahistidine tag. Dialysis buffer contained 50 mM

tris pH 7.5, 50 mM NaCl, and 1 mM $MgCl_2$. Following dialysis, uncleaved protein, the

hexahistidine tag, and thrombin were removed by flowing dialyzed protein over a benzamidine

Sepharose and nickel agarose bead column. Column flow through was further purified over a

HiLoad 16/60 Superdex 200 gel filtration column equilibrated with dialysis buffer. Protein was

concentrated to 8-10 mg/mL in an Amicon Ultra-15 centrifugal unit and frozen at -80°C.

4.3.8 Glyoxalase II activity assay. Glyoxalase II activity was assessed as previously with

minor changes (29, 37). Briefly, reactions were mixed to form a final concentration of 25 mM

Tris pH 7.5, 250 mM NaCl, 1 mM $MnCl_2$, 10% glycerol, 200 μM 5,5'-Dithiobis(2-nitrobenzoic

acid) (DTNB, Sigma D8130), 1 mM D-lactoylglutathione (Sigma L7140) and 0.15-0.63 µg

protein (130-550 nM GloB, 100-430 nM FrmB). Protein concentrations were varied to ensure the

reaction was linear across protein concentrations. Reactions without D-lactoylglutathione were

pre-incubated at 37 ºC for 10 minutes prior to assay initiation with the addition of substrate.

Release of glutathione from D-lactoylglutathione was quantified spectrophotometrically at 37 ºC

and 412 nm through the conversion of DTNB to TNB. Experiments were performed in triplicate

with technical duplicates.

4.3.9   4-nitrophenyl ester substrate activity assays. 4-nitrophenyl substrate specific activity

was determined in 50 µL reactions containing 25 mM Tris pH 7.5, 250 mM NaCl, 1 mM $MnCl_2$,

10% glycerol, 1 µM protein, and 1 mM 4-nitrophenyl substrate. The tested substrates, 4-

nitrophenyl acetate (Sigma, N8130), 4-nitrophenyl butyrate (Sigma N9876), and 4-nitrophenyl

trimethylacetate (Sigma 135046) were resuspended in acetonitrile at 100 mM. Reactions without

4-nitrophenyl substrate were preincubated at 37 ºC for 10 minutes prior to assay initiation via

substrate addition. Conversion of 4-nitrophenyl substrates to 4-nitrophenol was tracked

photometrically at 37 ºC and 405 nm. Experiments were performed in triplicate with technical

duplicates.

4.3.10 NMR characterization of GloB and FrmB activation products. 200 or 400 µM POM-

HEX was incubated with 4 nmol protein (GloB, FrmB, or 4 nmol each) in 500 µL reactions.

Reactions were buffered to a final concentration of 50 mM tris pH 7.5, 50 mM NaCl, 1 mM

$MgCl_2$. Reactions were allowed to proceed for 1 hour at 37 ˚C prior to analysis. Samples were

prepared for NMR studies by resuspending them in water and 10% (50 µL) D2O (Deuterium

Oxide 99.9% D, contains 0.75 wt% 3-(trimethylsilyl)propionic-2,2,3,3-d$_4$ acid, sodium salt,

Sigma–Aldrich). NMR spectra are acquired on a Bruker Avance III HD 500 MHz spectrometer

equipped with a cryoprobe. Two-dimensional (2D) ^{1}H-^{31}P heteronuclear single quantum

correlation (HSQC) measurements were obtained using hsqcetgp pulse program (with duration

of 15 minutes and scan parameters of 2 scans, td=1024 and 256, gpz2 %=32.40, ^{31}P SW= 40

ppm, O2p=20 ppm, cnst2=22.95) and analyzed using 3.1 TopSpin. The 1D projection of

columns excluding the water signal was obtained from the 2D ^{1}H-^{31}P HSQC spectrum by

obtaining spectra of positive projection of columns 1 to 600 and 650 to 1024 and adding them.

4.3.11 Esterase substrate specificity determination using fluorogenic SAR library. Kinetic

measurements were performed according to White *et al.* with minor variation (38). Lyophilized

human and mouse sera were resuspended according to manufacturer instructions in highly pure,

filtered water at protein concentrations of 85 mg/mL and 70 mg/mL respectively. 1 mL of

resuspended serum was added to a 24 mL mastermix for a final concentration of 31.25 mM tris

pH 7.5, 312.5 mM NaCl, 1.25 mM MgCl$_2$, 12.5% glycerol, and 3.4 mg/mL or 2.8 mg/mL protein

for human and mouse serum respectively. For purified proteins, 5 mL of a 75 µg/mL stock was

added to yield a 20 mL mastermix containing 31.25 mM tris pH 7.5, 312.5 mM NaCl, 1.25 mM

MgCl$_2$, 12.5% glycerol, and 18.75 µg/mL protein. Mastermix was stored on ice when not in use.

20 µL of mastermix was transferred to a black, 96-well half area microplate (Corning, CLS3993)

and prewarmed at 37 °C. Fluorogenic substrates were prepared as 10 mM stock solutions in

DMSO and were diluted in water to a starting concentration of 500 µM. Enzyme catalyzed

substrate hydrolysis was initiated by addition of 5 µL substrate dilution in technical duplicate to

the prewarmed serum or protein solution. Final assay concentrations were: 25 mM tris pH 7.5, 250 mM NaCl, 1 mM $MgCl_2$, 10% glycerol, and protein at a concentration of 2.72 mg/mL (human serum), 2.24 mg/mL (mouse serum), or 15 µg/mL (FrmB, GloB). The resulting change in fluorescence (λ_{ex} = 485 nm, λ_{em} = 520 nm) was followed for 15 minutes at 37 °C, collecting data every 30 seconds on a FLUOstar Omega microplate reader (BMG Labtech). Fluorescence measurements were converted to molar concentrations using a fluorescein standard curve (2.5 nmol-0.6 pmol). The initial rates of reaction were measured three independent times with two technical replicates per measurement and fit to a line using Graphpad Prism (GraphPad Software, La Jolla, CA). Initial rates of reaction were plotted versus the concentration of substrate and fit to a standard Michaelis-Menten equation, yielding estimates of V_{max} and K_m. Values for k_{cat} and k_{cat}/K_m were calculated based on amount of enzyme added when purified enzymes were used. For substrates where saturating conditions were not met, kcat/vmax was estimated using the following derivation of Michaelis Menten-

Equation (1) $$v = \frac{V_{max}[S]}{K_m + [S]}$$

When $K_m >> [S]$

Equation (2) $$v = \frac{V_{max}[S]}{K_m}$$

Therefore

Equation (3) $$\frac{V_{max}}{K_m} = \frac{v}{[S]}$$

145

4.3.12 Microfluidics measurements on S. aureus. Overnight cultures of *S. aureus* were grown in LB media, back diluted 1:500, and grown to early exponential phase (OD$_{600}$ 0.1-0.15), then washed in phosphate buffered saline and loaded on a bacterial CellASIC Onix microfluidic plate. Prior to cell loading, the microfluidics plate lines were flushed with PBS + 1% DMSO or 10 µM fluorescent prosubstrate in PBS + 1% DMSO, and the plate was preincubated at 37 °C. The microfluidics plate was loaded onto a Nikon Ti-E inverted microscope (Nikon Instruments, Inc) equipped with a 100x Plan N (N.A. = 1.45) Ph3 objective, X-cite 120 LED light source (Lumen Dynamics), and an OrcaERG CCD camera (Hammamatsu Photonics, Bridgewater, N.J), which was used to obtain both phase contrast and fluorescent images. Filter sets were purchased from Chroma Technology Corporation. Cells were loaded until a single field of view contained 50-150 cells or cell clusters. Following cell loading, PBS was flown through the flow cell (t = 0) and cells were observed in both phase and fluorescent channels for 10 minutes before the flow media was switched to PBS containing 1% DMSO and 10 µM fluorescent pro-substrate. Images were captured every two minutes for a total of 44 minutes, and all experiments were undertaken at 37 °C. The phase contrast exposure time was kept constant at: 200 ms, and the fluorescent channel exposure time was kept constant at 500 ms. For fluorescent images, the gain remained constant across all experiments. Image capture and analysis was performed using Nikon Elements Advanced Research software. Individual cells or clusters of cells were auto detected in the fluorescent channel using the intrinsic background fluorescence of each cell. Manual curation followed autodetection to remove debris or cells that did not stay within the field of view throughout the experiment. Fluorescent intensity for each individual cell or cluster of cells was measured through the duration of the experiment and normalized to the area of the identified cell

to yield the mean fluorescent intensity. Background cell autofluorescence was corrected by subtracting the average fluorescence across all identified objects from t = 0 through t = 10. Each experiment was performed in duplicate, with >50 individual cells analyzed in each experiment.

4.3.13 Protein crystallography, phasing, and data refinement. Crystals of *S. aureus* FrmB were grown at 16°C using vapor diffusion in 20 µL hanging drops containing a 1:1 mixture of protein (6 mg/mL) and crystallization buffer (0.1M Tricine pH 7.7, 15% PEG6K, 2.5M NaCl, 0.125% n-Dodecyl-B-D-glucoside). Crystals were observable as early as 2 days following mixing. Prior to data collection, crystals were stabilized in cryoprotectant (mother liquor supplemented with 20% glycerol) before flash freezing in liquid nitrogen for data collection at 100 K. Crystals of selenomethionine labeled *S. aureus* GloB were grown at 16 °C using vapor diffusion in 2 µL hanging drops containing a 1:1 mixture of protein (8 mg/mL) and crystallization buffer (0.1 M imidazole pH 6.9, 0.2 M ammonium sulfate, 0.1 M calcium chloride, and 21% PEG 8k). Selenomethionine labeled GloB crystals were stabilized in well solution supplemented with 15% glycerol and flash frozen in liquid nitrogen. All diffraction images were collected at beamline 19-ID of the Argonne National Laboratory Advanced Photon Source at Argonne National Laboratory. HKL3000 was used to index, integrate, and scale the data sets (39). To phase the initial dataset of FrmB, molecular replacement was performed in PHASER using the x-ray crystal structure of a low-temperature active alkaline esterase (PDB ID: 4RGY) as a search model (40, 41). Selenomethionine labeled GloB was phased using the x-ray crystal structure of TTHA1623 from *Thermus thermophilus* HB8 (PDB ID: 2ZWR) (42). Buccaneer was used to build both initial models, and subsequent, iterative rounds of model building and refinement used COOT and PHENIX respectively (43–45). Data collection and

refinement statistics are summarized in Table S6. Atomic coordinates and structure factors of *S. aureus* FrmB and *S. aureus* GloB are deposited in the RCSB Protein Data Bank.

4.3.13 Substrate Docking. GloB and FrmB structures were prepared for substrate autodocking using AutoDock Tools 1.5.7 (46). Metals and water molecules were removed from the crystal structure of FrmB as canonical serine hydrolases do not utilize metal in their reaction mechanism. Solvent water in the GloB crystal structure was removed, but the active site water and heavily coordinated zinc molecules were left in place. The three-dimensional structure of substrate 1^O was generated using ChemDraw3D, and prepared for docking using AutoDock Tools 1.5.7. Substrate docking of FrmB and GloB was performed using AutoDock Vina (47).

4.3.14 Fresh human serum was collected from a willing volunteer in untreated BD vacutainer tubes (BD, BD366430). Whole blood was allowed to clot at room temperature and aggregates were separated from the remaining serum through centrifugation at 400 x g for 8 minutes. Sera was obtained from the same volunteer on two separate occasions.

4.3.15 Serum half-life determination. Lyophilized human sera was obtained from Rockland Inc. and resuspended in pure water. 20 µL lyophilized sera or fresh sera was prewarmed at 37 ºC in a 96-well half area microplate (Corning, CLS3993). Following plate warming, 5 µL of the fluorogenic substrates were added to the plate for a final concentration of 25 µM. Substrate hydrolysis was tracked over a period of three hours at 37 ºC, with fluorescence measurements

(λ_{ex} = 485 nm, λ_{em} = 520 nm) being taken every two minutes on a FLUOstar Omega microplate reader (BMG Labtech). The resulting fluorescence values were converted to % substrate hydrolyzed using a fluorescein standard curve and fit to a one-phase decay model using GraphPad Prism. Experiments were performed in technical and biological duplicate.

4.4 Results

4.4.1 Identification of microbial esterases responsible for carboxylesterase activity.

Recently, we described that in the zoonotic staphylococcal species *S. schleiferi* and *S. pseudintermedius*, loss of the enzyme GloB, a hydroxyacylglutathione hydrolase, confers resistance to carboxy ester prodrugs because carboxy ester prodrugs do not become deprotected (29). However, purified GloB alone does not fully activate carboxy ester prodrugs in vitro, indicating that at least one additional cellular enzyme is required. Based on the predicted carboxy ester activation pathway, we predicted the missing enzyme(s) might be another carboxylesterase or a phosphodiesterase (Figure 1B). To identify the full suite of enzymes required for carboxy ester prodrug activation by *S. aureus* we made use of the Nebraska Transposon Mutant Library (NTML), in which nearly 2,000 of the non-essential genes of *S. aureus* have been individually disrupted by a stable transposon insertion (48). Using the gene ontology feature on the NTML website (https://app1.unmc.edu/fgx/gene-ontologies.html), we identified 6 carboxylic ester hydrolases (including GloB), 11 phosphatases, and 9 phosphoric diester hydrolases as candidate activators of carboxy ester prodrugs (Table S1), and screened each identified transposon mutant for resistance to the carboxy ester prodrug, POM-HEX. POM-HEX is a pivaloyloxymethyl prodrug of the compound, HEX, which inhibits enolase (Figure 1B, Figure 2A). Of the 26 candidate esterase transposon mutants, only two strains were significantly more resistant to

POM-HEX than the *S. aureus* parental strain, JE2, as determined by half maximal growth

inhibitory concentration (IC50) (Figure 2B). One of these strains had a transposon disrupting the

glyoxalase II enzyme, GloB, which we have previously found to function as a prodrug activating

enzyme, mutation in which confers resistance to POM-HEX in *S. schleiferi* (29). The second

strain harbored a transposon insertion in the locus encoding the predicted carboxylesterase

annotated as FrmB. FrmB has been previously identified as FphF, a serine hydrolase, and is the

primary S. aureus target of the fluorophosphonate, JCP678 (49). As S-formylglutathione

hydrolase is more likely to reflect the biological function of this protein, we will refer to this

protein as FrmB.

In parallel, we also employed an unbiased forward genetics approach to identify genetic changes

associated with POM-HEX resistance. POM-HEX-resistant staphylococci were derived by

exposing wild-type (WT) S. aureus Newman to growth inhibitory concentrations of POM-HEX.

In total, we selected and cloned 25 isolates with IC50 values ranging from 1.5-16x that of WT *S.*

aureus Newman (Figure 2 C, D, Supplemental Table 2).

Whole genome sequencing of POM-HEX-resistant strains revealed mutations in FrmB (n = 7)

and GloB (n = 10), with most mutations being nonsynonymous single nucleotide polymorphisms

(SNPs) (Figure 2D, Supplemental Table 2). In three instances, GloB was the only verified

genetic change in the genome. Additionally, FrmB and GloB each had one instance of a mutation

resulting in a premature stop codon truncating the protein at less than a 100 amino acid sequence.

Overwhelmingly the observed mutations in both FrmB and GloB are predicted to have deleterious effects on protein function (PROVEAN score below a threshold of -2.5) (Figure 2E).

To evaluate the sequence conservation of FrmB and GloB among *S. aureus*, we performed a WhatsGNU analysis on all available *S. aureus* genomes. WhatsGNU is a bioinformatic tool that can compress large databases and provide a readout of how many instances a specific gene has a 100% sequence and identity match within the entire database (50). This parameter, the gene novelty unit (GNU) score, is high when a sequence is under strong selective pressure within the population, and low when the gene is variable. GloB exhibits an exceptionally high GNU score of 8215 (of 10350 possible) indicating that there is very strong selective pressure to maintain GloB in *S. aureus*. Conversely, FrmB sequences appear to be extremely conserved within individual *S. aureus* clonal complexes but varies between each complex (GNU scores of 2218 or 3370 of 10350, Figure S1). We also built a phylogenetic tree of GloB and FrmB sequences among microbial populations. GloB orthologs are generally present, though the primary sequence is highly variable between bacteria and does not readily cluster according to the tree of life (Figure S2). FrmB sequences are also highly sequence divergent, though they tend to cluster closer to the expected tree of life (Figure S2).

Ultimately, the agreement between our forward and reverse genetic screens strongly suggest that prodrug activation is performed by two discrete predicted esterases and not a pool of redundant cellular esterases. Additionally, the finding that mutation in either FrmB or GloB is sufficient to

confer POM-HEX resistance suggests that the two enzymes may work in concert to bioconvert POM-HEX into HEX.

4.4.2   FrmB and GloB are carboxylesterases with diverging substrate specificity.

GloB is predicted to be a type II glyoxalase and a member of the large metallo-β-lactamase protein superfamily (INTERPRO IPR001279). Glyoxalase II enzymes, including the closely related GloB ortholog from *S. scheiferi*, catalyze the second step in the glyoxalase pathway which is responsible for the cellular conversion of methylglyoxal (a toxic glycolytic byproduct) to lactic acid (29, 37, 51). Conversely, FrmB orthologs hydrolyze p-nitrophenyl esters of short chain fatty acids (C2-C6) and are thought to mediate detoxification of cellular formaldehyde (52).

We purified recombinant WT SaFrmB and SaGloB and proceeded to evaluate the substrate utilization for each enzyme (Figure S3A). We first assessed glyoxalase II activity using an assay which couples hydrolysis of the glyoxalase II substrate, S-lactoylglutathione, to a change in absorbance (Figure S3B). SaGloB hydrolyzes S-lactoylglutathione with a specific activity comparable to previously characterized microbial type II glyoxalases, but SaFrmB lacks appreciable activity.

We next assessed the ability of FrmB and GloB to hydrolyze p-nitrophenyl esters of short chain fatty acids which have a photometric change upon hydrolysis (Figure S3C). FrmB has modest

152

activity against 4-nitrophenyl acetate and butyrate but no activity against 4-nitrophenyl

trimethylacetate suggesting a preference for simple short chain fatty acids (Figure S3C). This

finding is in agreement with a previous characterization of FrmB cleaving short chain

hydrophobic lipid substrates (53). GloB has no detectable activity against these substrates.

Notably, neither GloB nor FrmB has activity against 4-nitrophenyl trimethylacetate despite 4-

nitrophenyl trimethyl acetate bearing striking similarity to POM-HEX as a potential substrate.

This may be due to the absence of the acyloxymethyl ether moiety in 4-nitrophenyl substrates

which is found in POM-prodrugs.

We also sought to directly assess the role of GloB and FrmB in POM-HEX activation. We

incubated each enzyme, with POM-HEX, and characterized the products via 31P-1H-

heteronuclear single quantum coherence (HSQC) nuclear magnetic resonance (NMR). We have

previously shown that GloB removes only one POM moiety, resulting in an accumulation of

mono-POM-HEX (Figure 1B) (29). Similarly, FrmB is capable of removing only one POM-

moiety (Figure S4). We hypothesized that the two esterases may be stereoselective and incubated

both enzymes with POM-HEX. We find that incubation of POM-HEX with GloB and FrmB still

results in an accumulation of mono-POM-HEX, suggesting the two esterases may be unable to

cleave the charged mono-POM species (Figure S4)

4.4.3   GloB and FrmB substrate specificity.

To facilitate microbially targeted prodrug activation using these two enzymes, we next sought to

extensively characterize GloB and FrmB substrate specificity, using a 32-compound fluorescent

153

ester substrate library that fluoresces upon esterase activity (Figure S5) (30). This library systematically varies ester substrate length, branching patterns, and ether and sulfide positioning within the substrate, thereby allowing for the precise determination of structure-activity-relationships. Kinetic measurements were performed for both FrmB and GloB over a range of substrate concentrations for the entire library allowing for the extraction of the catalytic specificity (kcat/Km) (Supplemental table S4, S5).

We find that FrmB and GloB tend to have the highest activity towards oxygen ethers (Figure S6). GloB has the highest activity for short chain ethers (compounds 1-3) with some tolerance for branching at the first carbon beyond the ester carbonyl (compounds 7-9), though extensive branching strongly reduces activity (compound 10). Remarkably, GloB is also tolerant of the extreme steric bulk introduced with the phenoxyacetic acid substrate if the substrate contains an oxygen or sulfur ether (compound series 11). GloB exhibits a strong preference for oxygen at the β-position to the carbonyl over the γ-position but is indifferent to the positioning of sulfur. While GloB has a wider range of catalytic specificities, FrmB exhibits lower overall and narrower range of catalytic specificity. FrmB is generally capable of hydrolyzing unbranched substrates with little regard for chain length or the end of chain bulk (compound series 1-3, 11). Branching at the position following the ester carbonyl (compound series 7-9, 12) is deleterious to FrmB activity. When oxygen is included in the chain, positioning at the β-position to the carbonyl is strongly preferred over the γ-position.

4.4.4 Importance of substrate specificity in vivo.

While in vitro enzymatic substrate profiling is informative for how individual enzymes activate prodrugs, it does not necessarily reflect the complex biochemical processes happening in vivo, where additional cellular esterases may impact overall compound activation. We designed a live, single-cell assay to measure the real-time activation of pro-fluorescent substrates. *S. aureus* is loaded onto a microfluidics device and tracked on both fluorescent and phase contrast channels. Intracellular fluorescence resulting from the rapid introduction of substrate into the chamber was thus quantified through time.

We selected four pro-fluorescent substrates of varying catalytic specificity against FrmB and GloB to observe in our microfluidics experiments. In vitro, substrate 1O displays high catalytic specificity for both FrmB and GloB, 3C displays moderate catalytic specificity for FrmB and GloB, 5O has moderate catalytic specificity against GloB but poor catalytic specificity against FrmB, and 9C has poor catalytic specificity against both GloB and FrmB. Comparing the activation of these substrates through time, we find that our in vitro catalytic specificity determination correlates well with our in vivo activation rates (Figure 3, supplemental movies 1-4). Compound 1O, which exhibits high catalytic specificity for GloB and FrmB reaches fluorescence saturation within the initial time point observed. Compound 3C, which has moderate catalytic specificity for both GloB and FrmB, slowly activates over the duration of the experiment, and 5O and 9C, which have moderate to poor catalytic specificity against both GloB and FrmB never appreciably activate during the 30 minutes of observation (Figure 3). As fluorescent activation is quantified per cell, we can also assess the uniformity of prodrug

activation across the population. We observe remarkably homogenous activation of prodrugs across all observed cells (Figure 3).

4.4.5　Three-dimensional structure of FrmB

To establish the structural basis for FrmB and GloB substrate specificity and enable future structure guided design of protherapies, we solved the three-dimensional structures of both *S. aureus* FrmB and GloB. *S. aureus* FrmB was solved at 1.60 Å using molecular replacement with the low-temperature active alkaline esterase, est12 (PDB ID: 4RGY) as a search model (41). Refinement parameters and statistics are displayed in Table S6. A single dimer of FrmB is observable in the asymmetric unit, matching the apparent molecular weight of FrmB as we have observed via size exclusion chromatography. The overall fold of FrmB is characteristic of the α/β hydrolase fold. Six parallel β-strands and one anti-parallel β-strand pair form a central eight stranded β-sheet, which is encompassed by α-helices (Figure 4A). One monomer of FrmB has electron density for a single magnesium ion, whereas the second monomer has two magnesium present.

A structural similarity search was performed using the DALI server to identify proteins related to SaFrmB. The structure of SaFrmB was most similar to the molecular replacement model, Est12 from deep sea bacteria (PDB ID 4RGY, root mean squared deviation (r.m.s.d.) = 1.020 Å), but also had similarity to the ferulic acid esterase BiFae1A from *Bacteroides intestinalis* (PDB ID 5VOL, r.m.s.d. = 1.137 Å) and the tributyrin esterase, estA, from *Streptococcus pneumonia* (PDB ID 2UZ0, r.m.s.d. = 1.329 Å) (54, 55). All structures display strong structural conservation

156

including the positioning of the prototypic serine hydrolase catalytic triad: Ser120, Asp204, and His233 (*S. aureus*) (Figure S7). The most striking difference between the related structures is the flexible cap domain, implicated in substrate specificity of estA and est12 (41). While this manuscript was in preparation, an independent structure of FrmB was solved (53). The two structures are nearly identical (PDB ID 6ZHD, r.m.s.d = 0.433 Å), with slightly differential positioning of the capping domain.

We compared SaFrmB to its closest human ortholog, human esterase D (PDB ID 3fcx), finding moderate structural similarity both in the overall fold (r.m.s.d = 4.625 Å) and in the positioning of the catalytic triad. However, SaFrmB and human esterase D notably differ in the solvent-accessible surface around the active site, suggesting the potential for distinct substrate utilization, primarily driven by differential positioning of the cap domain (Figure 4B).

We modeled the highest catalytic specificity substrate of FrmB, 1O, onto the active site of FrmB. Serine hydrolases classically bind the substrate carbonyl oxygen in an oxyanion hole and substrate hydrolysis is initiated through attack of the catalytic serine on the ester carbonyl. The docking of 1O on FrmB mimics the initial state of a serine hydrolase reaction, with the carbonyl oxygen buried and the catalytic serine poised for attack (Figure 4C). The pocket directly next to the oxyanion hole is relatively narrow, suggesting that steric hindrance explains FrmB's poor ability to hydrolyze branched substrates. The active site pocket extends and opens significantly after passing by the oxyanion hole, supporting FrmB's ability to hydrolyze substrates with large steric groups far from the carbonyl carbon such as 11O.

4.4.6   Three-dimensional structure of GloB

We also solved the structure of SaGloB 1.65 Å, using selenomethionine (SeMet)-substituted GloB and molecular replacement using the metallo-β-lactamase, TTHA1623, from *Thermus thermophilus* as a search model. Final structural refinement parameters and statistics are presented in Table S6. Four monomers of SaGloB are observed in the asymmetric unit with each displaying crystallographic symmetry. SaGloB exhibits the classic αβ/βα-fold that defines the metallo-β-lactamase fold proteins, including glyoxalase II enzymes (Figure 5A).

As with SaFrmB, a DALI server search was performed to identify proteins structurally similar to SaGloB. SaGloB displays extremely high similarity to the unusual type II glyoxalase, YcbI from *Salmonella enterica* (PDB ID: 2XF4, r.m.s.d = 0.898 Å), the molecular replacement search model TTHA1623 from *Thermus thermophilus* (PDB ID: 2ZWR, r.m.s.d. = 0.767), and to the *Arabidopsis thaliana* glyoxalase II (PDB ID: 1XM8, r.m.s.d = 1.165 Å), with the exception that AtGloB has a 50 amino acid C-terminal extension (Figure S8A) (42, 37, 56). Also consistent with previously observed GloB structures, SaGloB shows clear electron density for two zinc molecules coordinated by six histidine residues and two aspartate residues (Figure S8B). Density for a water molecule is also visible and appears to be coordinated by the two zinc atoms, as observed for human glyoxalase II (57).

Overlaying S. aureus GloB with Homo sapiens GloB (PDB: 1qh5) reveals that the two structures are remarkably similar (r.m.s.d = 1.249 Å), with a few notable exceptions. HsGloB has two extensions – one a 34 amino acid insertion, the other a 32 amino acid C-terminal extension, both of which form helix-turn-helices that abut the active site (Figure 5B) (57). On the opposite side

of the active site, SaGloB has a 19 amino acid flexible loop which is partially observed in the electron density. This loop is positioned such that it may cover the active site or at the very least sterically hinder substrate access (Figure 5B). Overall, these differences between HsGloB and SaGloB suggest differential substrate utilization between S. aureus and humans.

We modeled the highest catalytic specificity substrate for GloB, 1O , onto our structure. Autodock places 1O with the carbonyl oxygen directly next to the active site water (Figure 5C). The GloB active site channel appears moderately wide, explaining why extensively branched substrates are not tolerated. Towards the end of the active site channel, GloB appears to form a tunnel. This is tunnel is not reached by substrate 1O, but presumably would be occupied in more sterically bulky substrates such as 11O. One arm of this tunnel is comprised of the highly flexible loop which is only partially visible in our electron density suggesting that during catalysis this loop may be movable to accommodate larger substrates such as 11O.

4.4.7   Esterase specificity of human and mouse sera

We sought to evaluate whether ester promoieties could be designed for microbe-specific activation. Using the same 32-compound fluorescent substrate library, we determine each substrate's serum half-life. Both reconstituted and fresh sera function comparably in their activity and substrate preferences (Figure S9).

We next proceeded to perform full kinetic profiling of lyophilized human sera. As sera is a mixture of multiple proteins instead of a single protein species, we are unable to obtain true k_{cat} values. Instead, we report a modified catalytic specificity, which is the V_{max}/Km, normalized to the total amount of protein added to the assay (Figure S10A). As we observed for FrmB and GloB (Figure S10B, C), human sera has highest catalytic specificity for oxygen and sulfur ethers. However, as opposed to FrmB and GloB, human sera is relatively uniform in its catalytic specificity across the substrate library. Short chain substrates exhibit the highest catalytic specificity, and though branching slightly reduces the catalytic specificity, it is not to the same extent as with FrmB. The substrates displaying the poorest catalytic specificity are universally the carbon series, with added branching resulting in the decreased substrate utilization.

As murine models are frequently used in the development and testing of novel pharmaceuticals, we wanted to additionally characterize the substrate preferences of mouse sera. Notably, mice are well known for their extremely active and broad serum esterase activity. Indeed, we find that mouse sera exhibits on average 100-fold more catalytic specificity per mg serum protein than human sera (Figure S10D, S11). However, this increase in catalytic specificity is not uniform across the substrate library. Human sera underperforms on the carbon series, and does comparatively better on the oxygen and sulfur ethers (Figure S11B). Thus, use of mouse sera alone is likely insufficient to predict prodrug human serum stability and accurately model human pharmacokinetics and dynamics.

Finally, we wanted to compare how GloB and FrmB substrate specificities could be used to drive microbe-targeted prodrugs. As each esterase is likely to encounter multiple potential substrates in vivo, we utilized our modified catalytic specificity (V_{max}/Km) as a comparator. We performed pairwise analysis for each combination of FrmB and GloB against human and mouse sera (Figure 6A-D). The exact enrichment of catalytic specificity for microbial esterases compared to serum esterases that will result in a host-resistant prodrug is difficult to estimate. Using a cutoff of 2^{10}-fold enrichment in catalytic specificity for the microbial enzymes over the serum enzymes, FrmB displays a preference over human sera for two compounds: 3C and 6C, whereas GloB displays a preference for 6 compounds: 2S, 3C, 10C, 11C, 11O, and 11S (Figure 6E). Conversely, mouse sera is able to hydrolyze all compounds within this cutoff. Lowering the cutoff to a 2^5-fold enrichment in catalytic specificity over mouse sera, FrmB and GloB both are more specific for compound 2S, and GloB additionally displays specificity for compound 11O.

4.5   Discussion

Targeted microbial delivery and activation of lipophilic ester prodrugs is a highly desirable strategy to enable the expansion of druggable targets within bacteria while simultaneously improving drug selectivity. Identification of microbe-specific pro-moieties is crucial to this goal. Here, we have demonstrated that *S. aureus* uses two discrete esterases, FrmB and GloB, to activate the carboxy ester prodrug, POM-HEX. FrmB and GloB both exhibit distinct ester substrate specificities, which are supported by the structure of their active sites. Importantly, enzymatic substrate specificity correlates with the rate of cellular ester activation. Accordingly, simple modifications to ester prodrugs are sufficient to change their rates of activation in vivo.

161

Simple ester modifications can also change the pattern of prodrug activation. For the development of microbially targeted ester prodrugs to be feasible, compounds need to be stable against human enzymes. Here we demonstrate that human sera has distinct ester substrate preferences, and that both FrmB and GloB utilize substrates differentially from human sera. How microbes beyond S. aureus activate prodrugs, as well as the substrate specificities of pathogenic and commensal microbes remains an important, open question which will dictate how narrow spectrum an ester prodrug will be. As microbe-specific prodrugs begin to enter clinical development, careful attention needs to be paid to the models used to establish the pharmacokinetic/pharmacodynamic profiles and efficacy of ester prodrugs. Our studies indicate that mice are an inadequate model for ester prodrug activation and therapeutic efficacy in humans. This work paves the way for structure-guided development of S. aureus-specific prodrugs and establishes a pipeline for the identification of microbial prodrug activating enzymes. We anticipate that these approaches will not only guide the development of novel antimicrobials, but also aid in the development of in vivo imaging for diagnostic purposes.

4.6 Figures
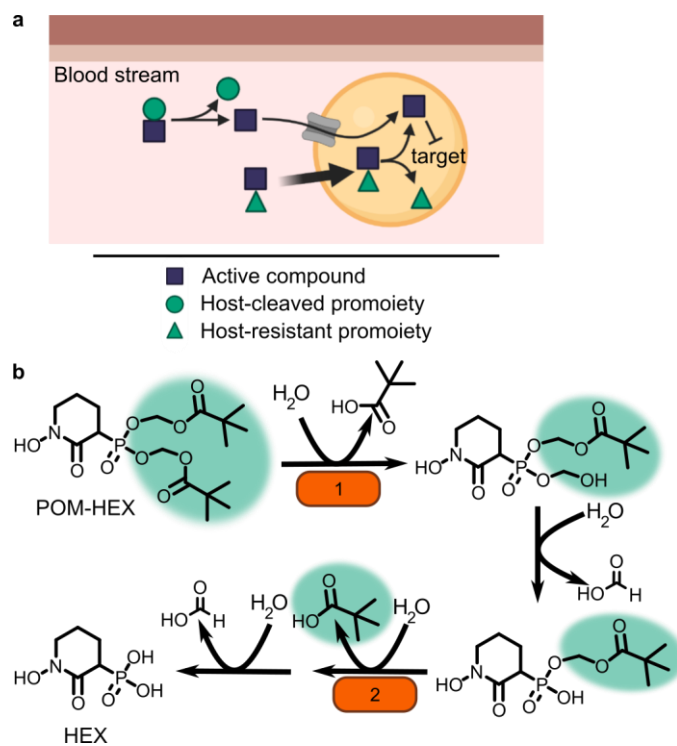
Figure 1 Prodrug activation model and proposed mechanism. Carboxy ester promoieties highlighted in green.
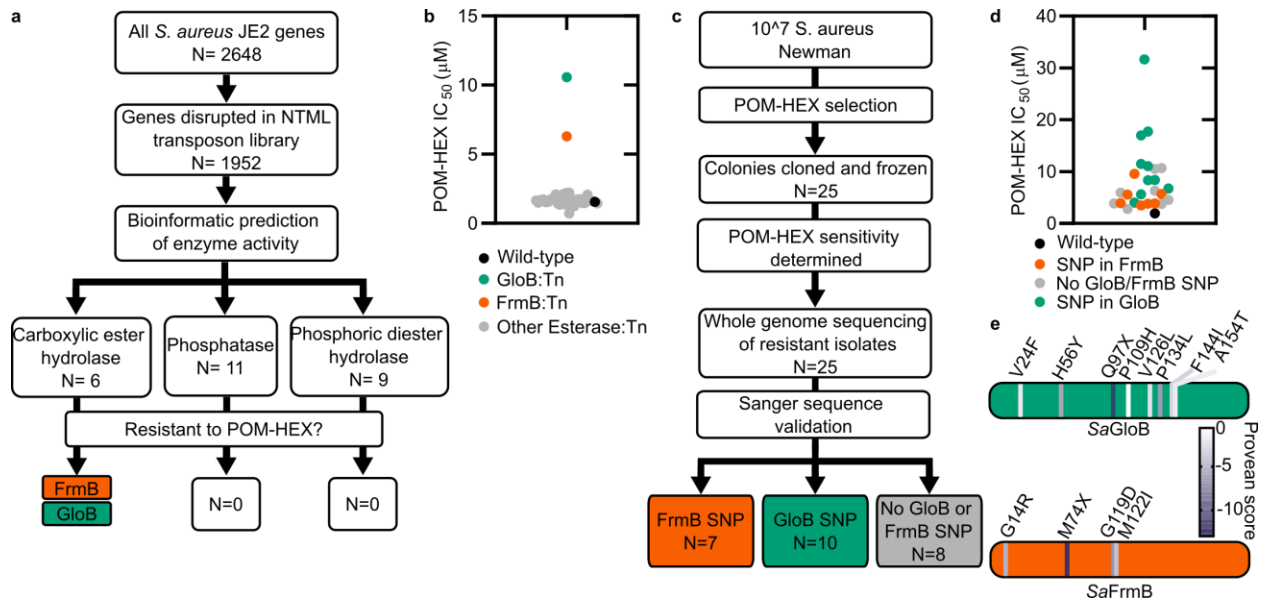
Figure 2 Forward and reverse genetics approaches identify FrmB and GloB as potential POM-prodrug hydrolases. (a) Reverse genetics identification of potential prodrug activating enzymes. (b) POM-HEX susceptibility of identified potential prodrug activating enzymes from (a). (c) Forward genetic screen approach. (d) POM-HEX susceptibility of POM-HEX resistant staphylococci. (e) Mutations identified by whole-genome sequencing in FrmB and GloB. In all experiments GloB is colored green and FrmB orange. Displayed are the means of three independent biological experiments.
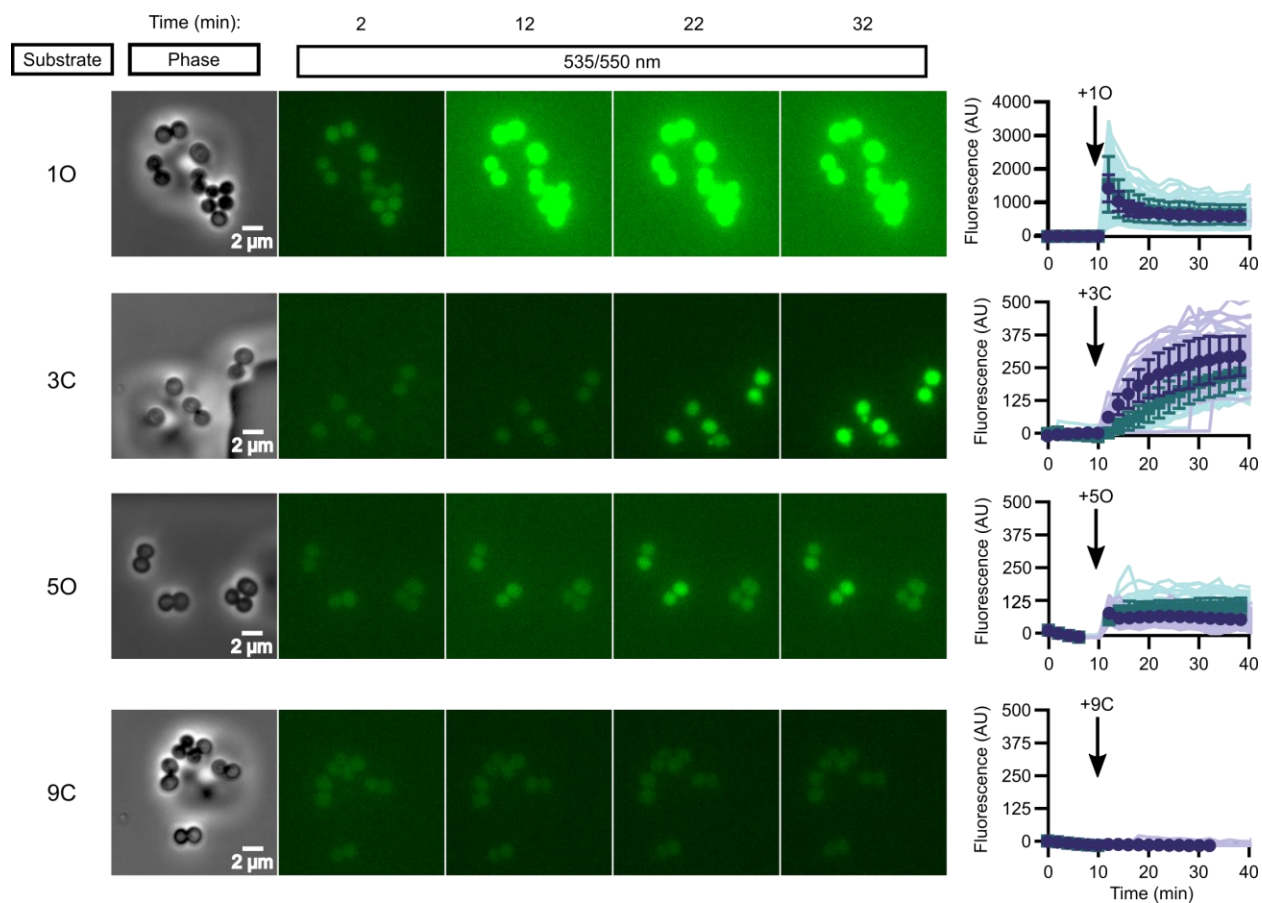
Figure 3 Ester promoiety selection impacts in vivo activation rates. Time series of activation of various pro-fluorescent substrates (Figure S5). Profluorescent substrates were added into the microfluidics chamber at t = 10 minutes. Displayed on the right is the quantification of individual cell or cell cluster fluorescence. Faint traces are individual cells and darker traces represent the mean of a given experiment. Each experiment was performed in biological duplicate. Error bars denote SD.
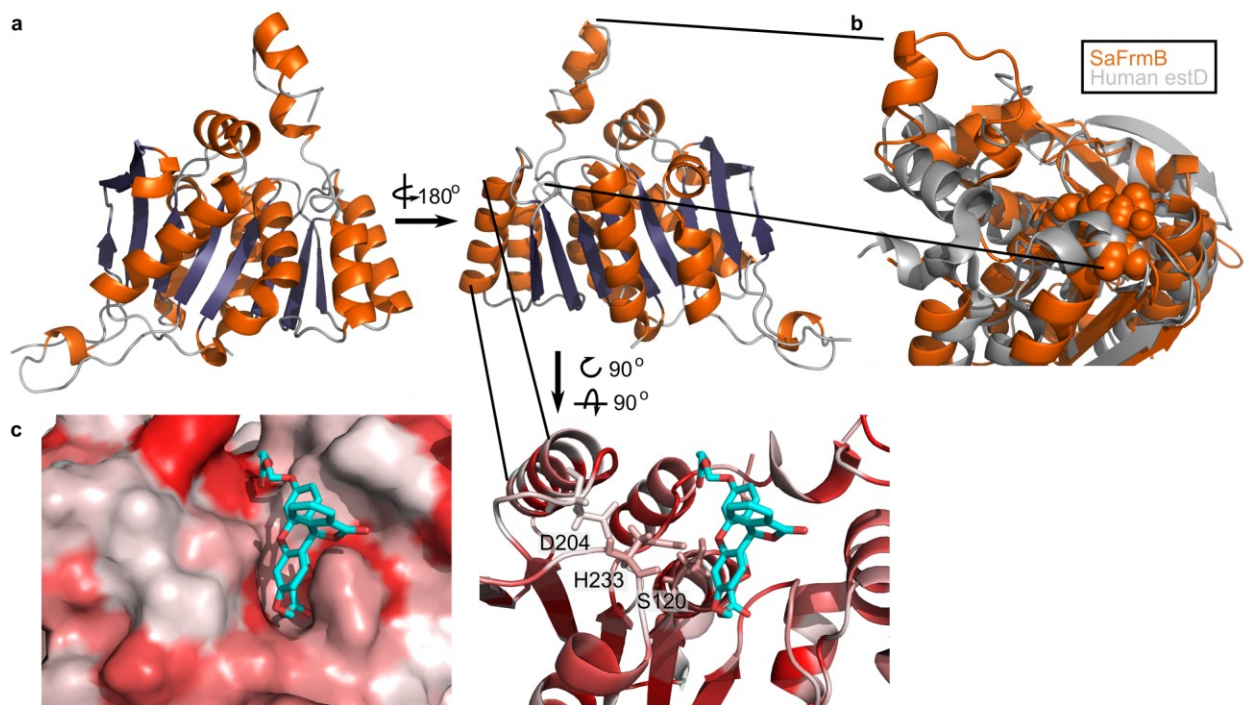
Figure 4 Three-dimensional structure of FrmB. (a) overall fold, alpha helices colored in orange and β-strands colored in purple. (b) comparison between SaFrmB (orange) and the closest human ortholog, estD (gray). Active site residues denoted in orange spheres. (c) docking of substrate 1O (sticks) in the active site of FrmB. Left, surface view, red indicates highly hydrophobic and white hydrophilic residues. Right, stick and cartoon view with catalytic triad annotated.
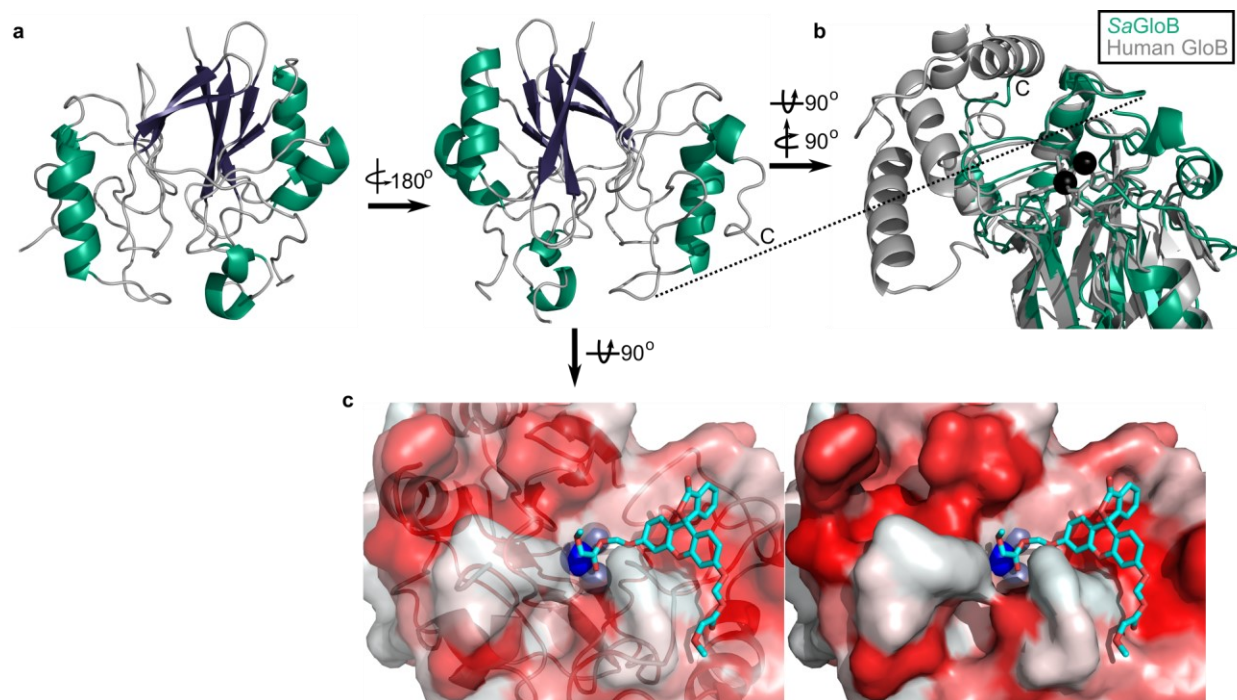
Figure 5 Three-dimensional structure of GloB. (a) overall fold, alpha helices colored in green and β-strands colored in purple. (b) comparison of SaGloB (green) and Human GloB (gray). (c) docking of the substrate 1O (sticks) in the active site of GloB. Left, partial cartoon view, Right surface view. White represents hydrophilic residues whereas red represents hydrophobic residues. Zn ions indicated as silver spheres; water indicated as blue sphere.
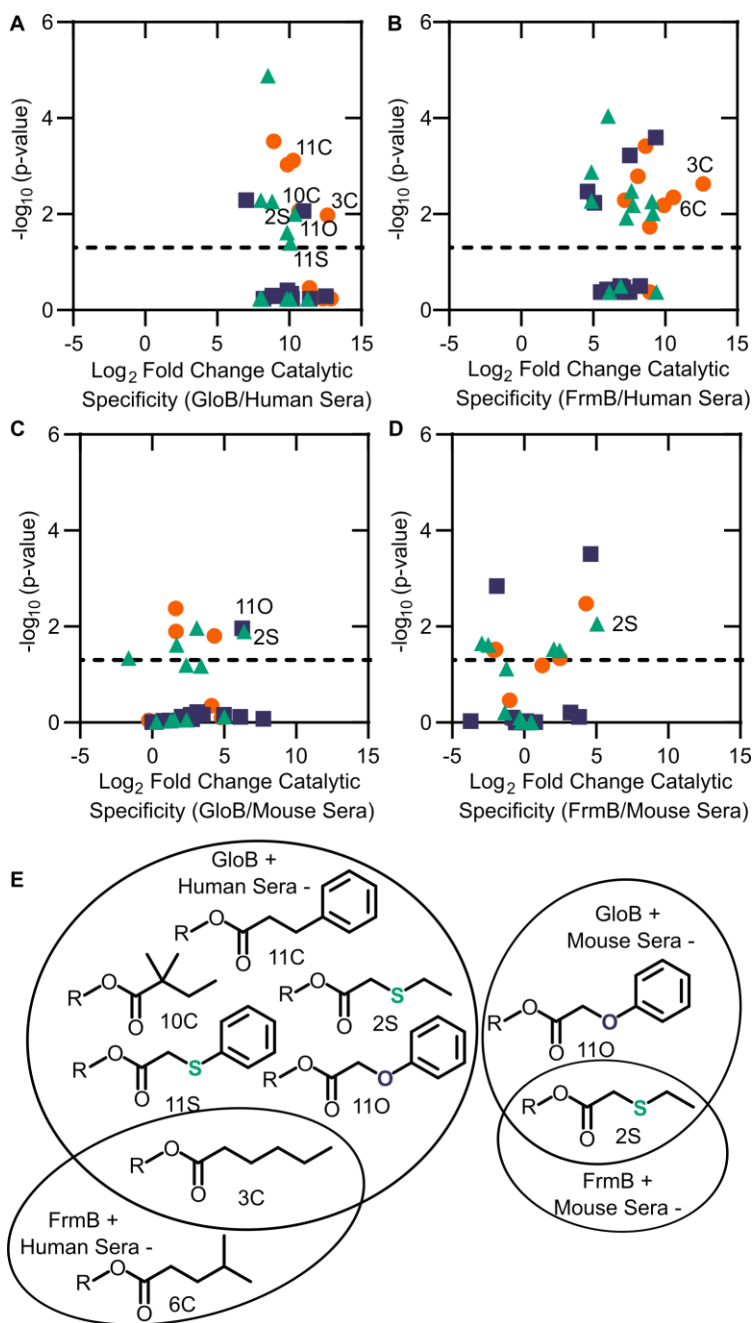
Figure 6 Comparison between microbial esterase and serum esterase catalytic specificity. (a-d) volcano plots of catalytic specificity. Displayed are the means of three independent experiments. P-values calculated as pairwise t-tests with Holm-Sidak correction for multiple comparisons. (a) comparison between human sera and GloB, (b) human sera and FrmB, (c) mouse sera and GloB, (d) mouse sera and FrmB). (e) structures of ester substrates with 2^{10} enrichment in catalytic specificity for microbial esterases over human serum (left), or 2^5 enrichment over mouse serum. Dashed line indicates a p-value of 0.05.
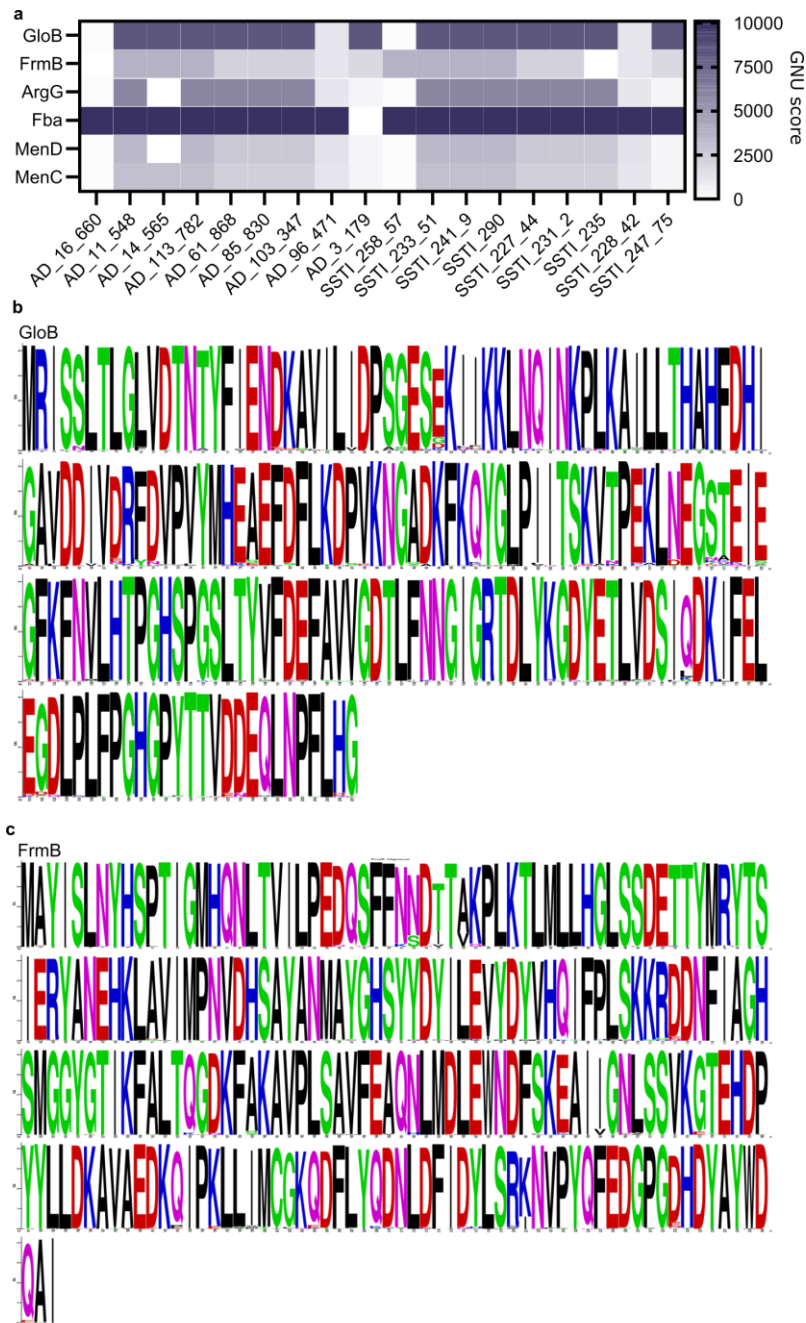
Figure S1 Conservation of FrmB and GloB within S. aureus. (a) WhatsGNU analysis of GloB and FrmB.
Control genes, argG – argininosuccinate synthase, fba- Fructose-bisphosphate aldolase, menD – 2-succinyl-5-enolpyruvyl-6-hydroxy-3-cyclohexene-1carboxylate synthase, menC- o-succinylbenzoate synthase. GNU stands for gene novelty unit and is a count of how many sequences in the database have an exact match to the queried sequence, with higher counts indicating sequence conservation. Strains across the x-axis are representative strains from the 18 S. aureus colony complexes which were used to query the S. aureus database. (b, c) MAFFT alignment of GloB (b) and FrmB (c) sequences across the S. aureus sequence database.

Figure S2 Phylogenetic tree of FrmB and GloB. Sequences of GloB, FrmB, and RpoB were retrieved from NCBI using BlastP against each organism. Sequence alignment performed using MUSCLE.
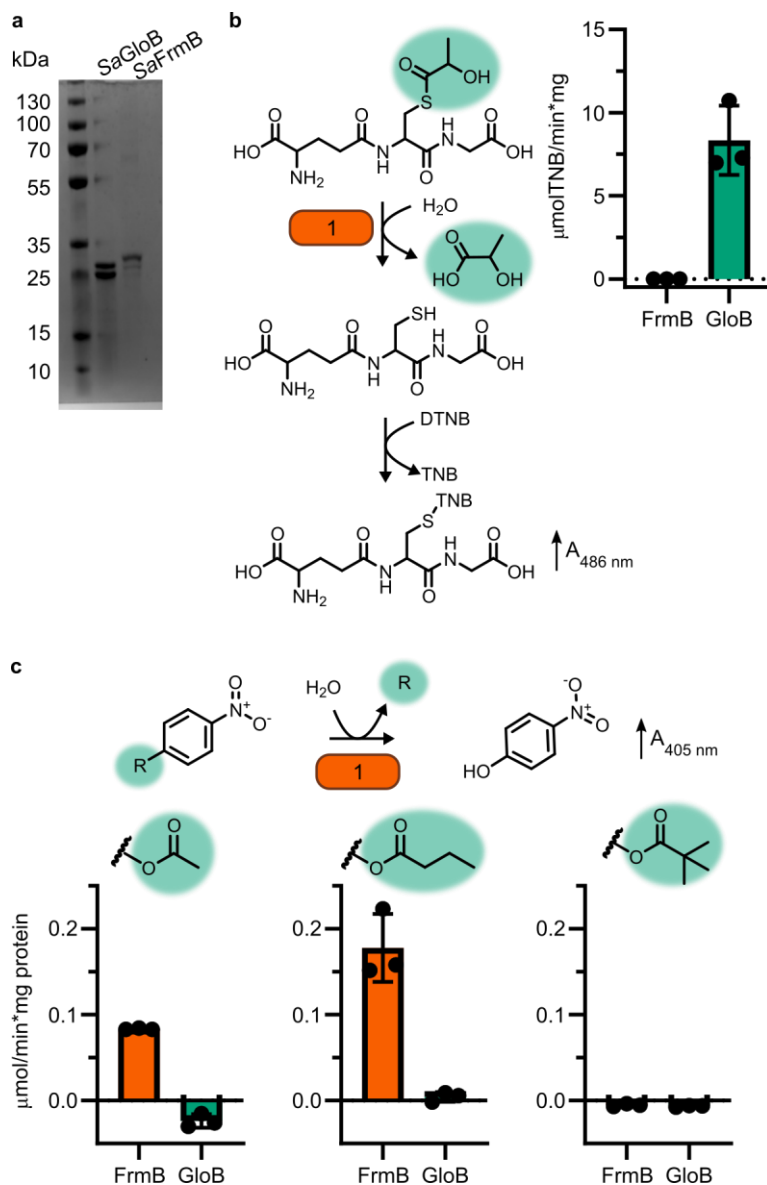
Figure S3 Enzymatic characterization of GloB and FrmB. (a) SDS-PAGE gel of GloB and FrmB protein preparations. Expected molecular weights are 23.3 kDa and 29.5 kDa respectively. (b) Glyoxalase II activity assay, enzymatic conversion of S-lactoylglutathione releases free glutathione and reacts with DTNB resulting in increased absorbance at 412 nm. (c) 4-nitrophenyl activation results in increased absorbance at 405 nm. Left to right, activity when supplied 4-nitrophenyl acetate, butyrate, and trimethyl acetate. Displayed in points is the mean of two technical replicates for individual experiments, bars indicate mean of three independent biological experiments performed in technical duplicate. Error bars denote SD.
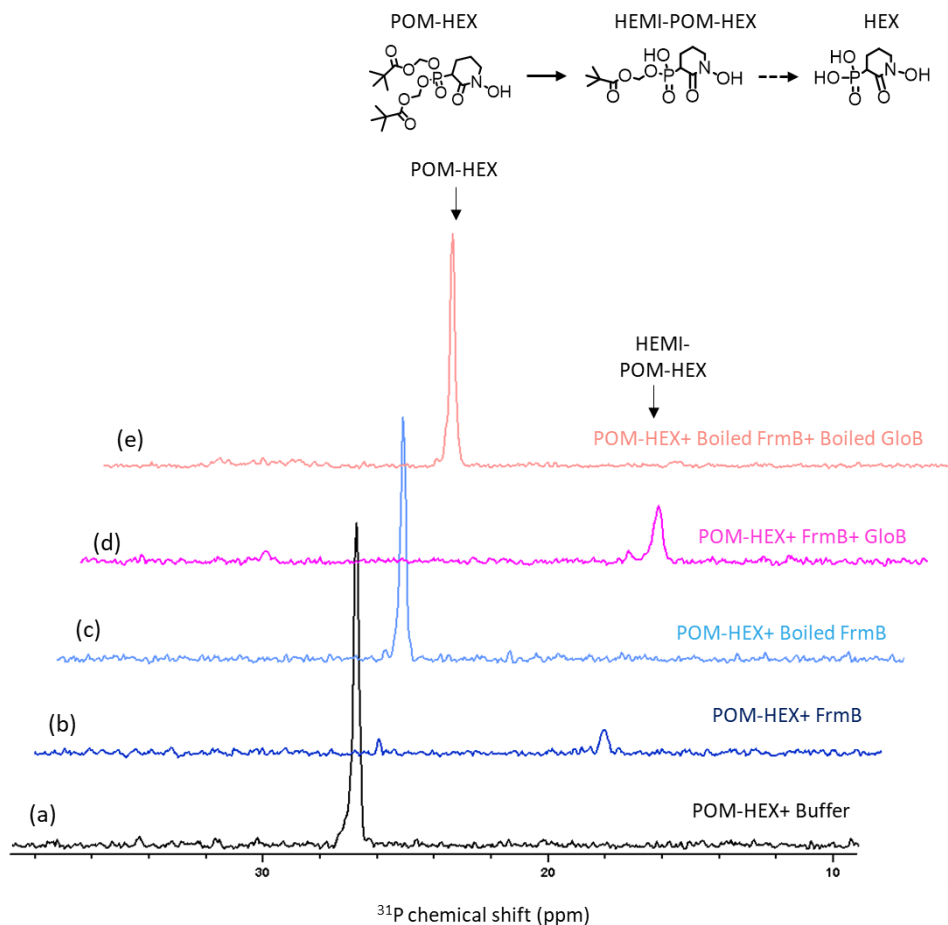
Figure S4 NMR characterization of POM-HEX activation by GloB and FrmB. Two-dimensional (2D) ^{1}H-^{31}P HSQC NMR spectra of products following incubation of FrmB, GloB, catalytically inactive (boiled) GloB and FrmB, or buffer alone. Also included are the ^{1}H-^{31}P HSQC NMR spectra of POM-HEX and HEX. Displayed are representative traces of three independent experiments. HEMI-POM HEX peak inferred by predicted shift.
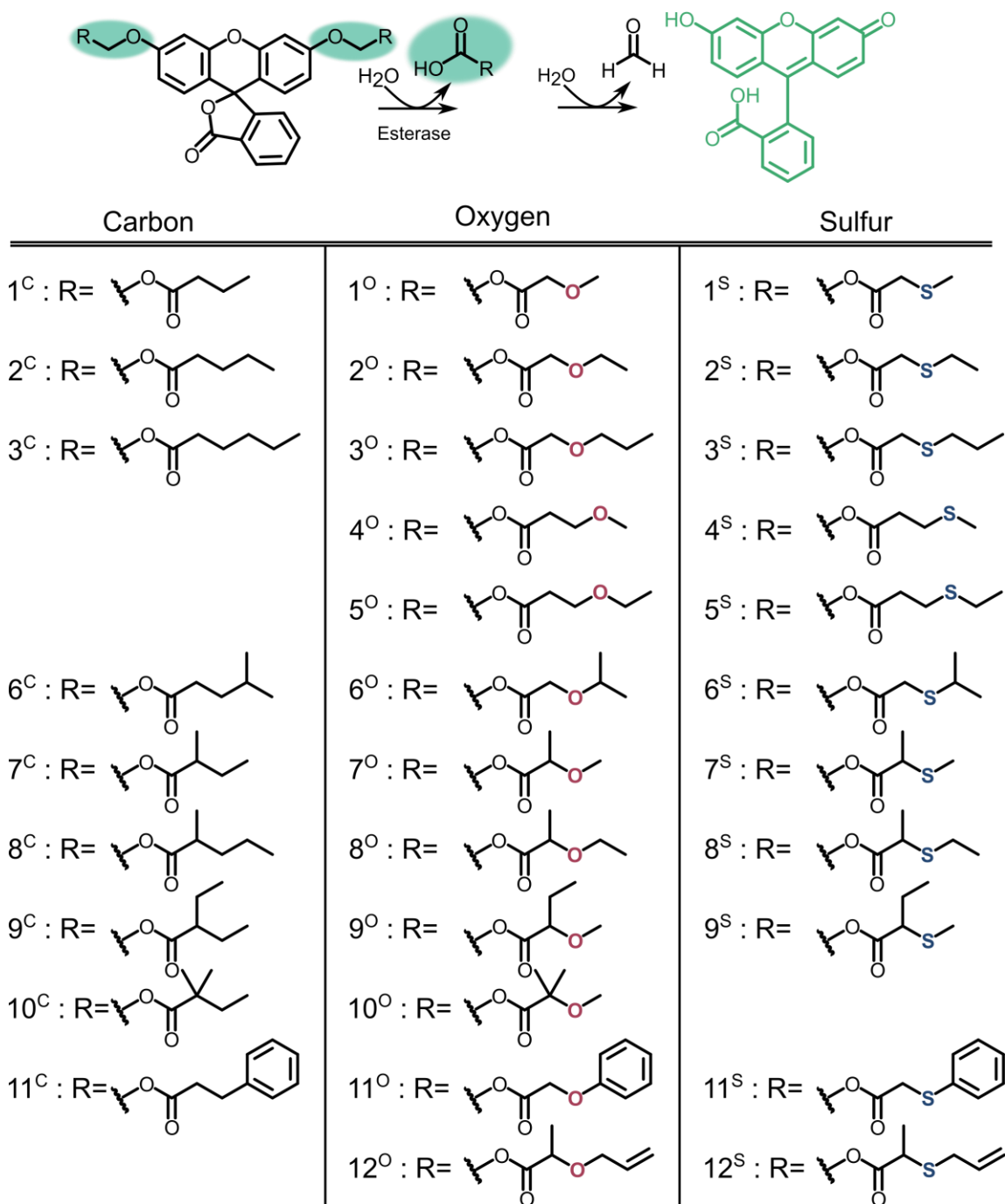
Figure S5 Profluorescent substrate library. Activation of substrates via esterase action results in fluorescence.
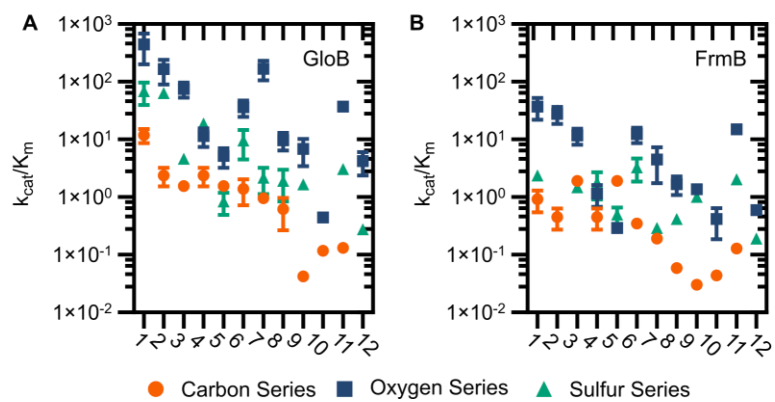
Figure S6 Catalytic specificity of GloB and FrmB. Numbers correspond to the structures displayed in Figure S5, compounds in the carbon series denoted in orange, oxygen series in blue, and sulfur series in green.
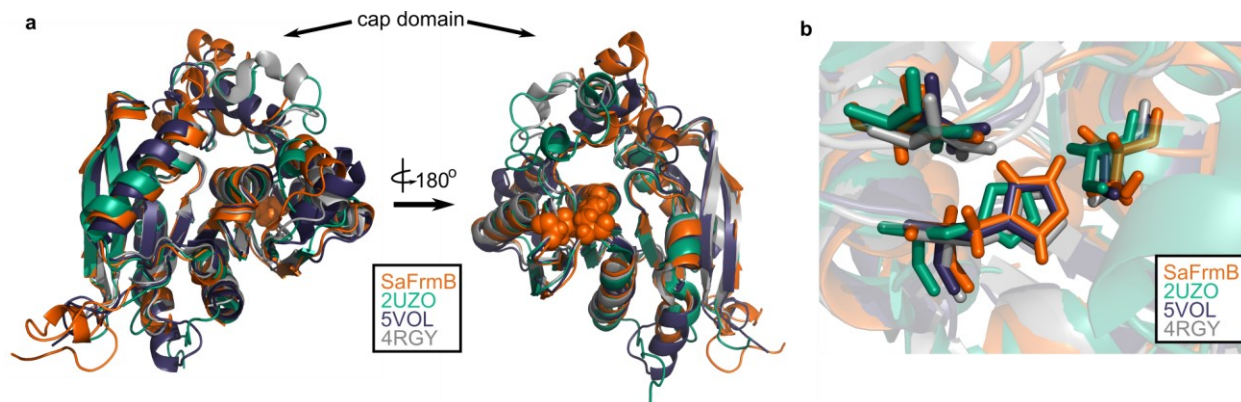
Figure S7 Structural conservation of FrmB. (a) Overall structural alignment of FrmB (orange) with estA from *S. pneumonia* (2UZ0), ferulic acid esterases from *B. intestinalis* (5VOL), and est12 from deep sea bacteria (4RGY). (b) positioning of the serine hydrolase catalytic triad, histidine, serine, aspartate.
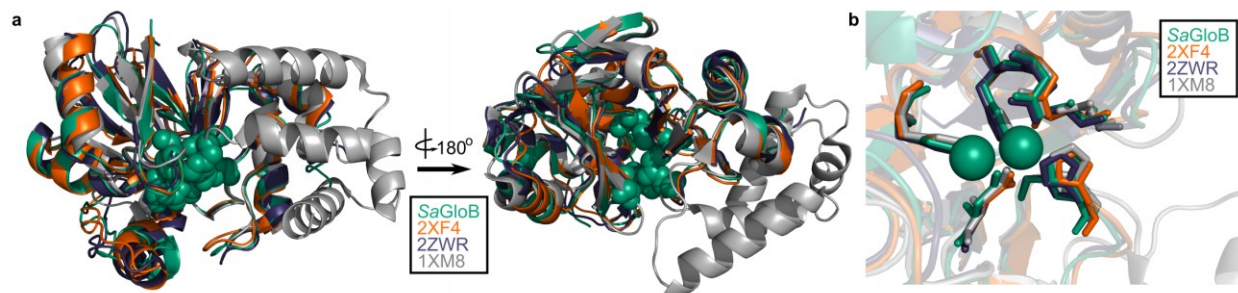
Figure S8 Structural conservation of GloB. (a) Overall structural alignment of GloB (green) with YcbI from *S. enterica* (2XF4), TTHA1623 from *T. thermophilus* (2ZWR), and *A. thaliana* glyoxalase II (1XM8). Zinc coordinating residues are colored in green spheres. (b) positioning of the Zinc coordinating residues, zinc colored in green spheres.
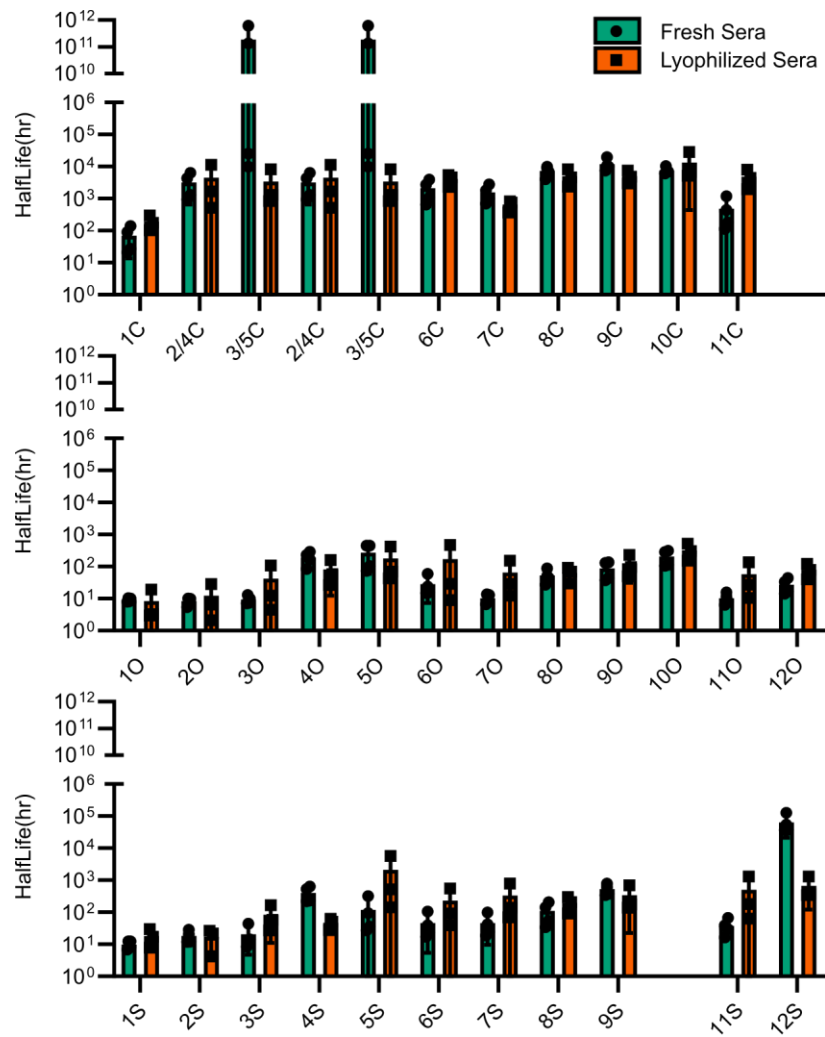
Figure S9 Comparison of esterase activity between fresh and lyophilized human sera. Points represent individual experiments; bars represent the mean of the four replicates. Error bars denote SD.
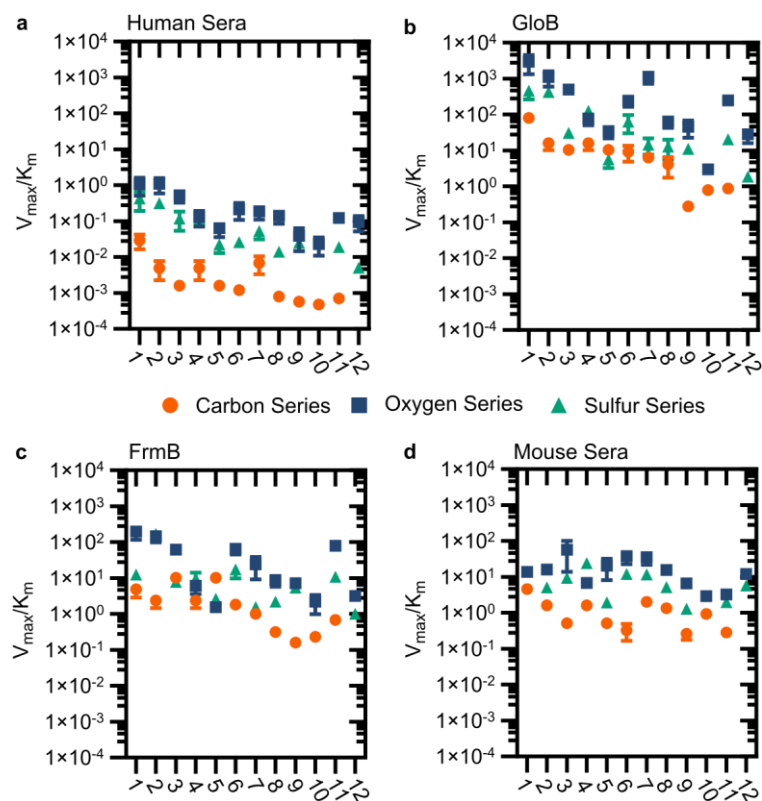
Figure S10 Modified catalytic specificity (pmol fluorescein produced * min^{-1}*µg^{-1} protein) of human sera, GloB, FrmB, and mouse sera. X-axis corresponds to compound identities in Figure S5. Carbon containing compounds indicated in orange, oxygen in blue, and sulfur in green. Displayed are the means of three independent biological experiments with error bars denoting SD.

178
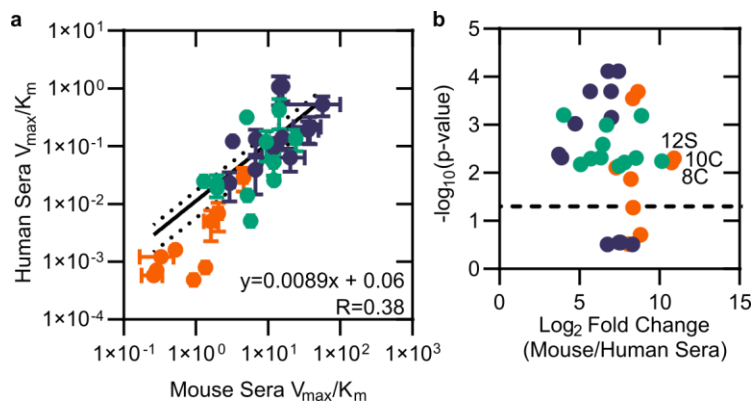
Figure 11 Comparison of mouse and human sera. (a) Modified catalytic specificity (pmol fluorescein produced * min^{-1}*µg^{-1} protein) of human and mouse sera. Displayed is a linear regression of the fit between mouse and human sera. (b) Volcano plot of catalytic specificity. Displayed are the means of three independent experiments. P-values calculated as pairwise t-tests with Holm-Sidak correction for multiple comparisons. Dashed line indicates a p-value of 0.05.

4.7 Tables

Table S1 Half maximal inhibitory concentration (IC50) values for POM-HEX against predicted prodrug activating esterases. * p<0.05, ** p<0.01, *** p<0.005, **** p<0.0001

SAUSA300 gene	Newman gene	StrID (NARSA)	Pan gene symbol	POM-HEX IC$_{50}$ (µM)	POM-HEX IC$_{50}$ SD (µM)	Significantly different from WT (JE2)?	Adjusted P-value	Predicted function	GO term
Parental Strain		JE2		1.54	0.40			N/A	Parental Strain
SAUSA300_0742	NWMN_0727	NE145	uvrA	1.46	0.17	ns	0.9999	Exonuclease ABC, A subunit	carboxylic ester hydrolase activity, carboxylesterase activity
SAUSA300_1902	NWMN_1859	NE202		0.700	0.066	ns	0.9101	Hypothetical protein	phosphoric diester hydrolase activity
SAUSA300_2173	NWMN_2121	NE223	truA	1.39	0.29	ns	0.9997	tRNA pseudouridine synthase A	phosphatase
SAUSA300_1285	NWMN_1303	NE293		1.41	0.64	ns	0.9997	ABC transporter, ATP-binding protein	phosphatase
SAUSA300_2515	NWMN_2477	NE355	gbaA	1.73	0.48	ns	0.9997	Transcriptional regulator, TetR family	carboxylic ester hydrolase activity
SAUSA300_1505	NWMN_1449	NE377	gloB	10.6	3.2	****	<0.0001	Hydroxyacylglutathione hydrolase	hydroxyacylglutathione hydrolase
SAUSA300_0142	NWMN_0084	NE478	phnE	1.61	0.81	ns	0.9999	Phosphonate ABC transporter, permease protein	phosphoric diester hydrolase activity
SAUSA300_2564	NWMN_2528	NE503	estA, frmB	6.28	2.25	****	<0.0001	Tributyrin esterase	carboxylic ester hydrolase activity
SAUSA300_2473	NWMN_2434	NE532		1.56	0.51	ns	>0.9999	Hypothetical Alkaline Phosphatase	phosphatase
SAUSA300_0581	NWMN_0561	NE621		1.62	0.55	ns	0.9999	Hypothetical protein	phosphatase activity
SAUSA300_0299		NE812		1.64	0.56	ns	0.9998	Hypothetical protein	phosphatase activity
SAUSA300_1993	NWMN_1947	NE937	fruC	1.67	0.52	ns	0.9998	PfkB family kinase	phosphatase
SAUSA300_1752	NWMN_1700	NE949	hsdM2	1.73	0.53	ns	0.9996	type I restriction-modification system, M subunit	phosphoric diester hydrolase activity
SAUSA300_0312	NWMN_0254	NE1039	psuG	1.73	0.51	ns	0.9997	Hypothetical protein	carboxylic ester hydrolase activity

SAUSA300 gene	Newman gene	StrID (NARSA)	Pan gene symbol	POM-HEX IC$_{50}$ (µM)	POM-HEX IC$_{50}$ SD (µM)	Significantly different from WT (JE2)?	Adjusted P-value	Predicted function	GO term
SAUSA300_0538	NWMN_0515	NE1071	capD	1.54	0.41	ns	>0.9999	NAD-dependent epimerase/dehydratase family protein	phosphatase activity
SAUSA300_1792	NWMN_1735	NE1173		1.84	0.40	ns	0.9994	Hypothetical protein	phosphatase activity
SAUSA300_0421	NWMN_0414	NE1225		2.15	0.48	ns	0.9938	Hypothetical protein	carboxylic ester hydrolase activity, carboxylesterase
SAUSA300_0214	NWMN_0156	NE1238		2.08	0.54	ns	0.9986	Hypothetical protein	phosphoric diester hydrolase activity
SAUSA300_0690	NWMN_0674	NE1296	saeS	2.07	0.53	ns	0.9986	Sensor histidine kinase SaeS	phosphatase
SAUSA300_1639	NWMN_1586	NE1486	phoP	2.18	0.41	ns	0.9932	Alkaline phosphatase synthesis transcriptional regulatory protein	phosphoric diester hydrolase activity
SAUSA300_0840	NWMN_0808	NE1505		2.20	0.54	ns	0.9927	Hypothetical protein	phosphoric diester hydrolase activity
SAUSA300_1563	NWMN_1507	NE1519	accC	1.75	0.70	ns	0.9996	Acetyl-CoA carboxylase, biotin carboxylase	phosphoric diester hydrolase activity
SAUSA300_2508		NE1547		1.48	0.23	ns	>0.9999	Hypothetical protein	phosphatase activity
SAUSA300_0996	NWMN_962	NE1610	pdhD	1.23	0.81	ns	0.9993	Dihydrolipoamide dehydrogenase	phosphoric diester hydrolase activity
SAUSA300_2367	NWMN_2320	NE1682	hlgB	1.37	0.19	ns	0.9997	Gamma-hemolysin component B	phosphatase

Table S2 Genotype and phenotype of POM-HEX resistant S. aureus. Displayed are the whole genome sequencing mutations that have been verified. Called mutations that were not observed via confirmatory Sanger sequencing are excluded.

Gene (Newman)	WT_SAUR	R1	R2	R3	R4	R5	R6	R7	R8	R9
NWMN_1449 (*gloB*)							c.376G>T p.Val126Leu		c.430T>A p.Phe144Ile	c.433G>A p.Ala145Thr
NWMN_2528 (*estA*, *frmB*)				c.40G>C p.Gly14Arg						
NWMN_0144					c.1472G>T p.Arg491Met					
NWMN_0240										
NWMN_0309				c.23A>C p.Asn8Thr		c.23A>C p.Asn8Thr				c.23A>C p.Asn8Thr
NWMN_0471 (*tilS*)										
NWMN_0523 (*sdrC*)										
NWMN_0564										
NWMN_0954										
NWMN_1152										
NWMN_1311 (*lysA*)										
NWMN_1425 (*recN*)										
NWMN_1655			c.17G>A p.Arg6His	c.17G>A p.Arg6His						
NWMN_1735										
NWMN_1754										
NWMN_2040 (*pdp*)										
NWMN_2253		c.1412C>T p.Ala471Val	c.1412C>T p.Ala471Val			c.1412C>T p.Ala471Val				
NWMN_2388										
POM-HEX IC$_{50}$ (µM)	1.921	6.337	5.932	9.561	10.54	3.752	11.09	10.71	16.96	17.71
Std. Deviation	1.111	0.8778	0.7325	0.4846	6.261	2.594	4.974	6.602	7.264	10.65

Gene (Newman)	R10	R11	R12	R13	R14	R15	R16	R17	R18
NWMN_1449 (*gloB*)	c.70G>T p.Val24Phe	c.166C>T p.His56Tyr	c.326C>A p.Pro109His	c.70G>T p.Val24Phe	c.70G>T p.Val24Phe	c.289C>T p.Gln97*			
NWMN_2528 (*estA*, *frmB*)							c.218_219insCATATGCCATGTTAGCA p.Met74fs	c.366G>A p.Met122Ile	
NWMN_0144									
NWMN_0240				c.432G>T p.Met144Ile					
NWMN_0309	c.23A>C p.Asn8Thr				c.23A>C p.Asn8Thr	c.23A>C p.Asn8Thr		c.23A>C p.Asn8Thr	
NWMN_0471 (*tilS*)								c.760_765dupTTTAAT p.Phe254_Asn255dup	
NWMN_0523 (*sdrC*)		c.2299A>G p.Asn767Asp							
NWMN_0564							c.230_231delCT p.Ser77fs		
NWMN_0954			c.359C>A p.Pro120His						
NWMN_1152									
NWMN_1311 (*lysA*)									
NWMN_1425 (*recN*)									
NWMN_1655		c.17G>A p.Arg6His		c.17G>A p.Arg6His	c.17G>A p.Arg6His	c.17G>A p.Arg6His		c.17G>A p.Arg6His	
NWMN_1735			c.2754C>A p.Phe918Leu						
NWMN_1754								c.232T>A p.Leu78Ile	
NWMN_2040 (*pdp*)		c.426G>T p.Leu142Phe							
NWMN_2253									c.1412C>T p.Ala471Val
NWMN_2388				c.195G>T p.Gln65His					
POM-HEX IC$_{50}$ (µM)	8.353	31.66	11.47	6.746	4.033	5.61	5.559	3.882	2.788
Std. Deviation	3.673	32.94	4.009	2.199	1.276	5.394	2.96	1.153	0.538

Gene (Newman)	R19	R20	R21	R22	R23	R24	R25
NWMN_1449 (*gloB*)						c.401C>T p.Pro134Leu	
NWMN_2528 (*estA*, *frmB*)	c.40G>C p.Gly14Arg		c.366G>A p.Met122Ile		c.356G>A p.Gly119Asp		c.40G>C p.Gly14Arg
NWMN_0144							
NWMN_0240							
NWMN_0309	c.23A>C p.Asn8Thr					c.23A>C p.Asn8Thr	c.23A>C p.Asn8Thr
NWMN_0471 (*tilS*)							
NWMN_0523 (*sdrC*)							
NWMN_0564							
NWMN_0954							
NWMN_1152						c.1570G>T p.Asp524Tyr	
NWMN_1311 (*lysA*)						c.1145C>A p.Ser382Tyr	
NWMN_1425 (*recN*)	c.1130T>C p.Leu377Ser						
NWMN_1655	c.17G>A p.Arg6His	c.17G>A p.Arg6His	c.17G>A p.Arg6His	c.17G>A p.Arg6His	c.17G>A p.Arg6His		
NWMN_1735							
NWMN_1754			c.232T>A p.Leu78Ile				
NWMN_2040 (*pdp*)							
NWMN_2253							
NWMN_2388							
POM-HEX IC$_{50}$ (µM)	5.678	3.847	3.923	4.568	3.794	8.396	3.519
Std. Deviation	2.073	1.061	1.087	4.194	0.903	1.049	0.112

Table S3 Half maximal inhibitory concentration (IC50) values for POM-HEX against transposon mutations in genes identified by whole-genome sequencing.

SAUSA300 gene	Newman gene	StrID (NARSA)	Pan gene symbol	POM-HEX IC$_{50}$ (µM)	POM-HEX IC$_{50}$ SD (µM)	Significantly different from WT (JE2)?	Adjusted P-value	Predicted function
Parental Strain		JE2		1.54	0.40			N/A
SAUSA300_1781	NWMN_1723	NE64	*hemY*	1.43	0.15	ns	0.9998	protoporphyrinogen oxidase
SAUSA300_0671	NWMN_0654	NE364		1.65	0.72	ns	0.9998	ABC transporter, ATP-binding protein, MsbA family
SAUSA300_1505	NWMN_1449	NE377	*gloB*	10.6	3.2	****	<0.0001	hydroxyacylglutathione hydrolase
SAUSA300_1708	NWMN_1655	NE386	*rot*	1.40	0.15	ns	0.9997	staphylococcal accessory regulator Rot
SAUSA300_2564	NWMN_2528	NE503	*estA, frmB*	6.28	2.25	****	<0.0001	tributyrin esterase
SAUSA300_1452	NWMN_1410	NE520	*proC*	1.47	0.75	ns	0.9999	pyrroline-5-carboxylate reductase
SAUSA300_0201	NWMN_0144	NE541		1.60	0.52	ns	>0.9999	peptide ABC transporter, permease protein
SAUSA300_1085	NWMN_1101	NE874		1.64	0.57	ns	0.9998	conserved hypothetical protein
SAUSA300_2105	NWMN_2057	NE929	*mtlF*	1.70	0.55	ns	0.9997	PTS system, mannitol specific IIBC component
SAUSA300_0778	NWMN_0762	NE1051		1.46	0.25	ns	0.9999	hypothetical protein
SAUSA300_1290	NWMN_1308	NE1118	*dapD*	1.69	0.59	ns	0.9997	tetrahydrodipicolinate acetyltransferase
SAUSA300_0414	NWMN_0407	NE1127	*lpl4*	1.72	0.62	ns	0.9997	tandem lipoprotein
SAUSA300_0028		NE1283	*tnp*	2.10	0.36	ns	0.9986	putative transposase

Table S4 Michaelis Menten parameters for *Sa*GloB

Substrate	V_{max} (pmol*min^{-1}*µg protein^{-1})		K_m (µM)		V_{max}/K_m (pmol*min^{-1}*mg GloB^{-1}µM^{-1})		k_{cat} (10^{-3} s^{-1})		k_{cat}/K_m (M^{-1} s^{-1})		k_{cat}/k_{uncat} (10^3)		((k_{cat}/K_m)/k_{uncat}) (10^9 M^{-1})		((V_{max}/K_m)/k_{uncat}) (10^{12}pmol*mg GloB^{-1}µM^{-1})	
	Value	SEM	Value	SEM	Value	SEM	Value	SEM	Value	SEM	Value	SEM	Value	SEM	Value	SEM
1C	0.497	0.074	6.23	3.39	79.9	22	0.0744	0.0111	11.9	3.28	21.2	16.3	3.41	4.81	380	536
2C	0.292	0.051	18.3	9.0	15.9	5.6	0.0436	0.0076	2.38	0.845	17.2	7.9	0.940	0.881	105	98
3C			>50		10.4	1.0			1.55	0.15			0.256	0.061	28.5	6.8
6C	0.444	0.130	48.0	29.5	9.24	4.40	0.0663	0.0194	1.38	0.658	12.7	33.4	0.265	1.133	29.6	126.3
7C			>50		6.43	0.31			0.961	0.046			0.109	0.041	12.2	4.6
8C	0.351	0.113	84.9	47.9	4.13	2.36	0.0524	0.0169	0.618	0.353	79.1	26.3	0.932	0.549	104	61
9C			>50		0.28	0.01			0.042	0.002			0.0244	0.0020	2.72	0.22
10C			>50		0.79	0.07			0.118	0.011			0.0752	0.0392	8.38	4.37
11C			>50		0.88	0.04			0.132	0.005			0.261	0.006	29.1	0.7
1O	217	41.5	73.5	25.7	2960	1620	32.5	6.2	442	242	38.6	15.3	0.525	0.595	58.6	66.5
2O	46.4	9.95	42.0	19.8	1103	503	6.93	1.49	165	75.3	19.4	11.8	0.462	0.595	51.5	66.4
3O	4.21	0.515	8.41	3.52	500.	146	0.630	0.077	74.8	21.9	4.91	1.41	0.584	0.400	65.0	44.6
4O	1.39	0.15	18.0	5.37	77.2	27.3	0.208	0.022	11.5	4.08	8.42	5.18	0.468	0.964	52.1	107.5
5O	0.731	0.15	21.2	11.8	34.5	12.7	0.109	0.023	5.15	1.91	17.0	24.1	0.803	2.038	89.5	227.2
6O	2.91	0.26	12.0	3.3	242	76.8	0.435	0.038	36.1	11.5	5.76	1.09	0.479	0.325	53.4	36.3
7O	23.1	4.50	20.5	10.9	1130	412	3.45	0.67	168	61.7	23.6	21.2	1.15	1.95	129	217
8O	1.01	0.149	15.5	6.8	64.9	22.0	0.151	0.022	9.71	3.30	6.80	1.80	0.437	0.267	48.7	29.7
9O	2.54	0.83	55.5	36.5	45.7	22.8	0.380	0.125	6.84	3.41	14.6	16.0	0.264	0.439	29.4	48.9
10O			>50		2.96	0.22			0.442	0.033			0.0715	0.0346	7.97	3.85
11O			>50		248	21.9			37.1	3.27			0.0411	0.0369	4.58	4.12
12O	1.04	0.190	36.9	15.4	28.2	12.3	0.156	0.028	4.21	1.84	1.28	0.67	0.0348	0.0438	3.87	4.88
1S	14.9	3.92	32.5	20.4	457	192	2.22	0.59	68.4	28.8	11.4	13.6	0.351	0.666	39.2	74.3
2S			>50		422	39.5			63.1	5.91			0.0529	0.0665	5.90	7.41
3S			>50		31.0	2.34			4.63	0.350			0.0259	0.0088	2.89	0.98
4S			>50		126	15.2			18.8	2.27			0.278	0.057	30.9	6.4
5S	0.18	0.049	31.7	21.1	5.60	2.34	0.0266	0.0074	0.840	0.351	4.35	2.45	0.137	0.116	15.3	12.9
6S	4.19	1.17	65.8	34.9	63.7	33.6	0.627	0.176	9.53	5.03	12.9	7.8	0.197	0.224	21.9	25.0
7S	0.722	0.150	49.5	21.4	14.6	7.01	0.108	0.022	2.18	1.05	7.86	3.04	0.159	0.142	17.7	15.9
8S	1.02	0.40	79.8	56.2	12.8	7.19	0.153	0.060	1.92	1.08	9.01	7.64	0.113	0.136	12.6	15.2
9S			>50		11.1	0.86			1.66	0.128			0.0215	0.0613	2.40	6.84
11S			>50		20.5	2.87			3.07	0.429			0.0662	0.0219	7.38	2.44
12S			>50		1.86	0.03			0.278	0.005			0.0310	0.0005	3.46	0.06

Table S5 Michaelis Menten parameters for *Sa*FrmB

Substrate	V_{max} (pmol*min^{-1}*μg protein^{-1})		K_m (μM)		V_{max}/K_m (pmol*min^{-1}*mg FrmB^{-1}μM^{-1})		k_{cat} (10^{-3} s^{-1})		k_{cat}/K_m (M^{-1} s^{-1})		k_{cat}/k_{uncat} (10^3)		$((k_{cat}/K_m)/k_{uncat})$ (10^9 M^{-1})		$((V_{max}/K_m)/k_{uncat})$ (10^{12} pmol*mg FrmB^{-1}μM^{-1})	
	Value	SEM	Value	SEM	Value	SEM	Value	SEM	Value	SEM	Value	SEM	Value	SEM	Value	SEM
1C	0.149	0.059	30.4	29.5	4.89	2.01	0.0280	0.0112	0.921	0.379	7.99	16.5	0.263	0.557	23.3	49.3
2C	0.0637	0.0274	26.5	28.9	2.40	0.95	0.0120	0.0052	0.452	0.179	4.74	5.38	0.179	0.186	15.8	16.5
3C			>50		10.2	0.64			1.92	0.12			0.316	0.050	28.0	4.4
6C			>50		1.84	0.14			0.347	0.026			0.0666	0.0444	5.90	3.93
7C			>50		1.01	0.08			0.191	0.015			0.0217	0.0133	1.92	1.17
8C			>50		0.314	0.012			0.0591	0.0022			0.0892	0.0034	7.89	0.30
9C			>50		0.160	0.009			0.0301	0.0018			0.0177	0.0019	1.56	0.17
10C			>50		0.233	0.029			0.0438	0.0055			0.0279	0.0194	2.47	1.72
11C			>50		0.682	0.062			0.128	0.012			0.254	0.014	22.5	1.2
1O	5.98	0.677	30.3	8.33	197	81.3	1.13	0.127	37.2	15.3	1.34	0.31	0.0442	0.0377	3.91	3.34
2O	2.04	0.328	13.9	6.76	147	48.6	0.385	0.062	27.7	9.14	1.08	0.49	0.0777	0.0723	6.88	6.40
3O	0.621	0.191	9.95	10.06	62.4	18.9	0.117	0.036	11.7	3.57	0.911	0.656	0.0916	0.0653	8.11	5.78
4O	0.183	0.038	30.0	15.2	6.12	2.51	0.0345	0.0072	1.15	0.47	1.40	1.70	0.0467	0.1118	4.14	9.89
5O			>50		1.54	0.10			0.290	0.020			0.0452	0.0210	4.00	1.86
6O	0.597	0.091	9.17	4.66	65.2	19.4	0.112	0.017	12.3	3.66	1.49	0.48	0.163	0.104	14.4	9.2
7O	2.57	0.96	107	64.8	24.0	14.8	0.485	0.180	4.52	2.78	3.31	5.69	0.0309	0.0877	2.73	7.77
8O	0.163	0.031	18.3	9.66	8.92	3.17	0.0307	0.0058	1.68	0.60	1.38	0.47	0.0757	0.0482	6.70	4.27
9O			>50		7.24	0.31			1.36	0.06			0.0525	0.0076	4.65	0.67
10O	0.163	0.053	74.2	43.6	2.20	1.21	0.0307	0.0099	0.414	0.227	4.97	10.26	0.0671	0.2351	5.94	20.81
11O			>50		79.1	2.7			14.9	0.51			0.0165	0.0058	1.46	0.51
12O			>50		3.18	0.26			0.598	0.048			0.00493	0.00115	0.44	0.10
1S			>50		12.5	0.6			2.36	0.11			0.0121	0.0026	1.07	0.23
2S			>50		169	14			31.8	2.58			0.0266	0.0290	2.36	2.57
3S			>50		7.79	0.19			1.47	0.04			0.0082	0.0009	0.728	0.081
4S	0.505	0.147	52.7	31.3	9.58	4.70	0.0950	0.0277	1.80	0.89	1.40	0.70	0.0266	0.0223	2.36	1.97
5S	0.0295	0.0030	11.1	3.61	2.66	0.83	0.00556	0.00056	0.500	0.156	0.910	0.187	0.0818	0.0517	7.24	4.58
6S	0.629	0.169	36.3	22.3	17.3	7.5	0.118	0.032	3.27	1.42	2.44	1.42	0.0674	0.0633	5.97	5.61
7S			>50		1.55	0.12			0.292	0.023			0.0213	0.0032	1.88	0.28
8S			>50		2.20	0.24			0.415	0.046			0.0244	0.0058	2.16	0.51
9S			>50		5.38	0.48			1.01	0.09			0.0131	0.0435	1.16	3.85
11S			>50		10.8	1.1			2.04	0.21			0.0440	0.0105	3.89	0.93
12S			>50		1.02	0.07			0.191	0.013			0.0213	0.0013	1.89	0.12

Table S6 Summary of crystallographic data collection and refinement statistics.

Data Collection	*Sa*FrmB	*Sa*GloB (SeMet)
Space Group	C2	P 1 21 1
Cell dimensions	a= 128.8Å, b= 80.6Å	a= 93.7Å, b= 44.76Å
	c=67.1Å, β=114.1°	c=105.0Å, β=96.7°
Wavelength (Å)	0.979	1.000
Resolution (Å) (highest shell)	36.8-1.60 (1.63-1.60)	48 - 1.65 (1.71 - 1.65)
Reflections (total/unique)	145907 / 78193	102457
Completeness (highest shell)	96.4% (99.1%)	96.1 % (88.8 %)
$<I/\sigma>$ (highest shell)	27.1 (4.1)	
R_{sym} (highest shell)	6.6% (57.3%)	
Refinement		
R_{cryst} / R_{free}	0.156 / 0.179	0.225 / 0.251
No. of protein atoms	4164	6323
No. of waters	496	431
No. of ligand atoms	3	28
R.m.s.d., bond lengths (Å)	0.009	0.007
R.m.s.d., bond angles (°)	1.34	1.21
Avg. B-factor (Å^2): protein, water, ligand	25.8, 37.6, 15.9	39.6, 44.9, 47.5
Stereochemistry: most favored, allowed, disallowed	98.4, 1.6, 0 %	96.2, 3.8, 0 %

Table S7 Michaelis Menten parameters for human sera

Substrate	V_{max} (pmol*min^{-1}*mg sera^{-1})		K_m (μM)		V_{max}/K_m (pmol*min^{-1}*mg sera^{-1}μM^{-1})		$((V_{max}/K_m)/k_{uncat})$ (10^{12} pmol*mg sera^{-1}μM^{-1})	
	Value	SEM	Value	SEM	Value	SEM	Value	SEM
1C	1.06	0.15	36.2	11.5	0.0293	0.0128	0.139	0.315
2C	0.356	0.191	71.5	70.6	0.00498	0.00271	0.0328	0.0471
3C			>50		0.00161	0.00022	0.00443	0.00151
6C			>50		0.00121	0.00013	0.00389	0.00381
7C	0.441	0.029	64.18	8.03	0.00688	0.00355	0.0130	0.0531
8C			>50		0.000791	0.000062	0.0199	0.0016
9C			>50		0.000581	0.000026	0.00568	0.00045
10C			>50		0.000483	0.000042	0.00513	0.00251
11C			>50		0.000711	0.000027	0.0234	0.0005
1O	68.6	25.6	64.1	45.8	1.07	0.560	0.0212	0.0230
2O	43.8	10.53	40.4	21.5	1.09	0.489	0.0507	0.0645
3O	11.7	2.81	22.2	14.2	0.529	0.198	0.0687	0.0604
4O	5.88	1.90	44.5	30.9	0.132	0.061	0.0894	0.2420
5O	2.25	0.48	35.4	17.4	0.0635	0.0274	0.165	0.489
6O	11.7	3.82	54.6	35.9	0.215	0.107	0.0475	0.0503
7O	5.73	1.16	30.3	14.9	0.189	0.078	0.0216	0.0411
8O	3.93	0.71	27.7	12.4	0.142	0.057	0.107	0.077
9O	4.35	1.18	111.7	48.9	0.0389	0.0242	0.0250	0.0519
10O	1.46	0.38	63.3	31.8	0.0230	0.0121	0.0621	0.2080
11O			>50		0.122	0.008	0.00225	0.00158
12O	4.00	0.68	42.2	15.7	0.0948	0.0433	0.0130	0.0171
1S	30.5	9.90	71.8	43.0	0.425	0.230	0.0364	0.0890
2S			>50		0.315	0.025	0.00440	0.00472
3S	8.80	2.92	74.3	45.0	0.118	0.065	0.0111	0.0273
4S	3.81	0.39	27.9	7.08	0.137	0.055	0.0336	0.0230
5S	0.690	0.246	31.0	26.7	0.0222	0.0092	0.0606	0.0510
6S			>50		0.0257	0.0025	0.00886	0.00182
7S	1.60	0.43	30.2	19.7	0.0528	0.0216	0.0641	0.0490
8S			>50		0.0140	0.0007	0.0138	0.0015
9S			>50		0.0247	0.0021	0.00532	0.01651
11S			>50		0.0190	0.0017	0.00682	0.00149
12S			>50		0.00504	0.00036	0.00937	0.00062

Table S8 Michaelis Menten parameters for mouse sera

Substrate	V_{max} (pmol*min^{-1}*mg sera^{-1})		K_m (μM)		V_{max}/K_m (pmol*min^{-1}*mg sera$^{-1}\mu$M^{-1})		$((V_{max}/K_m)/k_{uncat})$ (10^{12} pmol*mg sera$^{-1}\mu$M^{-1})	
	Value	SEM	Value	SEM	Value	SEM	Value	SEM
1C			>50		4.56	0.51	21.7	12.4
2C			>50		1.62	0.33	10.7	5.7
3C			>50		0.52	0.02	1.43	0.13
6C	17.6	9.4	53.5	58.1	0.33	0.16	1.05	4.65
7C			>50		2.04	0.27	3.86	4.04
8C			>50		1.35	0.13	34.0	3.3
9C	3.18	0.66	12.3	8.0	0.26	0.08	2.53	1.46
10C			>50		0.93	0.08	9.87	4.74
11C			>50		0.28	0.01	9.34	0.18
1O			>50		14.01	0.83	0.28	0.03
2O			>50		15.90	1.12	0.74	0.15
3O			>50		57.0	43.2	7.41	13.17
4O			>50		6.76	0.21	4.57	0.82
5O			>50		20.3	12.0	52.6	214.7
6O	437	135	11.5	8.65	38.1	15.6	8.42	7.39
7O	929	103	25.9	7.30	35.8	14.1	4.08	7.40
8O			>50		15.7	0.4	11.8	0.5
9O			>50		6.69	0.17	4.30	0.36
10O			>50		2.93	0.14	7.91	2.36
11O			>50		3.24	0.16	0.06	0.03
12O			>50		11.9	0.4	1.64	0.15
1S			>50		14.2	1.4	1.22	0.54
2S			>50		5.07	0.21	0.07	0.04
3S			>50		9.47	0.76	0.88	0.32
4S			>50		24.2	2.6	5.96	1.08
5S			>50		1.93	0.13	5.27	0.71
6S			>50		12.1	0.6	4.16	0.41
7S			>50		11.9	1.1	14.4	2.6
8S			>50		5.17	0.43	5.07	0.91
9S			>50		1.29	0.11	0.28	0.89
11S			>50		1.97	0.10	0.71	0.09
12S			>50		5.74	0.53	10.7	0.9

Table S9 Primers used during this study.

NO	NAME	SEQUENCE	USE
1	NWMN_0144_F	TTTTCCTGATCCTGATTCAC	Sanger Sequencing
2	NWMN_0144_R	ATGATGCTTCCATGTTTGTT	Sanger Sequencing
3	NWMN_0306_F	AATACACCGGGTAACACAAC	Sanger Sequencing
4	NWMN_0306_R	CGTTTTGTTGAGCTAATTCC	Sanger Sequencing
5	NWMN_0309_F	ACCATGCTTAAAGGGATTTT	Sanger Sequencing
6	NWMN_0309_R	TGTCACCTAAGTCAACACCA	Sanger Sequencing
7	NWMN_0407 (lpl4nm) _F	CCGTTGGAGATAGGAAGTTA	Sanger Sequencing
8	NWMN_0407 (lpl4nm) _R	TTTGTGCTTCTTTTGAACCT	Sanger Sequencing
9	NWMN_0654_F	GAAAATGGAAGACTGATTGC	Sanger Sequencing
10	NWMN_0654_R	TAATGCATCTGACAAAGTCG	Sanger Sequencing
11	NWMN_0762_F	GGTGAAGTTTTGGACGATAA	Sanger Sequencing
12	NWMN_0762_R	TTTTCATCTGTCCGACTTTT	Sanger Sequencing
13	NWMN_1101_F	TCCACCTATTGGAATTATCG	Sanger Sequencing
14	NWMN_1101_R	AGACGTTCAATTTCAGTGCT	Sanger Sequencing
15	NWMN_1192 (pgsA) _F	TGGGACGAAGTAATTACAGTT	Sanger Sequencing
16	NWMN_1192 (pgsA) _R	ATATCCCCCTTGTATCGTTT	Sanger Sequencing
17	NWMN_1308 (dapD) _F	TCTATTCGTGGAGGTACGAT	Sanger Sequencing
18	NWMN_1308 (dapD) _R	ATCGTATGTGAGCCATTACC	Sanger Sequencing
19	NWMN_1410_F	CGATAAACCTAAACCACTCG	Sanger Sequencing
20	NWMN_1410_R	ATAAACAATGCTTGCCAAAT	Sanger Sequencing
21	NWMN_1505_F	TGAAGGTGAATTAAGCGATG	Sanger Sequencing
22	NWMN_1505_R	TGCTATTCCCAATTTGTTCA	Sanger Sequencing
23	NWMN_1655_F	GAATTGTTGCAATTTAATGGT	Sanger Sequencing
24	NWMN_1655_R	AACGTAATCATGCTCCATTC	Sanger Sequencing
25	NWMN_1679_F	CCATGGGAAAAATTAGACAA	Sanger Sequencing
26	NWMN_1679_R	AAATATCGCCTCACCTTTTT	Sanger Sequencing
27	NWMN_1723 (hemY) _F	GCCGAATACACATCCATTAT	Sanger Sequencing
28	NWMN_1723 (hemY) _R	AACCTTTGTCTCTGCTTCAA	Sanger Sequencing
29	NWMN_1851 (nadC) _F	AGCCATTTTAGCACCATAAA	Sanger Sequencing
30	NWMN_1851 (nadC)_R	TAGAATCCTGTCCTCCTGAA	Sanger Sequencing
31	NWMN_2057 (mtlF)_F	TGTACAACGGTGTTGTTTTG	Sanger Sequencing
32	NWMN_2057 (mtlF)_R	CGGTGAATAGTACGAGAGGA	Sanger Sequencing
33	NWMN_2528_F	ACTGATGCTTTACCAGAAAC	Sanger Sequencing
34	NWMN_2528_R	TCAGCGGTAGTAATAAAGGT	Sanger Sequencing

Table S10 Accession numbers for the isolates used in WhatsGNU analysis.

Isolate	Bioproject	Biosample	WGS	SRA
AD_3_179	PRJNA512846	SAMN10689346	VYMI00000000	SRR8389007
AD_11_548	PRJNA512846	SAMN10689354	VYMN00000000	SRR8389002
AD_14_565	PRJNA512846	SAMN10689355	VYMO00000000	SRR8389003
AD_16_660	PRJNA512846	SAMN10689358	SJAX00000000	SRR8389044
AD_61_868	PRJNA512846	SAMN10689401	VYNS00000000	SRR11016776
AD_85_830	PRJNA512846	SAMN10689428	VYOK00000000	SRR8389056
AD_96_471	PRJNA512846	SAMN10689447	VYOW00000000	SRR8389016
AD_103_347	PRJNA512846	SAMN10689453	VYPC00000000	SRR8389035
AD_113_782	PRJNA512846	SAMN10689463	VYPL00000000	SRR8389099
SSTI_227_44	PRJNA563582	SAMN12642230	VUGB00000000	SRR11016228
SSTI_228_42	PRJNA563582	SAMN12642226	VUGF00000000	SRR11016232
SSTI_231_2	PRJNA563582	SAMN12642218	VUGN00000000	SRR11016241
SSTI_233_51	PRJNA563582	SAMN12642215	VUGQ00000000	SRR11016244
SSTI_235	PRJNA563582	SAMN12642210	VUGV00000000	SRR11016250
SSTI_241_9	PRJNA563582	SAMN12642203	VUHC00000000	SRR11016198
SSTI_247_75	PRJNA563582	SAMN12642193	VUHM00000000	SRR11016209
SSTI_258_57	PRJNA563582	SAMN12642177	VUIB00000000	SRR11016226
SSTI_290	PRJNA563582	SAMN12642174	VUIE00000000	SRR11016283

4.8 References

1.   Hsu J (2020) How COVID-19 is accelerating the threat of antimicrobial resistance. BMJ 1983(May):m1983.

2.   Antimicrobial resistance in the age of COVID-19 (2020) Nat Microbiol 5(6):779–779.

3.   CDC (2019) Antibiotic resistance threats in the United States 2019. Available at: https://www.cdc.gov/drugresistance/pdf/threats-report/2019-ar-threats-report-508.pdf.

4.   WHO (World Health Organisation) (2019) No Time to Wait: Securing the future from drug-resistant infections. Available at: who.int/antimicrobial-resistance/interagency-coordination-group/IACG_final_report_EN.pdf?ua=1.

5.   Turner NA, et al. (2019) Methicillin-resistant Staphylococcus aureus: an overview of basic and clinical research. Nat Rev Microbiol 17(4):203–218.

6.   Kourtis AP, et al. (2019) Vital Signs: Epidemiology and Recent Trends in Methicillin-Resistant and in Methicillin-Susceptible Staphylococcus aureus Bloodstream Infections — United States. MMWR Morb Mortal Wkly Rep 68(9):214–219.

7.   Global Antimicrobial Resistance Hub Available at: https://dashboard.globalamrhub.org/reports/pipelines/pipelines.

8.   WHO (World Health Organisation) (2019) Antibacterial agents in preclinical development: an open access database Available at: https://apps.who.int/iris/bitstream/handle/10665/330290/WHO-EMP-IAU-2019.12-eng.pdf.

9.   Haag NL, Velk KK, Wu C (2012) Potential antibacterial targets in bacterial central metabolism. Int J Adv life Sci 4(1–2):21–32.

10.   Murima P, McKinney JD, Pethe K (2014) Targeting Bacterial Central Metabolism for Drug Development. Chem Biol 21(11):1423–1432.

11.   Wellington S, Hung DT (2018) The Expanding Diversity of Mycobacterium tuberculosis Drug Targets. ACS Infect Dis 4(5):696–714.

12.   Azema L, Baron R, Ladame S (2006) Targeting enzymes with phosphonate-based inhibitors: mimics of tetrahedral transition states and stable isosteric analogues of phosphates. Curr Enzym Inhib 2(1):61–72.

13.   Kornberg RD, McNamee MG, McConnell HM (1972) Measurement of transmembrane potentials in phospholipid vesicles. Proc Natl Acad Sci U S A 69(6):1508–13.

14.   Edwards RL, et al. (2020) Potent, specific MEPicides for treatment of zoonotic staphylococci. PLoS Pathog 16(6):e1007806.

15.   Lin Y, et al. (2018) Eradication of ENO1-deleted glioblastoma through collateral lethality. bioRxiv. doi:10.1101/331538.

16.   McKenney ES, et al. (2012) Lipophilic prodrugs of FR900098 are antimicrobial against Francisella novicida in vivo and in vitro and show GlpT independent efficacy. PLoS One 7(10):e38167.

17.   Zhang Y, et al. (2006) Activity of nitrogen-containing and non-nitrogen-containing bisphosphonates on tumor cell lines. J Med Chem 49(19):5804–14.

18.   Hsiao C-HC, et al. (2014) Synthesis of a phosphoantigen prodrug that potently activates Vγ9Vδ2 T-lymphocytes. Chem Biol 21(8):945–954.

19.   Wiemer AJ, Wiemer DF (2015) Prodrugs of phosphonates and phosphates: crossing the membrane barrier. 200(1):115–160.

20.   Hecker SJ, Erion MD (2008) Prodrugs of phosphates and phosphonates. J Med Chem 51(8):2328–2345.

21.   Heidel KM, Dowd CS (2019) Phosphonate prodrugs: an overview and recent advances. Future Med Chem 11(13):1625–1643.

22.   Uh E, et al. (2011) Antibacterial and antitubercular activity of fosmidomycin, FR900098, and their lipophilic analogs. Bioorg Med Chem Lett 21(23):6973–6976.

23.   Edwards RL, et al. (2017) MEPicides: potent antimalarial prodrugs targeting isoprenoid biosynthesis. Sci Rep 7(1):8400.

24.   San Jose G, et al. (2013) Design of potential bisubstrate inhibitors against Mycobacterium tuberculosis (Mtb) 1-deoxy-D-xylulose 5-phosphate reductoisomerase (Dxr)—evidence of a novel binding mode. Medchemcomm:1099–1104.

25.   San Jose G, et al. (2016) Structure-activity relationships of the MEPicides: N-acyl and O-linked analogs of FR900098 as inhibitors of DXR from Mycobacterium tuberculosis and Yersinia pestis. ACS Infect Dis 2(12):923–935.

26.   Wang X, et al. (2018) MEPicides: α,β-Unsaturated Fosmidomycin Analogues as DXR Inhibitors against Malaria. J Med Chem 61:8847–8858.

27.   Erion MD, et al. (2005) Liver-targeted drug delivery using HepDirect prodrugs. J Pharmacol Exp Ther 312(2):554–60.

28.   Erion MD, et al. (2004) Design, Synthesis, and Characterization of a Series of Cytochrome P 450 3A-Activated Prodrugs (HepDirect Prodrugs) Useful for Targeting Phosph(on)ate-Based Drugs to the Liver §. J Am Chem Soc 126(16):5154–5163.

29.   Mikati MO, et al. (2020) Antimicrobial Prodrug Activation by the Staphylococcal Glyoxalase GloB. ACS Infect Dis:acsinfecdis.0c00582.

30.   White A, et al. (2018) Fluorogenic structure activity library pinpoints molecular variations in substrate specificity of structurally homologous esterases. JBC:1–23.

31.   European Committee for Antimicrobial Susceptibility Testing (EUCAST) of the European Society of Clinical Microbiology and Infectious Dieases (ESCMID) (2000) Determination of minimum inhibitory concentrations (MICs) of antibacterial agents by agar dilution. Clin Microbiol Infect 6(9):509–15.

32.   Yatsunenko T, et al. (2012) Human gut microbiome viewed across age and geography. Nature 486(7402):222–227.

33.   Madeira F, et al. (2019) The EMBL-EBI search and sequence analysis tools APIs in 2019. Nucleic Acids Res 47(W1):W636–W641.

34.   Letunic I, Bork P (2019) Interactive Tree Of Life (iTOL) v4: recent updates and new developments. Nucleic Acids Res 47(W1):W256–W259.

35.   Alexandrov A, et al. (2004) A facile method for high-throughput co-expression of protein pairs. Mol Cell Proteomics 3(9):934–8.

36.   Van Duyne GD, Standaert RF, Karplus PA, Schreiber SL, Clardy J (1993) Atomic structures of the human immunophilin FKBP-12 complexes with FK506 and rapamycin. J Mol Biol 229(1):105–24.

37.   Stamp AL, et al. (2010) Structural and functional characterization of Salmonella enterica serovar typhimurium YcbL: An unusual type II glyoxalase. Protein Sci 19(10):1897–1905.

38.   White A, et al. (2018) Fluorogenic structure activity library pinpoints molecular variations in substrate specificity of structurally homologous esterases. J Biol Chem 293:13851–13862.

39.   Minor W, Cymborowski M, Otwinowski Z, Chruszcz M (2006) HKL -3000: the integration of data reduction and structure solution – from diffraction images to an initial model in minutes. Acta Crystallogr Sect D Biol Crystallogr 62(8):859–866.

40.   McCoy AJ, et al. (2007) Phaser crystallographic software. J Appl Crystallogr 40(Pt 4):658–674.

41.   Hu Y, et al. (2015) Structural and functional analysis of a low-temperature-active alkaline esterase from South China Sea marine sediment microbial metagenomic library. J Ind Microbiol Biotechnol 42(11):1449–61.

42.   Yamamura A, et al. (2009) Structure of TTHA1623, a novel metallo-beta-lactamase superfamily protein from Thermus thermophilus HB8. Acta Crystallogr Sect F Struct Biol Cryst Commun 65(Pt 5):455–9.

43.   Cowtan K (2006) The Buccaneer software for automated model building. 1. Tracing protein chains. Acta Crystallogr Sect D Biol Crystallogr 62(9):1002–1011.

44.	Emsley P, Cowtan K (2004) Coot: model-building tools for molecular graphics. Acta Crystallogr D Biol Crystallogr 60(Pt 12 Pt 1):2126–32.

45.	Adams PD, et al. (2010) PHENIX : a comprehensive Python-based system for macromolecular structure solution. Acta Crystallogr Sect D Biol Crystallogr 66(2):213–221.

46.	Morris GM, et al. (2009) AutoDock4 and AutoDockTools4: Automated docking with selective receptor flexibility. J Comput Chem 30(16):2785–2791.

47.	Trott O, Olson AJ (2009) AutoDock Vina: Improving the speed and accuracy of docking with a new scoring function, efficient optimization, and multithreading. J Comput Chem:NA-NA.

48.	Fey PD, et al. (2013) A genetic resource for rapid and comprehensive phenotype screening of nonessential Staphylococcus aureus genes. MBio 4(1). doi:10.1128/mBio.00537-12.

49.	Lentz CS, et al. (2018) Identification of a S. aureus virulence factor by activity-based protein profiling (ABPP). Nat Chem Biol 14(6):609–617.

50.	Moustafa AM, Planet PJ (2020) WhatsGNU: a tool for identifying proteomic novelty. Genome Biol 21(1):58.

51.	vander Jagt D. (1989) The glyoxalase system. Chem Biochem Med Asp:597–641.

52.	Gonzalez CF, et al. (2006) Molecular basis of formaldehyde detoxification. Characterization of two S-formylglutathione hydrolases from Escherichia coli, FrmB and YeiG. J Biol Chem 281(20):14514–22.

53.	Fellner M, et al. (2020) Structural Basis for the Inhibitor and Substrate Specificity of the Unique Fph Serine Hydrolases of <i> Staphylococcus aureus. ACS Infect Dis 6(10):2771–2782.

54.	Wefers D, et al. (2017) Biochemical and Structural Analyses of Two Cryptic Esterases in Bacteroides intestinalis and their Synergistic Activities with Cognate Xylanases. J Mol Biol 429(16):2509–2527.

55.	Richardson CM, et al. (2007) Discovery of a potent CDK2 inhibitor with a novel binding mode, using virtual screening and initial, structure-guided lead scoping. Bioorg Med Chem Lett 17(14):3880–3885.

56.	Marasinghe GPK, et al. (2005) Structural Studies on a Mitochondrial Glyoxalase II. J Biol Chem 280(49):40668–40675.

57.	Cameron AD, Ridderström M, Olin B, Mannervik B (1999) Crystal structure of human glyoxalase II and its complex with a glutathione thiolester substrate analogue. Structure 7(9):1067–1078.

Chapter 5: Conclusion

5.1 Summary

As the prevalence of multidrug-resistant bacteria and parasites continues to grow, there is an urgent need to develop novel antimicrobials with new targets. One underdeveloped therapeutic strategy is targeting microbial metabolism. Metabolic inhibitors are simple to design as substrate mimics and have multiple druggable options in each organism (1–4). Unfortunately, metabolic based inhibitors often rely on phosphate or phosphonate residues which are cell impermeable (5–11). In this work, we add to a growing body of literature supporting the claim that lipophilic prodrugging strategies can increase the potency and cellular penetrability of phosphonate antibiotics (6, Chapter 2). However, current lipophilic prodrugging strategies are readily cleaved by host enzymes, greatly limiting the efficacy of these strategies in the clinic. For the first time, we have described how lipophilic prodrugs are activated intracellularly by microbial cells (12, Chapter 3). This key finding allowed us to launch a structure-activity relationship campaign on the two staphylococcal esterases responsible for prodrug activation, FrmB and GloB (Chapter 4). In addition to characterizing GloB (Chapter 4) and FrmB (Chapter 4, Appendix A), we also characterize the substrate specificity of human and mouse sera, demonstrating that simple modifications to ester prodrugs not only have an impact on rates of *in vivo* activation, but also can confer specificity to the location of prodrug activation (Chapter 4). This finding is also briefly examined for the unicellular parasite, *Plasmodium falciparum* (Appendix B). Together these studies lay an important groundwork for the development of targeted prodrug therapies. Finally, in work parallel to the primary focus of this thesis, we work to understand the origin of *P. falciparum* volatile compounds such as the mosquito attractive terpene, α-pinene (Appendix C and D).

5.2 Lipophilic prodrug transit

We find that addition of the lipophilic promoiety, pivaloyloxymethyl (POM), to the phosphonate residues of ERJ significantly increases potency against *S. schleiferi* and *S. pseudintermedius* (6). POM-dependent potency increases have similarly been observed for ERJ, ERJ analogues, and other phosphonate antibiotics against several other organisms. Presumably, the underlying mechanism of POM-prodrug increases in potency stems from increased cellular permeability of phosphonate antibiotics, however it is also feasible that lipophilic prodrugging increases transit via a yet unknown transporter or siderophore. Supporting the first hypothesis, we find that while ERJ requires the glycerol-3-phosphate transporter, GlpT, for cellular entry, POM-ERJ can bypass GlpT mediated transport (Chapter 2). This finding has also been demonstrated in the gram negative organism, *Francisella novicida* (7). The exact mechanism by which POM prodrugs enter cells remains unknown however defining this mechanism will be crucial for understanding the potential uses and limitations of lipophilic prodrugs.

One exciting application of lipophilic prodrugs is the targeting of drugs to specific cell types. How lipophilic prodrugs enter cells, whether through passive permeability or through enzyme mediated transit, remains unknown. Understanding how prodrugs enter cells will determine how broadly lipophilic prodrugging strategies can be applied. For instance, if lipophilic prodrugs truly passively enter cells, any lipophilic environment could harbor a prodrug. This is especially relevant when applying lipophilic prodrugs to the clinic and would impact the dosing strategies depending on the lipid content of each individual patient. Simple experiments utilizing mass-spectrometry to track prodrug localization in whole liposomes as opposed to washed and lysed liposomes would serve to address this question. Similarly, development of liposome transit assays will allow an understanding of how lipid composition impacts prodrug transit.

5.3 The (lack of) efficacy of lipophilic prodrugs on gram-negative bacteria

Consistently we and others have observed that POM-ERJ is ineffective against *E. coli* and other gram-negative organisms (*K. pneumoniae*, *S. typhimurium*, *S. sonnei*, *S. marcescens*, and *B. tahilandensis*) (6). Notably, the compound POM-ERJ is ineffective against *E. coli* despite the activated compound, ERJ, displaying potent activity both against whole-cell *E. coli* and ERJ's target, *Ec*DXR (6) (Chapter 2). POM-HEX is similarly ineffective against whole cell *E. coli*, though whether HEX has activity against *Ec*ENO remains unknown. Three hypotheses exist which explain this lack of activity (Figure 1). First, gram negative organisms may not maintain the enzymes responsible for prodrug activation resulting in no accumulation of activated drug *in vivo*. Second, POM-prodrugs may not effectively transit the double membrane of gram-negative bacteria. The final hypothesis is that POM-prodrugs are activated by gram-negative bacteria but are not activated in the correct cellular location to achieve target inhibition. In the following section we will discuss the cases for and against each of these hypotheses. Defining why POM-prodrugs do not have efficacy on gram-negative organisms will ultimately determine how efficacious targeted lipophilic prodrugging strategies will be as antimicrobials.

Hypothesis 1) POM-prodrugs are not activated in vivo by gram-negative organisms. We have shown that in the gram-positive organism, *S. aureus*, two carboxylesterases, FrmB and GloB, catalyze the removal of the first POM-moiety in di-POM prodrugs (Chapter 4). At least one additional enzyme is required for the final conversion from the mono-POM-prodrug to the fully deprotected version of this compound, though the identity of this protein is unknown. GloB and FrmB both have orthologs in *E. coli*, suggesting that at least the first step in prodrug

activation may be possible in *E. coli*. Low conservation of FrmB and GloB between *E. coli* and *S. aureus* raises the possibility that the substrate specificities of these two enzymes vary disallowing prodrug activation in *E. coli* (Chapter 4). We have expressed each *Sa*FrmB and *Sa*GloB individually in *E. coli* using classical IPTG inducible promoters and protein expression vectors and find that *E. coli* remains insensitive to POM-ERJ. It remains possible that the final enzyme(s) in POM-prodrug activation are not present in *E. coli*.

Hypothesis 2) POM-prodrugs do not diffuse through the periplasm. POM-prodrugs are hypothesized to bypass active transit mechanisms and diffuse freely into cells. In part, this hypothesis is founded on the GlpT independent transit of POM-prodrugged fosmidomycin and fosmidomycin analogues (6, 7). This hypothesis is also grounded in chemistry, as POM-prodrugs of small metabolites often have cLogP values > 1.5, reflective of the lipophilic nature of POM-prodrugs. As a result, one would imagine that in single membrane cellular environments, the POM-promoiety has a rate of transition between the being exposed extracellularly and intracellularly, while similarly transitioning between the aqueous environment and the lipophilic environment. Rapid hydrolysis of intracellular POM-prodrugs would thus result in an accumulation of activated drug inside the cell.

In gram-negative organisms which have two membranes separated by periplasmic space, pure diffusion of lipophilic compounds may result in no activation (Figure 1). An extracellular lipophilic prodrug entering a cell must first enter the extracellular membrane, subsequently diffuse into and across the periplasm before imbedding into the intracellular membrane, flipping from the periplasmic side of the intracellular membrane to the intracellular side of the

membrane, and finally dissociate into the cytoplasm for cleavage. For extremely lipophilic groups, the equilibrium between the extracellular membrane and periplasmic space would heavily favor the compound staying imbedded in the membrane. Any compound reaching the intracellular membrane would also heavily favor staying in that membrane. Given an infinite time, eventually the concentrations of POM-prodrug in each membrane would equilibrate, however this equilibration may not occur on a biologically relevant timescale.

Perhaps the strongest evidence against this hypothesis is the potent anti-*E. coli* activity of a lipophilic prodrug of FR900098 (13). The designed FR900098 prodrug is similarly lipophilic to POM-ERJ (cLogP 2.14 and 1.44 respectively), however the promoieties are highly divergent. This suggests that compound lipophobicity alone does not prevent drug penetrance across the gram-negative double membrane.

Hypothesis 3) POM-prodrugs are activated in periplasmic space and cannot cross the inner membrane. Several enzymes localize to the gram-negative periplasm, including at least three hydrolases (14). This raises the possibility that these hydrolases can activate, either fully or partially, POM-compounds. As even partially deprotected phosphonate molecules are membrane impermeable, any compound partially activated would be stuck in the periplasmic space (Figure 1) (15). Perhaps the strongest evidence against this hypothesis is that in *E. coli* the glycerol-3-phosphate transporter (GlpT) is localized to the inner membrane of *E. coli* (16, 17). This would suggest that in the case of POM-ERJ, conversion to ERJ in the periplasm would still result in inhibition of *E. coli*. One potential explanation remedying this disagreement is that partial conversion of POM-ERJ, for example to hemi-POM-ERJ, would likely be sufficient to prevent GlpT mediated transport while simultaneously leaving the molecule membrane impermeable.

With all three hypotheses addressed, POM-prodrug activation by two additional organisms needs to be considered. *Mycobacterium tuberculosis*, a gram intermediate, and *Francisella novicida*, a lightly stained gram-negative, are both killed by POM-prodrugs (7, 18). The cell wall of *M. tuberculosis* most closely resembles that of gram-positive organisms. However, the peptidoglycan layer of *M. tuberculosis* often accumulates a layer of lipids forming a pseudoperiplasm (19). This lipid layer is sufficient to retain gram-stain, though whether this layer recapitulates the typical gram-negative outer membrane for POM-prodrugs is not clear.

Defining why POM-prodrugs do not inhibit gram-negative organisms will ultimately inform how widely lipophilic microbe specific prodrug targeting can be applied. If POM-prodrugs fail because they cannot cross the periplasm lipophilic prodrugging strategies targeting cytoplasmic esterases will never work for gram-negative organisms. If substrate specificity is the limiting factor then alternative promoieties, cleavable by gram-negative organisms, can be designed. Several experiments can be quickly performed to identify which of the above hypotheses is correct. Quantifying POM-prodrug activation in intact and lysed *E. coli* will directly answer whether *E. coli* has the capacity to activate POM-promoieties. Similarly, these experiments could be performed with pro-fluorescent substrates as in Chapter 4. Alternatively, the activity of POM-prodrugs could be assayed in the presence of outer membrane pore formers such as polymyxin B as a means of decoupling prodrug transit and activity.

5.4 The Cellular Roles of FrmB and GloB

We have shown that carboxy ester prodrug activation in *Staphylococcus* spp. hijacks two esterases which are conserved throughout the tree of life, FrmB and GloB. Both enzymes have high GNU scores indicating they are well conserved within *S. aureus* and suggesting that their native function is important for cell survival and fitness. Somewhat surprisingly, deletion of

either FrmB or GloB results in no observable fitness defects in rich axenic culture. The native role(s) and physiological function(s) for FrmB and GloB remain unclear.

GloB is annotated as a hydroxyacylglutathione hydrolase and is the second enzymatic step of the two-step glyoxalase pathway (comprised of GloA and GloB). This pathway is canonically viewed as a means of cellular protection from the toxic cellular metabolite, methylglyoxal. Methylglyoxal is spontaneously generated via nonenzymatic decomposition of glyceraldehyde-3-phosphate (GAP) and dihydroxyacetone phosphate (DHAP) and is highly reactive impacting both protein function and glycating nucleic acids (20–22). Spontaneous coupling of methylglyoxal to glutathione, isomerization to D-lactoylglutathione, and subsequent hydrolysis to lactate and glutathione are catalyzed by GloA and GloB respectively. Despite endogenous methylglyoxal detoxification, addition of exogenous methylglyoxal kills *S. schleiferi* with a half-maximal inhibitory concentration (IC$_{50}$) in the low mM. Surprisingly, mutations in GloB do not impact *S. schleiferi* sensitivity to methylglyoxal, despite GloB having traditional GloB activity (Chapters 3 and 4). Two hypotheses potentially explain these findings. First, *Staphylococcus* spp. have multiple means of detoxifying methylglyoxal. *S. aureus* has 6 enzymes with predicted GloA activity and 3 enzymes with predicted GloB activity (including the GloB characterized here). In addition to the genetic redundancy within the glyoxalase pathway, *S. aureus* has recently been described to have a glutathione independent methylglyoxal detoxification mechanism (23). Beyond these two pathways, it is feasible that alternative oxidoreductases may play a role in methylglyoxal detoxification (24–26). Secondly, it is possible that while GloB mutations are tolerated in the short term, long term mutations in GloB become lethal. Protein glycation has only been demonstrated to slightly reduce the activity of glycolytic proteins suggesting some glycation may be tolerable (20). DNA glycation, conversely, is likely to be fatal

as it results in strand breaks and interstrand cross-linking, though these errors may be slow to accumulate (21).

Similar to GloB, FrmB is also annotated as a detoxification enzyme. Rather than detoxifying methylglyoxal, FrmB is reported as a formylglutathione hydrolase, responsible for protecting against free cellular formaldehyde. Formaldehyde detoxification mirrors the glyoxalase pathway. Free formaldehyde is coupled to glutathione, oxidized via a formaldehyde dehydrogenase, before subsequent hydrolysis to formate and glutathione by FrmB. FrmB and FrmB orthologs have been characterized in several eukaryotes and prokaryotes, however the conditions where FrmB is required remains unclear (27–32). In *Paracoccus denitrificans*, FrmB is required for growth on methanol, methylamine, and choline suggesting that the pathway is essential for growth on methylotrophic growth in some organisms. In humans, mutation of the analogous esterase, esterase D, have been linked to Wilson's disease and retinoblastoma (33).

Several intriguing questions remain regarding the native roles of FrmB and GloB. Are their conditions where these two genes are essential? How redundant are the two pathways that FrmB and GloB comprise respectively? Growing FrmB or GloB mutant strains in a variety of nutrient conditions and stressors may reveal growth phenotypes which can be traced to a native function. Performing these experiments in competition with WT *S. aureus* may improve the sensitivity of these assays. Additionally, generating reporter strains that fluoresce upon FrmB or GloB transcription should be a relatively easy process that stands to improve assay sensitivity enabling a secondary means of evaluating when the cell requires FrmB or GloB (34). The impact of GloB or FrmB loss on survival and virulence in *in vivo* settings remains another interesting avenue. Ultimately, understanding how essential GloB and FrmB are for *S. aureus* growth and virulence

is an important consideration given how quickly POM-prodrug resistance can arise due to mutations in these genes.

5.5   Alternative resistance mechanisms to POM-prodrugs

We have described here three independent screens of *Staphylococcus* spp. resulting in resistance to POM-prodrugs. Multiple SNPs were identified in two esterases, FrmB and GloB. We have demonstrated that mutations in FrmB and GloB disrupt protein functionality and lead to a lack of prodrug activation in these mutant cells. However, several strains (*S. aureus* 8/25, *S. schleiferi* 9/16, *S. pseudintermedius* 4/18) have no identified mutations in FrmB or GloB. The genetic cause of prodrug resistance in these staphylococci remains unclear. In several of the *S. aureus* strains, there are no candidate SNPs following Sanger sequencing. Further, of the strains with SNPs remaining, none of the impacted genes have an obvious mechanism of resistance.

To explore the possibility of SNPs that were missed by Whole Genome Sequencing, we performed Sanger Sequencing on GloB and FrmB for each unexplained mutant of *S. aureus*. In addition to sequencing the coding region, we also sequenced the 500 bp upstream of the FrmB start codon to find any potential promoter disruptions. No mutations were identified in the coding region of either gene, nor were SNPs discovered in the promoter region of FrmB. The promoter region of GloB was not sequenced as there is no clear 5' promoter region as GloB may be a member of an operon. Barring promoter disruptions in GloB and sequencing errors that obfuscate any existing SNPs one possible means of resistance in these strains is silencing of RNA encoding either GloB, FrmB, or yet unknown prodrug activating enzymes. The evolution of RNAi to change gene expression in response to drug selection has been observed in the fungal

pathogen *Mucor circinelloides* (35). *S. aureus* maintains several sRNAs indicating that the basal machinery to produce sRNAs (36–38). Further, addition of exogenous siRNA to *S. aureus* has been demonstrated to decrease gene expression (39). While siRNA mediated drug resistance has not yet been observed in bacteria, it appears all the requisite tools are in place. Investigation into how our remaining staphylococci have become POM-prodrug resistance will either result in identification of a new resistance mechanism for bacteria or more information about POM-prodrug activation.

5.6   Barriers to metabolic prodrug resistance

The work presented here focuses on the development of two anti-metabolites, POM-HEX and POM-ERJ. In the organisms where these inhibitors have been studied, very rarely does resistance arise due to mutations in the target of the inhibitor. In *E. coli*, resistance to the ERJ analogue, fosmidomycin, through mutation of the target, DXR, only occurs upon PCR-mediated generation of resistance (13, 40). Similarly, after repeated fosmidomycin selections in *P. falciparum*, only one mutation in DXR has been observed (data not shown). Instead of mutating metabolic enzymes, resistance tends to arise via other mechanisms for metabolic inhibitors. In *S. schleiferi* and *F. novicida*, fosmidomycin resistance arises by disrupting the transporter which allows fosmidomycin into the cell (6, 41). In *P. falciparum*, fosmidomycin resistance arises through manipulation of the metabolic flux through the isoprenoid biosynthetic pathway (42). In part, this is to be expected. The enzymes targeted by anti-metabolites are essential. Most anti-metabolites are competitive active site inhibitors. Most mutations that would prevent active site inhibitor binding also disrupt binding of the native substrate. While resistance can arise via other mechanisms, metabolic rerouting only confers a partial resistance to fosmidomycin in *P. falciparum* and results in decreased fitness in the absence of fosmidomycin (43). Fosmidomycin

resistance in *S. schleiferi* and *F. novicida* can be acquired through disruption of active transit mechanisms, but lipophilic prodrugging strategies circumvent this resistance mechanism.

Providing microbially targeted lipophilic promoieties can be developed, metabolism as an antibiotic target appears to be a ripe and underdeveloped area. Inhibitors can be readily designed as substrate mimics, and mutations in target proteins appear difficult to acquire. Quantifying the barrier to resistance for metabolic inhibitors and their prodrugged forms, as well as the development of animal models to study resistance generation are useful avenues for understanding the clinical efficacy of metabolic prodrugs. It is feasible that in clinical settings pathogens will simultaneously face both the prodrugged and active form of metabolic inhibitors. For POM-ERJ, it seems unlikely that *S. schleiferi* would simultaneously mutate both GlpT and either FrmB or GloB. Quantifying the likelihood of resistance in dual treatment would be more reflective of a clinical setting. Further, understanding the causes of this resistance may reveal mechanisms of metabolic regulation. Finally, combination therapy approaches to prodrug administration- using independent esterases for prodrug activation- may be an interesting avenue to pursue.

5.7 The Complete Prodrug Activation Pathway

We have demonstrated that mutations in the carboxylesterases GloB or FrmB confer resistance to di-POM-prodrugs. NMR characterization of the products of GloB and FrmB with di-POM prodrugs suggests that both enzymes remove the first POM moiety but are unable to remove the second and fully deprotect the compound (Figure 2). This is not altogether unsurprising when considering the reaction mechanisms for each FrmB and GloB. GloB is hypothesized to

deprotonate a water molecule and utilize the hydroxide ion to initiate attack on carbonyl substrates (44). A negatively charged, mono-POM compound may be repelled from the hydroxide, thereby preventing further hydrolysis. Similarly, FrmB is hypothesized to undergo several charge rearrangements during substrate hydrolysis. These charge transfers presumably become unfavorable for a charged mono-POM molecule. How mono-POM phosphonates are converted to the fully deprotected compound remains unknown. Understanding how prodrugs are fully activated affords an additional layer of specificity that can be engineered into prodrug activation. This approach may be especially useful in attempting to develop anti-metabolites which are otherwise host toxic.

One hypothesis is that a phosphodiesterase is required to terminate prodrug activation. We have performed three forward genetic and one reverse genetic screen in efforts to identify prodrug activating enzymes. Our reverse genetic screen purposefully included every non-essential phosphodiesterase of *S. aureus*. Unfortunately, we were unable to identify enzymes beyond GloB and FrmB that contribute to prodrug activation. Two hypotheses are likely to explain this finding. First, the final enzyme is required to *S. aureus* growth. Secondly, the final enzymatic step could be performed by multiple enzymes with each enzyme being supplied in excess. If this is the case, deletion of just one enzyme would have no impact on POM-prodrug survival as other cellular enzymes would compensate for the lost activity. Our screens are unable to differentiate between these two hypotheses. To identify the final enzyme(s) in the prodrug activation pathway, the most straightforward approach is likely to perform an activity-based-proteomics for enzymes hydrolyzing mono-POM substrates (45–48).

Targeting multiple microbial esterases simultaneously for prodrug activation may be an optimal strategy. While POM-prodrugs have no activity against enzymes, single mutations in either GloB

or FrmB do not fully protect *S. aureus* from POM-HEX. Presumably, this is because both GloB and FrmB can partially activate POM-HEX. Along this reasoning, creation of a *S. aureus* strain with mutations in both FrmB and GloB would likely result in high levels of resistance to POM-HEX. As the development of microbe targeted promoieties continues, promoieties that have redundant activation pathways in bacteria may be preferred. Promoieties taking advantage of multiple esterases increases the number of mutations required for full resistance to arise. Likely, redundant targeting of esterases also increases the rate of prodrug activation *in vivo*, thereby contributing to higher intracellular levels of active drug.

5.8   Prodrug activation in P. falciparum

In Appendix B we discuss prodrug activation by one of the malarial parasites, *Plasmodium falciparum*. Since 2000, rates of malaria cases and deaths have fallen, yet *P. falciparum* still causes an enormous disease burden annually. The increasing prevalence of artemisinin resistance threatens the progress made to date. New antimalarial inhibitors which are safe and effective, especially those capable of killing all parasites after administration as a single dose, are urgently needed. Prodrug targeted therapies, whether activated by the erythrocyte or by the parasite, present an intriguing opportunity to both increase antimalarial potency while simultaneously improving pharmacokinetic properties. Identification and characterization of erythrocyte and parasite esterases remains a high priority for the development of these inhibitors.

We developed a unique screening approach to identify the malarial esterase responsible for activation of POM-ERJ. In using parasites with mutations in HAD1 as a parental strain, we removed one mechanism of resistance to the activated compound, ERJ. Regrettably, we were not able to generate stable mutants resistant to POM-ERJ, and thus unable to identify the

Plasmodium esterase responsible for POM-ERJ activation. While this is promising for POM-ERJ, more attempts at raising resistance should be made before classifying POM-ERJ as "irresistible". One attractive explanation for the lack of resistance to POM-ERJ is that erythrocyte esterases activate POM-ERJ and release ERJ for normal uptake. As the parasites already have mutations in HAD1, resistance to ERJ may be more difficult for parasites to achieve. While it should be noted that increased resistance to fosmidomycin, an analogue of ERJ, has already been observed in HAD1 backgrounds (data not shown), POM-prodrugs being activated by erythrocyte esterases is not unheard of. Acyclic immucillin phosphonates (AIPs) are potent inhibitors of hypoxanthine-guanine-xanthine phosphoribosyltransferase (HGXPRT) *in vitro*, yet are ineffective at killing whole-cell parasites despite the enzyme being essential (49). POM-prodrugging of AIPs resulted in compounds that were membrane permeable, but still ineffective against *P. falciparum* due to cleavage in the erythrocyte (49). Similarly, POM-HEX, a potent inhibitor of enolase, potently inhibits erythrocyte enolase, ultimately causing hemolysis (15).

While on the surface, erythrocyte targeted prodrugs may appear to be undesirable, targeting erythrocytes for prodrug activation may be extremely beneficial. *P. falciparum* demonstrates a remarkable ability to become resistant to antimalarials, including prodrugs (50). Targeting erythrocytes for prodrug activation eliminates one potential resistance strategy for the parasite. Further, this targeting strategy has enormous pharmacokinetic potential. Inhibitors that are trapped inside erythrocytes (due to the exposed charge on phosphonate residues, for example) will not be subject to the same metabolic processing that free serum compounds would. Likewise, drugged erythrocytes are not generally cleared by the liver or kidney, thereby reducing the amount of drug eliminated from the system. Depending on the length of time drug-loaded

erythrocytes circulate, these compounds could be highly effective prophylactics and may enable a drug-based malaria elimination campaign. While the major benefit conferred by lipophilic prodrugging of phosphonates appears to be membrane permeability, some inhibitors, such as fosmidomycin, appear to be readily taken up by *P. falciparum.* Likely uptake of fosmidomycin requires an active transport mechanism, however resistance to fosmidomycin via transporter mutations has not been observed yet as it has in bacterial systems. Potentially other nutrients required for *P. falciparum* growth also transit through this channel.

While erythrocyte targeted prodrug activation is okay for some compounds, others, such as the AIPs, require parasite specific targeting. We have demonstrated that medium chain lipophilic ester promoieties are already targeted for parasite specific activation. These promoieties are removed at rates fast enough to observe significant fluorescence accumulation (Appendix B). More work defining the relevant esterases for *P. falciparum* and human erythrocytes is needed. Promoieties that are preferentially activated by either the *P. falciparum* esterase(s) or the erythrocyte esterase(s), and not serum esterases, have enormous potential to both increase the druggable space for antimalarials as well as improve dosing regimens and patient efficacy.

5.9   Clinical opportunities for microbially targeted prodrugs

Some microbial infections are difficult to treat as the pathogen becomes sequestered in locations that receive poor drug penetrance. For example, antituberculosis treatment courses exceeding 6 months are routinely prescribed to eliminate drug tolerant *Mycobacterium tuberculosis* (*Mtb*) (51). One of the hallmarks of *Mtb* infection is the formation of large aggregates of immune cells around replicating *Mtb*. These lesions are termed granulomas and serve to limit the spread and success of *Mtb*. Unfortunately, the formation of these lesions also restricts delivery of antibiotics

to replicating bacteria (52–55). Similarly, bacterial infections that result in biofilms, or infections that localize to the bone such as *S. aureus* osteomyelitis, can be recalcitrant to treatment due in part to poor drug penetrance (56–60). Development of lipophilic prodrugs targeting microbes may increase drug penetrance thereby facilitating the development of new antimicrobial agents while simultaneously improving treatment efficacy.

Selectively targeting prodrugs for microbial activation as opposed to host activation is likely feasible. How broadly prodrugs are activated amongst the microbial populations, however, remains an open and intriguing question. It is feasible that prodrug therapies will be broadly hydrolysable by all microbial populations. In this case, microbially targeted protherapies serve to help all microbial infections as broad-spectrum antibiotics. However, it is likewise possible that targeted protherapies will result in narrow-spectrum antibiotics, possibly even at the level of genus or species. On first glance, narrow-spectrum antibiotics may seem less useful as clinicians need to identify the cause of infection prior to treatment. However, narrow-spectrum antibiotics are less likely to acquire resistance mechanisms from microbial community members thereby prolonging their clinical efficacy (61). Additionally, treatment with narrow, as opposed to broad-spectrum, antibiotics is less likely to result in microbiome depletion and mitigates the risk of *Clostridium difficile* infection (62, 63).

If pro-therapies are indeed narrow-spectrum, promoieties can also be utilized to develop novel diagnostic imaging techniques. One can imagine *in vivo* imaging agents similar to the fluorescent pro-substrates that are inactive prior to activation. Once activated, these pro-substrates would subsequently yield high signal in the imaging channel. This diagnostic technique would be especially useful in diagnosing microbial infections in body sites where samples are difficult to

acquire, or where the diagnostic itself is slow or unreliable. For example, culture based *Mtb* diagnostics are limited by the growth rate of *Mtb,* and diagnosis of *S. aureus* osteomyelitis often requires invasive bone biopsies (64, 65).

5.10 Transitioning microbially targeted prodrugs to the clinic

In chapter 4 we demonstrate that the microbial esterases FrmB and GloB from *S. aureus* exhibit catalytic specificity differences for simple ester substrates. Further, the catalytic specificities of FrmB and GloB are discriminatory from human and mouse serum esterases suggesting that ester promoieties may be tuned to activation by staphylococcal esterases. This finding has many potential clinical implications. Microbially targeted prodrugs open significant druggable space for development. Additionally, selective prodrug activation will increase the therapeutic index of many antimicrobials. Before these compounds can move into clinical development, several questions need to be addressed.

In chapter 4 our analysis focuses on the catalytic specificity of microbial esterases and serum esterases using a fluorogenic reporter library. This analysis is likely an oversimplification of the true biological situation. We directly compare the activity of purified microbial esterases to the total protein in unpurified human sera. Additionally, when prodrugs are dosed in a clinical setting they circulate in the serum for an undefined period before eventually entering the target cells. We are unable to account for variable incubation time in our assays. Finally, the rate of prodrug activation required for each antimicrobial has the potential to vary. Some compounds will be exceptionally potent inhibitors only requiring a few molecules of inhibitor per cell, whereas others will require more. A slow rate of intracellular prodrug activation is tolerable for

exceptionally potent but will not suffice if large amounts of activated drug are required. While the fluorogenic substrate library facilitates high-throughput analysis, it is not capable of answering the question "how fast is fast enough?". Several prodrugs should be synthesized using the same active compound but selecting varying promoieties. These varying promoieties should subsequently be evaluated for their ability to survive hydrolysis in sera and their ability to kill the target organism. In doing this, direct comparisons back to the rates of prodrug activation identified via the fluorogenic screen can be used to benchmark relevant rates of microbial prodrug activation, and meaningful stability in human sera. This strategy also allows for the expansion of the fluorogenic substrate library, enabling promoiety screening independent of the warhead.

In addition to defining the relevance of prodrug activation rates, an important consideration prior to clinical deployment of these compounds is the toxicity of prodrug byproducts. POM-prodrug activation likely results in the release of formaldehyde and pivalic acid, however more chemical analysis of prodrug activation products is required (10). Both pivalic acid and formaldehyde raise concern for their release into humans. Long term exposure to pivalic acid in humans has associated with reduced levels of carnitine (66). For a full microbially targeted prodrug, toxic prodrug byproducts would be expected to remain microbially contained if the cell remained intact. Further research in understanding how prodrugs are activated, and what happens to prodrug byproducts following microbial activation, is necessary.

Perhaps the final challenge for the development of microbially targeted prodrugs will be assessing the pharmacokinetics and dynamics (PK/PD) profiles and efficacy of these prodrugs. PK/PD studies are necessary to understand how a developing drug performs in a more complex

system such as host. These studies directly inform the dosing of novel drugs and serve as preliminary proof that the developing drug is safe. Typically, PK/PD models are first tested in a murine model and subsequently performed in additional animal models that more closely replicate humans. In chapter 4, we demonstrate a longstanding understanding that the esterases in mouse sera are different than those in human sera. The benefits of targeted prodrugs stem from the prodrug being delivered intact at the site of infection. Thus, if prodrug PK/PD models do not accurately reflect prodrug cleavage, the efficacy and dosing requirements of prodrugs will be incorrect. Several tools exist already to combat this barrier. First, esterase inhibitors have been developed in effort to reduce esterase activity in mice (67). Second, esterase 1 knockout mice have been developed in an effort to recapitulate human sera in mice (68). Finally, alternative animals which more closely mimic human sera exist as model systems including guinea pigs, rabbits, and rats. Unfortunately, each organism has discrete differences in carboxylesterase activity (69–78). Carboxy ester stability will likely need to be evaluated in a serum model for each animal to find activity profiles matching those of humans before efficacy and PK/PD studies can be performed.

5.11 Closing thoughts

Rising rates of antimicrobial resistance are an important concern for global health and we urgently need to develop new therapeutic strategies and incentivize antimicrobial research. The development of microbially targeted prodrugs not only increases the druggable space for antimicrobials but also serves to de-risk antimicrobial development by increasing drug specificity. In this work, we have described the benefits of lipophilic prodrugging strategies.

Additionally, we have uncovered the partial activation mechanism for these prodrugs in staphylococci. Finally, we have highlighted how knowledge of the activation pathway for lipophilic prodrugs can guide targeted prodrug design. We expect that these studies will enable the development of microbe-specific prodrugs and novel imaging based diagnostic mechanisms for microbial infections.
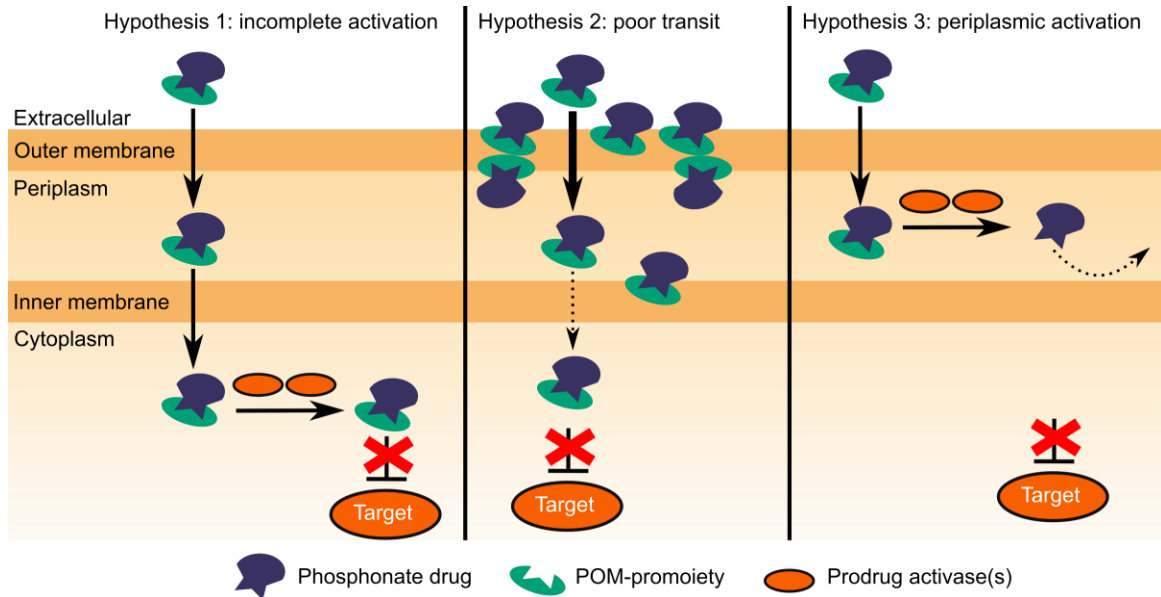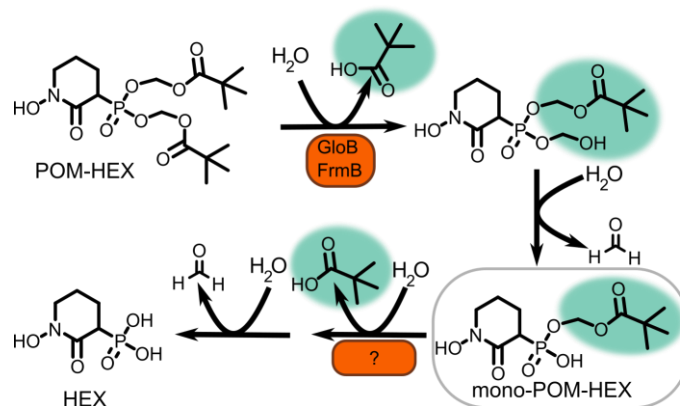
5.12 Figures

Figure 1 Models for lack of POM-prodrug activity on gram negative organisms.

Figure 2 Proposed POM-HEX activation mechanism. GloB and FrmB accumulate mono-POM-HEX (circled in gray) when incubated individually or in combination with POM-HEX. Promoieties highlighted in green.

218

5.13 References

1. Haag NL, Velk KK, Wu C (2012) Potential antibacterial targets in bacterial central metabolism. *Int J Adv life Sci* 4(1–2):21–32.

2. Murima P, McKinney JD, Pethe K (2014) Targeting bacterial central metabolism for drug development. *Chem Biol* 21(11):1423–32.

3. Andersen-Ranberg J, et al. (2016) Expanding the landscape of diterpene structural diversity through stereochemically controlled combinatorial biosynthesis. *Angew Chemie - Int Ed* 55(6):2142–2146.

4. Azema L, Baron R, Ladame S (2006) Targeting enzymes with phosphonate-based inhibitors: mimics of tetrahedral transition states and stable isosteric analogues of phosphates. *Curr Enzym Inhib* 2(1):61–72.

5. Kornberg RD, McNamee MG, McConnell HM (1972) Measurement of transmembrane potentials in phospholipid vesicles. *Proc Natl Acad Sci U S A* 69(6):1508–13.

6. Edwards RL, et al. (2020) Potent, specific MEPicides for treatment of zoonotic staphylococci. *PLoS Pathog* 16(6):e1007806.

7. McKenney ES, et al. (2012) Lipophilic prodrugs of FR900098 are antimicrobial against Francisella novicida *in vivo* and *in vitro* and show GlpT independent efficacy. *PLoS One* 7(10):e38167.

8. Zhang Y, et al. (2006) Activity of nitrogen-containing and non-nitrogen-containing bisphosphonates on tumor cell lines. *J Med Chem* 49(19):5804–14.

9. Hsiao C-HC, et al. (2014) Synthesis of a phosphoantigen prodrug that potently activates Vγ9Vδ2 T-lymphocytes. *Chem Biol* 21(8):945–954.

10. Hecker SJ, Erion MD (2008) Prodrugs of phosphates and phosphonates. *J Med Chem* 51(8):2328–2345.

11. Wiemer AJ, Wiemer DF (2015) Prodrugs of phosphonates and phosphates: crossing the membrane barrier. 200(1):115–160.

12. Mikati MO, et al. (2020) Antimicrobial prodrug activation by the staphylococcal glyoxalase GloB. *ACS Infect Dis*.

13. Armstrong CM, Meyers DJ, Imlay LS, Freel Meyers C, Odom AR (2015) Resistance to the antimicrobial agent fosmidomycin and an FR900098 prodrug through mutations in the deoxyxylulose phosphate reductoisomerase gene (dxr). *Antimicrob Agents Chemother* 59(9):5511–5519.

14. Beacham IR (1979) Periplasmic enzymes in gram-negative bacteria. *Int J Biochem* 10(11):877–883.

15. Lin Y, et al. (2018) Eradication of ENO1-deleted glioblastoma through collateral lethality. *bioRxiv*. doi:10.1101/331538.

16. Boos W, Hartig-Beecken I, Altendorf K (1977) Purification and Properties of a Periplasmic Protein. Related to sn-Glycerol-3-phosphate Transport in *Escherichia coli*. *Eur J Biochem* 72(3):571–581.

17. Lemieux MJ, Huang Y, Wang DN (2005) Crystal structure and mechanism of GlpT, the glycerol-3-phosphate transporter from *E. coli*. *Microscopy* 54(suppl_1):i43–i46.

18. San Jose G, et al. (2016) Structure-activity relationships of the MEPicides: N-acyl and O-linked analogs of FR900098 as inhibitors of DXR from *Mycobacterium tuberculosis* and *Yersinia pestis*. *ACS Infect Dis* 2(12):923–935.

19. Hett EC, Rubin EJ (2008) Bacterial Growth and Cell Division: a Mycobacterial Perspective. *Microbiol Mol Biol Rev* 72(1):126–156.

20. Gomes RA, et al. (2006) Yeast protein glycation in vivo by methylglyoxal. Molecular modification of glycolytic enzymes and heat shock proteins. *FEBS J* 273(23):5273–87.

21. Rahman A, Shahabuddin, Hadi SM (1990) Formation of strand breaks and interstrand cross-links in DNA by methylglyoxal. *J Biochem Toxicol* 5(3):161–166.

22. Migliore L, et al. (1990) Genotoxicity of methylglyoxal: cytogenetic damage in human lymphocytes in vitro

and in intesting cells of mice. *Carcinogenesis* 11(9):1503–1507.

23. Kim HJ, Lee K-Y, Kwon A-R, Lee B-J (2017) Structural and functional studies of SAV0551 from *Staphylococcus aureus* as a chaperone and glyoxalase III. *Biosci Rep* 37(6). doi:10.1042/BSR20171106.

24. Xu D, Liu X, Guo C, Zhao J (2006) Methylglyoxal detoxification by an aldo-keto reductase in the cyanobacterium *Synechococcus* sp. PCC 7002. *Microbiology* 152(7):2013–2021.

25. Ko J, et al. (2005) Conversion of Methylglyoxal to Acetol by *Escherichia coli* Aldo-Keto Reductases. *J Bacteriol* 187(16):5782–5789.

26. Murata K, Inoue Y, Rhee H, Kimura A (1989) 2-Oxoaldehyde metabolism in microorganisms. *Can J Microbiol* 35(4):423–431.

27. Kordic S, Cummins I, Edwards R (2002) Cloning and characterization of an S-formylglutathione hydrolase from *Arabidopsis thaliana*. *Arch Biochem Biophys* 399(2):232–238.

28. Harms N, Ras J, Reijnders WN, van Spanning RJ, Stouthamer AH (1996) S-formylglutathione hydrolase of *Paracoccus denitrificans* is homologous to human esterase D: a universal pathway for formaldehyde detoxification? *J Bacteriol* 178(21):6296–6299.

29. Gonzalez CF, et al. (2006) Molecular basis of formaldehyde detoxification. Characterization of two S-formylglutathione hydrolases from *Escherichia coli*, FrmB and YeiG. *J Biol Chem* 281(20):14514–22.

30. Lee WH, Wheatley W, Benedict WF, Huang CM, Lee EY (1986) Purification, biochemical characterization, and biological function of human esterase D. *Proc Natl Acad Sci* 83(18):6790–6794.

31. Uotila L, Koivusalo M (1979) Purification of formaldehyde and formate dehydrogenases from pea seeds by affinity chromatography and S-formylglutathione as the intermediate of formaldehyde metabolism. *Arch Biochem Biophys* 196(1):33–45.

32. Alterio V, et al. (2010) Crystal structure of an S-formylglutathione hydrolase from *Pseudoalteromonas haloplanktis* TAC125. *Biopolymers*:NA-NA.

33. Lee EY, Lee WH (1986) Molecular cloning of the human esterase D gene, a genetic marker of retinoblastoma. *Proc Natl Acad Sci* 83(17):6337–6341.

34. Fey PD, et al. (2013) A genetic resource for rapid and comprehensive phenotype screening of nonessential *Staphylococcus aureus* genes. *MBio* 4(1). doi:10.1128/mBio.00537-12.

35. Chang Z, Billmyre RB, Lee SC, Heitman J (2019) Broad antifungal resistance mediated by RNAi-dependent epimutation in the basal human fungal pathogen *Mucor circinelloides*. *PLOS Genet* 15(2):e1007957.

36. Liu W, et al. (2018) Assessment of Bona Fide sRNAs in *Staphylococcus aureus*. *Front Microbiol* 9. doi:10.3389/fmicb.2018.00228.

37. Bronsard J, et al. (2017) sRNA and cis-antisense sRNA identification in *Staphylococcus aureus* highlights an unusual sRNA gene cluster with one encoding a secreted peptide. *Sci Rep* 7(1):4565.

38. Romilly C, et al. (2012) Current knowledge on regulatory RNAs and their machineries in *Staphylococcus aureus*. *RNA Biol* 9(4):402–413.

39. Yanagihara K, et al. (2006) Effects of short interfering RNA against methicillin-resistant *Staphylococcus aureus* coagulase *in vitro* and *in vivo*. *J Antimicrob Chemother* 57(1):122–126.

40. Pines G, et al. (2018) Genomic deoxyxylulose phosphate reductoisomerase (DXR) mutations conferring resistance to the antimalarial drug fosmidomycin in *E. coli*. *ACS Synth Biol* 7(12):2824–2832.

41. Mackie RS, McKenney ES, van Hoek ML (2012) Resistance of *Francisella Novicida* to fosmidomycin associated with mutations in the glycerol-3-phosphate transporter. *Front Microbiol* 3. doi:10.3389/fmicb.2012.00226.

42. Guggisberg AM, et al. (2015) A sugar phosphatase regulates the methylerythritol phosphate (MEP) pathway in malaria parasites. *Nat Commun* 2(2):1–27.

43. Guggisberg AM, et al. (2018) Suppression of Drug Resistance Reveals a Genetic Mechanism of Metabolic Plasticity in Malaria Parasites. *MBio* 9(6). doi:10.1128/mBio.01193-18.

44. Cameron AD, Ridderström M, Olin B, Mannervik B (1999) Crystal structure of human glyoxalase II and its complex with a glutathione thiolester substrate analogue. *Structure* 7(9):1067–1078.

45. Saghatelian A, Jessani N, Joseph A, Humphrey M, Cravatt BF (2004) Activity-based probes for the proteomic profiling of metalloproteases. *Proc Natl Acad Sci* 101(27):10000–10005.

46. Liu Y, Patricelli MP, Cravatt BF (1999) Activity-based protein profiling: The serine hydrolases. *Proc Natl Acad Sci* 96(26):14694–14699.

47. Lentz CS, et al. (2018) Identification of a *S. aureus* virulence factor by activity-based protein profiling (ABPP). *Nat Chem Biol* 14(6):609–617.

48. Joachimiak Ł, Błażewska KM (2018) Phosphorus-based probes as molecular tools for proteome studies: recent advances in probe development and applications. *J Med Chem* 61(19):8536–8562.

49. Hazleton KZ, et al. (2012) Acyclic immucillin phosphonates: second-generation inhibitors of *Plasmodium falciparum* hypoxanthine- guanine-xanthine phosphoribosyltransferase. *Chem Biol* 19(6):721–730.

50. Istvan ES, et al. (2017) Esterase mutation is a mechanism of resistance to antimalarial compounds. *Nat Commun* 8(1):14240.

51. Nahid P, et al. (2016) Executive summary: Official American Thoracic Society/Centers for Disease Control and Prevention/Infectious Diseases Society of America Clinical Practice Guidelines: Treatment of drug-susceptible tuberculosis. *Clin Infect Dis* 63(7):853–867.

52. Cicchese JM, Dartois V, Kirschner DE, Linderman JJ (2020) Both pharmacokinetic variability and granuloma heterogeneity impact the ability of the first-line antibiotics to sterilize tuberculosis granulomas. *Front Pharmacol* 11. doi:10.3389/fphar.2020.00333.

53. Strydom N, et al. (2019) Tuberculosis drugs' distribution and emergence of resistance in patient's lung lesions: A mechanistic model and tool for regimen and dose optimization. *PLOS Med* 16(4):e1002773.

54. Prideaux B, et al. (2015) The association between sterilizing activity and drug distribution into tuberculosis lesions. *Nat Med* 21(10):1223–1227.

55. Sarathy JP, et al. (2016) Prediction of drug penetration in tuberculosis lesions. *ACS Infect Dis* 2(8):552–563.

56. Koo H, Allan RN, Howlin RP, Stoodley P, Hall-Stoodley L (2017) Targeting microbial biofilms: current and prospective therapeutic strategies. *Nat Rev Microbiol* 15(12):740–755.

57. Singh R, Sahore S, Kaur P, Rani A, Ray P (2016) Penetration barrier contributes to bacterial biofilm-associated resistance against only select antibiotics, and exhibits genus-, strain- and antibiotic-specific differences. *Pathog Dis* 74(6):ftw056.

58. Li B, Webster TJ (2017) Bacteria antibiotic resistance: New challenges and opportunities for implant-associated orthopedic infections. *J Orthop Res*. doi:10.1002/jor.23656.

59. Kavanagh N, et al. (2018) Staphylococcal osteomyelitis: disease progression, treatment challenges, and future directions. *Clin Microbiol Rev* 31(2). doi:10.1128/CMR.00084-17.

60. Thabit AK, et al. (2019) Antibiotic penetration into bone and joints: An updated review. *Int J Infect Dis* 81:128–136.

61. Alm RA, Lahiri SD (2020) Narrow-spectrum antibacterial agents—benefits and challenges. *Antibiotics* 9(7):418.

62. Webb BJ, Sorensen J, Jephson A, Mecham I, Dean NC (2019) Broad-spectrum antibiotic use and poor outcomes in community-onset pneumonia: a cohort study. *Eur Respir J* 54(1):1900057.

63. Melander RJ, Zurawski D V., Melander C (2018) Narrow-spectrum antibacterial agents. *Medchemcomm* 9(1):12–21.

64. Hatzenbuehler J, Pulling TJ (2011) Diagnosis and management of osteomyelitis. *Am Fam Physician* 84(9):1027–33.

65. Dunn JJ, Starke JR, Revell PA (2016) Laboratory diagnosis of *Mycobacterium tuberculosis* infection and disease in children. *J Clin Microbiol* 54(6):1434–1441.

66. Brass EP (2002) Pivalate-generating prodrugs and carnitine homeostasis in Man. *Pharmacol Rev* 54(4):589–598.

67. Bošković B (1979) The influence of 2-/o-cresyl/-4 H-1 : 3 : 2-benzodioxa-phosphorin-2-oxide (CBDP) on organophosphate poisoning and its therapy. *Arch Toxicol* 42(3):207–16.

68. Duysen EG, et al. (2011) Production of ES1 plasma carboxylesterase knockout mice for toxicity studies. 1891–1898.

69. Rudakova E V., Boltneva NP, Makhaeva GF (2011) Comparative analysis of esterase activities of human, mouse, and rat blood. *Bull Exp Biol Med* 152(1):73–75.

70. Cohen O, et al. (2006) Comparison of polyethylene glycol-conjugated recombinant human acetylcholinesterase and serum human butyrylcholinesterase as bioscavengers of organophosphate compounds. *Mol Pharmacol* 70(3):1121–1131.

71. Yang ZP, Dettbarn W-D (1998) Prevention of tolerance to the organophosphorus anticholinesterase paraoxon with carboxylesterase inhibitors. *Biochem Pharmacol* 55(9):1419–1426.

72. Due AH, Trap HC, Van Der Wiel HJ, Benschop HP (1993) Effect of pretreatment with CBDP on the toxicokinetics of soman stereoisomers in rats and guinea pigs. *Arch Toxicol* 67(10):706–711.

73. Bahar FG, Ohura K, Ogihara T, Imai T (2012) Species difference of esterase expression and hydrolase activity in plasma. *J Pharm Sci* 101(10):3979–3988.

74. Du B (1971) Plasma esterase activity and the metabolism of drugs with ester groups. *Ann N Y Acad Sci* 179(1 Drug Metaboli):684–694.

75. Williams FM (1985) Clinical significance of esterases in man. *Clin Pharmacokinet* 10(5):392–403.

76. Wang D, et al. (2018) Human carboxylesterases: a comprehensive review. *Acta Pharm Sin B* 8(5):699–712.

77. Fukami T, Yokoi T (2012) The emerging role of human esterases. *Drug Metab Pharmacokinet* 27(5):466–477.

78. Gao W, et al. (2015) The cyclic peptide ecumicin targeting CLpC1 is active against *Mycobacterium tuberculosis* in vivo. *Antimicrob Agents Chemother* 59(2):880–889.

Appendix A: FrmB mutational studies

Preface

This work is unpublished. Contributions are made by Justin J Miller, Wilhelm S. Cruz, the Spring 2019 Biol 4522 class, Joseph M Jez, and Audrey R. Odom John. JJM, WSC, and the Biol 4522 class designed primers, cloned, and purified mutant proteins. JJM performed enzyme assays. JJM, JMJ, and AROJ were responsible for experiment design. JMJ and AROJ were responsible for obtaining funding.

We are exceptionally grateful for Wilhelm Cruz for overseeing cloning and purification of mutant proteins, as well as the WUSTL Spring 2019 Biology 4522 course for all their work in the cloning and purification of these enzymes.

A.1 Introduction

S. aureus is a highly successful human pathogen responsible for a wide variety of invasive and life-threatening infections. Widespread methicillin resistance in *S. aureus* (MRSA) is especially concerning and has been labeled a "serious threat" by the Centers for Disease Control and Prevention (CDC) (1). New antimicrobials are urgently needed to address this pressing threat.

Recently, advancements in the understanding of prodrug activation in *S. aureus* have led to the possibility of *S. aureus* targeted prodrugs (Chapter 4). One of the identified proteins, FrmB, was found to have several mutations which resulted in resistance to pivaloyloxymethyl (POM) prodrugs. FrmB is a carboxylesterase with a suggested biological function of detoxifying formaldehyde (2). We previously hypothesized that mutations in FrmB prevent catalytic activity thereby conferring resistance to POM prodrugs. The structural rationale for FrmB mutations conferring POM-prodrug resistance, was not explored. Here, we examine how each of the previously identified mutations in FrmB impact catalytic activity. Further, we explore how FrmB dimerization impacts catalytic activity as well as the impact of mutations in the flexible capping domain.

A.2 Methods

A.2.1 Cloning of mutant FrmB

FrmB mutations (Table 1) were generated using QuikChange PCR mutagenesis (Agilent) using

the previously cloned WT FrmB from *S. aureus* as a template and the primers listed in Table 2.

Mutant FrmB constructs were cloned into the *E. coli* expression vector, pET28a, to introduce a

hexa-histidine tag, and plasmids were maintained in TOP10 chemically competent *E. coli*

(Thermofisher). All plasmids and mutations were verified using Sanger sequencing.

A.2.2 Mutant FrmB purification

FrmB mutant plasmids were introduced into chemically competent BL21 (DE3) *E. coli* cells

(Thermofisher) and selected for using 50 µg/mL kanamycin. A single colony was used to

inoculate a 5 mL overnight culture in LB media supplemented with 50 µg/mLkanamycin. The

following day, 2 mL of the overnight culture was back diluted into 1 L terrific broth (24 g Yeast

Extract, 12 g Tryptone, 9.4 g K_2HPO_4, 2.2 g KH_2PO_4, 0.04% glucose per liter) supplemented

with 50 µg/mL kanamycin. Cultures were grown at 37 ºC until reaching an OD_{600} of 0.4-0.7 at

which point the cultures were chilled to 16 ºC and protein expression was induced with 0.5 mM

isopropyl β-D-1-thiogalactopyranoside. Following 16 hours of induction, cell cultures were

harvested via centrifugation at 6000 x g for 15 min at 4 ºC. Cell pellets were resuspended in 45

mL lysis buffer (25 mM Tris pH 7.5, 250 mM NaCl, 1 mM $MgCl_2$, 10% glycerol, 1 mM PMSF,

and 20 mM imidazole). Pellets were lysed via sonication and insoluble cell fractions were

removed via centrifugation at 12,000 x g for 45 minutes at 4 ºC. Hexa-histidine tagged FrmB

mutants were purified via nickle agarose beads. Bound protein was washed with 50 mL lysis

buffer, and washed protein was eluted with lysis buffer supplemented with 300 mM imidazole.

Eluted proteins were dialyzed in dialysis buffer containing 25 mM Tris pH 7.5, 100 mM NaCl, and 20% glycerol. Protein concentrations were determined using the Bradford assay.

A.2.3 FrmB activity assay

FrmB activity against the substrate 4-nitrophenyl acetate was determined in 100 μL assays in 96 well clear flat bottom plates. Assays were performed in buffer consisting of 25 mM tris pH 7.5, 250 mM NaCl, 1 mM $MgCl_2$, 10% glycerol, and 5 μg purified protein. 4-nitrophenyl acetate concentrations were varied from 1 mM to 0.5 μM in 2-fold dilutions. Reactions were initiated through the addition of substrate and the formation of 4-nitrophenol was monitored spectrophotometrically at 405 nm using a Tecan platereader. Prior to assay initiation, assay plates were pre-warmed to a temperature of 37 ºC. Assays preformed without the addition of enzyme were used as a negative control for background substrate hydrolysis. Reactions were performed in triplicate with technical duplicates. The initial velocity for each reaction was fit to a line using Graphpad Prism. Initial rates of reaction were plotted versus the concentration of substrate to a standard Michaelis-Menten equation using Graphpad Prism to obtain estimates of the V_{max} and K_m for each mutant. For proteins where saturating conditions were not met, k_{cat}/K_m was estimated using the following derivation of Michaelis Menten-

Equation (1)
$$v = \frac{V_{max}[S]}{K_m + [S]}$$

When $K_m >> [S]$

Equation (2)
$$v = \frac{V_{max}[S]}{K_m}$$

Therefore

Equation (3) $$\frac{V_{max}}{K_m} = \frac{v}{[S]}$$

A.3 Results

A.3.1 SNPs near FrmB active site disrupt catalytic activity

Mutations in the formylglutathione hydrolase, FrmB, confer resistance to the carboxy ester prodrug POM-HEX in *S. aureus*. POM-HEX requires hydrolysis to inhibit the target enzyme, enolase. As, WT FrmB hydrolyzes POM-HEX, a natural conclusion of these two pieces of evidence is that mutations in FrmB disrupt catalytic activity, thereby conferring protection to POM-HEX. Three of the four observed mutations in FrmB rationally should disrupt protein function. M74X truncates a majority of FrmB including the active site. Two additional mutations, G119D and M122I, are located within the active site and conceivably disrupt protein function (Figure 1A).

To test the hypothesis that FrmB mutations disrupt catalytic activity we substituted G119 and M122 with alanine mutations (Table 1). We utilized the chromogenic esterase substrate, 4-nitrophenyl acetate, which results in a change of absorbance upon hydrolysis. Mutation of G119 to alanine or M122 to alanine results in protein with no detectable activity (Figure 1B).

A.3.2 *Sa*FrmB dimerization may be critical to FrmB function

The last observed mutation conferring resistance to POM-HEX, G14R, is puzzling as the G14 is located on a loop far from the active site (Figure 2A). Size exclusion chromatography indicates that FrmB is a dimer in solution, and the crystal structure of FrmB has two monomers in the asymmetric unit (Figure 2A). Thus, a natural hypothesis is that FrmB is only catalytically active as a dimer and disruption of the dimerization interface results in attenuated catalytic activity.

We next created a FrmB mutation with residue G14 mutated to an arginine. In addition to G14R, we generated two additional mutations in a different portion of the dimerization interface: S32A and V36L (Figure 2B). The resulting mutant proteins exhibit markedly reduced catalytic activity (Figure 2C, Table 3). Each of these mutations exhibits a >6-fold reduction in catalytic specificity which appears to be driven by a lack of enzyme turnover. Taken together, this structural and enzymatic data suggests that FrmB dimerization is important for substrate catalysis, but not substrate binding. Future studies should more rigorously assess the dimeric state of FrmB mutants as well as the binding affinity of FrmB mutants.

A.3.3 The flexible capping domain of FrmB is essential for protein function.

Previous studies on structurally similar esterases have suggested that the flexible cap domain of FrmB may be responsible for substrate specificity (Figure 3A) (3–5). Additionally, mutations in this region may impact the thermostability of the esterase (5). Unfortunately, the flexible cap domain is not entirely resolved in the crystal structure of *Sa*FrmB due to poor electron density. We generated mutations in several residues of the flexible cap domain including I167P, L170D, and G175A (Figure 3A). Surprisingly, each of these mutations completely ablated catalytic activity (Figure 3B, Table 3). I167P likely severely reduces the flexibility of this loop. Likewise, G175A introduces steric hindrance and presumably reduces the flexibility of the capping domain. While L170D adds some steric bulk, likely the more problematic change is the addition of a charge which may alter normal loop movement. In summation, these data suggest that the flexibility of the cap domain is essential for FrmB function. How these mutations impact

substrate utilization and temperature sensitivity, as well as the affect of less drastic substitutions, remains unknown.

A.4 Discussion

FrmB has been identified as an activator of POM-prodrugs in *S. aureus.* Preliminary structure-activity relationships have identified several substrates that are well-cleaved by FrmB but poorly cleaved by human sera, suggesting these substrates may be used to target FrmB for *S. aureus*-specific prodrugs. Here we characterize several domains of FrmB using targeted mutagenesis. We find that mutations in the active site, dimerization interface, and the capping domain all severely attenuate FrmB activity. Notably, mutations to the dimeric interface appear to reduce substrate turnover irrespective of substrate binding. This suggests that dimerization is critical for the catalytic competency of FrmB.

Previous studies have demonstrated esterases requiring dimerization for catalysis (6, 7). Other studies have demonstrated that mutation of the catalytic serine and histidine from other α/β hydrolases results in decreased substrate turnover and binding affinity. Conversely, mutagenesis of the catalytic aspartate only impacts substrate turnover (8). As a result, the prevailing model in the field suggests that esterase dimerization leads to movement of the catalytic aspartate into a catalytically competent orientation.

Further analysis, especially regarding the ability of FrmB to change substrate specificities, are warranted to understand the possibility of FrmB mediated prodrug resistance. Beyond FrmB as a potential prodrug activator, esterases also play an important role in industrial conversion and production of chemicals. Utilizing FrmB as a scaffold for specific esterase activity may be possible.

A.5 Figures
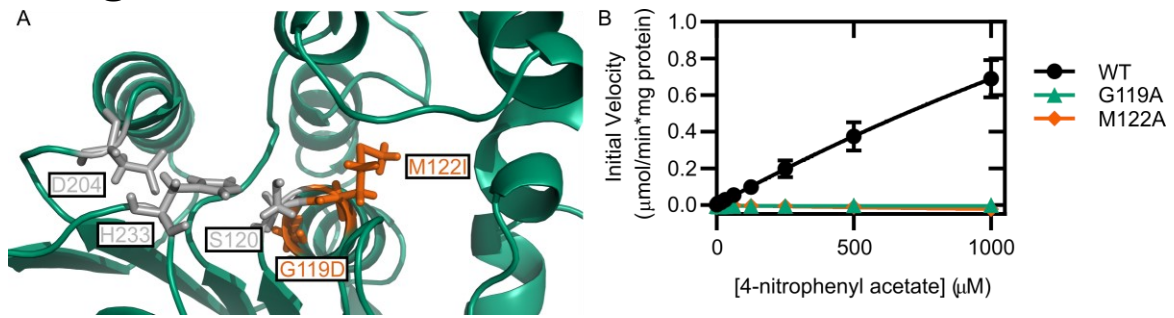
Figure 1 SNPs near the FrmB catalytic triad disrupt FrmB activity. (A) Crystal structure of *Sa*FrmB. Indicated in gray is the catalytic triad, indicated in orange are the mutations observed to confer POM-HEX resistance. (B) Catalytic activity of WT and mutant FrmB. Values are the means of three independent experiments performed in technical duplicate. Error bars denote SD.
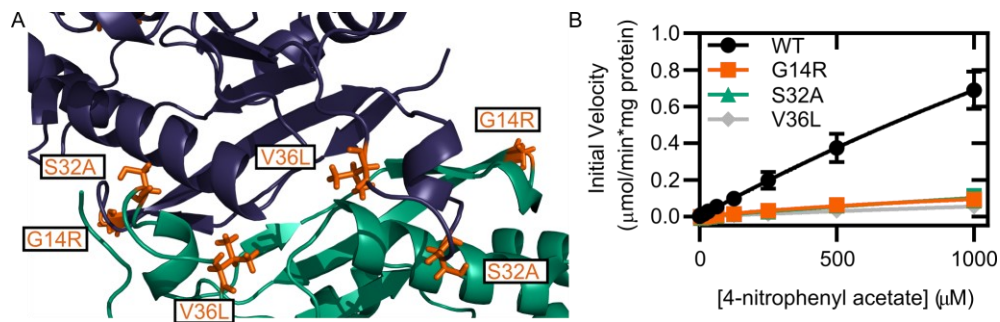
Figure 2 Mutations at the dimerization interface disrupt FrmB activity. (A) Locations of SNP G14R (orange sticks) in relation to catalytic triad (gray spheres). FrmB monomer A in green, monomer B in blue. (B) Location of mutations made at the dimerization interface. (C) Activity of mutant FrmB proteins. Displayed are the means of three independent experiments with technical duplicates. Error bars denote SD.
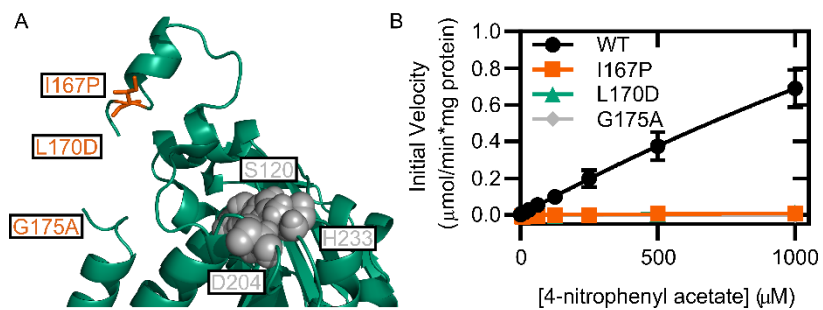
Figure 3. Mutations in the flexible cap of FrmB ablate catalytic activity. A) Locations of mutations made at in the flexible capping domain. Residues 168-175 are not observable in the electron density due to flexibility. Catalytic triad represented in gray spheres. (B) Activity of mutant FrmB proteins. Displayed are the means of three independent experiments with technical duplicates. Error bars denote SD.

A.6 Tables

Table 1. FrmB mutants generated and verified by Biol 4522.

Position	Natural Amino Acid	Substitutions Made	Kinetics Tested
14	Gly	Arg	Arg
32	Ser	Ala	Ala
36	Val	Ala, Leu	Leu
71	Ala	Asp, Trp	Trp
119	Gly	Ala, Cys	Ala
122	Met	Ala, Ser	Ala
167	Ile	Pro	Pro
170	Leu	Ala, Asp	Asp
175	Gly	Ala	Ala
221	Ile	Ala, Glu	Glu
245	Arg	Leu	

Table 2. Primers used during this study

Primer Name	Sequence
S32A Forward	CCGGAAGATCAAAGCTTCTTTAATGCGGATACAACTG
S32A Reverse	CAGTTGTATCCGCATTAAAGAAGCTTTGATCTTCGCG
S32R Forward	CCGGAAGATCAAAGCTTCTTTAATCGGGATACAACTG
S32R Reverse	CAGTTGTATCCCCATTAAAGAAGCTTTGATCTTCGCG
V36A Forward	ACGGATACAACTGCTAAACCATTAAAAACT
V36A Reverse	AGTTTTTAATGGTTTAGCAGTTGTATCGCT
V36L Forward	ACGGATACAACTCTTAAACCATTAAAAACT
V36L Reverse	AGTTTTTAATGGTTTAAGAGTTGTATCGCT
A71D Forward	GCGAATGAACACAAATTAGATGTGATTATGCCCAATGTGG
A71D Reverse	CCACATTGGGCATAATCACATCTAATTTGTGTTCATTCGC
A71W Forward	GCGAATGAACACAAATTATGGGTGATTATGCCCAATGTGG
A71W Reverse	CCACATTGGGCATAATCACCCATAATTTGTGTTCATTCGC
G119C Forward	GACAATTTTATAGCATGTCACTCTATGGGAGGATATGGC
G119C Reverse	GCCATATCCTCCCATAGAGTGACATGCTATAAAATTGTC
G119A Froward	GACAATTTTATAGCAGCTCACTCTATGGGAGGATATGGC
G119A Reverse	GCCATATCCTCCCATAGAGTGAGCTGCTATAAAATTGTC
M122A Forward	CAGGTCACTCTGCGGGAGGATATGGCAC
M122A Reverse	GTGCCATATCCTCCCGCAGAGTGACCTG
M122S Forward	GCAGGTCACTCTTCGGGAGGATATGGCAC
M122S Reverse	GTGCCATATCCTCCCGAAGAGTGACCTGC
I167A Forward	TCAAAAGAGGCCATAGCTGGCAATCTTTCAAGT
I167A Reverse	ACTTGAAAGATTGCCAGCTATGGCCTCTTTTGA
I167P Forward	TCAAAAGAGGCCATACCTGGCAATCTTTCAAGTG
I167P Reverse	CACTTGAAAGATTGCCAGGTATGGCCTCTTTTGA
L170D Forward	GAGGCCATAATTGGCAATGATTCAAGTGTTAAAGGAAC
L170D Reverse	GTTCCTTTAACACTTGAATCATTGCCAATTATGGCCTC
L170P Forward	GACGCCATAATTGGCAATGCTTCAAGTGTTAAAGGA
L170P Reverse	TCCTTTAACACTTGAAGCATTGCCAATTATGGCCTC
G175A Forward	GGCAATCTTTCAAGTGTTAAAGCTACTGAACATGATCCG
G175A Reverse	CGGATCATGTTCAGTAGCTTTAACACTTGAAAGATTGCC
G175H Forward	GGCAATCTTTCAAGTGTTAAACACACTGAACATGATCCG
G175H Reverse	CGGATCATGTTCAGTGTGTTTAACACTTGAAAGATTGCC
I221A Forward	ATTTATCACGCGCAAATGTTCCTTATCAATTTGAAGATGGACC
I221A Reverse	GGTCCATCTTCAAATTGATAAGGAACATTTGCGCGTGATAAAT
I221E Forward	ATTTATCACGCGAAAATGTTCCTTATCAATTTGAAGATGGACC
I221E Reverse	GGTCCATCTTCAAATTGATAAGGAACATTTTCGCGTGATAAAT

Table 3. Michaelis-Menten parameters for mutant FrmB. All values are the results of three independent experiments performed in technical duplicate. N/A indicates that no appreciable activity was detected using 5 μg protein.

Mutant	Kcat/Km (min^{-1}μM^{-1})		Kcat/Km*kuncat (μM^{-1})	
	Mean	SE	Mean	SD
WT	8.31E+02	2.4E+01	4.04E+09	2.50E+09
G14R	1.22E+02	7E+00	5.91E+08	6.70E+08
S32A	1.34E+02	9.7E+00	6.54E+08	9.97E+08
V36L	7.16E+01	6.3E+00	3.48E+08	6.5E+08
A71W	N/A	N/A	N/A	N/A
G119A	N/A	N/A	N/A	N/A
M122A	N/A	N/A	N/A	N/A
I167P	N/A	N/A	N/A	N/A
L170D	N/A	N/A	N/A	N/A
G175A	N/A	N/A	N/A	N/A
I221E	2.88E+01	4.5E+00	1.40E+08	4.61E+08

kuncat (1/min)	2.06E-07	9.7E-09

A.7 References

1.   CDC (2019) Antibiotic resistance threats in the United States 2019. Available at: https://www.cdc.gov/drugresistance/pdf/threats-report/2019-ar-threats-report-508.pdf.

2.   Gonzalez CF, et al. (2006) Molecular basis of formaldehyde detoxification. Characterization of two S-formylglutathione hydrolases from *Escherichia coli*, FrmB and YeiG. *J Biol Chem* 281(20):14514–22.

3.   Hu Y, et al. (2015) Structural and functional analysis of a low-temperature-active alkaline esterase from South China Sea marine sediment microbial metagenomic library. *J Ind Microbiol Biotechnol* 42(11):1449–1461.

4.   Nam KH, et al. (2009) Structural and functional analysis of a novel EstE5 belonging to the subfamily of hormone-sensitive lipase. *Biochem Biophys Res Commun* 379(2):553–556.

5.   Santarossa G, et al. (2005) Mutations in the "lid" region affect chain length specificity and thermostability of a *Pseudomonas fragi* lipase. *FEBS Lett* 579(11):2383–2386.

6.   Li P-Y, et al. (2014) Structural basis for dimerization and catalysis of a novel esterase from the GTSAG motif subfamily of the bacterial hormone-sensitive lipase family. *J Biol Chem* 289(27):19031–41.

7.   Varejão N, et al. (2018) Structural Mechanism for the Temperature-Dependent Activation of the Hyperthermophilic Pf2001 Esterase. *Structure* 26(2):199–208.e3.

8.   Pfeffer JM, Weadge JT, Clarke AJ (2013) Mechanism of Action of *Neisseria gonorrhoeae* O-Acetylpeptidoglycan Esterase, an SGNH Serine Esterase. *J Biol Chem* 288(4):2605–2613.

Appendix B: Carboxy ester prodrug activation by *Plasmodium falciparum*

Preface

This work is unpublished and reflects contributions by Justin J. Miller, Rachel L. Edwards, and Audrey R. Odom John. Experiments were performed by JJM and RLE. Data analysis done by JJM and RLE. All authors contributed to experimental design. AROJ was responsible for securing funding.

B.1 Introduction

Antimalarial drug resistance threatens an already fraught global health issue of enormous scale. In 2018, over 210 million individuals suffered a malaria infection (1). Further, resistance to the current frontline therapy, artemisinin, has become increasingly common and is detected at a significant prevalence (>5%) in south-east Asia, Guyana, Papua New Guinea, and Rwanda (2). New antimalarials are urgently needed to combat this looming crisis.

One approach to drug development which has attracted recent attention is prodrugging. A prodrug is a compound which has been chemically modified to be inactive until converted (chemically or enzymatically) back into the active compound. Prodrugging affords chemists a means of altering the drug-like properties of a drug (e.g. solubility, oral absorption), without modifying the underlying active drug. This is especially attractive when the goal is to develop inhibitors, such as phosphonates, which are otherwise cellularly impermeable as lipophilic promoieties may be attached to confer increased cellular penetrance.

We have previously deployed the lipophilic promoiety, pivaloyloxymethyl (POM) to improve the potency of the isoprenoid biosynthesis inhibitor, fosmidomycin, and several structural analogues (3). Unfortunately, the POM-promoiety is rapidly cleaved by serum esterases returning the less potent phosphonate warhead in any treatment setting (3). Identification of the POM-prodrug activating enzyme(s) of *P. falciparum* will allow for the structure-guided development of promoieties which are specifically activated by *P. falciparum*.

One *P. falciparum* esterase, *Pf*PARE, has recently garnered attention as a prodrug activatior for unbranched or minimally branched C6 esters (4–6). We have previously found that *Pf*PARE mutations do not confer resistance to our prodrugged analogue of fosmidomycin, POM-ERJ (Figure 1). This finding suggests that additional esterases, either parasite or erythrocyte resident, must be responsible for POM-ERJ activation. Here, we attempt to identify the esterase responsible for POM-prodrug activation in *P. falciparum*. We also demonstrate the localization of simple ester prosubstrates in *P. falciparum*, laying the groundwork for future exploration in *P. falciparum* targeted prodrug development.

B.2 Methods

B.2.1 *P. falciparum* maintenance and culturing

The *P. falciparum* strain used for POM-ERJ selection was the *had-1* strain, AM1-G3 (7). For

imaging experiments, the *P. falciparum* strain used was 3D7 (8). Strains were cultured at 37 °C

in a suspension of 2% human erythrocytes in RPMI-1640 medium (Sigma-Aldrich, SKU R4130)

supplemented with 27 mM sodium bicarbonate, 11 mM glucose, 5 mM HEPES, 1 mM sodium

pyruvate, 0.37 mM hypoxanthine, 0.01 mM thymidine, 10 μg ml^{-1} gentamycin, and 0.5%

albumax (Life Technologies) under an atmosphere of 5% O_2/ 5%CO_2 / 90% N_2 as previously

described (9). Culture growth was monitored by microscopic analysis of Giemsa-stained blood

smears.

B.2.2 Selection of POM-ERJ resistant *P. falciparum*

The *had-1* strain, AM1-G3 was used as the parental strain for resistant mutant selection. The

parental strain was seeded at 0.5 % parasitemia in 4 mL cultures at the initiation of POM-ERJ

selection. Parasites were cultured in media containing 60, 120, or 300 nM POM-ERJ (1, 2, and

5x the 3-day half maximal growth inhibitory concentration), and continuously maintained at or

below a parasitemia of 4 %. In some cases, drug was removed from the media once parasites

were no longer visible in culture wells.

B.2.3 Quantification of POM-ERJ resistance

Asynchronous *P. falciparum* cultures were counted microscopically via Giemsa-stained blood

smears and diluted to a parasitemia of 0.5%, prior to being cultured in POM-ERJ concentrations

ranging from 3 μM to 5.9 nM. After 3 days, parasite growth was quantified by measuring DNA

content using PicoGreen (Life Technologies) on a FLUOstar Omega platereader (BMG Labtech) at 485 excitation and 528 emission (10). The half maximal inhibitory concentration (IC_{50}) was calculated by nonlinear regression in GraphPad Prism.

B.2.4 *P. falciparum* microscopic analysis of prodrug activation

Asynchronous cultures of *P. falciparum* 3D7 were enriched for infected erythrocytes using a magnetic cell fractionation system (MACS, Mitenyi Biotec). Parasite cultures were loaded onto a MACS column pre-equilibrated with culture medium and placed within a magnetic field. Parasites were subsequently washed with culture medium until unbound erythrocytes no longer eluted from the column, at which point the column was removed from the magnetic field and infected erythrocytes were recovered in culture media. Immediately prior to cell loading, *P. falciparum* cultures were diluted to a concentration of $5x10^6$ cells/mL and transferred into sterile filtered Dulbecco's phosphate-buffered saline (DPBS) supplemented with 20 mM glucose. Cells were immediately loaded on a bacterial CellASIC Onix microfluidic plate (Millipore Sigma B04A-03) prewarmed to 37 °C and pre-equilibrated with DPBS + 20 mM glucose. Prior to plate loading, CellASIC Onix microfluidic lines were flushed with DPBS + 20 mM glucose or 10 µM fluorescent prosubstrate in DPBS + 1% DMSO + 20 mM glucose.

The microfluidics plate was loaded onto a Nikon Ti-E inverted microscope (Nikon Instruments, Inc) equipped with a 100x Plan N (N.A. = 1.45) Ph3 objective, X-cite 120 LED light source (Lumen Dynamics), and an OrcaERG CCD camera (Hammamatsu Photonics, Bridgewater, N.J), which was used to obtain both phase contrast and fluorescent images. Filter sets were purchased

from Chroma Technology Corporation. Cells were loaded until a single field of view contained 20-50 cells. Following cell loading, PBS was flown through the flow cell (t = 0) and cells were observed in both phase and fluorescent channels for 10 minutes before the flow media was switched to PBS containing 1% DMSO and 10 μM fluorescent pro-substrate. Images were captured every two minutes for a total of 44 minutes, and all experiments were undertaken at 37 °C. The phase contrast exposure time was kept constant at: 200 ms, and the fluorescent channel exposure time was kept constant at 500 ms. For fluorescent images, the gain remained constant across all experiments. Image capture and analysis was performed using Nikon Elements Advanced Research software.

B.3 Results

B.3.1 Generation of POM-ERJ resistant *P. falciparum*

We attempted to generate POM-ERJ resistant *P. falciparum* by culturing the *had1* strain, AM1-G3 in the presence of 1x, 2x, or 5x the half maximal inhibitory concentration (IC_{50}) of POM-ERJ. We selected AM1-G3 as the parental strain as we were interested in identifying the prodrug activating enzymes responsible for POM-ERJ activation, and HAD1 loss appears to be a rapid and easy means of generating resistance to isoprenoid biosynthesis inhibitors. Within 3-5 days of drug application no parasites were visibly replicating in the 2x and 5x IC_{50} conditions. Parasites were cultured continuously in the presence of POM-ERJ, and following 3 weeks of culturing, the 1xIC_{50} condition had robust levels of parasites present. The IC_{50} of these strains against POM-ERJ was determined and found to be insignificantly different than the wild-type parental strain (Figure 2A).

We next attempted an alternative selection method wherein drug is kept in the culture media until parasites are no longer visible and then is removed to allow an expansion of any surviving parasite populations. 2x or 5x the IC_{50} of POM-ERJ was applied to AM1-G3 until parasites were no longer visible via thick smear. Once parasites had recovered, the IC_{50} of these strains against POM-ERJ was again determined and found to be insignificantly different than the parental strain (Figure 2B).

B.3.2 *P. falciparum* carboxyester activation

We next sought to understand where whole-cell *P. falciparum* activates prodrugs. We enriched

for late-stage parasites (trophozoites and schizonts) via magnetic bead sorting and transferred

parasites into a microfluidics device placed under a fluorescence microscope. This microfluidics

device allows for individual cells to be held in place while the surrounding media is rapidly

exchanged. We acquired a 32-compound pro-fluorescent carboxy ester substrate library which

fluoresces upon ester cleavage (11). We selected 2 compounds, 3C and 1O, which display

moderate and high catalytic specificity respectively, for the *Staphylococcus aureus* esterases,

FrmB and GloB, and tracked pro-substrate activation by *P. falciparum* (Figure 3A).

As observed for wild-type *S. aureus*, compound 1O is rapidly activated and the fluorescent signal

reaches saturation within the first frame of the experiment. Conversely, pro-substrate 3C is

slowly activated and the fluorescent signal increases steadily through the course of the

experiment (Figure 3B). As observed in our experiments with *S. aureus*, compound 1O has a

significant amount of background fluorescence, suggesting that the probe has slowly activated

ahead of introduction to the microfluidics device.

One attractive advantage of prodrugs is targeted activation to specific tissues or cellular

compartments. *P. falciparum* has several compartments where prodrug activation could be

targeted, including the parasite cytoplasm, food vacuole, and the surrounding erythrocyte

cytoplasm. Again, using our microfluidics setup we use compound 3C to visualize where the

substrate is activated in *P. falciparum*. Fluorescence predominantly accumulates in the parasite

cytoplasm and appears to be excluded from the parasite food vacuole and the erythrocyte cytoplasm (Figure 4).

While our imaging field was dominated by trophozoites, we were fortunately able to capture some cells infected with early stage schizonts, and one instance of schizonts egressing. We find that trophozoites and early schizonts activate compound 3C to similar levels (Figure 4 middle, bottom). While egressed schizonts still accumulate fluorescence, it is attenuated in comparison to intact schizonts (Figure 4 bottom).

B.4 Discussion

Targeted prodrug delivery to *P. falciparum* is an exciting possibility with potential to fundamentally change drug design for antimalarials. Identifying the malarial enzymes responsible for prodrug activation will allow a structure-guided approach to prodrug development. While one esterase, *Pf*PARE, is responsible for the activation of hexylester prodrugs, it is not responsible for the activation of POM-ERJ (4). This finding is unsurprising as *Pf*PARE does not act on the tertiary carbamate, MMV030666, whose prodrug motif is highly similar to the POM moiety. Unfortunately, the activation mechanism for POM- prodrug motifs by *P. falciparum* remains an intriguing question. Here, we have attempted to identify the *P. falciparum* esterase responsible for POM-prodrug activation, by raising resistance to the prodrug, POM-ERJ.

Unfortunately, we were unsuccessful in generating long-lasting resistance to POM-ERJ. Parasites grew in the presence of inhibitory concentrations of POM-ERJ but were not shown to be resistant to POM-ERJ via a 3-day IC_{50}. Additional studies in this area remain a valuable endeavor and future studies should employ a varied approach in resistance generation, such as the step-up approach where parasites are cultured in low levels of drug and the concentration of drug is slowly increased in response to parasite tolerance. Alternatively, multiple rounds of drug-pulsing may be an appropriate route forward. It is interesting to hypothesize that POM-ERJ may be an "irresistible" drug, however multiple rounds of attempted resistance selection with large pools of parasites being screened before this claim is made. All resistance attempts in this manuscript were carried out using the *had1* null strain, AM1-G3, to reduce the potential number of non-esterase mutations acquired. Resistance should still be achievable in these strains,

however, as *P. falciparum* can become more resistant to the POM-ERJ non-prodrugged analog, fosmidomycin, through loss of HAD2 among other genes (12).

Erythrocyte esterases are a second candidate for antimalarial prodrug activation. While erythrocyte esterase mediated activation does not protect host cells from potential antimalarial toxicity, it still has several appealing benefits. Resistance to hexyl ester prodrugs is rapidly achieved by *P. falciparum* through mutation of *Pf*PARE, however, parasite modification of host esterases would be a substantial feat and is unlikely to occur. Additionally, erythrocyte targeted prodrugs may have an extensive lifetime within the host as the converted drug would be sequestered inside erythrocytes and thus safe from host metabolism and excretion. One major potential drawback to erythrocyte targeted prodrugs is that activated drugs may not transit from the erythrocyte cytoplasm to the parasite cytoplasm. This appears to be the case with the POM-prodrug of the hypoxanthine-guanine-xanthine-phosphoribosyltransferase (HGXPRT) inhibitor, Immucillin-H 5'phosphate (ImmHP) (13). While ImmHP is a potent inhibitor of HGXPRT *in vitro*, it has no activity against whole cell *P. falciparum*. Further investigation has revealed that the POM-prodrug of ImmHP effectively enters the erythrocyte but is rapidly converted back to ImmHP and is unable to enter the parasite cytoplasm to exert its activity.

Ultimately, the localization and timing of prodrug activation across *P. falciparum* lifecycles is an important consideration in antimalarial prodrug development. Here, we have shown that simple lipophilic esters 1O and 3C are activated primarily in the cytoplasm of *P. falciparum* though at different speeds. Expanding the understanding of how prodrugs are activated in *P. falciparum*,

li

specifically how different ester promoieties act, is an important next step for *P. falciparum* prodrug development. Finally, how fast a prodrug needs to activate *in vivo* remains an open question which will dictate prodrug efficacy.

B.5 Figures
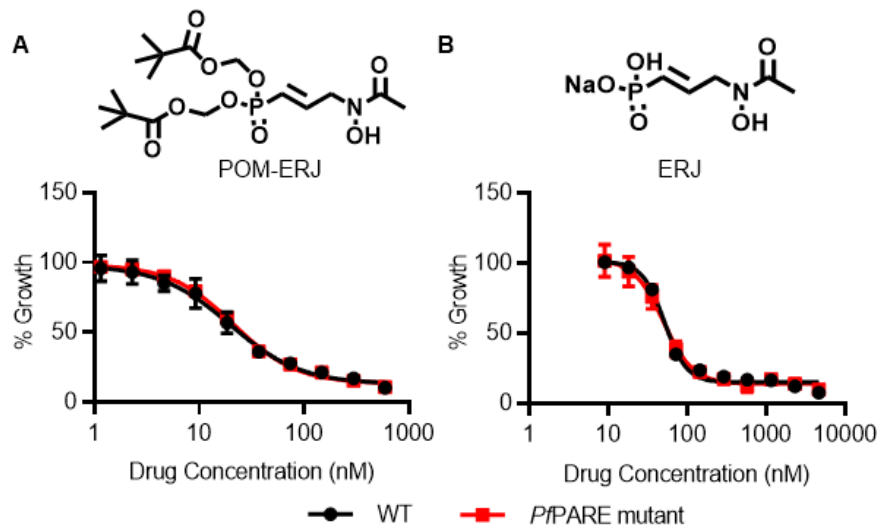
Figure 1 ERJ and POM-ERJ sensitivity of WT and *Pf*PARE mutant *P. falciparum*. Black- wild-type *P. falciparum,* red- *Pf*PARE mutant parasites. IC$_{50}$ determined by Rachel Edwards, points represent the mean of a single biological replicate in technical duplicate (A) ERJ (B) POM-ERJ.
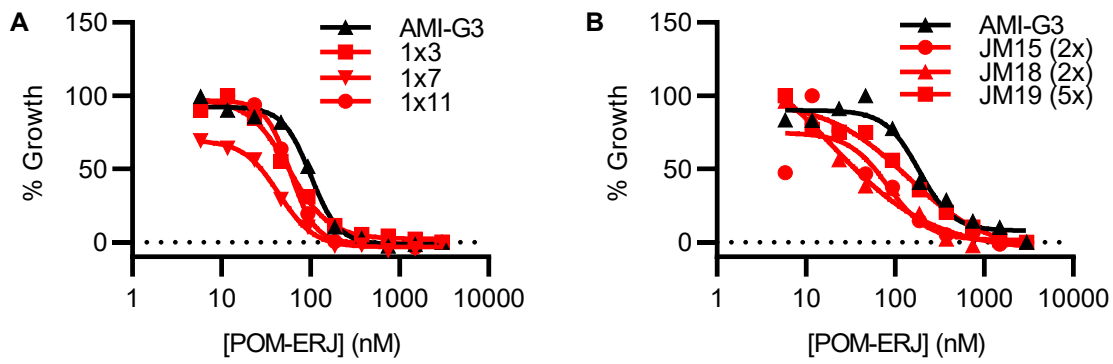
Figure 2 Quantification of POM-ERJ resistance for parasites growing in media containing POM-ERJ. Black- parental strain, AM1-G3, red- parasites grown in POM-ERJ. (A) Parasites grown for 3 weeks in media containing $1xIC_{50}$ POM-ERJ. (B) Parasites pulsed with POM-ERJ until parasites were no longer visible by microscopy. Points represent the mean of a single experiment in technical duplicate.
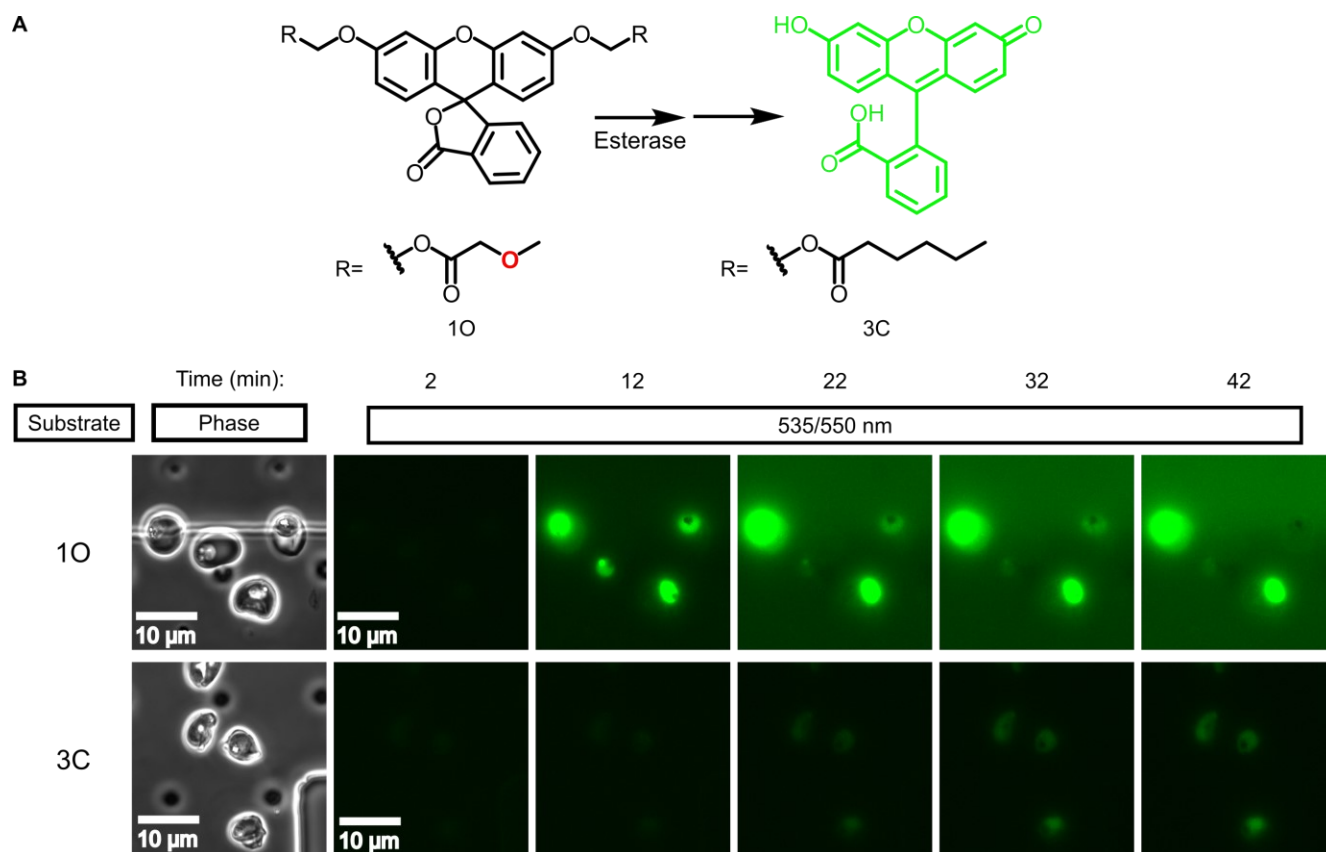
Figure 3 Time-dependent pro-substrate activation by *P. falciparum*. (A) Activation mechanism and structure of pro-fluorescent substrates tested. (B) Time-lapse imaging of single cell *P. falciparum*. Pro-fluorescent substrate was rapidly added to media 10 minutes into the experiment. Images representative of experiments performed in technical duplicate.
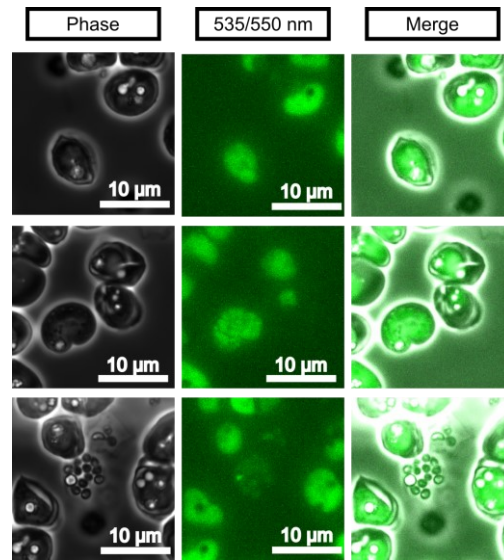
Figure 4 Pro-fluorescent substrate 3C activation by *P. falciparum*. Parasites were incubated with pro-fluorescent substrate for 30 minutes and subsequently imaged. Images representative of experiments performed in technical duplicate.

B.6 References

1.   WHO (World Health Organisation) (2019) World Malaria Report 2019. 1–24.

2.   WHO (World Health Organisation) (2019) Artemisinin resistance and artemisinin-based combination therapy efficacy. Available at: https://www.who.int/docs/default-source/documents/publications/gmp/who-cds-gmp-2019-17-eng.pdf?ua=1.

3.   Edwards RL, et al. (2017) MEPicides: potent antimalarial prodrugs targeting isoprenoid biosynthesis. *Sci Rep* 7(1):8400.

4.   Istvan ES, et al. (2017) Esterase mutation is a mechanism of resistance to antimalarial compounds. *Nat Commun* 8(1):14240.

5.   Butler JH, et al. (2020) Resistance to Some But Not Other Dimeric Lindenane Sesquiterpenoid Esters Is Mediated by Mutations in a *Plasmodium falciparum* Esterase. *ACS Infect Dis*:acsinfecdis.0c00487.

6.   Sindhe KM V., et al. (2020) *Plasmodium falciparum* Resistance to a Lead Benzoxaborole Due to Blocked Compound Activation and Altered Ubiquitination or Sumoylation. *MBio* 11(1). doi:10.1128/mBio.02640-19.

7.   Guggisberg AM, et al. (2015) A sugar phosphatase regulates the methylerythritol phosphate (MEP) pathway in malaria parasites. *Nat Commun* 2(2):1–27.

8.   Gardner MJ, et al. (2002) Genome sequence of the human malaria parasite *Plasmodium falciparum*. *Nature* 419(6906):498–511.

9.   Trager W, Jensen JB (1976) Human malaria parasites in continuous culture. *Science* 193(4254):673–5.

10.   Corbett Y, et al. (2004) A novel DNA-based microfluorimetric method to evaluate antimalarial drug activity. *Am J Trop Med Hyg* 70(2):119–24.

11.   White A, et al. (2018) Fluorogenic structure activity library pinpoints molecular variations in substrate specificity of structurally homologous esterases. *J Biol Chem* 293:13851–13862.

12.   Guggisberg AM, et al. (2018) Suppression of Drug Resistance Reveals a Genetic Mechanism of Metabolic Plasticity in Malaria Parasites. *MBio* 9(6). doi:10.1128/mBio.01193-18.

13.   Hazleton KZ, et al. (2012) Acyclic Immucillin Phosphonates: Second-Generation Inhibitors of *Plasmodium falciparum* Hypoxanthine- Guanine-Xanthine Phosphoribosyltransferase. *Chem Biol* 19(6):721–730.

Appendix C: Volatile Biomarkers of Malaria Infection

Preface

The following review was conceived of, researched, and written by Amalia Berna, myself, and

Audrey R. Odom John. I made the figures. This review has been published in its entirety as a

book chapter in Breathborne Biomarkers and the Human Volaitome (June 2020).

Abstract

Plasmodium falciparum, the primary cause of deadly human malaria, remains a critical global health concern, particularly for young infants and children who are uniquely susceptible to severe disease and death. Unfortunately, the most widespread rapid diagnostics tests for malaria have high false positive rates and are increasingly at risk due to the spread of parasite strains that avoid detection. There is an urgent need for new malaria diagnostics, and the World Health Organization has declared this a key global health priority. Multiple studies indicate that *Plasmodium*-infected hosts are more attractive to *Anopheles* mosquitoes than uninfected and gametocyte negative controls. This altered behavioral preference is likely due to changes in the infected host's odor profile, as reflected in the skin and breath. In this chapter, we examine the changes that *Plasmodium* spp. infection imparts on host odors and the resulting influences on vector behavior. We also review recent studies on human malaria, which have investigated the malaria-induced changes in skin and breath odors in asymptomatic and symptomatic malaria patients.

C.1 Overview of malaria

In 2017, an estimated 219 million cases of malaria occurred worldwide, resulting in an estimated 435,000 deaths. Aggressive global efforts to control malaria over the last fifteen years have been highly successful, with 20 million fewer cases in 2017 than in 2010. However, progress has stalled alarmingly over the last several years [1]. Among the more pressing current challenges to malaria control is the need for additional effective diagnostic tools to detect both symptomatic and asymptomatic infections.

Malaria is caused by infection by protozoan parasites in the genus *Plasmodium*. While several *Plasmodium* spp. infect humans, the majority of severe and life-threatening malaria is due to *P. falciparum* infection. Transmitted person-to-person by *Anopheles* mosquitoes, symptomatic *P. falciparum* malaria is characterized by repeated cycles of asexual replication within mature human erythrocytes. A small proportion of asexual bloodstream parasites undergo sexual differentiation. Ongoing malaria transmission requires consumption of these sexual-stage parasites, termed gametocytes, during blood meals by female *Anopheles*. Malaria diagnostics used for point-of-care clinical diagnostic testing of symptomatic individuals in malaria-endemic areas must be highly sensitive to the presence of asexual bloodstream *Plasmodium* infection. In contrast, a diagnostic test that reflects gametocytemia would impact public health strategies to identify individuals at risk of malaria transmission.

For more than a century, microscopic evaluation of capillary blood samples has been used to identify bloodstream malaria parasites [2]. Highly sensitive and specific nucleic acid-based tests have been also developed [3, 4], but are not readily available in low- and middle-income countries (LMIC) where malaria is endemic. Conversely, lateral-flow-based rapid diagnostic tests (RDTs)

are sensitive and require little training, making them overwhelmingly the method of choice to evaluate for point-of-care diagnosis in malaria-endemic areas. In 2017, 276 million RDTs were sold, and an estimated 75% of diagnostic testing in sub-Saharan Africa was performed by RDT[1].

The current generation of RDTs largely relies on detection of a distinct *P. falciparum*-specific protein, HRP2. Unfortunately, HRP2-based RDTs possess critical weaknesses. False positive RDTs are common as HRP2 can be detected up to one month after malaria clearance, making it impossible to distinguish acute from recent infections [5]. More importantly, HRP2-based RDTs are at risk due to the recent emergence and spread of *P. falciparum* strains that lack HRP2. *Hrp2* null parasites were first reported in 2010 in South America [6], but deletions have subsequently been found in several locations in Africa [7-10]. In a recent study in Eritrea, up to 80% of all patients were infected with *hrp2-* parasites [7]. Computational modeling projects a dramatic rise in RDT-undetectable parasites, as widespread use of RDTs has maintained ongoing selective pressure against parasites that still express HRP2 [11].

Other challenges in the diagnosis of malaria include addressing the large asymptomatic reservoir, as nearly 75% of individuals infected with *Plasmodium* spp. are asymptomatic. Asymptomatic individuals constitute a major source of ongoing transmission, because they are more likely to be bitten by mosquitoes than parasite-free individuals, they do not present for care (and are therefore not diagnosed or treated), and are often mobile, increasing their potential for malaria transmission and geographic spread [12].

Growing evidence suggests that vector mosquito species can differentiate between malaria-infected and uninfected individuals based on odor. This finding has inspired recent work to address the possibility of diagnosing malaria via volatile biomarkers emitted by breath and/or

skin. In this chapter, we examine the changes that *Plasmodium* spp. infection imparts on host odors and the resulting impacts on vector behavior. We also review recent studies on human malaria that have evaluated volatiles from the skin and breath of *Plasmodium*-infected individuals.

C.2 Mosquito attraction to malaria-infected hosts

Female *Anopheles* mosquitoes require mammalian blood meals to mature eggs; however, mosquito biting behavior is highly complex and context-dependent. Mosquitoes detect human hosts using a combination of cues, with olfactory cues being undoubtedly the most important group of external stimuli affecting mosquito behavior [13]. From a distance, female mosquitoes sense CO_2 and preferentially migrate to areas of higher CO_2. As they move closer to the target blood meal, they sense host heat, skin odors, and potentially the breath volatiles of the target host [14]. Increasing evidence, reviewed below, indicates that host volatiles—and, as a result, mosquito behavior—are exploited by mammalian *Plasmodium* spp. parasites, including *P. falciparum*, to increase likelihood of transmission (Figure 1).

Humans infected with *P. falciparum* may be more mosquito-attractive than uninfected humans. For example, investigators evaluated the attraction of *Anopheles gambiae* to 5-12 year old Kenyan children of variable infection status and their uninfected classmates, using a dual-choice olfactometer (a setup which allows testing preference of one odor against another) [15]. *Plasmodium*-infected children were treated with antimalarials and, following parasite clearance, the attraction of mosquitoes to these children was reassessed. Investigators found that *A.*

gambiae mosquitoes were nearly twice as attracted to children carrying high burdens of gametocytes (microscopically visible) than parasite-free individuals, individuals infected with only asexual stages, or individuals carrying sub-microscopic levels of gametocytes [15]. As expected, treatment with antimalarials reduced asexual and sexual-stage parasite levels below the limits of molecular detection. Importantly, following antimalarial treatment, *Plasmodium*-infected children were no longer preferentially attractive to *A. gambiae* mosquitoes. This is in agreement with a previous study by Lacroix et al [16] in which mosquito attractiveness was seen to be approximately double in gametocyte-positive children, relative to uninfected children or those with asexual-stage parasitemia.

While there is increasing evidence that *P. falciparum* infection alters *A. gambiae* host-seeking behavior, it is not clear which volatile compounds may be responsible. To address this question, Robinson et al [17] assessed the behavioral response of *A. gambiae* to the foot odors of 5-12 year old Kenyan school children, before and after antimalarial treatment. Foot odors of asymptomatic *P. falciparum*-infected and -uninfected children were collected on socks over 20 h and extracted for mass-spectrometry analysis. For infected individuals, odors were collected after administration of the first dose of treatment with the antimalarial. Following confirmed parasite clearance (21 days later), odor samples were collected in the same manner from the same children. *A. gambiae* mosquitoes were offered the choice of either Day 1 or Day 21 odor samples from the same child, in a dual-choice cage assay. Investigators found that mosquitoes did not differentiate between Day 1 and Day 21 odor samples from uninfected children but were more attracted to the Day 1 samples from children harboring asexual or gametocyte-stage *Plasmodium* parasites. Somewhat unexpectedly, researchers did not observe the gametocyte-specific effect that was previously described [15, 16]. The authors suggest that imperfect detection of low densities

of gametocytes could play a role in this discrepancy. Alternatively, gametocyte-specific attraction may be communicated through a distinct mechanism.

Non-human animal studies also provide evidence for increased mosquito attractiveness of *Plasmodium*-infected individuals. For example, De Moraes et al [18] evaluated whole-body volatiles from healthy and *P. chabaudi*-infected mice throughout the course of infection. Investigators found that *A. stephensi* were preferentially attracted to infected mice, relative to control mice, during the time period in which mice harbored relatively high levels of gametocytes. The investigators also observed increased attraction to gametocyte-positive vs. gametocyte-negative individuals during this period. Alongside these behavioral studies, the investigators observed distinct body odor profiles between healthy and *Plasmodium*-infected individuals, during both acute and chronic stages of infection. The characteristic components of *Plasmodium*-infected odor profiles were identified by mass spectrometry and subsequently confirmed to increase mosquito attraction individually, when added to the odor of healthy mice. Specifically, hexanoic acid, 2- and 3-methyl butanoic acid, and tridecane were increased in abundance in the odor profiles of malaria-infected animals and displayed a direct relationship with mosquito attractiveness. Conversely, benzothiazole, present in reduced amounts in chronically infected mice, was inversely related with mosquito attraction.

While several studies have focused on identifying the changes in odor profiles resulting from *Plasmodium* infection, fewer studies have focused on the origin of these changes. Three hypotheses currently exist for the basis of *Plasmodium*-dependent odor changes: 1) *Plasmodium* infection leads to changes in the skin microbiome that indirectly change the host odor profile; 2) *Plasmodium* infection stimulates endogenous host changes that alter the host odor profile; and 3) *Plasmodium* spp. directly generate and release malaria-associated volatile compounds.

The direct production of *Plasmodium*-volatile compounds by *Plasmodium* garnered early attention as Kelly et al [19] identified the plant-like terpenes α-pinene and limonene as arising from cultured *P. falciparum*-erythrocytes. Apicomplexan parasites, including *Plasmodium* species, contain an apicoplast, an organelle with a similar endosymbiotic evolutionary origin to plant chloroplasts, which synthesizes isoprenoids (such as α-pinene and limonene) via the methylerythritol phosphate (MEP) pathway. This pathway is not present in animals, though a parallel metabolic route, the mevalonate pathway, does exist. Kelly et al [19] hypothesized that *P. falciparum* parasites might utilize the MEP pathway to produce terpenes and indeed saw that inhibition of the pathway via the MEP-pathway specific inhibitor (fosmidomycin) ablated accumulation of α-pinene and limonene. Interestingly, Emami et al[20] found that, even in the absence of *P. falciparum* parasites, introduction of the isoprenoid precursor (E)-4-hydroxy-3-methyl-but-2-enyl pyrophosphate (HMBPP) altered erythrocyte headspace volatile profiles and increased mosquito attractiveness. Specifically, HMBPP-treated erythrocytes produced higher headspace levels of aldehydes (octanal, nonanal, and decanal) and monoterpenes (α-pinene, ß-pinene, and limonene). This result remains surprising, as there is no clear biosynthetic route to monoterpenes in human erythrocytes and the metabolic origin of these compounds in erythrocytes is enigmatic. There is some overlap in the types of compounds (terpenes and aldehydes) found in *P. falciparum*-infected and HMBPP-treated erythrocytes. Indeed, as noted below, several of these compounds have been also detected in the odor profiles of malaria-infected human subjects [21-24].

Given the important role of host odor profiles on *Anopheles* spp. mosquito attraction, the finding that *Plasmodium* spp. infection consistently alters mosquito attraction provides an important proof-of-concept that malaria parasites reproducibly alter host volatile profiles. Below we review

the current literature on breath and skin odor changes during asymptomatic and symptomatic *Plasmodium* spp. infection in humans.

C.3   Breath odor profiles in asymptomatic malaria

While acute, uncomplicated *P. falciparum* infection in children is most often characterized by fever, a large proportion of *P. falciparum* infections in semi-immune individuals in highly endemic regions will be asymptomatic. As individuals with asymptomatic infections do not present for care, asymptomatic infections are an important public health concern as they represent a hidden reservoir that contributes to persistent malaria transmission. Detecting sub-microscopic infections requires sensitive molecular diagnostic methods, such as polymerase chain reaction (PCR) or loop-attenuated isothermal amplification (LAMP). These molecular diagnostic tests have shown that even in regions of low endemicity, asymptomatic *Plasmodium* spp. infection is common, representing up to 75% of positive individuals in community surveys [25].

To identify biomarkers of asymptomatic malaria, odor profiles of breath and skin have been characterized both under natural field conditions in malaria-endemic regions and during controlled human malaria infection (CHMI). During CHMI, volunteers receive a direct intravenous inoculation of *Plasmodium*-infected erythrocytes, followed by close monitoring and treatment. CHMI trials are increasingly being used to aid vaccine and drug development.

The first study on breath biomarkers of *P. falciparum* CHMI volunteers was published by Berna et al [26]. One liter of breath was collected from each volunteer as malaria infection progressed and additional samples were taken following antimalarial administration. Exhaled breath was collected using sampling bags, and volatiles were then transferred from the bags to sorbent tubes

(Tenax/ Unicarb) via a pump. The authors identified nine compounds whose concentrations varied significantly over the course of malaria infection: carbon dioxide, isoprene, acetone, benzene, cyclohexanone, and 4 thioethers (allyl methyl sulfide, 1-methylthio-propane, (Z)-1-methylthio-1-propene, and (E)-1-methylthio-1-propene) (Table 26.1). The malaria-associated thioethers were of particular interest as a potential disease biomarker, because they have not previously been associated with any pathological condition, and because their concentrations changed during infection for all individuals. Machine learning methods were further applied, which accurately classified all samples into "active infection" and baseline/post-*P. falciparum* clearance on the basis of thioester levels. Of note, due to the nature of CHMI, parasite counts were quite low and gametocytes, which take approximately two weeks to develop, were never detected. Berna et al [26] attempted to detect thioethers in *in vitro* cultures of *P. falciparum*, but did not find any appreciable levels. While the metabolic origin of breath thioethers found during CHMI is not known, these results suggest that interplay between host and parasite metabolic pathways may be required. In a follow-up study, these same researchers [21] found that thioether concentrations in breath exhibit a diurnal cyclical pattern and, in general, thioether levels are significantly higher in *P. falciparum* CHMI volunteers compared to healthy control individuals. Moreover, the authors demonstrated that breath volatiles have a time-of-day variation that impacts the ability to predict *P. falciparum* infection using the thioethers. Additionally, this study found that terpenes (α-terpinene, m-cymene, limonene, and terpinolene) were elevated in the breath of *P. falciparum*-infected individuals. Of these terpenes, limonene had been previously reported to be associated with cultured asexual *P. falciparum*[19]. The top two compounds with the highest classification accuracies (healthy vs *P. facliparum*) were terpinolene (87.7% correct classification), followed by m-cymene (92.7% correct classification).

Malaria-associated volatile biomarkers have also been investigated in skin samples. De Boer et al [23] collected skin odor samples from two cohorts of *P. falciparum* CHMI volunteers. Skin odors were collected by placing one foot of the volunteer into a clean bag, and volatiles from the bag were then pumped into Tenax filter and Porapak filters. Skin odor samples were collected two days prior to parasite challenge, during *Plasmodium* infection, and post-treatment. Foot odor profiles were distinct in *P. falciparum*-challenged individuals. In Table 26.1, we report those volatile compounds that showed significant differences "before treatment" versus "during malaria infection" (qPCR-positive for *P. falciparum*). Several compounds (e.g., sesquiterpene, 1-dodecene, 2-methyl butanal, and dodecanal) increased significantly upon infection. Aldehydes have been previously found in mammalian skin odors and are well recognized as host attractants for hematophagous insects. The authors hypothesize that the increased aldehyde levels found in malarious samples originate from lipid peroxidation, caused by oxidative stress induced by *P. falciparum*. Alternatively, the authors postulate that the aldehydes might be produced directly by *Plasmodium* parasites, as aldehydes are emitted by HMBPP-treated erythrocyte cultures [20]. In parallel with compound identification, researchers performed dual-choice olfactometer experiments to determine whether changes in body odor during *P. falciparum* infection affect mosquito behavior. Unexpectedly, they found reduced attractiveness of parasite positive participants in one cohort and no significant effect of *P. falciparum* infection in a second group. They attributed this discrepancy to the use of different parasite strains in both cohorts. Mature gametocytes were not detected in any of the participants during any portion of this study.

A more recent study also aimed to identify malaria-associated skin odor biomarkers, through evaluation of more than 400 primary school children (aged ≤12 y) in western Kenya [24]. In this study, investigators profiled arm and foot volatiles from each individual, using a portable volatile

collection system. Collection from both sites occurred in parallel, prior to treatment of malaria-positive individuals, and odors were stored on HayeSep adsorbant polymer prior to gas chromatography-mass spectrometry (GC-MS). Machine learning was employed to identify volatile patterns that predicted malaria infection (Table 26.1). Of these, only 2-ethylhexan-1-ol and ethylbenzene were found in both foot and arm samples. Critically, predictive models successfully identified asymptomatic infections with 100% sensitivity in foot samples and 75% sensitivity in arm samples. The majority of the identified foot volatiles increased in concentration during infection, whereas the direction of the change was not specified for the majority of skin volatiles. The authors indicate that all identified compounds have either previously been reported from human volatile collections or have known mechanisms of natural production from humans or potentially human-associated microbes. Interestingly, none of the volatiles reported in this study were also reported from skin volatile profiling from asymptomatic CHMI volunteers [23].

To explore the molecular basis of odor manipulation by malaria, Robinson et al [17] both quantitatively and qualitatively compared the volatile compounds emitted from the feet of asymptomatic infected children in Western Kenya. This work was done in parallel with the mosquito attraction work mentioned earlier in this chapter. Of note is that the study site was the same as De Moraes [24] and Busula [15]. For each child, one foot was placed in a plastic bag, and volatiles were collected in Porapak filters (similar to De Boer et al. [23]) and sampled for 100 min (at 500 mL/min). Detailed infection status (uninfected, infected with low parasitemia, high parasitemia, or infected with gametocytes) was collected using an 18S-based qPCR for *P. falciparum* asexual stages and QT-NASBA qPCR for quantifying gametocytes. (E)-2-decenal was the only compound that showed significant differences if individuals were categorized simply as *Plasmodium*-positive or parasite-free (Table 26.1). The analysis also revealed higher

abundance in the levels of the aldehydes heptanal, octanal, nonanal, (E)-2-octenal, and (E)-2-decenal by infected asymptomatic individuals compared to control (solvent) or empty bag. A positive trend on the levels of these VOCs was also observed when associated to the parasite densities (low and high). Additionally, the ketone 2-octanone was found to be associated with the presence of microscopic gametocytes. Although similar VOC collection technique was used by De Boer et al [23] (from the same research group), none of the compounds identified by De Boer et al were reported in this work. Inconsistencies could be due to the low parasitemia present in De Boer et al [23] as well as the absence of gametocytes.

Taken together, the results from this collection of recent studies on volatiles emitted from skin and breath clearly establish that malaria infection is associated with changes in volatile profiles. Of the malaria-associated VOCs reported (Table 26.1), only nonanal was detected in two independent studies of individuals with asymptomatic parasitemia. However, the two studies problematically disagree about the direction of change with infection: in one study, nonanal levels increase with malaria infection [17]; in the other, nonanal levels decrease[24]. A possible source of this discrepancy may be the variability in volatile collection methods, absorbent materials, and/or analytical techniques employed. While diet is thought to influence breath and skin volatile profiles, both studies in question recruited from the same locality in western Kenya. More broadly, the use of malaria-naïve individuals (as in CHMI) versus naturally infected individuals (in endemic areas) also presents challenges for comparison purposes, as study participants in field studies are likely to have had previous malaria exposure.

C.4 Breath odor profiles of symptomatic *Plasmodium* infection

The first report of candidate diagnostic biomarkers in the breath of symptomatic *P. falciparum*–infected children from a typical malaria-endemic clinical setting was published recently by Schaber et al. [22] Samples were collected in Malawi from children 3–15 years old presenting for care for fever. In the study, 1 L of exhaled breath was collected in a sample bag and transferred to stainless-steel sorbent tube (Tenax/Carbograph/Carboxen). Investigators found global differences in breath VOC composition based on infection status. In addition, six breath volatiles were highly correlated with infection status, and together yielded a classification accuracy of 83%: methyl undecane, dimethyl decane, trimethyl hexane, nonanal, isoprene, and tridecane (Table 26.2). Of these six VOCs, methyl undecane and dimethyl decane levels increased with malaria infection. The only compound that had previously been associated with *Plasmodium* infection was nonanal. *Plasmodium*-infected individuals have decreased levels of skin-emitted nonanal, when arm volatiles were sampled [24]. In contrast, skin-emitted nonanal from the feet of *Plasmodium*-infected individuals was elevated compared to controls [17].

Schaber *et al.* [22] also found significantly increased breath levels of two terpenes, α-pinene (p = 0.04, with 20% higher mean) and 3-carene (p = 0.01, with a 28% higher mean). α-Pinene has been observed reproducibly to arise during *P. falciparum* asexual infection of erythrocytes in culture [19]. In addition, this terpene is a direct, potent, and specific activator of *A. gambiae* odorant receptors [19]. Both α-pinene and the related 3-carene are among the volatiles produced by mosquito-preferred nectar-providing plant species [27]. The investigators postulate that because malaria-induced volatiles are chemically identical to those produced by mosquito-preferred

plants, parasites might produce or induce production of these volatiles in order to hijack mosquito behavior and increase transmission.

Of note, the results of this research group were somewhat distinct from the previous breath metabolite findings reported by Berna et al [26], from a population of naïve healthy adults undergoing CHMI *P. falciparum* infection. Thioethers were not detected, suggesting that parasite densities, parasite stage, or age of host might induce a range of physiological changes in the human body that manifest in the breath and body odor. Alternatively, *P. falciparum* may produce volatiles in a density- or stage-specific manner. Prior parasite exposure may also be required for host-generated volatiles produced during *P. falciparum* infection. The different sorbent material and storage conditions used in both studies, may also contribute to an absence of thioethers in the work of Schaber et al. [22]

De Moraes et al [24] also examined symptomatic *Plasmodium*-infected children at a primary school located in western Kenya. In this work, researchers collected foot and arm volatiles and employed machine learning algorithms to develop predictive models for infection status. The following volatiles were found to be key predictors of malaria: 4-hydroxy-4-methylpentan-2-one, toluene, ethylcyclohexane, and ethylbenzene (Table 26.2). Toluene is notable in that it has previously been reported to be produced by *P. falciparum in vitro* [19] and has also been found to be associated with human skin. De Moraes et al [24] suggest that toluene could be produced by *Clostridium* spp. residing in the human microbiome [28]. Most of the volatiles found by De Moraes et al [24] in arm and foot samples were in lower abundance in *Plasmodium*-infected individuals. Importantly seven of the volatiles reported in symptomatic malaria cases were also detected in samples from asymptomatic *Plasmodium*-infected individuals (VOCs in boldface text - Tables 26.1 and 26.2). Predictive models using foot volatiles exhibited greater sensitivity (91%) than

using arm volatiles (89%). It is important to note that these sensitivities were achieved using samples that were collected over 3 years across 41 schools in western Kenya. Additionally, some subjects were co-infected with multiple *Plasmodium* species, and, in some cases, were co-infected with other organisms including HIV and intestinal helminths.

No volatiles were found in common among studies with symptomatic patients, possibly due to variations in collection methods and/or materials.

C.5 Summary

Despite substantial global investment, malaria remains a serious global health problem. Young infants and children are particularly at risk, with more than 400,000 deaths each year. Over the past decade, rapid diagnostic tests (RDTs) have transformed malaria diagnosis and have been instrumental to malaria control efforts. However, there is an urgent need to develop new malaria diagnostics. Because parasite proteins can persist in the bloodstream long after treatment, "false positive" tests are common in children who do not have malaria, meaning that non-malaria infections can be missed and untreated. Even more ominously, variant parasite strains have emerged, such that in some parts of the world, 80% of parasites are no longer detected by current tests. There is a pressing need for highly sensitive and specific malaria diagnostics that are also simple and affordable. For public health campaigns, noninvasive testing would also represent a major advance, since all current malaria tests require blood samples.

There is mounting evidence that malaria parasites affect the behavior of *Anopheles* mosquito vectors and hosts in ways that increase the contacts between them to favor parasite transmission. Such changes in attractiveness have been demonstrated in both animal and human malaria systems, as well as in other vector-borne disease systems. Body odor, comprising the volatile

compounds emitted from the skin and breath of vertebrates, is the most important cue used by *Anopheles* for host location. While increased attractiveness of *Plasmodium*-infected individuals has been demonstrated in a malaria-endemic setting, remarkably, very few studies have investigated the chemical ecology underlying this phenomenon. Volatiles emitted from human skin, breath, and from cultured human red blood cells are all altered in the presence of *Plasmodium* spp. infection. Of note, the identified volatile biomarkers have been highly variable from study-to-study. These differences may reflect variability in volatile collection methods, absorbent materials, and/or analytical techniques employed. In addition, study populations were distinct with respect to prior exposure to malaria and duration of infection, which may influence the volatile profiles due to presence/absence of gametocytes and parasite densities. However, the reproducible finding that malaria induces volatile changes provides compelling hope for a future malaria diagnostic that identifies both asexual parasitemia and the presence of gametocytes. Future work should include research in different geographical regions using collection methods and analytical techniques similar to those used in previous studies. In addition, a compelling question is how diet, age of host, genetic, and environmental factors affect the volatile fingerprint of malaria-infected individuals. The biological origin of those volatile compounds induced by malaria are yet unknown, and remains an outstanding question of importance in understanding the specificity of these volatiles as biomarkers to be used in a noninvasive diagnostic for malaria.

C.6 Figures

Figure 1 Life cycle of *P. falciparum* and volatile attraction schematic. *(A) Life cycle of Plasmodium falciparum. (B) Human body odor is altered upon malaria infection and attracts Anopheles spp. mosquitoes.*

C.7 Tables

Table 1 Summary of studies on individuals with asymptomatic *Plasmodium* spp. Infection.

Sample type	Compounds	Study population	Ref
Breath	(E)-1-methylthio-1-propene (Z)-1-methylthio-1-propene 1-methylthio-propane allyl methyl sulfide α-terpinene m-cymene limonene terpinolene	Controlled human malaria infection (malaria-naïve adults)	Berna et al [21, 26]
Skin	sesquiterpene 1-dodecene 2-methyl butanal dodecanal	Controlled human malaria infection (malaria-naïve adults); foot odors	De Boer et al [23]
	Foot **nonanal** **2-ethylhexan-1-ol** benzaldehyde 1-ethyl-3-methylbenzene **toluene** **4-hydroxy-4-methylpentan-2-one** **ethylbenzene** **hexanal** **Arm** **2-ethylhexan-1-ol** **ethylbenzene** **toluene** dodecane **octanal** octane 2,4-dimethylhept-1-ene	Naturally infected school-children; foot/arm odors	De Moraes et al [24]
	(E)-2-decenal	Naturally infected school-children; foot/arm odors	*Robinson et al [17]

In bold, volatiles were also found in subjects with symptomatic *Plasmodium* infection (Table 26.2). In blue, levels of volatile increased with infection. In coral, volatile levels decreased with infection. In black, direction of change was not provided. *Volatiles reported in this table are based on comparisons relative to parasite-free individuals vs. all individuals with detectable *Plasmodium* spp. parasitemia.

Table 2 Summary of studies on individuals with symptomatic *Plasmodium* spp. infection.

Sample type	Compounds	Patients/volunteers	Ref
Breath	dimethyl decane isoprene methyl undecane **nonanal** tridecane trimethyl hexane 3-carene α-pinene	Naturally infected children (age 3-15)	Schaber et al [22]
Skin	**Foot** **hexanal** **4-hydroxy-4-methylpentan-2-one** **toluene** ethylcyclohexane **ethylbenzene** 1-ethyl-3-methylbenzene **Arm** **octanal** **2-ethylhexan-1-ol** m-xylene (or p-xylene) **4-hydroxy-4-methylpentan-2-one** **toluene** ethylcyclohexane **ethylbenzene** 2,4-dimethylhept-1-ene	Naturally infected school-aged children; foot/arm odors	De Moraes et al [24]

In boldface, volatiles were also found in subjects with asymptomatic *Plasmodium* infection (Table 26.1). In blue, levels of volatile increased with infection. In coral, volatile levels decreased with infection. In black, direction of change was not provided.

C.8 References

1. WHO. World health organization, global malaria programme. World malaria report. Geneva. 2018.

2. Tangpukdee, N, Duangdee, C, Wilairatana, P, Krudsood, S Malaria diagnosis: A brief review The Korean journal of parasitology 2009; 47:93-102.

3. Kobayashi, T, Gamboa, D, Ndiaye, D, Cui, LW, Sutton, PL, Vinetz, JM Malaria diagnosis across the international centers of excellence for malaria research: Platforms, performance, and standardization Am J Trop Med Hyg 2015; 93:99-109.

4. Walk, J, Schats, R, Langenberg, MCC, Reuling, IJ, Teelen, K, Roestenberg, M, et al. Diagnosis and treatment based on quantitative pcr after controlled human malaria infection Malaria Journal 2016; 15.

5. Wilson, ML Malaria rapid diagnostic tests Clinical Infectious Diseases 2012; 54:1637-41.

6. Gamboa, D, Ho, MF, Bendezu, J, Torres, K, Chiodini, PL, Barnwell, JW, et al. A large proportion of p. Falciparum isolates in the amazon region of peru lack pfhrp2 and pfhrp3: Implications for malaria rapid diagnostic tests PLoS One 2010; 5.

7. Berhane, A, Anderson, K, Mihreteab, S, Gresty, K, Rogier, E, Mohamed, S, et al. Major threat to malaria control programs by plasmodium falciparum lacking histidine-rich protein 2, eritrea Emerg Infect Dis 2018; 24:462-70.

8. Beshir, KB, Sepulveda, N, Bharmal, J, Robinson, A, Mwanguzi, J, Busula, AO, et al. Plasmodium falciparum parasites with histidine-rich protein 2 (pfhrp2) and pfhrp3 gene deletions in two endemic regions of kenya Sci Rep-Uk 2017; 7.

9. Cheng, Q, Gatton, ML, Barnwell, J, Chiodini, P, McCarthy, J, Bell, D, et al. Plasmodium falciparum parasites lacking histidine-rich protein 2 and 3: A review and recommendations for accurate reporting Malaria Journal 2014; 13.

10. Koita, OA, Doumbo, OK, Ouattara, A, Tall, LK, Konare, A, Diakite, M, et al. False-negative rapid diagnostic tests for malaria and deletion of the histidine-rich repeat region of the hrp2 gene Am J Trop Med Hyg 2012; 86:194-98.

11. Watson, OJ, Slater, HC, Verity, R, Parr, JB, Mwandagarlirwa, MK, Tshefu, A, et al. Modelling the drivers of the spread of plasmodium falciparum hrp2 gene deletions in sub-saharan africa Elife 2017; 6.

12. Peprah, S, Tenge, C, Genga, IO, Mumia, M, Were, PA, Kuremu, RT, et al. A cross-sectional population study of geographic, age-specific, and household risk factors for asymptomatic plasmodium falciparum malaria infection in western kenya Am J Trop Med Hyg 2019; 100:54-65.

13. Takken, W, Knols, BGJ Odor-mediated behavior of afrotropical malaria mosquitoes Annual Review of Entomology 1999; 44:131-57.

14. Raji, JI, DeGennaro, M Genetic analysis of mosquito detection of humans Current opinion in insect science 2017; 20:34-38.

15. Busula, AO, Bousema, T, Mweresa, CK, Masiga, D, Logan, JG, Sauerwein, RW, et al. Gametocytemia and attractiveness of plasmodium falciparum-infected kenyan children to anopheles gambiae mosquitoes J Infect Dis 2017; 216:291-95.

16. Lacroix, R, Mukabana, WR, Gouagna, LC, Koella, JC Malaria infection increases atractiveness of humans to mosquitoes PLoS Biol 2005; 3:e298.

17. Robinson, A, Busula, AO, Voets, MA, Beshir, KB, Caulfield, JC, Powers, SJ, et al. Plasmodium associated changes in human odor attract mosquitoes Proceedings of the National Academy of Sciences 2018; 115:E4209-E18.

18. De Moraes, CM, Stanczyk, NM, Betz, HS, Pulido, H, Sim, DG, Read, AF, et al. Malaria-induced changes in host odors enhance mosquito attraction P Natl Acad Sci USA 2014; 111:11079-84.

19. Kelly, M, Su, C-Y, Schaber, C, Crowley, JR, Hsu, F-F, Carlson, JR, et al. Malaria parasites produce volatile mosquito attractants mBio 2015; 6.

20. Emami, SN, Lindberg, BG, Hua, S, Hill, SR, Mozuraitis, R, Lehmann, P, et al. A key malaria metabolite modulates vector blood seeking, feeding, and susceptibility to infection Science 2017; 355.

21. Berna, AZ, McCarthy, JS, Wang, XR, Michie, M, Bravo, FG, Cassells, J, et al. Diurnal variation in expired breath volatiles in malaria-infected and healthy volunteers J Breath Res 2018; 12.

22. Schaber, C, Katta, N, Bollinger, LB, Mwawi, M, Mlotha-Mitole, R, Trehan, I, et al. Breathprinting reveals malaria-associated biomarkers and mosquito attractants J Infect Dis 2018; 217:1553-60.

23. de Boer, JG, Robinson, A, Powers, SJ, Burgers, SLGE, Caulfield, JC, Birkett, MA, et al. Odours of plasmodium falciparum-infected participants influence mosquito-host interactions Sci Rep-Uk 2017; 7.

24. De Moraes, CM, Wanjiku, C, Stanczyk, NM, Pulido, H, Sims, JW, Betz, HS, et al. Volatile biomarkers of symptomatic and asymptomatic malaria infection in humans P Natl Acad Sci USA 2018; 115:5780-85.

25. Bousema, T, Okell, L, Felger, I, Drakeley, C Asymptomatic malaria infections: Detectability, transmissibility and public health relevance Nat Rev Microbiol 2014; 12:833-40.

26. Berna, AZ, McCarthy, JS, Wang, RX, Saliba, KJ, Bravo, FG, Cassells, J, et al. Analysis of breath specimens for biomarkers of plasmodium falciparum infection J Infect Dis 2015; 212:1120-28.

27. Nyasembe, VO, Tchouassi, DP, Kirwa, HK, Foster, WA, Teal, PEA, Borgemeister, C, et al. Development and assessment of plant-based synthetic odor baits for surveillance and control of malaria vectors PLoS One 2014; 9.

28. Peng, G, Hakim, M, Broza, YY, Billan, S, Abdah-Bortnyak, R, Kuten, A, et al. Detection of lung, breast, colorectal, and prostate cancers from exhaled breath using a single array of nanosensors Brit J Cancer 2010; 103:542-51.

Appendix D: The malaria metabolite HMBPP does not trigger erythrocyte terpene release

Preface

The following work was performed by myself and Audrey R. Odom John. I performed all experimental procedures. AROJ and I designed experiments, performed analysis, wrote the manuscript, and prepared the figures. This chapter has been published in its entirety (Miller JJ, Odom John AR, The malaria metabolite HMBPP does not trigger erythrocyte terpene release. *ACS Infectious Disease* September 2020.)

D.1 Abstract

Infection with malarial parasites renders hosts more mosquito attractive than their uninfected, healthy, counterparts. One volatile organic compound, α-pinene, is associated with *Plasmodium* spp. infection in multiple studies and is a known mosquito attractant. However, how malarial infection results in elevated levels of host-associated α-pinene remains unclear. One study suggests that erythrocyte exposure to the malarial metabolite, (E)-4-hydroxy-3-methyl-but-2-enyl pyrophosphate (HMBPP), results in increased levels of α-pinene. Here, we establish that endogenous levels of α-pinene are present in human erythrocytes, that these levels vary widely by erythrocyte donor, and that α-pinene levels are not altered by HMBPP treatment.

D.2 Introduction

Plasmodium falciparum, the primary causative agent of lethal malaria infections, has a two-host life cycle between humans and mosquitoes. Transit between the two hosts is a critical requirement for the parasite lifecycle and represents a substantial population bottleneck(1). Mosquitoes are more attracted to humans(2–5), mice(6), and birds(7) infected with malaria parasites in comparison to uninfected, healthy hosts. This observation has led to the hypothesis that *Plasmodium* species actively manipulate host odor profiles to coordinate transmission to the mosquito. Indeed, changes in the composition of host odor profiles have been observed in humans(8–13) and mice(6) infected with malaria; however the molecular basis for infection-induced changes in volatile organic compound (VOC) production or release remains unknown.

Of particular interest has been the mosquito semiochemical, α-pinene, which is found in higher concentrations in the breath of humans with symptomatic *Plasmodium* infection(8) vs healthy controls. Additionally, α-pinene has been identified in the headspace above *Plasmodium falciparum* infected erythrocytes(14). The VOC α-pinene is a member of the large and bioactive class of molecules termed terpenes. Terpenes are biosynthesized by a variety of plants, soil and environmental organisms, mammalian commensal and pathogenic microbes, and some insects(15–22). α-pinene is a known component of plant-derived odorant blends that are attractive to the *Anopheles* spp. mosquitoes that transmit malaria(23, 24). As for other terpenes, biosynthesis of α-pinene begins with the 5-carbon isoprenoid precursor, isopentyl pyrophosphate (IPP), which is enzymatically condensed with a second molecule of IPP by geranyl pyrophosphate synthase (GPPS) to form the 10-carbon metabolite, geranyl pyrophosphate (GPP).

Subsequent rearrangement and cyclization are catalyzed by a monoterpene synthase (pinene synthase) to yield α-pinene (Figure 1A).

Recently, it was reported that incubation of the microbial metabolite (E)-4-hydroxy-3-methyl-but-2-enyl pyrophosphate (HMBPP) with uninfected human erythrocytes results in increased attraction and feeding behavior of anopheline mosquitoes. Concordantly, an increase in the headspace concentration of α-pinene above HMBPP-treated erythrocytes was also reported(25). HMBPP is a late intermediate in the 2-C-methyl-D-erythritol 4-phosphate (MEP) pathway for synthesis of IPP and downstream isoprenoids (Figure 1A). While eubacteria and apicomplexan parasites, such as *Plasmodium* spp., utilize the MEP pathway for isoprenoid biosynthesis(26), humans utilize a distinct and evolutionarily divergent biosynthetic pathway (mevalonate pathway) to synthesize IPP(27).

The mechanism by which HMBPP exposure of erythrocytes may lead to α-pinene production or release is unclear, but two possibilities may explain these findings. First, HMBPP may serve as an exogenous signal that triggers erythrocytes to release stores of α-pinene which may have accumulated via metabolic, environmental, or dietary routes. A potent activator of human Vγ9Vδ2-T cells(28), HMBPP is recognized as a pathogen-associated molecular pattern (PAMP) through its interaction with butyrophilin receptors(29), suggesting that HMBPP may serve a signaling role to mediate erythrocyte α-pinene release. Alternatively, because HMBPP is itself a precursor to isoprenoids and terpenes in bacteria and plants, this metabolite may be directly incorporated into α-pinene in erythrocytes via the pathway illustrated in Figure 1A, or via an as-

yet-undescribed alternative enzymatic route. However, human erythrocytes do not express the known biosynthetic machinery for synthesis of α-pinene from HMBPP; mammals lack the MEP pathway and specifically do not express the final enzyme in the pathway, IspH, which converts HMBPP to the immediate α-pinene precursor, IPP. Finally, no erythrocyte monoterpene synthases, nor any proteins with the terpene synthase fold, have yet been described that might mediate the final biocatalysis of GPP to α-pinene. In contrast, humans do express other prenyl diphosphate synthase orthologs, and these enzymes have been reported to moonlight as terpene synthases(20–22). For this reason, we sought to interrogate the possibility of HMBPP-triggered, erythrocyte-produced α-pinene.

D.3 Methods

D.3.1 Materials and reagents

(E)-4-hydroxy-3-methyl-but-2-enyl pyrophosphate, HMBPP, was purchased from both Sigma

Aldrich and Echelon Biosciences Incorporated (Salt Lake City, Utah, USA), resuspended at 4

mM in highly purified water, and stored at -80 °C. Human erythrocytes (types A, B, and O,

leukocyte reduced and irradiated) were obtained from the St. Louis Children's Hospital Blood

Bank (St. Louis, Missouri, USA).

D.3.2 Volatile collection and GC-MS analysis

Erythrocytes were washed 3 times with an equal volume of RPMI-1640 media (Sigma-Aldrich,

SKU R4130) supplemented with: 27 mM sodium bicarbonate, 11 mM glucose, 5 mM HEPES, 1

mM sodium pyruvate, 0.37 mM hypoxanthine, 0.01 mM thymidine, 10 µg/mL gentamycin, and

0.5% albumax (Thermo Fisher Scientific, 11020039) and stored at 50% hematocrit at 4 °C. When

testing responses of erythrocytes to HMBPP and water, erythrocytes were stored as 1.4 mL

aliquots in individual 1.5 mL microfuge tubes (Thermo Fisher Scientific, 05-408-129), wrapped

in parafilm (Sigma-Aldrick, SKU P7793) and stored at 4 °C. Prior to sampling, 1 mL 50%

erythrocytes were transferred to 4 mL glass autosampler tubes (Thermo Fisher Scientific, 03-

391-19), closed with screw caps with septa (Thermo Fisher Scientific 03-391-21), and

equilibrated at 38 °C for 15 minutes. Following equilibration, 2.5 µL of 4 mM HMBPP (final

concentration 10 µM) or purified water were added to the erythrocytes, caps were closed, and

parafilm was used to seal the vial. Volatiles were immediately collected from the headspace

using solid phase micro-extraction (n=5, randomized order for each sample). Directly before

sampling, the Divinylbenzene/Caboxen/Polydimethylsiloxane fiber (Sigma-Aldrich, SKU

57348) was conditioned for 30 minutes at 225 °C in the inlet of an Agilent 7890A gas chromatographer. Headspace sampling occurred over 30 minutes with temperatures maintained at 38 °C. Following sampling, the collected volatiles were desorbed onto the injector of the Agilent 7890A gas chromatographer with an Agilent HP-5MS column (30m, 0.25-mm inner diameter, 0.25-μm film thickness) and interfaced with an Agilent 5975C mass spectrometer. Throughout the run, the inlet temperature was held constant at 225 °C. Injection was performed in the splitless mode for one minute before split vent opening. The oven program followed a linear temperature gradient, with an initial temperature of 60 °C (held for 2 minutes), a ramp of 10 °C/min until 225 °C, and a final hold for 5 minutes at 225 °C. Helium was used as the carrier gas with a constant flow of 1 mL/min (25.6 cm/sec). The transfer line temperature was held constant at 300 °C. Ionization was performed using electron ionization, with an ion source temperature, electron energy, and emission current set at 230 °C, 70 eV, and 300 μA respectively. Mass spectra were acquired in scan mode between 40.0 and 170.0 m/z. α-pinene was identified based on retention time of an analytical standard (Sigma-Aldrich, SKU 80605), and abundance was quantified using the area under the curve of extracted ion 93. Integration was performed in Agilent MassHunter (Version B.05.00 Build 5.0.519.0) using the Agile integrator. To measure the background contamination of HMBPP with α-pinene 2.5 μL of 4 mM HMBPP (final concentration 10 μM) was added to 1 mL of erythrocyte storage media.

An α-pinene standard curve was generated through the addition of 2.5 μL of commercial α-pinene diluted in hexanes to autosampler tubes containing 1 mL pure water and sampled as with erythrocyte treatments. Tested concentrations of α-pinene were 500 ng, 250 ng, 100 ng, 75 ng, 50 ng, 25 ng, 10 ng, and 0 ng (hexanes spiked into water). Standard curve generated by measuring samples in three independent experiments. The limit of detection was defined as 3

times the area under the curve (ion 93) at the retention time for commercial α-pinene in negative

controls containing only water and sampled as with erythrocytes.

D.3.3 Measuring α-pinene time-dependent concentration

To measure α-pinene loss over time, 14 mL of washed erythrocytes were placed in a 15 mL

conical (Sigma-Aldrich, SKU CLS430791) and stored at 4°C. For some experiments, analytical

α-pinene, diluted in water, was added to a final concentration of 10 ng/mL in erythrocytes at the

time of aliquoting. During the experiment, erythrocytes were stored, capped, on ice and

iteratively sampled from. Volatile collection and GC-MS analysis proceeded as above.

D.4 Results

D.4.1 Erythrocytes do not release α-pinene upon HMBPP exposure

We established a working method for sampling the volatile organic compounds associated with cultured erythrocytes. Similar to Emami *et al*., we sealed donated human erythrocytes within a closed, airtight chromatography vial, prewarmed to 38 $^{\circ}$C, and performed headspace sampling using solid phase microextraction (SPME) (Figure 1B) (25). Headspace composition was determined using gas chromatography-mass spectrometry. Using a pure commercial α-pinene standard, we established the sensitivity and dynamic range of this assay (Figure 1C), yielding a signal-to-noise ratio of 3 and a limit-of-detection of 0.3 ng α-pinene (area under the curve for ion 93, 2.36 x 10^3) . Accommodating volumes up to 1 mL of blood, we can detect α-pinene blood concentrations as low as 2.2 nmol/L. We next sought to determine whether α-pinene was present in the headspace above untreated erythrocytes. Indeed, we confirmed that α-pinene can be detected in the headspace from donor erythrocytes, and both the retention time and mass spectra match that of the pure α-pinene standard (Figure 1D,E).

A previous study had indicated that treatment of human erythrocytes with the microbial metabolite HMBPP leads to substantial release of α-pinene. To control for batch-to-batch variability in low-level contaminants present in purified HMBPP, we acquired HMBPP from two independent chemical suppliers. Headspace sampling from both pure preparations of HMBPP confirmed that neither had contaminating levels of α-pinene above our limit-of-detection (Figure 2A). We next treated erythrocytes with either HMBPP or water (vehicle control) and quantified headspace α-pinene. Because monoterpenes such as α-pinene can diffuse into the ambient air, we pre-aliquoted all blood samples into sealed individual-use aliquots. Treatment of erythrocytes

with HMBPP did not result in increased levels of α-pinene (Figure 2B), and this finding was not donor-dependent. A previous study also indicated that levels of other monoterpenes (β-pinene and limonene), as well as several aldehydes (octanal, nonanal, and decanal), were increased in response to HMBPP treatment. While we searched for the presence of these additional VOCs they were not detected in our assay. Our studies thus indicate that if erythrocytes can sense HMBPP, this signal is not accompanied by a substantial release of α-pinene within the thirty minutes our experiment proceeded. Alternatively, if erythrocytes do incorporate HMBPP for the direct *de novo* synthesis of α-pinene, it does not occur during the thirty minutes our experiment proceeded.

D.4.2 Erythrocyte α-pinene levels are donor-dependent

In the course of the above experiments, we noted substantial donor-to-donor variability in the endogenous levels of α-pinene present in a given erythrocyte culture. We therefore secured erythrocytes from an additional 3 independent, unrelated donors and quantified α-pinene levels as before. We find that α-pinene levels are strongly dependent on donor identity and range widely among our 6 donors (Figure 3). We find that blood α-pinene concentrations range from 0.37 ng/mL - 2.57 ng/mL (mean and standard deviation, 0.91 +/- 0.84 ng/mL). While biosynthesis of α-pinene has not been documented in humans, α-pinene is a volatile component of several common dietary plants, suggesting that one explanation for the variability in α-pinene levels is due to the variability in diet of individual donors. Alternatively, α-pinene may be synthesized by members of the human microbiome that may contribute to endogenous α-pinene levels. Unfortunately, blood samples were provided anonymously with no dietary recall or additional sampling available, prohibiting additional analysis.

D.4.3 α-pinene levels deplete with repeated sampling

To reconcile our findings with previous studies that had reported HMBPP-induced α-pinene release we hypothesized that loss of volatile α-pinene through diffusion, following repeated sampling of the same sample over time, may be a possible explanation for the results observed by the previous study. To test this hypothesis, we filled a single air-tight sample tube with erythrocytes from a single donor. At t=0, we removed 1 mL of erythrocytes from the conical tube and measured the headspace concentration of α-pinene according to our previous assay. We left the remainder of the sample sealed (Figure 4A). We repeated this process for a total of 10 iterations, allowing the tube of erythrocytes to reequilibrate for one hour between sampling. We find that α-pinene levels decrease by 25-60% (100 * first run / final run) as a result of repeated sampling (Figure 4B). As expected given its vapor pressure (4.75 mm Hg at 25 °C), α-pinene is in a vapor-liquid equilibrium(30). Each time our pooled erythrocytes are uncapped and sampled, vaporous α-pinene diffuses away, and a new vapor-liquid equilibrium is established. The total concentration of liquid α-pinene is thus depleted over time, thereby resulting in a reduced pool of α-pinene in each subsequent sampling. To confirm that this is not unique to α-pinene naturally absorbed within erythrocytes, we supplemented erythrocytes with 10 ng/mL (73.4 nM) α-pinene and found that α-pinene levels drop by 66-80% over the course of repeated sampling (Figure 4C).

D.5 Discussion

While run-to-run variability and the run-order effect is a commonly observed problem for mass spectrometry, our results highlight an additional precaution that needs to be taken when sampling biologically generated volatiles. All samples should be aliquoted and sealed in an air-tight container prior to the start of the experiment, as repeated sampling from the same container will result in artificially decreased volatile concentration over time. Investigators should continue to control for run-order effects by randomizing the order in which samples are run.

While mounting evidence suggests that *Plasmodium* infection alters host odor profiles and results in increased mosquito attraction, the mechanism by which this occurs remains unclear. One class of molecules, terpenes, notably α-pinene, has been repeatedly highlighted for being both mosquito attractive and enriched during *Plasmodium* infection. The metabolic origin of terpenes during *Plasmodium* infection remains unclear as mammals do not express orthologs of the terpene synthases required for terpene production. Here, we establish that endogenous levels of α-pinene are present in human erythrocytes. While α-pinene levels from erythrocytes from a single donor sample are highly reproducible, α-pinene levels vary widely by erythrocyte donor. While the source of erythrocyte α-pinene remains enigmatic, it is possible that α-pinene may be dietary in origin, explaining the donor-to-donor variability that we observe.

While HMBPP-mediated α-pinene release has been previously reported(25), we do not find evidence that the headspace of HMBPP-treated erythrocytes contains increased levels of α-

pinene. HMBPP-treated erythrocytes also appear more mosquito attractive than untreated erythrocytes(25). Human erythrocytes bind several chemokines(31, 32) and human Vγ9Vδ2-T cells actively respond to HMBPP(28), raising the possibility that HMBPP exposure of erythrocytes may result in other properties that increase mosquito attraction, independent of α-pinene release. CO_2 emission from erythrocytes has also been reported to be elevated upon HMBPP exposure. As CO_2 is also a mosquito semiochemical(33, 34), elevated CO_2 levels could be responsible for mosquito attraction to HMBPP-treated erythrocytes. However, supplementation of 5 ppm CO_2 to untreated erythrocytes was not sufficient to sway mosquitoes from HMBPP-treated erythrocytes.

Subsequent experiments are needed to identify the origin of *Plasmodium* infection-associated volatiles. Infection of germ-free animal models may be valuable in discerning volatiles that arise from microbiome vs. host or *Plasmodium* parasite metabolism. Identification of either human or malarial terpene synthases or metabolic labeling studies are required to understand the origin of *Plasmodium* infection-associated terpenes. Carefully controlled dietary recall studies are necessary to understand whether erythrocyte endogenous α-pinene is biosynthesized by humans or human microbiome members.

D.6 Figures
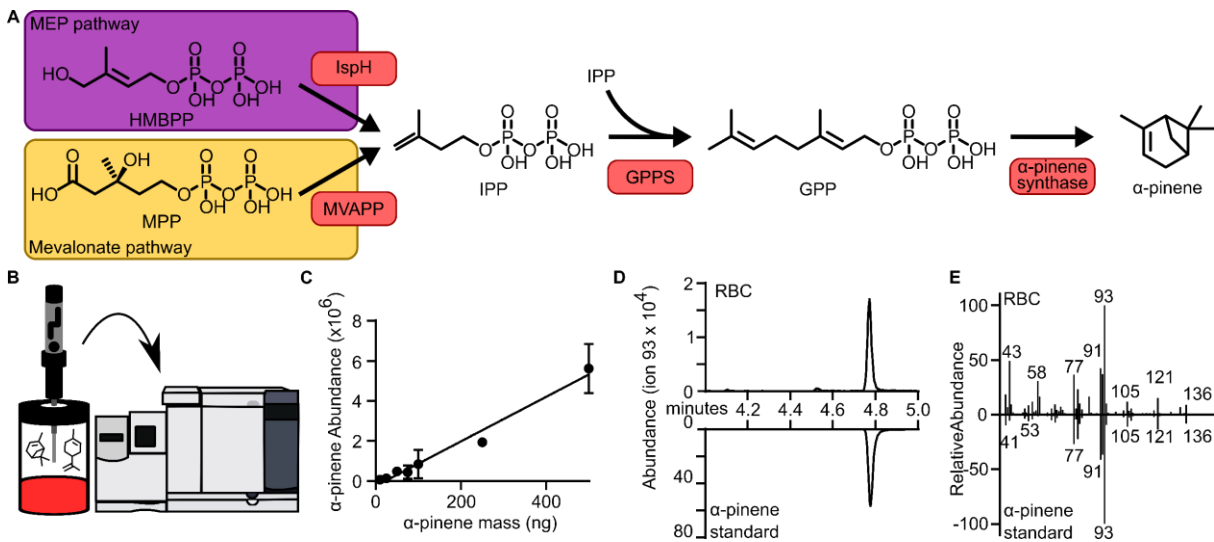
Figure 1. α-pinene biosynthesis and detection. (A) Metabolic pathways leading to α-pinene. Enzymes highlighted with salmon boxes. HMBPP- E-4-hydroxy-3-methyl-but-2-enyl pyrophosphate, MPP- mevalonate pyrophosphate, IPP- isopentenyl pyrophosphate, GPP- geranyl pyrophosphate. (B) Schematic of α-pinene detection assay. (C) α-pinene standard curve generated using commercial α-pinene over a range of 500 ng/mL to 0 ng/mL. Displayed are the means of standards measured in triplicate, error bars denote SD. (D) gas chromatography-mass spectroscopy trace of commercial α-pinene (bottom) and erythrocyte headspace (top) for α-pinene parent ion, 93. (E) Mass spectra from retention time 4.77 min, the elution time for commercial α-pinene, for erythrocyte headspace (top) and commercial α-pinene (bottom).
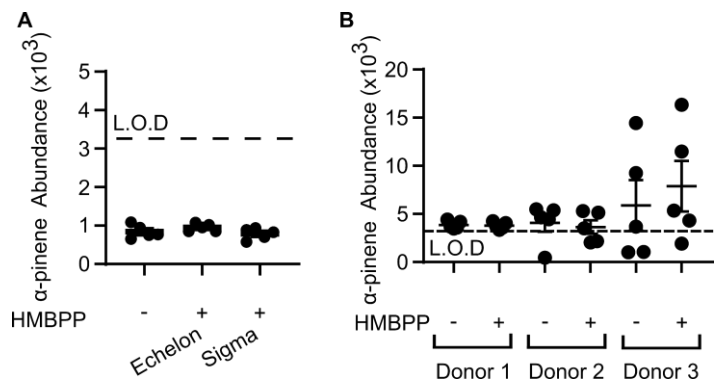
Figure 2. Erythrocytes do not release α-pinene following HMBPP exposure. (A) α-pinene abundance in HMBPP from Echelon Biosciences, Sigma Aldrich, or vehicle control (water). (B) Erythrocyte α-pinene abundance following treatment with HMBPP or vehicle control (water). Values are not significantly different by Mann-Whitney U test (Donor 1: p = 0.841, Donor 2: p = 0.548, Donor 3: p = 0.420). All assays performed with n = 5. Line indicates the mean of each sample, with error bars indicating standard error of the mean.
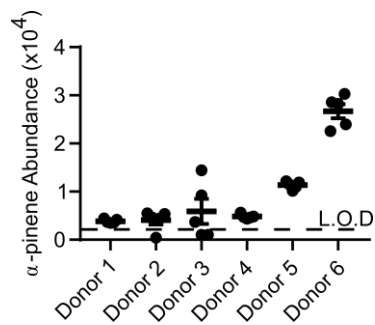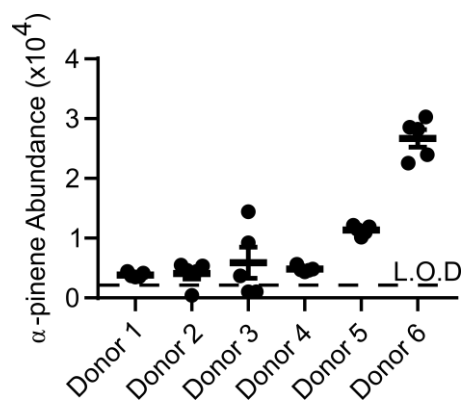
Figure 3 α-pinene abundance in the headspace of untreated human erythrocytes, n = 5.

Figure 4. α-pinene levels decrease with repeated sampling. (A) Schematic of repeated sampling mechanism. Time between each sampling is one hour. At each sampling, one mL erythrocytes are removed and the headspace composition of the removed cells is assessed. (B, C) Headspace concentration of α-pinene over untreated human erythrocytes (B) or erythrocytes (C) supplemented with 10 ng/mL commercial α-pinene as a function of GC-MS run (and accordingly number of tube openings). Displayed are the values of experiments performed in duplicate, with connecting lines indicating an individual replicate.

D.7 References

1. Alavi Y, et al. (2003) The dynamics of interactions between *Plasmodium* and the mosquito: a study of the infectivity of *Plasmodium berghei* and *Plasmodium gallinaceum*, and their transmission by *Anopheles stephensi, Anopheles gambiae* and <i>Aedes aegypt. *Int J Parasitol* 33(9):933–43.

2. Koella JC, Sørensen FL, Anderson RA (1998) The malaria parasite, *Plasmodium falciparum*, increases the frequency of multiple feeding of its mosquito vector, *Anopheles gambiae* . *Proc Biol Sci* 265(1398):763–8.

3. Lacroix R, Mukabana WR, Gouagna LC, Koella JC (2005) Malaria infection increases attractiveness of humans to mosquitoes. *PLoS Biol* 3(9):1590–1593.

4. Busula AO, et al. (2017) Gametocytemia and attractiveness of *Plasmodium falciparum*–infected Kenyan children to *Anopheles gambiae* mosquitoes. *J Infect Dis* 216(3):291–295.

5. Batista EP, Costa EF, Silva A a (2014) *Anopheles darlingi (Diptera: Culicidae)* displays increased attractiveness to infected individuals with *Plasmodium vivax* gametocytes. *Parasit Vectors* 7(1):251.

6. De Moraes CM, et al. (2014) Malaria-induced changes in host odors enhance mosquito attraction. *Proc Natl Acad Sci U S A* 111(30):11079–84.

7. Cornet S, Nicot A, Rivero A, Gandon S (2013) Malaria infection increases bird attractiveness to uninfected mosquitoes. *Ecol Lett* 16(3):323–329.

8. Schaber CL, et al. (2018) Breathprinting reveals malaria-associated biomarkers and mosquito attractants. *J Infect Dis* 217(10):1553–1560.

9. Berna AZ, et al. (2018) Diurnal variation in expired breath volatiles in malaria-infected and healthy volunteers. *J Breath Res* 12(4):46014.

10. De Moraes CM, et al. (2018) Volatile biomarkers of symptomatic and asymptomatic malaria infection in humans. *Proc Natl Acad Sci* 115(22):5780–5785.

11. Berna AZ, et al. (2015) Analysis of breath specimens for biomarkers of Plasmodium falciparum infection. *J Infect Dis* 212(7):1120–1128.

12. Robinson A, et al. (2018) Plasmodium-associated changes in human odor attract mosquitoes. *Proc Natl Acad Sci U S A* 115(18):E4209–E4218.

13. de Boer JG, et al. (2017) Odours of *Plasmodium falciparum*-infected participants influence mosquito-host interactions. *Sci Rep* 7(1):9283.

14. Kelly M, et al. (2015) Malaria parasites produce volatile mosquito attractants. *MBio* 6(2):1–6.

15. Stotzky G, Schenck S (1976) Volatile organic compounds and microorganisms. *CRC Crit Rev Microbiol* 4(4):333–82.

16. Cane DE, Ikeda H (2012) Exploration and mining of the bacterial terpenome. *Acc Chem Res* 45(3):463–72.

17. Yamada Y, et al. (2015) Terpene synthases are widely distributed in bacteria. *Proc Natl Acad Sci* 112(3):857–862.

18. Ditengou FA, et al. (2015) Volatile signalling by sesquiterpenes from ectomycorrhizal fungi reprogrammes root architecture. *Nat Commun* 6:6279.

19.   Mann FM, Peters RJ (2012) Isotuberculosinol: the unusual case of an immunomodulatory diterpenoid from Mycobacterium tuberculosis. *Medchemcomm* 3(8):899–904.

20.   Beran F, et al. (2016) Novel family of terpene synthases evolved from trans-isoprenyl diphosphate synthases in a flea beetle. *Proc Natl Acad Sci* 113(11):2922–2927.

21.   Gilg AB, Tittiger C, Blomquist GJ (2009) Unique animal prenyltransferase with monoterpene synthase activity. *Naturwissenschaften* 96(6):731–735.

22.   Lancaster J, et al. (2018) De novo formation of an aggregation pheromone precursor by an isoprenyl diphosphate synthase-related terpene synthase in the harlequin bug. *Proc Natl Acad Sci* 115(37):E8634–E8641.

23.   Wondwosen B, et al. (2018) Sweet attraction: sugarcane pollen-associated volatiles attract gravid Anopheles arabiensis. *Malar J* 17(1):90.

24.   Wondwosen B, et al. (2016) Rice volatiles lure gravid malaria mosquitoes, *Anopheles arabiensis*. *Sci Rep* 6(1):37930.

25.   Emami SN, et al. (2017) A key malaria metabolite modulates vector blood seeking, feeding, and susceptibility to infection. 4563(February):1–9.

26.   Lange BM, Rujan T, Martin W, Croteau R (2000) Isoprenoid biosynthesis: the evolution of two ancient and distinct pathways across genomes. *Proc Natl Acad Sci U S A* 97(24):13172–7.

27.   Goldstein JL, Brown MS (1990) Regulation of the mevalonate pathway. *Nature* 343(6257):425–30.

28.   Eberl M, et al. (2003) Microbial isoprenoid biosynthesis and human γδ T cell activation. *FEBS Lett* 544(1–3):4–10.

29.   Rigau M, et al. (2020) Butyrophilin 2A1 is essential for phosphoantigen reactivity by γδ T cells. *Science (80-)* 367(6478):eaay5516.

30.   Daubert T, Danner R (1989) *Physical and Thermodynamic Properties of Pure Chemicals: Data Compilation* (Washington, DC: Taylor & Francis).

31.   Darbonne WC, et al. (1991) Red blood cells are a sink for interleukin 8, a leukocyte chemotaxin. *J Clin Invest* 88(4):1362–9.

32.   Neote K, Darbonne W, Ogez J, Horuk R, Schall TJ (1993) Identification of a promiscuous inflammatory peptide receptor on the surface of red blood cells. *J Biol Chem* 268(17):12247–9.

33.   Omondi BA, Majeed S, Ignell R (2015) Functional development of carbon dioxide detection in the maxillary palp of *Anopheles gambiae*. *J Exp Biol* 218(15):2482–2488.

34.   Dekker T (2005) Carbon dioxide instantly sensitizes female yellow fever mosquitoes to human skin odours. *J Exp Biol* 208(15):2963–2972.